Modeling and simulation of near-wall combustion of renewable fuels

Zur Erlangung des akademischen Grades Doktor-Ingenieur (Dr.-Ing.)
genehmigte Dissertation von Yujuan Luo aus China
Tag der Einreichung: November 29, 2022, Tag der Prüfung: January 25, 2023

1. Gutachten: Prof. Dr.-Ing. Christian Hasse
2. Gutachten: Prof. Dr. rer. nat. habil Ulrich Maas
Darmstadt – D 17

TECHNISCHE
UNIVERSITÄT
DARMSTADT

STFS
Simulation of reactive Thermo-Fluid Systems

Modeling and simulation of near-wall combustion of renewable fuels

Doctoral thesis by Yujuan Luo

1. Review: Prof. Dr.-Ing. Christian Hasse
2. Review: Prof. Dr. rer. nat. habil Ulrich Maas

Date of submission: November 29, 2022
Date of thesis defense: January 25, 2023

Darmstadt – D 17

List of papers

This thesis was written during my time as Ph.D. candidate since 2019 at the Institute of Simulation of reactive Thermo-Fluid Systems (STFS) of the Department of Mechanical Engineering at the Technical University of Darmstadt. Parts of the work have already been included in the following publications:

[1] **Y. Luo**, C. Strassacker, X. Wen, Z. Sun, U. Maas, and C. Hasse. Strain rate effects on head-on quenching of laminar premixed methane-air flames. *Flow, Turbulence and Combustion* 106(2) (2021), 631–647.

[2] **Y. Luo**, C. Strassacker, C. Hasse, and U. Maas. Simulation of side-wall quenching of laminar premixed flames with manifold-based reduced kinetic models implemented in generalised coordinates. *Combustion Theory and Modelling* 25(4) (2021), 669–694.

[3] **Y. Luo**, C. Strassacker, U. Maas, and C. Hasse. Model reduction on the fly: Simultaneous identification and application of reduced kinetics for the example of flame-wall interactions. *Proceedings of the Combustion Institute* (2022). DOI: https://doi.org/10.1016/j.proci.2022.07.227.

[4] **Y. Luo**, C. Strassacker, F. Ferraro, F. Zentgraf, A. Dreizler, U. Maas, and C. Hasse. A manifold-based reduction method for side-wall quenching considering differential diffusion effects and its application to a laminar lean dimethyl ether flame. *International Journal of Heat and Fluid Flow* 97 (2022), 109042.

[5] **Y. Luo**, F. Ferraro, A. Breicher, H. Böttler, A. Dreizler, D. Geyer, C. Hasse, and A. Scholtissek. A novel flamelet manifold parametrization approach for lean CH_4–H_2-air flames. *International Journal of Hydrogen Energy* 48(1) (2023), 407–421.

[6] **Y. Luo**, M. Steinhausen, D. Kaddar, C. Hasse, and F. Ferraro. Assessment of flamelet manifolds for turbulent flame-wall interactions in Large-Eddy Simulations. *submitted to Combustion and Flame* (2023).

Other publications not included in the thesis:

[7] M. Steinhausen, **Y. Luo**, S. Popp, C. Strassacker, T. Zirwes, H. Kosaka, F. Zentgraf, U. Maas, A. Sadiki, A. Dreizler, et al. Numerical investigation of local heat-release rates and thermo-chemical states in side-wall quenching of laminar methane and dimethyl ether flames. *Flow, Turbulence and Combustion* 106(2) (2021), 681–700.

[8] A. Stagni, **Y. Luo**, M. Steinhausen, A. Dreizler, and C. Hasse. Chemistry effects in the wall quenching of laminar premixed DME flames. *Combustion and Flame* 232 (2021), 111529.

[9] J. Bissantz, J. Karpowski, M. Steinhausen, **Y. Luo**, F. Ferraro, A. Scholtissek, C. Hasse, and L. Vervisch. Application of dense neural networks for manifold-based modeling of flame-wall interactions. *Applications in Energy and Combustion Science* 13 (2023), 100113.

Acknowledgments

The work could not be accomplished without guidance and support from my supervisors, colleagues, families and friends. At this point, I would like to thank all people who contributed to the completion of this work.

Firstly, I would like to express my greatest thanks to my supervisor, Prof. Dr.-Ing. Christian Hasse, for his supervision, advice and encouragement during my doctoral studies. His abundant experiences and novel insights in the field of combustion and numerical simulation have helped me to grow rapidly in this professional area. He was always patient to answer my questions and willing to provide suggestions. There were warm encouragements from him when I faced difficulties and failures, which gave me great confidence to move on. Besides, his seriousness in work has inspired me a lot.

Besides, I would like to thank Prof. Dr. rer. nat. habil. Ulrich Maas from Karlsruhe Institute of Technology (KIT), not only for making reports on my thesis, but also for his tremendous support and help during my research. He always quickly answered my questions when I started the new project that I had no experience at all, and gave a lot of useful suggestions to improve the quality of my work.

I would also like to say thanks to Prof. Dr. habil. Andreas Dreizler from Technical University of Darmstadt (TU Darmstadt) and Prof. Dr.-Ing. Dirk Geyer from Darmstadt University of Applied Sciences for their valuable suggestions on publications.

Moreover, I wish to give my special thanks to Dr. Federica Ferraro. She provided not only a lot of professional advice on my investigations, but also much help in research related stuff.

The success of this work mostly attributes to various great collaborations, both externally and internally. During the past three years, I really enjoyed collaborating with Dr.-Ing. Christina Strassacker from KIT, and want to express my sincere gratitude to her. I'm grateful that we can have so many excellent collaborations and publications together. I'll never forget our enormous e-mails regarding the development of the methods and paper revision, her special drive from Karlsruhe to Darmstadt for discussion, and her accompany until the late night before the deadline of the Combustion Symposium. For me, we are not just collaborators, but good friends as well. It was also a pleasure to work with Prof. Dr. Alessandro Stagni from Politecnico di Milano so that I could have the opportunity to learn how to analyze the combustion processes from another perspective. I also appreciate the collaboration with Dr. Thorsten Zirwes from KIT, who provided DNS datasets for my research and answered my questions with regard to OpenFOAM.

Besides external partners, I would also like to thank my colleagues from STFS, TU Darmstadt and RSM, TU Darmstadt. Many thanks to Dr. Arne Scholtissek, Dr. Xu Wen, Dr. Zhen Sun, Dr. Sandro Gierth, Matthias Steinhausen, Driss Kaddar, Hannes Böttler and Dr. Xinyi Chen for the fruitful discussions , as well as their guidance in ULF, OpenFOAM and pyFLUT codes and other academia stuff. Additionally, I would like to thank Dr.-Ing. Florian Zentgraf and Adrian Breicher for providing experimental data and useful discussions. Moreover, I would like to express my thanks to Andrea Pati, Hanna Reinhardt, Philip Haspel and Magnus Kircher for providing help in registration, account renewal and computational resources, etc. Also, I want to thank all other colleagues whose names are not mentioned here and I feel very happy to work with them.

The financial support from the Darmstadt Graduate School of Excellence Energy Science and Engineering (GSESE) and the computational resources provided by the Lichtenberg High Performance Computer at TU Darmstadt are highly appreciated.

Finally, I would like to thank my families for their selfless love and unconditional support, which give me the greatest motivation to move forward. Thanks to my friends for their accompany.

Yujuan Luo Darmstadt, im November 2022

Abstract

The downsizing concepts in the design of modern combustion engines and gas turbines result in an increased surface-to-volume ratio in combustion chambers, which amplifies the influence of flame-wall interaction (FWI). Due to the low temperature in the near-wall region, the flame structure may be significantly altered and quenching is likely to occur, which leads to lower combustion efficiency and increased pollutant formation. Therefore, near-wall combustion is substantially different from unconfined combustion. Furthermore, the coexistence of heat loss and other phenomena such as differential diffusion effects, mixing-induced mixture fraction variation, and turbulence brings additional complexity.

In order to gain a deep understanding of the unique characteristics caused by FWI, combustion processes in a small vicinity of the wall need to be investigated in detail. Besides experimental measurements, numerical simulations have become an increasingly powerful tool for such purposes. Although fully resolved simulations with detailed kinetics provide the most accurate results and are useful for comprehensive analyses, they are usually adopted in simple configurations. For complicated industrial applications, manifold-based reduced kinetic models represent an ideal alternative that is able to reduce the computational cost significantly while maintaining high accuracy.

Based on the above background, this thesis mainly contributes to the development and application of manifold-based reduced kinetic models for near-wall combustion. Specifically, this thesis deals with (1) analyses of the fundamentals of the FWI processes, providing guidance for modeling, (2) the development of manifold-based reduced kinetic models with different levels of complexity, and (3) the application of various manifold-based reduced kinetic models.

Different scenarios where near-wall combustion plays a role are investigated numerically. Starting from the simplest canonical configuration for FWI, one-dimensional laminar premixed head-on quenching (HOQ) is simulated with detailed kinetics and transport. Unlike previous studies that focused only on unstrained conditions, the relevance of the underlying flow is taken into consideration in the present study. The focus is the analysis of the influence of the strain rate and finding suitable parameters that can characterize the strain rate both for propagating and quenching flamelet manifolds. As for the two-dimensional laminar side-wall quenching (SWQ) setup, efforts are put on the development of reduced kinetics based on Reaction-Diffusion Manifolds (REDIM) generated and formulated within the framework of generalized coordinates. Compared to the manifold-based reduced kinetic models in thermokinetic coordinates that were adopted in all previous related studies, this kind of new model presents advantages in dealing with non-invariant manifolds. Different models are proposed for scenarios where strong heat losses exist without and with prominent differential diffusion effects, respectively. Model validation is carried out on configurations where experimental data is available. As an extension, an *on the fly* technique is further developed to reduce the dependence of the model accuracy on the *a-priori* identification of the system. While it was shown for laminar FWI that the choice of the manifold is crucial in the fully coupled simulations, this has not been investigated for turbulent FWI yet. To fill the gap, three different flamelet manifolds: Flame-Generated Manifold (FGM), the Quenching Flamelet-Generated Manifold (QFM), and the Quenching Flamelet-Generated Manifold with Exhaust Gas Recirculation (QFM-EGR), are coupled to the Large-Eddy Simulations (LES) of turbulent SWQ of a premixed CH_4-air flame. The performance of the manifolds is assessed by comparison with

the flame-resolved simulation, and the advantages and disadvantages of each model are identified and discussed.

Being a carbon-free energy carrier, hydrogen is a promising substitute for fossil fuels. To enable its application in combustion chambers, detailed investigations on the FWI of H_2-enriched fuels are necessary. As a starting point, a new flamelet model extended from the FGM used in turbulent SWQ is proposed to simultaneously include multiple complex physics that may appear in realistic configurations, such as differential diffusion effects, heat losses, and mixing of different streams. The new model is validated for a CH_4-H_2-air Bunsen flame by comparing the results with those from the detailed kinetic simulation and experiments.

Kurzzusammenfassung

Die Downsizing-Konzepte bei der Konstruktion moderner Verbrennungsmotoren und Gasturbinen führen zu einem erhöhten Oberflächen-Volumen-Verhältnis in den Brennkammern, wodurch der Einfluss der Flamme-Wand-Wechselwirkung (FWI) verstärkt wird. Aufgrund der niedrigen Temperatur im wandnahen Bereich kann die Flammenstruktur erheblich verändert werden, und es ist wahrscheinlich, dass es zu Flammenverlöschung kommt. Das führt zu einer geringeren Verbrennungseffizienz und einer erhöhten Schadstoffbildung. Daher unterscheidet sich die wandnahe Verbrennung wesentlich von der Verbrennung ohne Wände. Zusätzlich erhöht die Koexistenz von Wärmeverlusten und anderen Phänomenen, wie differenzieller Diffusion, Schwankungen des Mischungsbruchs oder Turbulenz, zusätzlich die Komplexität.

Um ein tieferes Verständnis der besonderen Charakteristiken von FWI zu erlangen, müssen die Verbrennungsprozesse in unmittelbarer Nähe der Wand im Detail untersucht werden. Neben experimentellen Messungen haben sich numerische Simulationen zu einem zunehmend leistungsfähigen Werkzeug für solche Zwecke entwickelt. Obwohl vollständig aufgelöste Simulationen mit detaillierter Kinetik die genauesten Ergebnisse liefern und für umfassende Analysen nützlich sind, werden sie gewöhnlich für einfache Konfigurationen eingesetzt. Für komplizierte industrielle Anwendungen stellen mannigfaltigkeitsbasierte, reduzierte kinetische Modelle eine ideale Alternative dar, welche die Rechenkosten erheblich senken und gleichzeitig eine hohe Genauigkeit beibehalten.

Vor diesem Hintergrund trägt diese Arbeit hauptsächlich zur Entwicklung und Anwendung mannigfaltigkeitsbasierter reduzierter kinetischer Modelle für die wandnahe Verbrennung bei. Konkret geht es in dieser Arbeit um (1) Analysen der grundlegenden Prozesse der FWI, die Erkenntnisse für die Modellentwicklung liefern, (2) die Entwicklung mannigfaltigkeitsbasierter reduzierter kinetischer Modelle mit unterschiedlichen Komplexitätsgraden und (3) die Anwendung verschiedener mannigfaltigkeitsbasierter reduzierter kinetischer Modelle.

Verschiedene Szenarien, bei denen die wandnahe Verbrennung eine Rolle spielt, werden numerisch untersucht. Das eindimensionale laminare vorgemischte Head-On Quenching (HOQ), die einfachste kanonische Konfiguration für FWI, wird mit detaillierter Kinetik und Transport simuliert. Im Gegensatz zu früheren Studien, die sich nur auf ungesteckte Flammen konzentrierten, wird in der vorliegenden Arbeit die Relevanz der zugrunde liegenden Strömung berücksichtigt. Der Schwerpunkt ist die Analyse des Einflusses der Streckungsrate und der Suche nach geeigneten Parametern, um die Streckungsrate in Flamelet-Mannigfaltigkeiten sowohl für frei propagierende, als auch verlöschende Flammen charakterisieren zu können. Für das zweidimensionale laminare senkrechte Flammenverlöschen (SWQ) wird ein reduziertes Modell auf der Basis von Reaktions-Diffusions-Mannigfaltigkeiten (REDIM) in generalisierten Koordinaten entwickelt. Im Gegensatz zu den auf physikalischen Koordinaten basierenden Mannigfaltigkeiten, die in allen früheren Studien verwendet wurden, bietet diese Art von Modell Vorteile im Umgang mit nicht-invarianten Mannigfaltigkeiten. Es werden verschiedene Modelle für Szenarien vorgeschlagen, in denen starke Wärmeverluste ohne und mit ausgeprägter differentieller Diffusion auftreten. Die Validierung des Modells erfolgt anhand von Konfigurationen, für die experimentelle Daten verfügbar sind. Weiterhin wird eine *on-the-fly* Technik entwickelt, um die Abhängigkeit von der Modellgenauigkeit von der *a-priori* Identifikation des Systems zu redizueren. Während für die laminare FWI gezeigt wurde, dass die Wahl der Mannigfaltigkeit für die vollständig gekoppelten

Simulationen entscheidend ist, wurde dies für die turbulente FWI noch nicht untersucht. Um diese Lücke zu schließen, werden drei verschiedene Flamelet-Mannigfaltigkeiten: Flame-Generated Manifold (FGM), Quenching Flamelet-Generated Manifold (QFM), und Quenching Flamelet-Generated Manifold with Exhaust Gas Recirculation (QFM-EGR) in einer gekoppelten Large-Eddy-Simulationen (LES) einer vorgemischten CH_4-Luft-Flamme untersucht, die senkrecht an den Wänden verlischt. Die Vorhersagegüte wird durch den Vergleich mit einer flammenaufgelösten Simulation bewertet, und die Vor- und Nachteile jedes Modells ermittelt und diskutiert.

Als kohlenstofffreier Energieträger ist Wasserstoff ein vielversprechender Ersatz für fossile Brennstoffe. Um seine Anwendung in Brennkammern zu ermöglichen, sind detaillierte Untersuchungen zur FWI von H_2-angereicherten Brennstoffen nötig. Als Ausgangspunkt wird ein neues Flamelet-Modell, basierend auf dem FGM, der auch in der turbulenten SWQ Konfiguration verwendet wurde, vorgeschlagen, um gleichzeitig mehrere komplexe physikalische Faktoren zu berücksichtigen, die in realistischen Konfigurationen auftreten können, wie z. B. Diffusionseffekte, Wärmeverluste und die Vermischung verschiedener Ströme. Das neue Modell wird für eine CH_4-H_2-Luft-Bunsenflamme validiert, indem die Ergebnisse mit denen einer detaillierten kinetischen Simulation und Experimenten verglichen werden.

Table of Contents

List of papers iii

Acknowledgments vii

Abstract ix

Kurzzusammenfassung xi

1 Introduction 1
- 1.1 Background and motivation . . . 1
- 1.2 State of the art in flame-wall interaction studies . . . 2
  - 1.2.1 Head-on quenching . . . 2
  - 1.2.2 Side-wall quenching . . . 4
- 1.3 Chemistry reduction . . . 6
- 1.4 Aim of this work . . . 7
- 1.5 Structure of this work . . . 8

2 Fundamentals of reacting and turbulent flows 11
- 2.1 Reacting flows . . . 11
  - 2.1.1 Governing equations . . . 11
  - 2.1.2 Modeling of species diffusion . . . 13
  - 2.1.3 Chemical kinetics . . . 14
- 2.2 Premixed combustion . . . 15
  - 2.2.1 Flame stretch . . . 15
  - 2.2.2 Flame speed . . . 16
  - 2.2.3 Flame thickness . . . 17
  - 2.2.4 Quantification of differential diffusion effects . . . 17
- 2.3 Turbulence . . . 18
  - 2.3.1 Statistical description of turbulent flows . . . 18
  - 2.3.2 Computational approaches for turbulent flows . . . 19
  - 2.3.3 Subgrid models in Large-Eddy Simulations . . . 21

3 Combustion modeling 25
- 3.1 Manifold-based reduced kinetic models . . . 25
  - 3.1.1 REDIM . . . 25
  - 3.1.2 Flamelet-based approaches . . . 26
- 3.2 REDIM-based CFD simulations for laminar flames . . . 28
  - 3.2.1 Reduced model equations in generalized coordinates . . . 29
  - 3.2.2 Reduced model equations in thermokinetic coordinates . . . 30
- 3.3 LES of turbulent flames . . . 30
  - 3.3.1 Turbulence-chemistry interaction . . . 30
  - 3.3.2 Flamelet-based reduced model equations in thermokinetic coordinates . . . 33

3.4 Special treatment of CO with tabulated chemistry . . . 33
3.5 CFD implementation . . . 34

4 Strained laminar premixed CH_4-air head-on quenching 35
4.1 Numerical implementation . . . 35
4.1.1 Numerical description . . . 36
4.1.2 Computational domain and boundary conditions . . . 37
4.1.3 Dimensionless parameters . . . 37
4.2 Results and discussion . . . 38
4.2.1 Comparison between the simulation and the experiment . . . 38
4.2.2 Global quenching quantities . . . 39
4.2.3 Local thermo-chemical states . . . 41
4.2.4 Strain rate effects on differential diffusion . . . 42
4.2.5 Guidance to near-wall flamelet modeling . . . 45
4.3 Summary . . . 46

5 Laminar premixed CH_4-air side-wall quenching 47
5.1 Numerical implementation . . . 47
5.1.1 Numerical description . . . 48
5.1.2 Computational domain . . . 50
5.1.3 Boundary conditions . . . 51
5.2 Validation . . . 51
5.3 Results and discussion . . . 54
5.3.1 Comparison of reduced model equations in different coordinates . . . 54
5.3.2 Simplification of gradient estimations . . . 58
5.4 Summary . . . 62

6 Model reduction *on the fly* for the example of laminar premixed CH_4-air side-wall quenching 63
6.1 Numerical implementation . . . 63
6.2 Results and discussion . . . 64
6.3 Summary . . . 69

7 Laminar premixed DME-air side-wall quenching 71
7.1 Numerical implementation . . . 72
7.1.1 Numerical description . . . 72
7.1.2 Computational domain and boundary conditions . . . 75
7.2 Results and discussion . . . 76
7.3 Summary . . . 81

8 Turbulent premixed CH_4-air side-wall quenching 83
8.1 Numerical implementation . . . 83
8.1.1 Numerical description . . . 84
8.1.2 Computational domain and boundary conditions . . . 84
8.2 Results and discussion . . . 84
8.2.1 Comparison of mean quantities . . . 85
8.2.2 Comparison of probability distribution functions . . . 88
8.2.3 Prediction of flame-vortex interaction . . . 90
8.3 Summary . . . 93

9 Laminar CH_4-H_2-air Bunsen flames **95**
9.1 Numerical implementation . . . 96
9.1.1 Numerical description . . . 96
9.1.2 Computational domain and boundary conditions . . . 99
9.2 Results and discussion . . . 100
9.2.1 Comparison between detailed kinetics and experimental results . . . 100
9.2.2 Comparison between detailed kinetics and FGM results . . . 101
9.3 Summary . . . 103

10 Summary and outlook **105**

Bibliography **107**

Nomenclature **121**

List of Figures **121**

List of Tables **129**

Appendix A: Grid dependency study for the laminar CH_4-air side-wall quenching simulations **131**

Appendix B: Validation of the reduced model equations in generalized coordinates for head-on quenching **133**

Appendix C: An *a-priori* analysis for FGM, QFM, and QFM-EGR **135**

Appendix D: Workflow of FGM-3D and FGM-4D **137**

Appendix E: An *a-priori* analysis for FGM-3D and FGM-4D **139**

Appendix F: Comparison of equilibrium states from FGM-3D and FGM-4D approaches **141**

1 Introduction

1.1 Background and motivation

Combustion is a major way to obtain energy in modern society. According to bp Statistical Review of World Energy 2022 [10], 82% of the world's primary energy demand in 2020 was satisfied by the combustion of fossil fuels, and this high level of fossil fuel energy consumption almost kept unchanged between 2019 and 2021. It is predicted that fossil fuels will still make important contributions to the energy supply in the near future [10]. However, for fossil fuel combustion, the major issue is the emission of carbon dioxide (CO_2), unburned hydrocarbons (UHCs), carbon monoxide (CO), nitrogen oxides (NO_x), and soot, which brings damages to the climate and the environment. Within such a context, enormous efforts have been made to find suitable clean substitutes and develop low-carbon energy systems. For example, H_2, as a carbon-free fuel, is attracting increasing attention worldwide. Therefore, in the long run, combustion will still be of importance, and continuous improvements in combustion technology are still required.

Flame-wall interaction (FWI) is a common phenomenon in confined combustion systems such as gas turbines or internal combustion engines (IC engines). During this process, the flame structure is altered by the presence of the wall, and quenching may occur. Due to the low temperature in the near-wall region, the combustion efficiency is reduced and pollutants are formed. These are different characteristics compared with unconfined combustion. Deep insights into FWI processes are being increasingly necessary since downsizing concepts have become a trend in the design of energy systems [11].

As a promising alternative chemical energy carrier, the application of H_2 in combustion chambers is gaining great interest. Therefore, the investigation on H_2-related FWI becomes important, e.g., providing guidance for the design and renovation of combustors. However, H_2 exhibits special combustion characteristics different from common hydrocarbon fuels, such as high reactivity and diffusivity, wide flammability limits, high flame speed, and ignition propensity. These properties represent challenges for its usage in combustion chambers [12] that are related to combustion instabilities, ignition and blow-off, thermal load, as well as pollutant formation and safety. Therefore, using pure H_2 as fuel requires significant modifications to existing combustors. Based on the current infrastructure and technology, blending H_2 into natural gas is a feasible option for the forthcoming transition to pure H_2 combustion. To ensure the safety and effective control of combustors operating with H_2-enriched fuels, deeper insights into the combustion characteristics of the fuel blends are required.

Numerical simulations represent an increasingly powerful tool for investigating the combustion processes, in addition to theoretical analyses and experiments. For both laminar and turbulent combustion, simulations with detailed kinetics provide the most accurate prediction results, which enables detailed investigations of the complex combustion processes. However, since transport equations have to be solved for all species involved, high computational costs are required for detailed kinetic simulations. Therefore, their current application mainly focuses on simple or generic configurations. Within this context, a simplification of the chemistry description may allow the possibility for simulations of real combustion chambers, since it is effective in reducing the computational effort. One promising approach is to use the manifold-based reduced kinetic models, which are further developed in this work to take into account (1) the essential physics involved in the flame-wall interaction, e.g., strong heat losses, and (2) other aspects such as differential diffusion and mixing related to a realistic flame configuration.

1.2 State of the art in flame-wall interaction studies

Head-on quenching (HOQ) and side-wall quenching (SWQ) are two canonical configurations of flame-wall interaction (FWI). In HOQ, the flame moves perpendicular to the wall, and starts to quench when the heat loss to the wall exceeds the heat released by the chemical reactions. In SWQ, the flame propagates parallel to the wall, with only a small part of the flame tip quenching at the wall. Both HOQ and SWQ may happen in flow fields that can be either laminar or turbulent. Turbulent HOQ and SWQ are both transient processes, due to the strong variation of the flow field. In laminar flows, the HOQ process still changes with time, while the SWQ process is almost in a quasi-stationary state. Typical experimental HOQ and SWQ configurations are presented in Fig. 1.1.

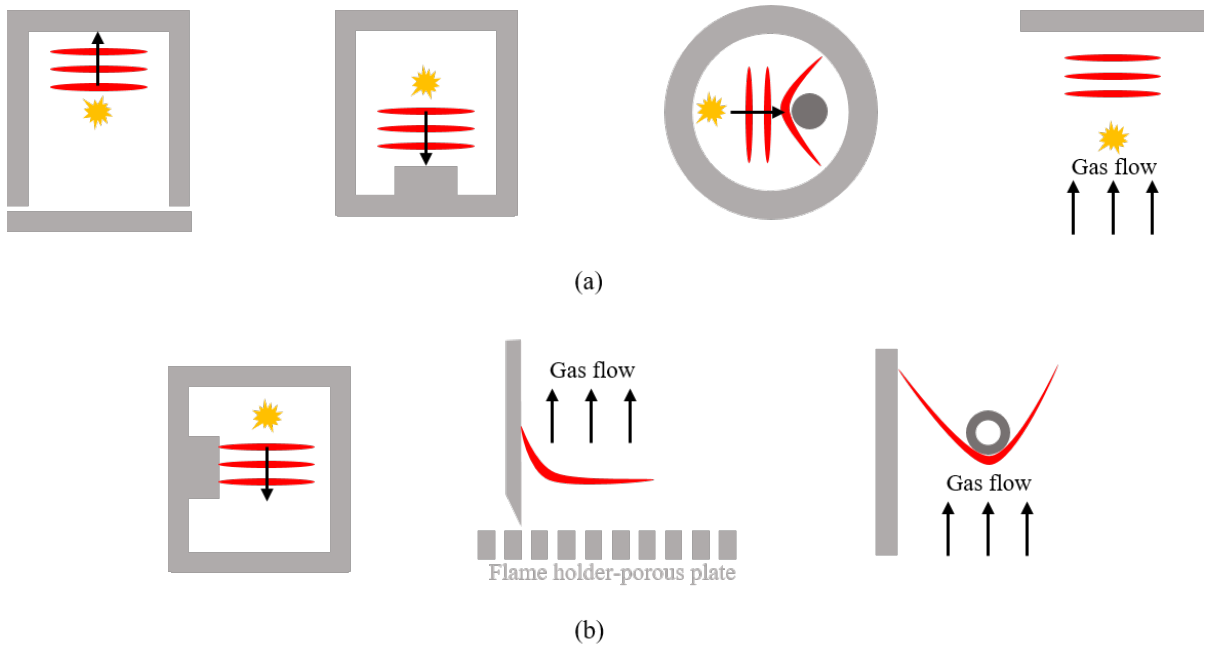

Figure 1.1: Illustration of typical experimental configurations of HOQ (a) and SWQ (b). This figure is adapted from [11].

1.2.1 Head-on quenching

Experimental studies on HOQ can be traced back to the 1980s. At the early stage, the research mainly focused on global quantities such as the wall heat flux and the quenching distance. For example, Vosen et al. [13] measured the heat transfer during the quenching of laminar premixed CH_4-air flames with different equivalence ratios, using a platinum thin film resistance thermometer. It was found that the maximum heat flux and the quenching distance are related, and the heat transfer can be predicted by a single-step reaction model. Temperature profiles of laminar stoichiometric CH_4-air and CH_3OH-air HOQ flames towards a spherical obstacle under various pressures were measured by Saggau et al. [14], and these results were used to evaluate the heat transfer coefficients of the transition gas phase-wall. Based on the measurement of heat flux during the quenching of premixed laminar CH_4-air and C_3H_8-air flames in a constant volume chamber for various wall temperatures and equivalence ratios, the correlation between the maximum heat flux and the heat release rate in the steady flame prior to quenching was obtained by Ezekoye et al. [15]. Different from [13], the heat flux was found to be sensitive to the specification of the reaction mechanism parameters in [15]. Regarding the quenching distance, Bellenoue et al. [16] performed measurements for the HOQ of a laminar premixed stoichiometric CH_4-air flame using direct photography and found that the

wall material has influences on the quenching distance and therefore the maximum wall heat flux. The influence of pressure was investigated by Sotton et al. [17]. Based on the quenching distance and wall heat flux measured from laminar stoichiometric CH_4-air HOQ flames under different pressures, the quenching distance was found to be negatively correlated with the pressure, while an opposite trend was observed for the maximum wall heat flux. A similar configuration was adopted in [18], where the experimental data was used to validate the equation describing the behavior of single-wall flame quenching, which was derived from a simplified model of laminar FWI. To investigate the effect of stretch, Foucher et al. [19] measured the flow field during the HOQ of laminar CH_4-air flames at three different equivalent ratios with particle image velocimetry (PIV). More recently, multi-parameter measurements became possible due to the development of experimental techniques and equipment. For example, Mann et al. [20] conducted simultaneous measurements of temperature and CO concentration for atmospheric laminar CH_4-air HOQ flames with different equivalence ratios, using nanosecond coherent anti-Stokes Raman spectroscopy (CARS) of nitrogen and two-photon laser-induced fluorescence (LIF), respectively. Different from [20] where point-wise CARS was applied, two-beam femtosecond/picosecond one-dimensional rotational CARS was developed by Bohlin et al. [21] to achieve time-resolved measurements of the laminar CH_4-air HOQ. Comparatively, experiments on turbulent HOQ are rather limited, e.g., measurements of turbulent HOQ of stoichiometric CH_4-air and C_2H_4-air flames based on PIV and LIF of the OH molecule by Rißmann et al. [22]. Quenching distances were measured and a decrease in the intrinsic flame speed was observed for both flames.

Numerical studies on laminar HOQ started even earlier than experiments. Based on the type of walls, the configurations can be generally divided into three categories: (1) inert, impermeable walls, (2) impermeable walls with surface reactions, and (3) inert, permeable walls. In most studies, the wall is assumed to be inert and impermeable. For example, Hocks et al. [23] simulated the transient process of a laminar flame quenching at a cold wall, revealing the advantages of using two-step kinetics over a one-step global mechanism. Based on the computation of the HOQ of laminar stoichiometric CH_4-air and CH_3OH-air flames with a detailed chemical kinetic reaction mechanism, it was found that chemical kinetic factors lead to the quenching near the wall [24]. The applicability of various physico-intuitive approaches was investigated by Wichmann et al. [25], who computed one-dimensional laminar HOQ flames with a single-step chemistry. Ezekoye et al. [26] investigated the effects of water condensation on wall heat flux and the reaction rates for the HOQ of a laminar stoichiometric C_3H_8-air flame. Dabireau et al. [27] simulated the HOQ of a laminar premixed stoichiometric H_2-air flame, and found that HOQ of premixed flame leads to higher fluxes to the wall for a shorter time before quenching than the wall-stabilized diffusion flame. Some studies were performed to investigate the influences of several parameters. Considering varying pressures, initial temperatures, and equivalence ratios, the HOQ of laminar premixed isooctane-air flames was computed by Hasse et al. [28]. It was found that both the global chemistry and a short mechanism are inadequate to describe the quenching process, which is different from low-molecular-weight fuels. To understand the production of unburnt HC in the near-wall region for laminar stoichiometric isooctane-air flames, Chauvy et al. [29] investigated the influences of the wall temperature, the equivalence ratio, and the geometry. Based on the configuration of HOQ of laminar premixed stoichiometric CH_4-air flames diluted with hot combustion products, the impacts of the dilution level, pressure, and wall temperature on CO emissions were examined by Jiang et al. [30]. Regarding model development, Strassacker et al. [31–33] conducted a series of research on the HOQ of CH_4-air and isooctane-air flames to demonstrate the capability of the so-called reaction-diffusion manifold (REDIM) method [34] to describe such complex physical processes. In [32], the reduced model formulations in generalized coordinates were proposed, and the advantages over reduced model equations in thermokinetic coordinates were demonstrated. Here, generalized coordinates refer to the local coordinates on the manifold, and thermokinetic coordinates denote the coordinates in thermokinetic variable space. Considering increasing wall temperature, surface chemistry begins to play a role. Popp and Baum [35] conducted the first simulations of the HOQ of laminar premixed stoichiometric CH_4-air flames with detailed mechanisms for both kinetics and diffusion, and found that only for low wall

temperature (300 $\sim$ 400 K), the wall can be considered as inert and thermal diffusion can be neglected during quenching. The necessity to take into account the transport and surface chemistry effects for high wall temperature was further demonstrated in [36]. In [37, 38], heterogeneous wall reactions in laminar HOQ were accounted for within the framework of REDIM reduced kinetics. All the numerical studies mentioned above assumed that the walls were impermeable. To explore a different configuration which could potentially be a new design approach for combustors, Salimath et al. [39–41] performed simulations of HOQ of laminar CH_4-air and H_2-air flames with H_2 porous walls. Calculations for turbulent cases started in 1990s, with impermeable and inert walls considered. Poinsot et al. [42] performed a two-dimensional direct numerical simulation (DNS) for premixed turbulent HOQ with simple chemistry, with the focus on global quantities such as quenching distances and maximum heat fluxes. This work was extended by Bruneaux et al. [43] to three-dimensional. With a similar configuration to [43], the budgets for the flame surface density evolution equation were analyzed in [44]. Based on the DNS of the HOQ of turbulent premixed flames with a single-step Arrhenius type irreversible chemistry, Lai et al. [45–47] and Sellmann et al. [48] conducted a series of detailed analysis on various aspects, such as the effect of Lewis number [45], statistical behavior of scalar dissipation rates [46], vorticity and enstrophy transport [47], and the flow topology distribution [49, 50]. Moreover, the suitability of the existing modeling of progress variable variance transport, flame surface density (FSD), scalar dissipation rate transport, turbulent kinetic energy transport, and turbulent scalar flux transport, was analyzed and modifications were proposed in [48, 51–55]. Ahmed et al. [56] simulated the HOQ of a turbulent statistically planar stoichiometric CH_4-air flame with both a simple one-step irreversible and a skeletal mechanism. It was found that the mechanism of vortex stretching is altered and the small scales contribute to the tangential strain rate when the flame is in the vicinity of the wall. Besides, the underlying fluid mechanical processes are not affected by the choice of the chemical mechanism. Differences between the HOQ of stoichiometric CH_4-air and H_2-air premixed flames were investigated in [57], focusing on statistics of normalized maximum wall heat flux and Peclet number, and the suitability of the wall-modified scalar dissipation rate closure. Different from the DNS studies mentioned before, Pantangi et al. [58] performed a Large-Eddy Simulation (LES) for the HOQ of a turbulent CH_4-air flame based on the configuration described in [20] using Flamelet-Generated Manifold (FGM) [59], and comparison with available experimental data shows satisfactory agreement.

1.2.2 Side-wall quenching

SWQ is inherently a multi-dimensional problem that has been studied for more than 40 years. Experiments were performed to measure parameters such as the velocity, wall heat flux, etc. Cheng et al. [60] investigated the characteristics of the velocity boundary layer of the SWQ of H_2-air flames with different equivalence ratios and wall temperatures. Similar experiments for a lean turbulent C_2H_4-air flame can be found in [61], where significant changes were observed in the turbulent kinetic energy diffusion pattern in the boundary layer. Through measuring the flame thickness for H_2-air and CH_4-air flames with different equivalence ratios, Enomoto et al. [62] investigated the characteristics of the quenching layer, finding that the wall affects the flame quenching from two aspects, with the one being the cooling effect and the other being stretching the flame by the velocity gradient in the velocity boundary layer formed on the surface of the wall. Based on the wall heat flux of SWQ of laminar C_3H_8-air, CH_4-air, and C_2H_4-air flames with varying equivalence ratios in a constant volume chamber, Lu et al. [63] found the correlation between the maximum heat flux during SWQ and the rate of heat release in the flame prior to quenching. The quenching distances of laminar CH_4-air SWQ flames were measured by Bellenoue et al. [16], and it was found that the SWQ flame is characterized by a larger quenching distance and a smaller wall heat flux, compared to HOQ. Similarly, measurements of the quenching distance and the wall heat flux for a laminar SWQ configuration can also be found in Boust et al. [18], with the intention to verify a thermal formulation. A generic SWQ burner setup with well-defined boundary conditions, which can be operated under either turbulent or laminar flow

conditions, was developed by Prof. Dreizler's group in TU Darmstadt, and many studies were conducted based on this configuration. Bohlin et al. [64] measured the temperature and major species simultaneously using ultrabroadband CARS during the SWQ of laminar CH_4-air flames at different equivalence ratios. The effects of wall materials and thermal-barrier coatings on the quenching distance of SWQ of laminar CH_4-air and C_3H_8-air flames for different equivalence ratios were investigated by Häber et al. [65]. It was found that the quenching distance depends on the stoichiometry, the fuel type, and the thickness of coatings, while has weak relation with the wall material and type of coating. Jainski et al. [66] investigated the mean velocity boundary layer profiles and the turbulent characteristics of the boundary layer during the SWQ of turbulent CH_4-air flames at different equivalence ratios. Using data from the SWQ of a turbulent stoichiometric CH_4-air flame, flame surface density and mean reaction rate were derived in [67]. Based on the same burner, thermal-chemical states in the CO-T space were investigated for laminar operating conditions in [68]. Kosaka et al. [69] extended the research to other types of fuel, such as Dimethyl ether (DME), for both laminar and turbulent cases. Moreover, the effects of SWQ on local heat release rate were discussed in [70], where the correlation of HRR and flame curvature indicates the importance of Lewis-number effects. Recently, previous diagnostic approaches were further developed by Zentgraf et al. [71] to measure CO, CO_2, and T simultaneously for a laminar DME-air SWQ flame, and the importance of differential diffusion effects was revealed. Similar methods were also adopted for turbulent DME-air SWQ flames in [72], where the recirculation of burned gas was observed near the flame tip. Johe et al. [73] designed a novel pressurized SWQ burner, and high-speed PIV and planar laser-induced fluorescence of the OH radical (OH-PLIF) were simultaneously performed for the SWQ of lean CH_4-air flames under both laminar and turbulent flow conditions, with different pressures.

Besides experimental investigations, there are also many numerical studies. Andrae et al. [74] studied the SWQ of laminar C_3H_8-air flames in a boundary-layer flow using a two-dimensional stationary model, focusing on the effects of the equivalence ratio of the fresh gas on the thermal coupling between the flame and the wall and the hydrocarbon emissions. The laminar SWQ of a CH_4-air flame experimentally studied in [68] was numerically investigated by Heinrich et al. [75], using LES with FGM. The results show that flow and temperature fields agree well with the experiment, however the near-wall CO mole fractions can not be reproduced accurately. To enable the use of detailed kinetics, a reduced two-dimensional sub-domain was adopted by Ganter et al. [76]. The influence of the chemical mechanisms and the transport models was analyzed. Besides, the origin of CO near the wall was discovered using budget analysis and FGM shows to be unable to produce accurate prediction, similar to the findings in [75]. The root cause for the deficiencies of the tabulated chemistry was identified in [77]. To solve the issue, Quenching Flamelet-Generated Manifold (QFM) was proposed by Efimov et al. [78], which shows evident improvement in CO prediction than FGM. In addition, REDIM based on HOQ solutions can also help to improve the pollutant prediction [77]. Palulli et al. [79] investigated the SWQ of a two-dimensional laminar stoichiometric CH_4-air premixed flame, where velocity perturbations were used at the inlet to study the transient effects with a reduced computational cost. Both SWQ-like and HOQ-like scenarios were observed, which is similar to the findings in turbulent cases [80]. The importance of the low temperature chemistry was confirmed and the formation of CO was analyzed in detail. With the focus on the CO emission, other different configurations were also studied. For example, the configuration in [79] was modified in [81] where the coolant (air or N_2) was injected from a cooling hole located on the wall with the same temperature as the fresh mixture, and CO emissions under various conditions were investigated. CO emissions in a turbulent SWQ setup with several cooling jets for preheated, CH_4-air mixtures were investigated in [82]. Zirwes et al. [83] performed both two-dimensional and three-dimensional simulations for the SWQ of laminar CH_4-air and C_3H_8-air flames. Comparing with experimental data from [65], a systematic error either in the experiments or in the simulations was identified for the quenching distance, and several possible factors were investigated. Zhang et al. [84] investigated the near-wall dynamics of the SWQ of a laminar stoichiometric CH_4-air flame based on the highly-resolved numerical simulation employing detailed reaction kinetics and molecular transport,

and found that the wall has influences on the variation of flame curvature and strain. Research on the SWQ of laminar premixed biogas-H_2 flames with different equivalence ratios using numerical simulations with detailed reaction kinetics and molecular transport can be found in Wei et al. [85], focusing on the variation of parameters like the quenching distance, wall heat flux and CO/NO emissions. Simulations for turbulent SWQ flames started with single-step reaction mechanisms. For example, Alshaalan et al. [86] performed a three-dimensional DNS for a turbulent SWQ flame with single-step chemistry, and the results were compared with standard Bray-Moss-Libby (BML) expressions or the turbulent scalar flux and flame surface density. Considering a more detailed chemistry description, Gruber et al. [87] conducted a three-dimensional DNS for a turbulent H_2-air SWQ flame using a detailed chemical mechanism, showing a thickened flame at the wall and the importance of exothermic radical recombination reactions was identified. More recently, fuels with increasing complexity were taken into account within the context of DNS. Steinhausen et al. [88] performed a three-dimensional quasi-DNS for the interaction of a CH_4-air V-shaped flame with two cold walls, adopting a reduced chemical mechanism. The validity of the use of QFM in conjunction with Quadrature-based Moment Methods (QbMM) was proved based on an *a-priori* analysis. Based on the same dataset in [88], a novel Quenching Flamelet-Generated Manifold with Exhaust Gas Recirculation (QFM-EGR) was proposed to account for the effects of flame dilution due to exhaust gas recirculation near the flame tip, which were also found in the experiment of turbulent SWQ [72]. Turbulent SWQ of a CH_4-air flame diluted by hot combustion products was simulated by Jiang et al. [89] using DNS, where two walls with different temperatures were included. It was found that CO emissions near the cold wall are higher than the hot wall. Similar to the laminar cases, CO formation in the near-wall region was found to be also caused by diffusion and convection. For larger-scale configurations where the computational cost for DNS is beyond affordability, LES and Reynolds-Averaged Navier-Stokes (RANS) are usually adopted. For example, the turbulent SWQ of CH_4-air flames experimentally studied in [67] was numerically investigated by Heinrich et al. [90], using LES coupled with FGM and the artificial thickened flame (ATF) approach. A description of the physics within the burner was illustrated from various aspects, e.g., the distribution of several global quenching quantities. The transient behavior of the movement of the flame tip was analyzed in [80], and three different scenarios were identified: the upstream, the downstream, and the jump-like upstream movement.

1.3 Chemistry reduction

Although simulations with detailed kinetics produce the most accurate results, they can not be used for complex geometries or practical combustors due to the high computational effort required. Within this context, reduction methods are preferred, which reduce the computational cost without losing much accuracy. One approach is to use skeletal or reduced chemistry mechanisms. As a subset of a full mechanism, they are derived to identify the key reactions that determine the essential properties of the flame. Another alternative is the manifold-based reduced kinetics, where the reduction of the chemical mechanism is not necessary. For such kind of tabulation methods, chemistry manifolds are obtained with one-dimensional calculations with full chemical mechanisms, and they contain the entire thermo-chemical states. They are accessed with control variables, which are computed during the CFD simulation. One category of the method is based on the flamelet concept [91], i.e., a turbulent flame is viewed as an ensemble of laminar flamelets, and the inner structure of the flamelets is one-dimensional and time-dependent. The flamelet model was extensively extended, and many variants were proposed, such as Flamelet/Progress Variable (FPV) approach [92], Flame Prolongation of Intrinsic Low-Dimensional Manifold (FPI) [93] and Flamelet-Generated Manifold (FGM) [59]. Another category of the method is based on the separation of the relevant physical and chemical time scales in reacting flows. As shown in Fig. 1.2, the chemical time scales cover a much wider range than the physical time scales, therefore only chemical processes with comparable time scales to physical processes are considered. Such tabulation methods were developed by Maas and Bykov [34, 94] based on a strong mathematical foundation, and they can be applied to both premixed and non-premixed combustion.

All original methods mentioned above were further developed to take into account various aspects involved in combustion, such as curvature [95], differential diffusion [96], inhomogeneous combustion [97], and the non-adiabatic effects [98], etc., through including additional parameters in the tabulation.

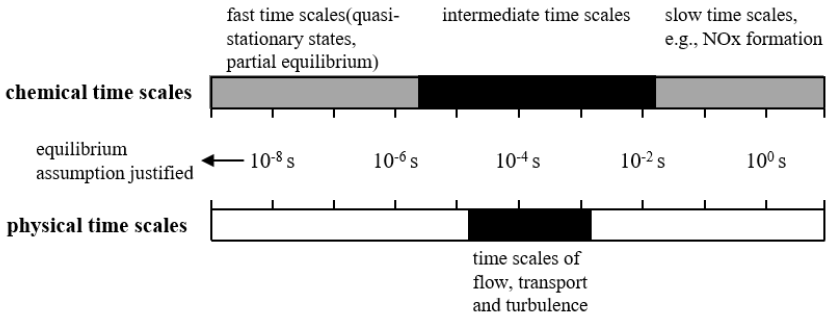

Figure 1.2: Schematic representation of the time scales in chemically reacting flows, adapted from [99].

1.4 Aim of this work

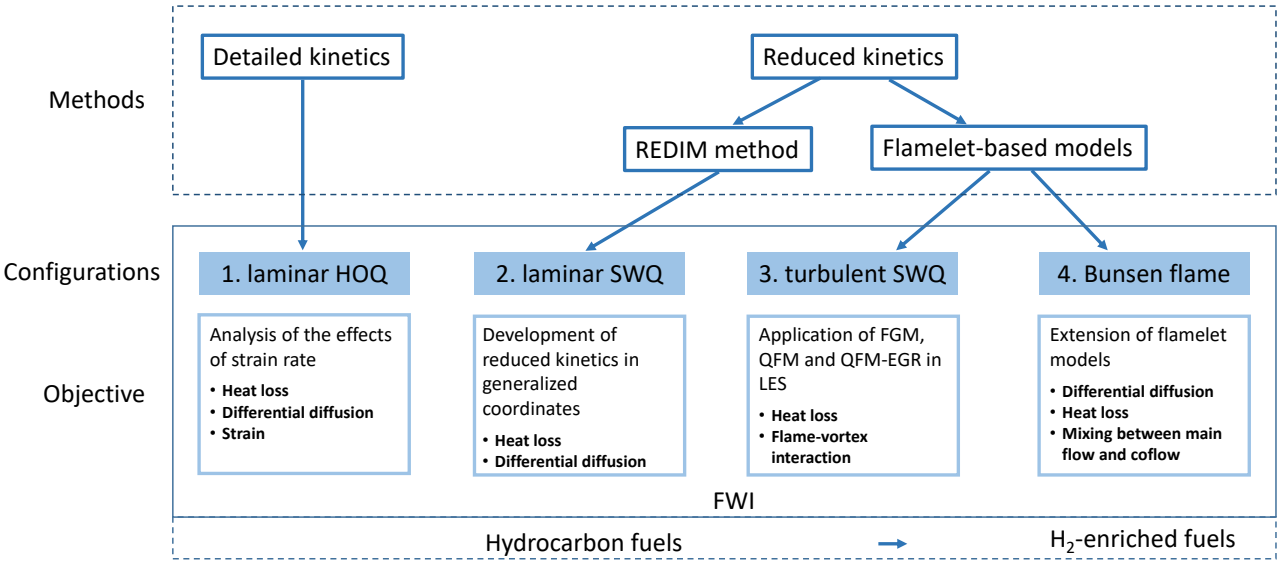

Figure 1.3: Four configurations, including the laminar HOQ, the laminar SWQ, the turbulent SWQ, and the Bunsen flame, investigated in the thesis, with the purpose to develop manifold-based reduced kinetic models. The fuels considered range from pure hydrocarbon to H_2-enriched.

This work aims to contribute to the understanding and modeling of near-wall combustion processes. In particular, the focus is (1) to extend manifold-based modeling approaches to improve their capability in predicting the complex physics in near-wall combustion, such as heat losses, differential diffusion, etc., and (2) to apply manifold-based modeling approaches in more realistic scenarios. With a close connection to recent advances in experimental measurements and flame-resolved simulations, four configurations of different levels of complexity are investigated:

1. A laminar HOQ setup. Different from previous studies that mostly focused on unstrained conditions, the transient HOQ process of laminar premixed flames is investigated with detailed kinetics and transport based on a counterflow configuration with varying strain rates.

2. A laminar SWQ setup. This configuration is mainly adopted to evaluate the manifold-based reduced model REDIM formulated and solved in generalized coordinates, in contrast to the commonly used parametrization with thermokinetic variables in other manifold-based reduced kinetics.

3. A turbulent SWQ setup. The turbulent SWQ is simulated with flamelet models, including QFM and QFM-EGR that have never been used in coupled LES simulations before.

4. A Bunsen burner. With the transition of the focus from hydrocarbon fuels to H_2-enriched fuels, a new flamelet modeling approach based on FGM is developed, and a Bunsen flame configuration is selected to evaluate the flamelet model since it offers sufficient complexity for the model assessment.

The specific objective for each configuration is:

1. Analyzing the influence of the strain rate on the transient laminar HOQ processes systematically, and finding suitable parameters to characterize the strain rate effects within the framework of manifold-based reduced kinetic models.

2. Developing reduced kinetic model equations in generalized coordinates for laminar SWQ and illustrating their advantages over thermokinetic coordinates. Extending this newly developed framework to: (1) realize an *on the fly* technique to relax the dependence of the model accuracy on the *a-priori* identification of the system, and (2) include differential diffusion effects in the near-wall combustion, which is of great significance for fuels such as DME.

3. Applying flamelet manifolds (FGM, QFM, and QFM-EGR) in the LES of a turbulent SWQ. Assessing the performance of each manifold and demonstrating the importance of the choice of the manifold for turbulent cases.

4. Extending the flamelet model to simulate a realistic flame configuration operated with H_2-enriched fuels with multiple physics, such as differential diffusion, heat loss, and mixing, being simultaneously considered.

1.5 Structure of this work

The thesis is divided into 10 chapters. Following the introduction, the fundamentals to describe the reacting flows are given in Chapter 2. Besides, important parameters to characterize premixed combustion are introduced. Furthermore, theoretical principles and modeling of turbulent flows are presented. The combustion models including modeling for chemical kinetics and turbulence-combustion interaction (TCI) are illustrated in Chapter 3. The investigation of one-dimensional strained CH_4-air HOQ is described in Chapter 4, where the simulation results are validated against the experimental data first, and strain rates effects on quenching related quantities are presented. In Chapter 5, studies on the two-dimensional CH_4-air SWQ are conducted, focusing on developing the reduced model equations in generalized coordinates. Moreover, reasonable simplifications of gradient estimations are analyzed. Following the work in Chapter 5, model reduction *on the fly* technique is developed in Chapter 6. In Chapter 7, the work in Chapter 5 is further extended to account for the differential diffusion effects. The model is validated by an experimentally studied DME-air SWQ flame. In Chapter 8, a three-dimensional turbulent CH_4-air SWQ is investigated using LES coupled with ATF and manifold-based reduced models, and the suitability of different flamelet

manifolds FGM, QFM, and QFM-EGR is demonstrated by comparing with a flame resolved simulation. Transferring from hydrocarbon fuels to fuel blends with H_2 addition, the FGM applied in Chapter 8 is further developed to take into account the differential diffusion effects and mixing between the main jet and the coflow in Chapter 9. The approach is validated against an experimental laminar CH_4-H_2-air Bunsen flame configuration where near-wall combustion is also involved. Finally, The thesis concludes with a summary and an outlook in Chapter 10.

2 Fundamentals of reacting and turbulent flows

In this chapter, the governing equations to describe the reacting flows are first introduced. Then important definitions related to premixed combustion are explained, such as flame stretch, flame speed, and flame thickness. Finally, theories related to turbulence are presented, including statistical descriptions of turbulent flows and commonly used computational approaches.

2.1 Reacting flows

2.1.1 Governing equations

The equations for mass and momentum for the flow field can be written as

$$\frac{\partial \rho}{\partial t} + \nabla \cdot (\rho \boldsymbol{u}) = 0 \,, \tag{2.1}$$

$$\frac{\partial (\rho \boldsymbol{u})}{\partial t} + \nabla \cdot (\rho \boldsymbol{u} \otimes \boldsymbol{u}) = \boldsymbol{f}_{\text{surface}} + \boldsymbol{f}_{\text{body}} = -\nabla P + \nabla \cdot \boldsymbol{\tau} + \boldsymbol{f}_{\text{body}} \,, \tag{2.2}$$

where ρ is the density, $\boldsymbol{u}$ the velocity vector, P the total thermodynamic pressure, $\boldsymbol{\tau}$ the viscous stress tensor and $\otimes$ the outer product. $\boldsymbol{f}$ stands for the force per unit volume in N/m^3, which can also be regarded as the momentum flux vector. In the present study, body forces such as gravity are neglected, meaning $\boldsymbol{f}_{\text{body}} \approx 0$. Therefore, only surface forces $\boldsymbol{f}_{\text{surface}}$ are taken into account, which are determined from the divergence of the stress tensor $\boldsymbol{T}$. Namely $\boldsymbol{f}_{\text{surface}} = \nabla \cdot \boldsymbol{T} = -\nabla P + \nabla \cdot \boldsymbol{\tau}$. For the closure of the stress tensor, the assumption of a Newtonian fluid is adopted. According to Newton's law, the viscous stress tensor is proportional to the symmetric, trace-free part of the velocity gradient, which can be expressed as

$$\boldsymbol{\tau} = \mu (2\boldsymbol{S} - \frac{2}{3} \nabla \cdot \boldsymbol{u}\, \boldsymbol{I}) \,, \tag{2.3}$$

where $\boldsymbol{I}$ is the unit tensor, $\boldsymbol{S}$ the rate of strain tensor $\boldsymbol{S} = \frac{1}{2}(\nabla \boldsymbol{u} + \nabla \boldsymbol{u}^T)$. Here, $\nabla \boldsymbol{u}^T$ is the transpose of the velocity gradient and μ is the dynamic viscosity, which is related to the kinematic viscosity ν through $\mu = \rho \nu$.

Taking into account the chemical reactions, governing equations describing the evolution of the species involved have to be solved. The mass conservation equation for species k can be written as

$$\frac{\partial (\rho Y_k)}{\partial t} + \nabla \cdot (\rho \boldsymbol{u} Y_k) + \nabla \cdot \boldsymbol{j}_k = \dot{\omega}_k \,, \tag{2.4}$$

where Y_k is the mass fraction, $\boldsymbol{j}_k$ the diffusion flux and $\dot{\omega}_k$ the reaction rate of species k, respectively. By definition, it can be obtained that $\sum_{k=1}^{n_s} Y_k = 1$, $\sum_{k=1}^{n_s} \boldsymbol{j}_k = 0$, and $\sum_{k=1}^{n_s} \dot{\omega}_k = 0$, where n_s denotes the total number of species.

As for the energy conservation, it can be expressed in the form of total enthalpy, which is the sum of

sensible enthalpy and enthalpy of formation

$$h = \sum_{k=1}^{n_s} h_{s,k} Y_k + \sum_{k=1}^{n_s} \Delta h_{f,k}^0 Y_k = \sum_{k=1}^{n_s} \left(\int_{T_0}^{T} c_{p,k}\, dT + \Delta h_{f,k}^0 \right) Y_k = \int_{T_0}^{T} c_p\, dT + \sum_{k=1}^{n_s} \Delta h_{f,k}^0 Y_k \ . \tag{2.5}$$

Here $h_{s,k}$ stands for the sensible enthalpy of species k, $\Delta h_{f,k}^0$ the mass enthalpy of formation of species k at the reference temperature T_0 (298.15 K here), $c_{p,k}$ the heat capacities at a constant pressure of species k, and c_p the heat capacity at a constant pressure of the mixture $c_p = \sum_{k=1}^{n_s} c_{p,k} Y_k$. The governing equation for h is given as

$$\rho \frac{Dh}{Dt} = \frac{\partial (\rho h)}{\partial t} + \nabla \cdot (\rho \boldsymbol{u} h) = \frac{DP}{Dt} + \boldsymbol{\tau} : \nabla \boldsymbol{u} + \dot{Q} + \rho \sum_{k=1}^{n_s} Y_k \boldsymbol{f}_{\text{body},k} \boldsymbol{V}_k - \nabla \cdot \boldsymbol{q} \ , \tag{2.6}$$

where the first term and the second term on the right hand side denote the enthalpy variation due to pressure change and the dissipation of the kinetic energy by friction, respectively. The third term $\dot{Q}$ is the heat source term, which can, for example, be ignition sparks in gasoline engines or heat radiation in coal combustion chambers. The fourth term is the power produced by the body forces, where $\boldsymbol{V}_k$ denotes the diffusion velocity of species k. The last term stands for the heat fluxes associated with heat conduction and species diffusion

$$\boldsymbol{q} = -\lambda \nabla T + \sum_{k=1}^{n_s} h_k \boldsymbol{j}_k \ , \tag{2.7}$$

where the Dufour heat flux has been neglected. Here λ stands for the thermal conductivity.

Sometimes the energy equation can also be expressed in the form of sensible enthalpy h_s. Based on its definition ($h_s = h - \sum_{k=1}^{n_s} \Delta h_{f,k}^0 Y_k$) and the species equation (Eq. (2.4)), the balance equation for the sensible enthalpy can be written as

$$\begin{aligned} \rho \frac{Dh_s}{Dt} = \frac{\partial (\rho h_s)}{\partial t} + \nabla \cdot (\rho \boldsymbol{u} h_s) = \frac{DP}{Dt} + \boldsymbol{\tau} : \nabla \boldsymbol{u} + \dot{Q} + \rho \sum_{k=1}^{n_s} Y_k \boldsymbol{f}_{\text{body},k} \boldsymbol{V}_k \\ + \nabla \cdot (\lambda \nabla T) - \nabla \cdot \left(\sum_{k=1}^{n_s} h_{s,k} \boldsymbol{j}_k \right) + \dot{\omega}_T \ , \end{aligned} \tag{2.8}$$

where $\dot{\omega}_T$ stands for the heat release due to the combustion $\dot{\omega}_T = -\sum_{k=1}^{n_s} \Delta h_{f,k}^0 \dot{\omega}_k$.

Another way to express the energy equation is in the form of temperature. Starting from $h_s = \sum_{k=1}^{n_s} h_{s,k} Y_k$, it can be obtained that

$$\rho \frac{Dh_s}{Dt} = \sum_{k=1}^{n_s} h_{s,k} \rho \frac{DY_k}{Dt} + \rho c_p \frac{DT}{Dt} \ . \tag{2.9}$$

Replacing Eq.(2.9) in Eq. (2.8) gives

$$\rho c_p \frac{DT}{Dt} = \frac{DP}{Dt} + \boldsymbol{\tau} : \nabla \boldsymbol{u} + \dot{Q} + \rho \sum_{k=1}^{n_s} Y_k \boldsymbol{f}_{\text{body},k} \boldsymbol{V}_k + \nabla \cdot (\lambda \nabla T) - \left(\sum_{k=1}^{n_s} c_{p,k} \boldsymbol{j}_k \right) \nabla T + \dot{\omega}_T' \ , \tag{2.10}$$

where $\dot{\omega}_T' = -\sum_{k=1}^{n_s} h_k \dot{\omega}_k = -\sum_{k=1}^{n_s} h_{s,k} \dot{\omega}_k - \sum_{k=1}^{n_s} \Delta h_{f,k}^0 \dot{\omega}_k$.

In order to close the system, the ideal gas equation is additionally solved, which reads

$$P = \rho \frac{R}{\overline{M}} T \ , \tag{2.11}$$

where R is the universal gas constant and $\overline{M}$ the mean molecular weight of the mixture.

In the following chapters, specific forms for the governing equations of species and enthalpy will be illustrated based on the processes considered in certain configurations.

2.1.2 Modeling of species diffusion

In order to solve the governing equations for species (Eq. (2.4)) and enthalpy (Eqs. (2.6) or (2.8) or (2.10)), the species diffusion flux $\boldsymbol{j}_k$ needs to be modeled.

The multi-component species diffusion flux can be calculated through

$$\boldsymbol{j}_k = \rho Y_k \boldsymbol{V}_k = \frac{M_k}{\overline{M}} \sum_{j=1}^{n_s} M_j D_{kj} \boldsymbol{d}_j - \frac{D_k^T}{T} \nabla T \ , \tag{2.12}$$

where M_k is the molecular weight of species k, D_{kj} the ordinary multicomponent diffusion coefficients of species k in species j determined from the binary diffusion coefficient $\mathcal{D}_{kj}$, and D_k^T the thermal diffusion coefficient of species k. $\boldsymbol{d}_j$ stands for the diffusion driving force, which can be calculated as

$$\boldsymbol{d}_j = \nabla X_j + (X_j - Y_j) \frac{1}{P} \nabla P \ , \tag{2.13}$$

where X_j is the mole fraction of species j. Therefore, the species mass diffusion can be attributed to a concentration gradient, a pressure gradient, and a temperature gradient (thermodiffusion, which is also called the Soret effect). In the present study, only the first term is considered, while the latter two are neglected since they are relatively small for the cases considered. Therefore, Eq (2.12) reduces to

$$\boldsymbol{j}_k = \frac{M_k}{\overline{M}} \sum_{j=1}^{n_s} M_j D_{kj} \nabla X_j \ . \tag{2.14}$$

In this approach, the diffusion of species k depends on the gradients of all other species, and a $n_s \times n_s$ diffusion matrix needs to be built and inverted.

For simplification, a widely used approximation is the so-called mixture-averaged diffusion model, where the diffusion of species depends only on its own concentration gradient. One example is the Hirschfelder and Curtiss approximation [100]. The diffusion velocity of species k is calculated as

$$\boldsymbol{V}_k = -\frac{D_{km}}{X_k} \nabla X_k \ , \tag{2.15}$$

where D_{km} is an equivalent diffusion coefficient of species k into other gases of the mixture

$$D_{km} = \frac{1 - Y_k}{\sum_{j \neq k} X_j / \mathcal{D}_{kj}} \ . \tag{2.16}$$

Then the mass flux $\boldsymbol{j}_k$ can be estimated via

$$\boldsymbol{j}_k = \rho Y_k \boldsymbol{V}_k = -\rho Y_k \frac{D_{km}}{X_k} \nabla X_k \ . \tag{2.17}$$

Besides, the diffusion velocity can also be computed based on the mass fraction gradient through

$$\boldsymbol{V}_k = -\frac{D'_{km}}{Y_k}\nabla Y_k \ , \tag{2.18}$$

where

$$\frac{1}{D'_{km}} = \sum_{\substack{j=1,\\ j\neq k}}^{n_s} \frac{X_j}{D_{kj}} + \frac{X_k}{1-Y_k}\sum_{\substack{j=1,\\ j\neq k}}^{n_s} \frac{Y_j}{D_{kj}} \ . \tag{2.19}$$

Then the mass flux $\boldsymbol{j}_k$ can be estimated via

$$\boldsymbol{j}_k = \rho Y_k \boldsymbol{V}_k = -\rho D'_{km}\nabla Y_k \ . \tag{2.20}$$

With the mixture-averaged diffusion model, ${n_s}^2$ binary diffusion coefficients $\mathcal{D}_{kj}$ still need to be evaluated.

For further simplification, the unity Lewis number ($Le = 1$) assumption is adopted. In this case, the diffusion coefficients of all species are assumed to be the same, which are equal to the thermal diffusivity α, namely $D_k = D = \alpha = \lambda/(\rho c_p)$. Then the diffusion velocity $\boldsymbol{V}_k$ reads

$$\boldsymbol{V}_k = -\frac{D}{Y_k}\nabla Y_k = -\frac{\lambda}{\rho c_p Y_k}\nabla Y_k \ , \tag{2.21}$$

and the mass flux $\boldsymbol{j}_k$ reads

$$\boldsymbol{j}_k = \rho Y_k \boldsymbol{V}_k = -\rho D\nabla Y_k = \frac{\lambda}{c_p}\nabla Y_k \ . \tag{2.22}$$

2.1.3 Chemical kinetics

For the closure of the species mass conservation equation (Eq. (2.4)), the reaction rate of each species $\dot{\omega}_k$ needs to be determined.

For a reacting system consisting of n_s species and M reactions,

$$\sum_{k=1}^{n_s} \nu'_{kj}\mathcal{M}_k \rightleftharpoons \sum_{k=1}^{n_s} \nu''_{kj}\mathcal{M}_k \qquad \text{for } j = 1, ..., M \ , \tag{2.23}$$

where $\mathcal{M}_k$ stands for species k. ν'_{kj} and ν''_{kj} are the molar stoichiometric coefficients of species k in the forward and reverse directions of reaction j, respectively. The net production or destruction rate for species k in kg/($\mathrm{m}^3 \cdot \mathrm{s}$) is the sum of the reaction rate produced by each reaction

$$\dot{\omega}_k = \sum_{j=1}^{M} \dot{\omega}_{kj} = M_k \sum_{j=1}^{M} (\nu''_{kj} - \nu'_{kj}) r_j \ . \tag{2.24}$$

Here, r_j is the rate of progress of reaction j in mol/($\mathrm{m}^3 \cdot \mathrm{s}$), and it can be estimated via

$$r_j = K_{fj} \prod_{k=1}^{n_s} [X_k]^{\nu'_{kj}} - K_{rj} \prod_{k=1}^{n_s} [X_k]^{\nu''_{kj}} \ , \tag{2.25}$$

where K_{fj} and K_{rj} are the forward and reverse rate constants for reaction j. They are usually modeled

with the empirical Arrhenius law, where the expression for K_{fj} reads

$$K_{fj} = A_{fj} T^{\beta_j} \exp\left(-\frac{E_j}{RT}\right) = A_{fj} T^{\beta_j} \exp\left(-\frac{T_{aj}}{T}\right) , \tag{2.26}$$

and K_{rj} can be computed from K_{fj} through the equilibrium constant K_e [101]

$$K_{rj} = \frac{K_{fj}}{K_e} . \tag{2.27}$$

To obtain the forward and reverse reaction rates, the preexponential constant A_{ij}, the temperature exponent β_j, and the activation energy E_j can be found in the corresponding chemical schemes.

2.2 Premixed combustion

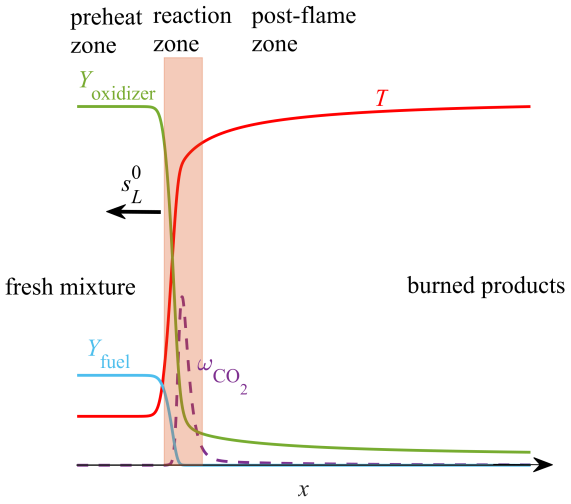

Figure 2.1: Flame structure of a 1D freely propagating lean flame.

In premixed combustion, the fuel and the oxidizer are mixed first, and a flame is established due to the combustion of the mixture. The characteristics of the flame structure of the premixed flame are illustrated based on a canonical configuration, as shown in Fig. 2.1 for a one-dimensional freely propagating flame. In the configuration, a flame propagates towards the fresh mixture with the laminar burning velocity s_L^0. When the fresh mixture is injected with a velocity of the same magnitude as s_L^0, the flame can achieve a steady state. The flame structure along the x direction is plotted in Fig. 2.1, which is featured by a preheated zone, a thin reaction zone, and a post-flame zone. Reaction zone is where most chemical reactions occur, and significant variations of species and temperature can be observed. Upstream of the reaction zone is the preheated zone, where the fresh mixture absorbs heat through diffusion processes. Downstream of the reaction zone lies the post-flame zone. In this region, the temperature and the product concentration keep at a high level, with gradual changes towards the equilibrium state.

2.2.1 Flame stretch

When a flame front propagates in a nonuniform flow, the flame area changes. The fractional rate of change of a flame surface element is defined as flame stretch. For a thin flame sheet, the expression of the stretch

can be written as

$$K = K_s + K_c = (\boldsymbol{I} - \boldsymbol{n} \otimes \boldsymbol{n}) : \nabla \boldsymbol{u} + S_d \nabla \cdot \boldsymbol{n} = \nabla_t \cdot \boldsymbol{u} + s_d \nabla_t \cdot \boldsymbol{n} \ , \tag{2.28}$$

where $\boldsymbol{n}$ is the unit vector normal to the flame surface pointing towards the fresh gases, ∇_t the tangential component of the ∇ operator. s_d is the displacement speed which will be introduced in detail later. In Eq. (2.28), the term K_s is attributed to the non-uniformity of the flow therefore represents the strain, and the term K_c is related to the curvature of the flame front.

For the one-dimensional freely propagating flame mentioned above, the flow is only in the normal direction of the flame front, and the planar flame is free from curvature effects, therefore the flame is unstretched.

2.2.2 Flame speed

Flame speed is an important parameter for premixed flames that characterizes the propagation of the flame. There are multiple definitions for the flame speed.

- *The absolute flame speed* s_a
  This refers to the flame front speed relative to a fixed reference frame. It can be expressed as

  $$s_a = \boldsymbol{w} \cdot \boldsymbol{n} \ , \tag{2.29}$$

  where $\boldsymbol{w}$ is the velocity at which the point must move to remain on the flame surface.

- *The displacement speed* s_d
  This denotes the flame front speed with respect to the flow. It is calculated as

  $$s_d = (\boldsymbol{w} - \boldsymbol{u}) \cdot \boldsymbol{n} = s_a - \boldsymbol{u} \cdot \boldsymbol{n} \ , \tag{2.30}$$

  where $\boldsymbol{u}$ is the flow speed.

- *The consumption speed* s_c
  This is the speed at which the reactants are consumed. It is defined based on the reaction rates of the fuel

  $$s_c = -\frac{1}{\rho_u \left(Y_{F_u} - Y_{F_b}\right)} \int_{-\infty}^{\infty} \dot{\omega}_F dx \ , \tag{2.31}$$

  where ρ_u stands for the density of the unburned gas, Y_{F_u} the mass fraction of the fuel on the unburned side, and Y_{F_b} the mass fraction of residual fuel on the burned side. $\dot{\omega}_F$ denotes the reaction rate of the fuel.

Among all the three definitions, the first and the second are local quantities that depend on the flame surface where they are evaluated, while the third one is a global quantity from an integral over all flame surfaces across the flame front. All these quantities can be influenced by factors such as stretch and heat losses.

For the specific case of a laminar one-dimensional freely propagating flame, a unique definition of the flame speed, the laminar burning velocity s_L^0 is adopted. The value equals to the consumption speed s_c and it is often used as the reference speed for investigations.

2.2.3 Flame thickness

Flame thickness is another important quantity of premixed flames, which determines the required mesh resolution for the computation. For most combustion methods, having enough points within the flame thickness is the key to resolving the flame structure. The laminar flame thickness of an unstretched flame δ is often used as a reference to characterize the premixed flames. It can be evaluated in different ways:

- Based on scaling laws

$$\delta = \frac{\lambda_u}{\rho_u c_p s_L^0} , \tag{2.32}$$

  where the subscript $_u$ refers to the quantities of the unburned gas. In this way, the laminar flame thickness can be obtained easily once the flame speed is known.

- Based on the gradient of a scalar ψ

$$\delta = \frac{\psi_{\max} - \psi_{\min}}{\max\left(\frac{\partial \psi}{\partial x}\right)} . \tag{2.33}$$

  Usually the temperature or species profile can be used here for calculation.

- Based on the source term of species
  In this case, the flame thickness is defined as the width of the region where the magnitude of the source term is greater than 0.5 times the maximum.

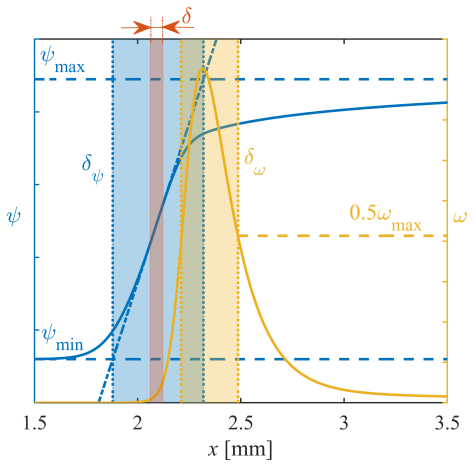

Figure 2.2: Illustration of the laminar flame thickness by different definitions. The width of the colored rectangle denotes the thickness based on scaling laws (red), the scalar gradient (blue), and the species source term (yellow).

Figure 2.2 compares the flame thickness obtained by all definitions mentioned above.
In the following chapters, the first definition Eq. (2.32) is applied unless specified.

2.2.4 Quantification of differential diffusion effects

To quantify the degree of differential diffusion, the differential diffusion parameter Z_{HC} [102] is used, which is defined as

$$Z_{\mathrm{HC}} = F_{\mathrm{H}} - F_{\mathrm{C}}, \tag{2.34}$$

where F_{H} = (Y_{H} - $Y_{\mathrm{H},1}$)/($Y_{\mathrm{H},2}$ - $Y_{\mathrm{H},1}$) and F_{C} = (Y_{C} - $Y_{\mathrm{C},1}$)/($Y_{\mathrm{C},2}$ - $Y_{\mathrm{C},1}$). Y stands for the mass fraction of the respective element (H or C), and subscripts $_1$ and $_2$ refer to pure fuel and air, i.e., $Y_{\mathrm{C},2} = Y_{\mathrm{H},2} = 0$, respectively. Larger absolute values of Z_{HC} indicate stronger differential diffusion.

2.3 Turbulence

Turbulent flows are relevant to many practical engineering applications. For comparable laminar and turbulent flows, the latter is able to enhance the transport and mixing of the fluid more effectively. The turbulent flow can be characterized by the Reynolds number Re, which is defined as

$$Re = \frac{uL}{\nu} \,, \tag{2.35}$$

where u and L are the characteristic velocity and length scale of the flow, respectively. This single dimensionless parameter indicates the ratio between the inertial and viscous forces. When Re exceeds a limit, i.e., the viscous dissipation is small, the flow is identified as turbulent.

For turbulent flows, a separation of scales appears, with the large-scale motions affected by the geometry of the flow and the small-scale motions sharing a universal character. The largest scale is the integral length scale l_t, which is usually close to the characteristic size of the flow. The minimum scale is called Kolmogorov length scale l_k, which fulfills the condition that $Re_k = 1$. According to [101], the relation between l_t and l_k can be expressed as

$$\frac{l_t}{l_k} = Re_t^{3/4} \,. \tag{2.36}$$

This indicates that the difference between the size of small and large eddies increases with increasing Reynolds number.

Furthermore, turbulent flows are mainly featured by a significant and irregular variation of the fluid velocity field in both space and time. For highly turbulent flows, small changes in initial conditions, boundary conditions, and material properties will lead to a substantial change in the flow field evolution. Consequently, the motion of the fluid becomes unpredictable. Due to the random nature of turbulent flows, a statistical description is often adopted.

2.3.1 Statistical description of turbulent flows

To describe the statistical distributions of the vector or scalar fields, distribution functions are used. For an arbitrary quantity φ, the distribution function $g_\varphi(\Phi)$ is defined as the probability $\mathfrak{p}$ of finding a value $\varphi < \Phi$:

$$g_\varphi(\Phi) = \mathfrak{p}\left(\varphi < \Phi\right) \,. \tag{2.37}$$

The probability density function (PDF) of φ can be defined as

$$\mathcal{P}_\varphi\left(\Phi\right) = \frac{dg_\varphi\left(\Phi\right)}{d\Phi} \,, \tag{2.38}$$

and it fulfills the condition that $\int_{-\infty}^{\infty} \mathcal{P}_\varphi\left(\Phi\right) d\Phi = 1$, if φ is likely to vary from $-\infty$ to ∞.

The momentum of φ is defined by

$$\overline{\varphi^n} = \int_{-\infty}^{+\infty} \varphi^n \mathcal{P} d\varphi. \tag{2.39}$$

Specifically, the first momentum ($n = 1$) corresponds to the mean of φ:

$$\overline{\varphi} = \int_{-\infty}^{+\infty} \varphi \mathcal{P} d\varphi. \tag{2.40}$$

If φ is decomposed into the mean and fluctuation parts

$$\varphi = \overline{\varphi} + \varphi' \,, \tag{2.41}$$

then the variance $\overline{\varphi'^2}$ can be calculated with the first and second momentum through $\overline{\varphi'^2} = \overline{\varphi^2} - \overline{\varphi}^2$.

For systems with large density variation, such as combustion, it is more common to use density-weighted average $\widetilde{\varphi}$, which is also called the Favre average. Its value can be obtained from

$$\widetilde{\varphi} = \overline{\rho\varphi}/\overline{\rho} \,. \tag{2.42}$$

In this case, φ can be expressed as

$$\varphi = \widetilde{\varphi} + \varphi'' \,. \tag{2.43}$$

2.3.2 Computational approaches for turbulent flows

Direct numerical simulation (DNS)

Within the framework of DNS, the full Navier-Stokes equations are directly solved without any models. Due to the wide ranges of time and length scales involved in turbulent flows, high computational cost is needed. On one hand, the computational domain must be large enough to resolve the characteristic scale l_t. On the other hand, restrictive requirements on mesh resolution need to be satisfied so that the Kolmogorov length scale l_k can be resolved.
Take an example of a one-dimensional computational domain with a length of L and a number of grid N; the grid size is $\Delta_x = L/N$. Then the requirements of $l_t \leq L$ and $\Delta_x \leq l_k$ should be satisfied, which gives

$$\frac{l_t}{l_k} \leq \frac{L}{\Delta_x} = N \,. \tag{2.44}$$

Combined with Eq. (2.36), one can obtain

$$N \geq Re_t^{3/4} \,. \tag{2.45}$$

Therefore, for a three-dimensional simulation, the minimum total grid number required is $Re_t^{9/4}$. Its value increases significantly with increasing Reynolds number, as shown in Fig. 2.3.

Within this context, DNS can only be applied to turbulence in simplified generic flow configurations that are intended for academic research, while is usually unfeasible for practical applications such as turbines or engines.

Reynolds averaged Navier Stokes (RANS) simulation

RANS simulations have been the first possible approach to compute turbulent flows in history. In RANS, time-averaged values of all quantities are obtained by solving the transport equations averaged from the instantaneous equations Eqs. (2.1) and (2.2) (and also Eqs. (2.4) and (2.6) for reacting flows). Using Eq. (2.43) with $\widetilde{\varphi''} = 0$, the averaged transport equations can be written as

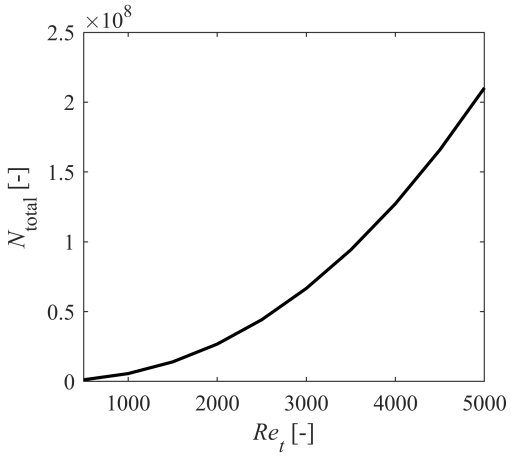

Figure 2.3: Minimum required total grid number for a 3D DNS for different Reynolds numbers.

$$\frac{\partial \overline{\rho}}{\partial t} + \nabla \cdot (\overline{\rho}\widetilde{\boldsymbol{u}}) = 0 \,, \tag{2.46}$$

$$\frac{\partial \overline{\rho}\widetilde{\boldsymbol{u}}}{\partial t} + +\nabla \cdot (\overline{\rho}\widetilde{\boldsymbol{u}} \otimes \widetilde{\boldsymbol{u}}) = -\nabla \cdot \overline{\boldsymbol{\tau}} - \nabla \cdot \left(\overline{\rho}\widetilde{\boldsymbol{u}''\boldsymbol{u}''}\right) - \nabla \overline{P} \,, \tag{2.47}$$

$$\frac{\partial \overline{\rho}\widetilde{Y}_k}{\partial t} + \nabla \cdot \left(\overline{\rho}\widetilde{\boldsymbol{u}}\widetilde{Y}_k\right) + \nabla \cdot \overline{\boldsymbol{j}}_k + \nabla \cdot \left(\overline{\rho}\widetilde{\boldsymbol{u}''Y_k''}\right) = \overline{\dot{\omega}}_k \,, \tag{2.48}$$

$$\frac{\partial \overline{\rho}\widetilde{h}}{\partial t} + \nabla \cdot \left(\overline{\rho}\widetilde{\boldsymbol{u}}\widetilde{h}\right) = \frac{\overline{DP}}{Dt} + \overline{\boldsymbol{\tau}} : \nabla \widetilde{\boldsymbol{u}} + \nabla \left(\overline{\lambda}\nabla\widetilde{T}\right) - \nabla \cdot \left(\sum_{k=1}^{n_s} \overline{\rho h_k \boldsymbol{j}_k}\right) - \nabla \cdot \left(\overline{\rho}\widetilde{\boldsymbol{u}''h''}\right) \,, \tag{2.49}$$

where

$$\frac{\overline{DP}}{Dt} = \frac{\partial \overline{P}}{\partial t} + \overline{\boldsymbol{u}\nabla P} = \frac{\partial \overline{P}}{\partial t} + \widetilde{\boldsymbol{u}}\nabla\overline{P} + \overline{\boldsymbol{u}''\nabla P} \,. \tag{2.50}$$

To solve the above equations, closures for the Reynolds stresses ($\widetilde{\boldsymbol{u}''\boldsymbol{u}''}$), turbulent fluxes of species ($\widetilde{\boldsymbol{u}''Y_k''}$) and enthalpy ($\widetilde{\boldsymbol{u}''h''}$), laminar diffusive fluxes for species ($\overline{\boldsymbol{j}}_k$) or enthalpy ($\overline{\lambda}\nabla\widetilde{T}$), and species chemical reaction rates ($\overline{\dot{\omega}}_k$) need to be determined first. Classical models can be found in [101].

Compared to DNS, the computational cost of RANS is largely reduced due to the coarser grid resolution required, which makes it possible to be used in industrial applications. However, only the mean flow field can be directly obtained from the transport equations, therefore the turbulent motion is described by models. Within this context, the large modeling effort leads to the inaccuracy of the RANS models.

Large-Eddy Simulation (LES)

LES is a compromise between DNS and RANS, where the large-scale eddies are directly resolved while the effect of the small-scale eddies is estimated with subgrid models. To achieve this, all quantities are

filtered in physical space, and the filtered quantity of φ at location $\mathbf{x}$ is defined as

$$\overline{\varphi}(\mathbf{x}) = \int \varphi\left(\mathbf{x}'\right) G\left(\mathbf{x} - \mathbf{x}'\right) d\mathbf{x}' \,, \tag{2.51}$$

where G is the filter kernel. In this case, a quantity φ can be decomposed to the filtered part $\overline{\varphi}$ and the unresolved part φ'. The resolved part is obtained by solving the transport equations filtered from the instantaneous equations Eqs. (2.1) and (2.2) (and also Eqs. (2.4) and (2.6) for reacting flows):

$$\frac{\partial \overline{\rho}}{\partial t} + \nabla \cdot (\overline{\rho}\widetilde{\boldsymbol{u}}) = 0 \,, \tag{2.52}$$

$$\frac{\partial \overline{\rho}\widetilde{\boldsymbol{u}}}{\partial t} + + \nabla \cdot (\overline{\rho}\widetilde{\boldsymbol{u}} \otimes \widetilde{\boldsymbol{u}}) = -\nabla \cdot \overline{\boldsymbol{\tau}} - \nabla \cdot \left(\widetilde{\overline{\rho}\boldsymbol{u} \otimes \boldsymbol{u}}\right) + \nabla \cdot (\overline{\rho}\widetilde{\boldsymbol{u}} \otimes \widetilde{\boldsymbol{u}}) - \nabla \overline{P} \,, \tag{2.53}$$

$$\frac{\partial \overline{\rho}\widetilde{Y}_k}{\partial t} + \nabla \cdot \left(\overline{\rho}\widetilde{\boldsymbol{u}}\widetilde{Y}_k\right) + \nabla \cdot \overline{\boldsymbol{j}}_k + \nabla \cdot \left(\widetilde{\overline{\rho}\boldsymbol{u}Y_k}\right) - \nabla \cdot \left(\overline{\rho}\widetilde{\boldsymbol{u}}\widetilde{Y}_k\right) = \overline{\dot{\omega}}_k \,, \tag{2.54}$$

$$\begin{aligned} \frac{\partial \overline{\rho}\widetilde{h}}{\partial t} + \nabla \cdot \left(\overline{\rho}\widetilde{\boldsymbol{u}}\widetilde{h}\right) =& \frac{\overline{DP}}{Dt} + \overline{\boldsymbol{\tau}} : \nabla \widetilde{\boldsymbol{u}} + \nabla \left(\overline{\lambda}\nabla \widetilde{T}\right) - \nabla \cdot \left(\sum_{k=1}^{n_s} \overline{\rho h_k \boldsymbol{j}_k}\right) \\ & - \nabla \cdot \left(\widetilde{\overline{\rho}\boldsymbol{u}h}\right) + \nabla \cdot \left(\overline{\rho}\widetilde{\boldsymbol{u}}\widetilde{h}\right) \,. \end{aligned} \tag{2.55}$$

These filtered transport equations have a similar form as the Reynolds averaged transport equations Eqs. (2.46), (2.47), (2.48), and (2.49). However, differently from RANS, the filtered value of a perturbation is non-zero in LES, namely $\overline{\varphi'} \neq 0$. Besides, the double filtered value is not equal to the filtered value, i.e., $\overline{\overline{\varphi}} \neq \overline{\varphi}$. These also applies to Favre filtering values, i.e., $\widetilde{\varphi'} \neq 0$ and $\widetilde{\widetilde{\varphi}} \neq \widetilde{\varphi}$.

2.3.3 Subgrid models in Large-Eddy Simulations

Reynolds stresses

Based on the *Boussinesq hypothesis* that the impact of the turbulent mixing of the momentum is similar to the corresponding molecular transport, the eddy viscosity models are introduced to model the Reynolds stresses $\boldsymbol{\tau}^{sgs} = \widetilde{\boldsymbol{u} \otimes \boldsymbol{u}} - \widetilde{\boldsymbol{u}} \otimes \widetilde{\boldsymbol{u}}$. The unresolved momentum fluxes can be calculated with the eddy viscosity ν_t via

$$\boldsymbol{\tau}^{sgs} = -2\nu_t \left(\widetilde{\boldsymbol{S}} - \frac{1}{3}\nabla \cdot \widetilde{\boldsymbol{u}}\boldsymbol{I}\right) + \frac{2}{3}\widetilde{k} \,, \tag{2.56}$$

where $\overline{\boldsymbol{S}}$ denotes the Favre filtered strain rate tensor. $\widetilde{k}$ refers to the Favre filtered turbulent kinetic energy $\widetilde{k} = \frac{1}{2}\widetilde{\boldsymbol{u}'' \cdot \boldsymbol{u}''}$. Within the limit of low Mach number flows, the second term in Eq. (2.56) is included in the filtered pressure [101].

Based on dimensional analysis, the eddy viscosity ν_t can be expressed with a general formulation:

$$\nu_t = (C_m \Delta)^2 \, \overline{OP}\left(\mathbf{x}, t\right) \,, \tag{2.57}$$

where C_m is the model constant, Δ the subgrid characteristic length scale (often the grid size in practice), and $\overline{OP}$ a differential operator associated with the model. The determination of C_m and $\overline{OP}\,(\mathbf{x}, t)$ is different for different eddy viscosity models, which will be introduced in the following.

- The Smagorinsky model
  This model was introduced by Smagorinsky [103], and it has been widely used in LES. In this model, ν_t is proportional to the local strain rate $|\overline{\boldsymbol{S}}| = \left(2\overline{\boldsymbol{S}}\,\overline{\boldsymbol{S}}\right)^{1/2}$. Assuming that the integral scale l_t and the filter width Δ have the same order, the local strain rate $|\overline{\boldsymbol{S}}|$ is chosen as the operator, namely

$$\overline{OP}_s = |\overline{\boldsymbol{S}}| = \left(2\overline{\boldsymbol{S}}\,\overline{\boldsymbol{S}}\right)^{1/2} \ . \tag{2.58}$$

  Then the eddy viscosity ν_t is calculated as

$$\nu_t = (C_s\Delta)^2\,|\overline{\boldsymbol{S}}| = (C_s\Delta)^2\left(2\overline{\boldsymbol{S}}\,\overline{\boldsymbol{S}}\right)^{1/2} \ , \tag{2.59}$$

  where C_s is a model constant that can be evaluated with different methods.
  For this model, the biggest advantage is the simplicity. However, the value of C_s is configuration-specific. For example, C_s is about 0.2 for homogeneous isotropic turbulence. Besides, this model is too dissipative, namely too much energy is transferred to the subgrid component in inhomogeneous flows. This problem is even prominent for near-wall regions. Near the wall, all turbulent fluctuations are damped, which should lead to a zero ν_t. However, this is not the case with Smagorinsky model where ν_t is non-zero as long as a velocity gradient exists. To ensure zero ν_t at the wall, damping functions [104, 105] or dynamic procedure [106] are additionally required.

- The WALE model
  Different from Smagorinsky model, a new operator $\overline{OP}$ is proposed in the WALE model [107], which reads

$$\overline{OP}_{\mathrm{WALE}} = \frac{\left(\mathfrak{s}^d\mathfrak{s}^d\right)^{3/2}}{\left(\overline{\boldsymbol{S}}\,\overline{\boldsymbol{S}}\right)^{5/2} + \left(\mathfrak{s}^d\mathfrak{s}^d\right)^{5/4}} \ . \tag{2.60}$$

  Here, the component of $\mathfrak{s}^d$ can be calculated via $\mathfrak{s}^d_{ij} = \overline{S}_{ik}\,\overline{S}_{kj} + \overline{\Omega}_{ik}\,\overline{\Omega}_{kj} - \frac{1}{3}\delta_{ij}\left[\overline{S}_{mn}\,\overline{S}_{mn} - \overline{\Omega}_{mn}\,\overline{\Omega}_{mn}\right]$, where $\overline{\Omega}_{ij} = \frac{1}{2}\left(\frac{\partial\overline{u}_i}{\partial x_j} - \frac{\partial\overline{u}_j}{\partial x_i}\right)$ and δ_{ij} stands for the Kronecker symbol. Using such an operator, ν_t is a function of both strain and rotation rates, which agrees with the findings regarding the contribution of the turbulent structures to the global dissipation. Moreover, ν_t goes to zero at the wall so that the effect of the no-slip condition is naturally reproduced. The eddy viscosity can be calculated as

$$\nu_t = (C_w\Delta)^2\,\overline{OP}_{\mathrm{WALE}} \ , \tag{2.61}$$

  where C_w is a model constant. Assuming that the WALE model gives the same dissipation as the Smagorinsky model, one can obtain

$$C_w^2 = C_s^2\,\frac{2^{1/2}\left(\overline{\boldsymbol{S}}\,\overline{\boldsymbol{S}}\right)^{3/2}}{\overline{\boldsymbol{S}}\,\overline{\boldsymbol{S}}\,\overline{OP}_{\mathrm{WALE}}} \ . \tag{2.62}$$

  However, for this model, the major drawback is that ν_t does not vanish in the particular case of a solid rotation.

- The Sigma model
  The Sigma model is another advanced eddy viscosity model introduced by Nicoud et al. [108]. Based

on the singular values of the resolved velocity gradient tensor, the operator $\overline{OP}$ is defined as

$$\overline{OP}_\sigma = \frac{\sigma_3 \left(\sigma_1 - \sigma_2\right) \left(\sigma_2 - \sigma_3\right)}{\sigma_1^2} \ , \tag{2.63}$$

where σ_1, σ_2, and σ_3 are the three singular values of the velocity gradient tensor that fulfills $\sigma_1 \geq \sigma_2 \geq \sigma_3 \geq 0$, so that this model is positive by construction. More details can be found in [108]. Then ν_t can be calculated as

$$\nu_t = \left(C_\sigma \Delta\right)^2 \overline{OP}_\sigma \ . \tag{2.64}$$

Similar to Smagorinky and WALE models, only local gradients are involved in the computation of ν_t for the Sigma model. Moreover, this model leads to zero ν_t for any two-dimensional or two-component flows, also for axisymmetric and isotropic compression/expansions. Besides, it presents the proper cubic behavior in the near-wall regions. With all the merits mentioned above, as well as the low computational cost, this method is promising for LES. In this work, this model is applied in the turbulent combustion investigation.

Scalar fluxes

The gradient assumption is used to estimate the unresolved scalar fluxes, which gives

$$\widetilde{\boldsymbol{u}Y_k} - \widetilde{\boldsymbol{u}}\widetilde{Y}_k = -\frac{\nu_t}{Sc_t}\nabla\widetilde{Y}_k \ , \tag{2.65}$$

and

$$\widetilde{\boldsymbol{u}h} - \widetilde{\boldsymbol{u}}\widetilde{h} = -\frac{\nu_t}{Pr_t}\nabla\widetilde{h} \ , \tag{2.66}$$

where Sc_t and Pr_t are subgrid scale Schmidt and Prandtl numbers, respectively. Following Pitsch et al. [109], a constant value of 0.4 is used in this work.

3 Combustion modeling

In this chapter, manifold-based reduced kinetic models, turbulence-chemistry interaction (TCI) closure, and the implementation of these combustion models within a CFD framework are introduced. Firstly, several manifolds such as the so-called Reaction-diffusion Manifold (REDIM) method, Flamelet-Generated Manifold (FGM), Quenching Flamelet-Generated Manifold (QFM), and Quenching Flamelet-Generated Manifold with Exhaust Gas Recirculation (QFM-EGR) are illustrated. Afterwards, the projection of governing equations within the framework of the manifold-based reduced kinetics is given. Then, models used to deal with turbulence-chemistry interaction are presented. Finally, the inclusion of these models in the CFD framework is depicted.

3.1 Manifold-based reduced kinetic models

3.1.1 REDIM

Within the framework of detailed kinetics, a reacting system can be expressed by a set of partial differential equations for the state vector $\boldsymbol{\psi} = (h, P, \frac{Y_1}{M_1}, ..., \frac{Y_n}{M_n}, ..., \frac{Y_{ns}}{M_{ns}})^T$, where h represents the enthalpy as a sum of sensible and enthalpy of formation, P the pressure and $\frac{Y_n}{M_n}$ the specific mole number consisting of the mass fraction Y_n and the molar mass M_n of the species n.

The REDIM [34] method is based on the assumption that the fast and slow chemical processes of a reacting system can be decoupled. The fast chemical processes can be assumed to be quasi-stationary since they complete in a short period of time. Only the time scales of relatively slow chemical processes overlap with physical processes such as molecular transport and they are both accounted for in the context of the REDIM. This makes the REDIM a reduced kinetic model that accounts for both chemical kinetics and molecular transport. Within the REDIM method, the system state vector $\boldsymbol{\psi}$ can be written as $\boldsymbol{\psi} = \boldsymbol{\psi}(\boldsymbol{\theta})$. Here, $\boldsymbol{\theta}$ is the parametrization vector representing the local coordinates of the m-dimensional manifold, and it can be expressed as $\boldsymbol{\theta} = (\theta_1, \theta_2, ..., \theta_m)^T$. Hence, the dimension of the system is reduced from $n_s + 2$ to m, where $m << n_s + 2$. Finally, the REDIM evolution equation [34] reads

$$\frac{\partial \boldsymbol{\psi}(\boldsymbol{\theta})}{\partial t} = (\boldsymbol{I} - \boldsymbol{\psi}_{\boldsymbol{\theta}}(\boldsymbol{\theta})\boldsymbol{\psi}^{+}_{\boldsymbol{\theta}}(\boldsymbol{\theta})) \cdot \{\boldsymbol{F}(\boldsymbol{\psi}(\boldsymbol{\theta})) - \frac{1}{\rho}(\boldsymbol{D}\boldsymbol{\psi}_{\boldsymbol{\theta}}(\boldsymbol{\theta})\boldsymbol{\chi})_{\theta}\boldsymbol{\chi}\} \,, \tag{3.1}$$

where $\boldsymbol{D}$ is the diffusion matrix and $\boldsymbol{F}(\boldsymbol{\psi}(\boldsymbol{\theta}))$ the source term. $(\boldsymbol{\psi}_{\boldsymbol{\theta}}(\boldsymbol{\theta}))_{i,j}$ denotes the partial derivative of $\boldsymbol{\psi}(\boldsymbol{\theta})_i$ with respect to $\boldsymbol{\theta}_j$. $\boldsymbol{\psi}^{+}_{\boldsymbol{\theta}}(\boldsymbol{\theta})$ is the generalized scaled Moore-Penrose pseudo-inverse [110] of $\boldsymbol{\psi}_{\boldsymbol{\theta}}(\boldsymbol{\theta})$, which can be obtained via $\boldsymbol{\psi}^{+}_{\boldsymbol{\theta}} = \left(\boldsymbol{\psi}_{\boldsymbol{\theta}}\boldsymbol{\psi}^{T}_{\boldsymbol{\theta}}\right)^{-1}\boldsymbol{\psi}^{T}_{\boldsymbol{\theta}}$. $\boldsymbol{I}$ is the Identity matrix. $\boldsymbol{\psi}_{\boldsymbol{\theta}}$, $\boldsymbol{\psi}^{+}_{\boldsymbol{\theta}}$ and $\boldsymbol{I}$ build the projection operator projecting on the normal subspace of the manifold to identify the invariant manifold. $\boldsymbol{\chi} = \boldsymbol{\chi}(\boldsymbol{\theta})$ is the estimation of the local gradients of the generalized coordinates.

In order to generate the manifold, Eq. (3.1) is integrated till the stationary state is achieved ($t \to \infty$). Before Eq. (3.1) is solved, an initial guess is needed to determine the mesh distribution, and the boundary conditions for the REDIM need to be formulated. Besides, a gradient estimation of the generalized coordinates needs to be provided to specify the coupling between the chemical and physical processes. Since the steady solution of Eq. (3.1) gives the final REDIM, the initial guess is of less importance. This means that the initial

guess will not influence the final results, but only affect the convergence speed of the evolution equation. As for the boundary conditions, they define the application regime of the REDIM, and are dependent on the specific problem. Regarding the gradient estimation of the generalized coordinates χ, there are two approaches to provide it:

- χ can be directly estimated. This may cause problems in the REDIM integration procedure, e.g., for generalized meshes.
- χ can be obtained with the spatial gradients of the state variables $\nabla\psi$ via

$$\chi = \psi_{\theta}^{+}\nabla\psi. \tag{3.2}$$

Within this work, the second method is used. More details about the initial guess, the gradient estimation, and the boundary conditions will be discussed in the following chapters, corresponding to each specific configuration.

3.1.2 Flamelet-based approaches

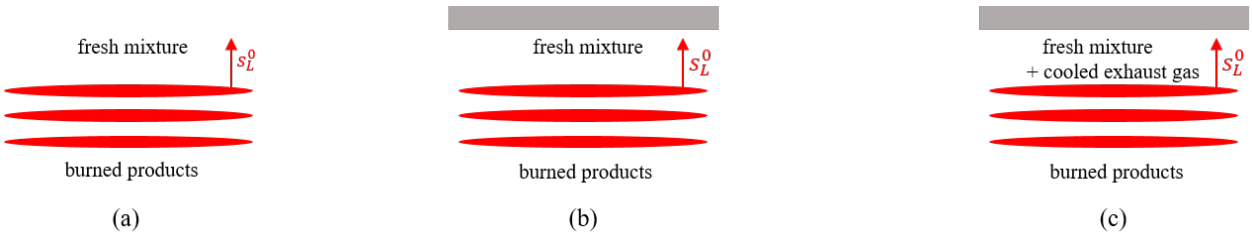

Figure 3.1: Canonical 1D flame configurations for FGM (a), QFM (b), and QFM-EGR (c).

In this section, three flamelet-based approaches, i.e., FGM, QFM, and QFM-EGR, are introduced. The canonical flame configurations for the manifold generation are sketched in Fig. 3.1.

FGM

FGM [59] is a method that accounts for a balance between the convection, molecular diffusion, and chemical reaction. The manifold is obtained based on the solutions for one-dimensional freely propagating flames

$$\frac{\partial \rho u}{\partial x} = 0 \ , \tag{3.3}$$

$$\rho u \frac{\partial Y_k}{\partial x} = -\frac{\partial}{\partial x}\left(\rho Y_k V_k\right) + \dot{\omega}_k \ , \tag{3.4}$$

$$\rho c_p u \frac{\partial T}{\partial x} = \frac{\partial}{\partial x}\left(\lambda \frac{\partial T}{\partial x}\right) - \rho \sum_{k=1}^{Ns} c_{p,k} Y_k V_k \frac{\partial T}{\partial x} + \dot{\omega}_T \ . \tag{3.5}$$

The manifold is characterized by the so-called control variables, which are used to identify the major characteristics of the combustion systems. For the simplest combustion system, e.g., one-dimensional freely propagating flames as shown in Fig. 3.1(a), only the chemical reaction process needs to be considered. In

this case, a progress variable which is usually defined as a linear combination of species mass fractions is introduced ($Y_{\mathrm{PV}} = \sum_{i=1}^{n_s} \alpha_i Y_i$). For more complex scenarios where variations of other scalars such as enthalpy, pressure, and elemental mass fractions need to be taken into account, additional dimensions should be added to the manifold. This can be realized by calculating a series of flamelets with varying conditions for the corresponding quantities. Within this method, the system state vector can be expressed as $\boldsymbol{\psi} = \boldsymbol{\psi}(\boldsymbol{\xi})$, where $\boldsymbol{\xi}$ is the control variable vector $\boldsymbol{\xi} = (Y_{\mathrm{PV}}, ...)^T$.

In this work, heat loss to the wall is additionally taken into consideration for FWI processes. Therefore, considering $Le = 1$, the flamelet manifold is generated based on several one-dimensional freely propagating flames with varying enthalpy levels. To account for the strong heat loss, flamelets with exhaust gas recirculation (EGR) are computed to expand the lower limit of h. The amount of the cooled burned gas added to the fresh gas is determined by EGR = $\dot{m}_{\mathrm{bg}}/(\dot{m}_{\mathrm{fg}} + \dot{m}_{\mathrm{bg}})$, where $\dot{m}_{\mathrm{bg}}$ denotes the mass flux of the cooled burned gas and $\dot{m}_{\mathrm{fg}}$ the mass flux of the fresh gases. Additionally, the upper enthalpy limit is expanded using one-dimensional freely propagating flames with EGR = 0 and increased inflow temperature. Finally, the spanned manifold $\boldsymbol{\psi} = \boldsymbol{\psi}(x, \mathrm{EGR})$ is parameterized by a progress variable (Y_{PV}) and the enthalpy (h), with the former one characterizing the progress of the chemical reaction and the latter the heat loss to the wall, i.e., $\boldsymbol{\xi} = (Y_{\mathrm{PV}}, h)^T$. Here x is the spatial coordinate. In the present study, the reaction progress variable is chosen as $Y_{\mathrm{PV}} = Y_{\mathrm{CO_2}}$. For efficient access to the manifold, both control variables are normalized to values between 0 and 1, namely

$$h^* = \frac{h - h_{\min}}{h_{\max} - h_{\min}} \,, \tag{3.6}$$

$$Y_{\mathrm{PV}}^* = \frac{Y_{\mathrm{PV}} - Y_{\mathrm{PV,\,min}}\left(h^*\right)}{Y_{\mathrm{PV,\,max}}\left(h^*\right) - Y_{\mathrm{PV,\,min}}\left(h^*\right)} \,. \tag{3.7}$$

Therefore, the thermo-chemical states stored in the flamelet table can be expressed as $\boldsymbol{\psi} = \boldsymbol{\psi}\left(Y_{\mathrm{PV}}^*, h^*\right)$.

Besides, this FGM is further extended to consider multiple complex physics, which will be introduced in detail in Chapter 9.

QFM

QFM is proposed by Efimov et al. [78] to account for the strong heat loss within the framework of FWI. With the unity Lewis number assumption, the flamelet manifold is obtained based on a single one-dimensional HOQ flame, as shown in Fig. 3.1(b), resulting in a thermo-chemical state $\boldsymbol{\psi} = \boldsymbol{\psi}(x, t)$, where t denotes the time. The wall and the fresh gas temperature are set to be the same, while the fresh gas composition is set according to the inflow conditions of the reference simulation. Similar to FGM, this two-dimensional manifold is mapped to a progress variable-enthalpy state, i.e., $\boldsymbol{\psi} = \boldsymbol{\psi}(Y_{\mathrm{PV}}, h)$, with the upper enthalpy limit extended by one-dimensional freely propagating flames with increased inflow temperature, where $Y_{\mathrm{PV}} = Y_{\mathrm{CO_2}}$. Normalization is applied to both Y_{PV} and h, which leads to $\boldsymbol{\psi} = \boldsymbol{\psi}\left(Y_{\mathrm{PV}}^*, h^*\right)$.

QFM-EGR

For turbulent FWI, based on the observation that thermo-chemical states in the turbulent SWQ scenario differ significantly from its laminar counterpart, a flame-vortex interaction (FVI) mechanism was proposed in [72]. To take into account the effects of flame dilution due to exhaust gas recirculation in the FVI area, Steinhausen et al. [111] recently proposed the QFM-EGR tabulation approach. For the generation of QFM-EGR, a series of one-dimensional HOQ flames is calculated. The transient HOQ flames are initialized with one-dimensional freely propagating flames with different fresh gas compositions, as shown in Fig. 3.1(c), leading to different thermo-chemical states. Considering $Le = 1$, the initial freely propagating flames consist of (1) flames with varying EGR levels and the same inflow temperature, with the fresh gas mixture gradually diluted

with cold exhaust gases, similar to the FGM, and (2) preheated one-dimensional flames with increased inflow temperatures. All single HOQ simulations result in a three-dimensional manifold $\boldsymbol{\psi} = \boldsymbol{\psi}(x, t, \mathrm{EGR})$, which is mapped to $\boldsymbol{\psi} = \boldsymbol{\psi}\left(Y_{\mathrm{PV}}, Y_{\mathrm{PV2}}, h\right)$, with $Y_{\mathrm{PV}} = Y_{\mathrm{CO_2}}$ and a second progress variable $Y_{\mathrm{PV2}} = Y_{\mathrm{CO}}$ that accounts for the level of exhaust gases added to the flame. Similar to before, normalization is applied to all control variables, which reads

$$Y^*_{\mathrm{PV}} = \frac{Y_{\mathrm{PV}} - Y_{\mathrm{PV,\,min}}}{Y_{\mathrm{PV,\,max}} - Y_{\mathrm{PV,\,min}}} \,, \tag{3.8}$$

$$Y^*_{\mathrm{PV2}} = \frac{Y_{\mathrm{PV2}} - Y_{\mathrm{PV2,\,min}}\left(Y^*_{\mathrm{PV}}\right)}{Y_{\mathrm{PV2,\,max}}\left(Y^*_{\mathrm{PV}}\right) - Y_{\mathrm{PV2,\,min}}\left(Y^*_{\mathrm{PV}}\right)} \,, \tag{3.9}$$

$$h^* = \frac{h - h_{\mathrm{min}}\left(Y^*_{\mathrm{PV}}, Y^*_{\mathrm{PV2}}\right)}{h_{\mathrm{max}}\left(Y^*_{\mathrm{PV}}, Y^*_{\mathrm{PV2}}\right) - h_{\mathrm{min}}\left(Y^*_{\mathrm{PV}}, Y^*_{\mathrm{PV2}}\right)} \,. \tag{3.10}$$

In this case, the thermo-chemical states stored in the flamelet table can be expressed as $\boldsymbol{\psi} = \boldsymbol{\psi}\left(Y^*_{\mathrm{PV}}, Y^*_{\mathrm{PV2}}, h^*\right)$.

3.2 REDIM-based CFD simulations for laminar flames

The evolution equations of the state variables of a reacting system with detailed kinetics can be generally formulated as

$$\frac{\partial \boldsymbol{\psi}}{\partial t} = -\nabla \boldsymbol{\psi}\, \boldsymbol{u} + \frac{1}{\rho} \nabla \cdot \left(\boldsymbol{D} \nabla \boldsymbol{\psi}\right) + \boldsymbol{F} = \boldsymbol{Z} \,, \tag{3.11}$$

where the vector field $\boldsymbol{Z}$ can be viewed as perturbations of the reaction system, which includes physical processes such as convection, molecular diffusion, and chemical reaction.

In the concept of manifold-based reduced kinetics, Eq. (3.11) can be simplified, since $\boldsymbol{\psi}$ can be parameterized by a m-dimensional parametrization vector [32, 38]. In this case, reduced model equations are solved instead of Eq. (3.11). Therefore, besides the governing equations for mass (Eq. (2.1)) and momentum (Eq. (2.2)), m more reduced model equations have to be solved in the CFD solver. Generally speaking, there are two different ways to perform the computations, which can be either in thermokinetic coordinates or generalized coordinates. Here, thermokinetic coordinates represent the coordinates in the space of control variables of the manifold, which have been often used in previous studies. Within this context, the system state vector $\boldsymbol{\psi}$ can be expressed as $\boldsymbol{\psi} = \boldsymbol{\psi}(\boldsymbol{\xi})$. Generalized coordinates refer to the local coordinates of the manifold. In this case, the system state vector $\boldsymbol{\psi}$ can be expressed as $\boldsymbol{\psi} = \boldsymbol{\psi}(\boldsymbol{\theta})$.

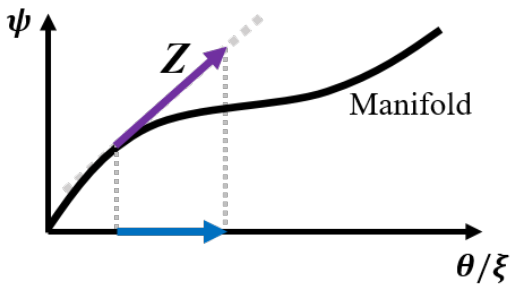

Figure 3.2: Illustration of the invariant manifold. The purple line denotes the vector field, and the blue line the projection of the vector field to the parametrization vector. The thick gray dashed line indicates the tangential space of the manifold.

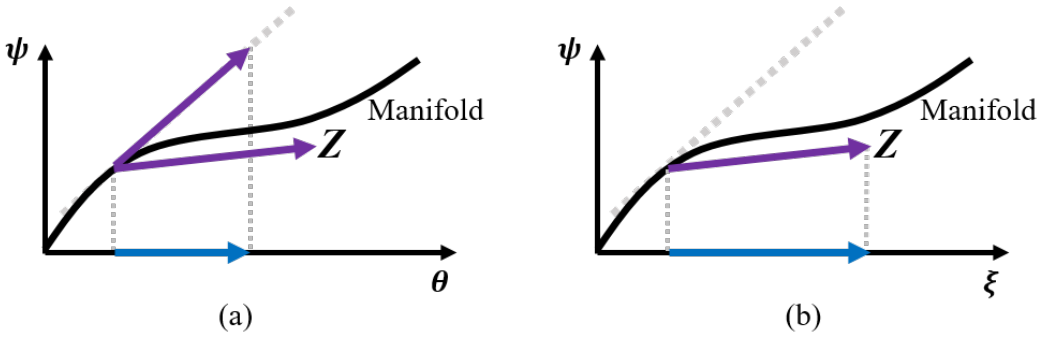

Figure 3.3: Projection of the governing equations when the manifold is non-invariant: (a) in generalized coordinates, and (b) in thermokinetic coordinates. The purple line denotes the vector field, and the blue line the projection of the vector field to the parametrization vector. The thick gray dashed line indicates the tangential space of the manifold.

3.2.1 Reduced model equations in generalized coordinates

For reduced kinetic models within the framework of generalized coordinates, the system state vector ψ can be expressed as $\psi = \psi(\boldsymbol{\theta})$, where $\boldsymbol{\theta}$ is the vector of the m-dimensional generalized coordinates $\boldsymbol{\theta} = (\theta_1, \theta_2, ..., \theta_m)^T$. Thus Eq. (3.11) can be transformed as

$$\frac{\partial \psi}{\partial t} = -\psi_{\boldsymbol{\theta}} \nabla \boldsymbol{\theta}\, \boldsymbol{u} + \frac{1}{\rho} \nabla \cdot (\boldsymbol{D} \psi_{\boldsymbol{\theta}} \nabla \boldsymbol{\theta}) + \boldsymbol{F} = \boldsymbol{Z} \,. \tag{3.12}$$

When the manifold is perfectly invariant, vector field $\boldsymbol{Z}$ is automatically in the tangential subspace of the manifold, as shown in Fig. 3.2.

The Moore-Penrose pseudo-inverse of $\psi_{\boldsymbol{\theta}}$ ($\psi_{\boldsymbol{\theta}}^{+}$) fulfills the condition that

$$\psi_{\boldsymbol{\theta}}^{+} \psi_{\boldsymbol{\theta}} = \boldsymbol{I} \,. \tag{3.13}$$

Multiplying both sides of Eq. (3.12) with $\psi_{\boldsymbol{\theta}}^{+}$, the reduced equations in generalized coordinates $\boldsymbol{\theta}$ can be derived

$$\frac{\partial \boldsymbol{\theta}}{\partial t} + \nabla \boldsymbol{\theta}\, \boldsymbol{u} = \frac{1}{\rho} \psi_{\boldsymbol{\theta}}^{+} \nabla \cdot (\boldsymbol{D} \psi_{\boldsymbol{\theta}} \nabla \boldsymbol{\theta}) + \psi_{\boldsymbol{\theta}}^{+} \boldsymbol{F} \,, \tag{3.14}$$

where $\psi_{\boldsymbol{\theta}}^{+} \boldsymbol{F}$, $\psi_{\boldsymbol{\theta}}^{+}$, and $\boldsymbol{D}\psi_{\boldsymbol{\theta}}$ can be accessed from the REDIM table since they are functions of $\boldsymbol{\theta}$. Since $\psi_{\boldsymbol{\theta}}$ is the partial derivative of ψ with respect to $\boldsymbol{\theta}$, it spans the tangential subspace of the manifold. Due to the multiplication with $\psi_{\boldsymbol{\theta}}^{+}$, all processes are projected orthogonally onto the tangential space of the manifold, as shown in Fig. 3.3(a). In this way, the projected vectors for diffusion, convection, and source terms are converted into a representation of local coordinates. This means that even if the manifold is not perfectly invariant, the system dynamics for the generalized coordinates evolves automatically in the tangential subspace of the manifold when Eq. (3.14) is applied. A further major advantage of the implementation in generalized coordinates is that it is consistent with the calculation of the REDIM in generalized coordinates. In this way an *a-priori* choice of suitable coordinates for the parametrization (based on detailed knowledge about the chemical system) and an *a-posteriori* check of the uniqueness of the representation are no longer necessary. Furthermore, this allows a tabulation of the REDIM with a natural adaptation of the mesh in regions where the manifold is strongly non-linear.

The conservative form of Eq.(3.14) is written as

$$\frac{\partial(\rho\boldsymbol{\theta})}{\partial t} + \nabla\cdot(\rho\boldsymbol{\theta}\otimes\boldsymbol{u}) = \boldsymbol{\psi}_{\boldsymbol{\theta}}^{+}\nabla\cdot(\boldsymbol{D}\boldsymbol{\psi}_{\boldsymbol{\theta}}\nabla\boldsymbol{\theta}) + \rho\boldsymbol{\psi}_{\boldsymbol{\theta}}^{+}\boldsymbol{F}\ . \tag{3.15}$$

Considering convection, molecular transport, and chemical reaction, the development of a laminar flame can be described by Eqs. (2.1), (2.2), and (3.15). Note that Eq. (3.15) applies to both cases with detailed transport models and cases using unity Lewis number assumption.

3.2.2 Reduced model equations in thermokinetic coordinates

For reduced kinetic models in thermokinetic variable space, the system state vector $\boldsymbol{\psi}$ can be expressed as $\boldsymbol{\psi} = \boldsymbol{\psi}(\boldsymbol{\xi})$, where $\boldsymbol{\xi}$ is the control variable vector, which can simply be projected from the system state vector $\boldsymbol{\psi}$ by a constant parametrization matrix $\boldsymbol{C}$, meaning $\boldsymbol{\xi} = \boldsymbol{C}\boldsymbol{\psi}$. Thus, Eq. (3.11) can be transformed as

$$\frac{\partial\boldsymbol{\xi}}{\partial t} + \boldsymbol{C}\nabla\boldsymbol{\psi}\,\boldsymbol{u} = \frac{1}{\rho}\boldsymbol{C}\nabla\cdot(\boldsymbol{D}\nabla\boldsymbol{\psi}) + \boldsymbol{C}\boldsymbol{F}\ , \tag{3.16}$$

with its conservative form presented as

$$\frac{\partial(\rho\boldsymbol{\xi})}{\partial t} + \boldsymbol{C}\nabla\cdot(\rho\boldsymbol{\psi}\otimes\boldsymbol{u}) = \boldsymbol{C}\nabla\cdot(\boldsymbol{D}\nabla\boldsymbol{\psi}) + \rho\boldsymbol{C}\boldsymbol{F}\ . \tag{3.17}$$

Overall, Eqs. (2.1), (2.2), and (3.17) have to be solved in the flow solver.

This method is the same as reduced model equations in generalized coordinates when the manifold is perfectly invariant, as shown in Fig. 3.2. However, using this method when the manifold is not perfectly invariant, the vector field will move the state off the tangential subspace of the manifold and the results become dependent on the parametrization, as illustrated in Fig. 3.3(b).

3.3 LES of turbulent flames

3.3.1 Turbulence-chemistry interaction

For LES of turbulent premixed combustion, the coupling between the chemistry and the turbulent flow needs to be considered. One issue is that the flame thickness is often much smaller than the LES grid size, and contributions from the subgrid-scale level may be dominant for the reactions. To account for the non-resolved subgrid contributions, different models to consider the turbulence-chemistry interaction (TCI) were proposed, which can generally be classified into two categories: (1) statistical approaches based on filtered density functions (FDF) such as presumed FDF, transported PDF, etc., and (2) geometrical approaches such as G-equation model, artificial thickened flame (ATF) model, etc. For statistical approaches, the subgrid scale distribution of the thermo-chemical states is described with FDF. Geometrical approaches mainly relate to the prediction of the turbulent flame propagation. In G-equation model, the flame thickness is assumed to be zero, and the flame front is presented by a propagating surface tracked by a field variable G. In contrast, the flame is thickened in ATF approach so that it can be resolved on the LES mesh. This model is mainly adopted in this work to model the TCI, and it will be introduced in detail in the following.

The basic idea of ATF is to thicken the flame while preserving the flame propagation speed, as shown in Fig. 3.4.

According to premixed flame theory, the laminar burning velocity and the flame thickness can be expressed

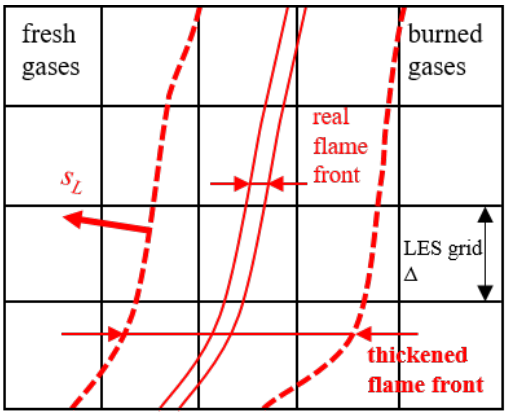

Figure 3.4: Schematic of the ATF approach.

as

$$s_L^0 \propto \sqrt{D\dot{\omega}} \text{ and } \delta \propto \sqrt{\frac{D}{\dot{\omega}}}\,, \tag{3.18}$$

where D is the molecular diffusivity and $\dot{\omega}$ the reaction rate. According to Eq. (3.18), when the diffusivity is increased by a factor of F and the reaction rate is simultaneously decreased by F, the laminar burning velocity s_L^0 remains unchanged while the flame thickness δ is thickened by a factor of F. With such a transformation, the chemical structure of the flame is not altered under laminar flow conditions.

However, when the flame is subjected to turbulent flows, the flame thickening modifies TCI. This is reflected in the variation of the Damköhler number $Da = \tau_t/\tau_c = l_t s_L^0/(u'\delta)$, which compares the turbulent (τ_t) and chemical (τ_c) time scales. Here u' denotes the integral RMS velocity. When the flame is thickened by a factor of F, the newly Damköhler number Da_F becomes

$$Da_F = \frac{l_t s_L^0}{u' F\delta} = \frac{Da}{F}\,. \tag{3.19}$$

In this case, the flame becomes less sensitive to turbulent motions since the ratio between the turbulent length scale and the laminar flame thickness is reduced from l_t/δ to $l_t/(F\delta)$. On one hand, the flame only interacts with the eddies larger than $F\delta$. Even for those eddies interacting with the flame, the efficiency might be affected. Besides, the flame wrinkling is reduced with the flame thickening, which results in a reduction in the overall flame surface, causing a reduced fuel consumption. To overcome this drawback, an efficiency function E is proposed by Colin et al. [112], which is defined as the ratio between the total flame surface and its resolved part in the filtered volume. With E, the diffusivity and the reaction rate becomes

$$EFD \text{ and } \frac{E\dot{\omega}}{F}\,. \tag{3.20}$$

Then the flame speed and the flame thickness become Es_L^0 and $F\delta$, respectively. Therefore, the flame thickness keeps the same as the laminar case, while the propagating speed changes to turbulent burning velocity.

Models for E were derived based on DNS studies. In this work, the power-law flame wrinkling model developed by Charlette et al. [113] is adopted. Modeling is required for length scales between the inner and outer cut-off limits. When the laminar flame thickness δ and the filter size Δ are used as the inner and

outer cut-off scales, the efficiency function can be formulated as

$$E = \Xi_\Delta(\delta) = \left(1 + \min\left[\frac{\Delta}{\delta}, \Gamma\frac{u'_\Delta}{s_L^0}\right]\right)^\beta , \tag{3.21}$$

where Ξ_Δ stands for the subgrid scale wrinkling factor, u'_Δ the unresolved subgrid velocity fluctuation. β is a non-universal constant that depends on the cut-off scales, Reynolds number, and turbulent intensity. For a wide range of turbulent flame applications, $\beta = 0.5$ shows to perform well. Γ is the spectral efficiency function that accounts for the net straining effect of all relevant turbulent scales smaller than Δ, and it can be fitted by

$$\Gamma = \Gamma\left(\frac{\Delta}{\delta}, \frac{u'_\Delta}{s_L^0}, Re_\Delta\right) = \left[\left(\left(f_u^{-a} + f_\Delta^{-a}\right)^{-\frac{1}{a}}\right)^{-b} + f_{Re}^{-b}\right]^{-\frac{1}{b}} , \tag{3.22}$$

where the exponents a and b are determined by $a = 0.6 + 0.2\exp\left(-0.1u'_\Delta/s_L^0\right) - 0.2\exp\left(-0.01\Delta/\delta\right)$ and $b = 1.4$, respectively. Re_Δ is the subgrid-scale Reynolds number, which can be obtained through $Re_\Delta = u'_\Delta\Delta/\nu = 4u'_\Delta\Delta/\left(\delta s_L^0\right)$.

The respective terms in Eq. (3.22) are are expressed as

$$f_u = 4\left(\frac{27C_k}{110}\right)^{\frac{1}{2}}\left(\frac{18C_k}{55}\right)\left(\frac{u'_\Delta}{s_L^0}\right)^2 , \tag{3.23}$$

$$f_\Delta = \left[\frac{27C_k\pi^{\frac{4}{3}}}{110} \times \left(\left(\frac{\Delta}{\delta}\right)^{\frac{4}{3}} - 1\right)\right]^{\frac{1}{2}} , \tag{3.24}$$

$$f_{Re} = \left[\frac{9}{55}\exp\left(-\frac{3}{2}C_k\pi^{\frac{4}{3}}Re_\Delta^{-1}\right)\right]^{\frac{1}{2}} Re_\Delta^{\frac{1}{2}} , \tag{3.25}$$

where $C_k \approx 1.5$ is the universal Kolmogorov constant.

Considering the flame thickening and efficiency function discussed above, the thickened species transport equation can be written as

$$\frac{\partial}{\partial t}(\rho Y_k) + \nabla\cdot(\rho\boldsymbol{u}Y_k) = \nabla\cdot(FE\rho D\,\nabla Y_k) + \frac{E\dot{\omega}}{F} . \tag{3.26}$$

Here unity Lewis number assumption is used for simplicity. However, it can be found that in Eq. (3.26), the diffusion term is modified everywhere, also for regions where flame does not exist. This leads to errors in the case of pure mixing, which is typical in combustion applications. To solve this issue, a flame sensor Ω was proposed by Legier et al. [114] to ensure that the modification is only applied to the reaction zone, which results in a filtered species transport equation in the form of

$$\frac{\partial}{\partial t}\left(\overline{\rho}\widetilde{Y}_k\right) + \nabla\cdot\left(\overline{\rho}\widetilde{\boldsymbol{u}}\widetilde{Y}_k\right) = \nabla\cdot\left(FE\overline{\rho}D\nabla\widetilde{Y}_k\right) + \nabla\cdot\left[(1-\Omega)\frac{\mu_t}{Sc_t}\nabla\widetilde{Y}_k\right] + \frac{E}{F}\overline{\dot{\omega}} . \tag{3.27}$$

The flame thickening factor F can be calculated through

$$F = 1 + \Omega\left(F_{\max} - 1\right) , \tag{3.28}$$

where $F_{\max}$ stands for the prescribed thickening factor, which is usually dynamically determined based on the grid size. Since non-uniform meshes are often adopted in the LES of technical applications, regions with coarse grids require large thickening factors to resolve the flame, while only small values are needed for regions with fine grids to decrease the impact of the modifications in TCI. In this work, $F_{\max}$ is defined based on a minimum number of cells n to resolve the laminar flame thickness

$$F_{\max} = \max\left(1, \frac{n\Delta_x}{\delta}\right) , \tag{3.29}$$

where Δ_x denotes the local cell size. It can be found that the lower bound of $F_{\max}$ is 1, which ensures that the flame is not thickened when the mesh is fine enough. According to [115], it is suggested that $4 \leq n \leq 10$. In this work, $n = 4$.

The employed flame sensor is an adaption of the sensor used in [90] using a second-order polynomial with the maximum located at the maximum reaction rate of the progress variable for each enthalpy level. To avoid thickening in the quenched regions of the flame the flame sensor is blended to zero.

3.3.2 Flamelet-based reduced model equations in thermokinetic coordinates

In the current study, the ATF approach is coupled to FGM, QFM, and QFM-EGR in the LES. For FGM and QFM, the transport equations are solved for the progress variable $\widetilde{Y}_{\mathrm{PV}}$ and the enthalpy $\widetilde{h}$, which read

$$\frac{\partial}{\partial t}\left(\overline{\rho}\widetilde{Y}_{\mathrm{PV}}\right) + \nabla\cdot\left(\overline{\rho}\widetilde{\boldsymbol{u}}\widetilde{Y}_{\mathrm{PV}}\right) = \nabla\cdot\left(FE\overline{\rho}D\nabla\widetilde{Y}_{\mathrm{PV}}\right) + \nabla\cdot\left[(1-\Omega)\,\frac{\mu_t}{Sc_t}\nabla\widetilde{Y}_{\mathrm{PV}}\right] + \frac{E}{F}\overline{\dot{\omega}}_{\mathrm{PV}} , \tag{3.30}$$

and

$$\frac{\partial}{\partial t}\left(\overline{\rho}\widetilde{h}\right) + \nabla\cdot\left(\overline{\rho}\widetilde{\boldsymbol{u}}\widetilde{h}\right) = \nabla\cdot\left(FE\overline{\rho}D\nabla\widetilde{h}\right) + \nabla\cdot\left[(1-\Omega)\,\frac{\mu_t}{Sc_t}\nabla\widetilde{h}\right] . \tag{3.31}$$

For the coupled simulation with QFM-EGR, one more equation for the second progress variable needs to be solved

$$\frac{\partial}{\partial t}\left(\overline{\rho}\widetilde{Y}_{\mathrm{PV2}}\right) + \nabla\cdot\left(\overline{\rho}\widetilde{\boldsymbol{u}}\widetilde{Y}_{\mathrm{PV2}}\right) = \nabla\cdot\left(FE\overline{\rho}D\nabla\widetilde{Y}_{\mathrm{PV2}}\right) + \nabla\cdot\left[(1-\Omega)\,\frac{\mu_t}{Sc_t}\nabla\widetilde{Y}_{\mathrm{PV2}}\right] + \frac{E}{F}\overline{\dot{\omega}}_{\mathrm{PV2}} . \tag{3.32}$$

3.4 Special treatment of CO with tabulated chemistry

When CO is introduced as a control variable, the source term in the governing equation is not directly retrieved from the flamelet manifold, while special treatment is needed. This is due to that the formation of CO may last long, which leads to a violation of the steady-state assumption of the models based on the flamelet concept.

Generally, the reaction rate $\dot{\omega}_{\mathrm{CO}}$ can be decomposed into the production rate $\dot{\omega}^{+}_{\mathrm{CO}}$ and the consumption rate $\dot{\omega}^{-}_{\mathrm{CO}}$, namely

$$\dot{\omega}_{\mathrm{CO}} = \dot{\omega}^{+}_{\mathrm{CO}} + \dot{\omega}^{-}_{\mathrm{CO}} . \tag{3.33}$$

To consider the impact of the local species distribution, the consumption rate is modified as $\frac{Y^{\mathrm{tr}}_{\mathrm{CO}}}{Y^{\mathrm{FLT}}_{\mathrm{CO}}}\dot{\omega}^{-}$, where $Y^{\mathrm{tr}}_{\mathrm{CO}}$ is the transported CO mass fraction, and $Y^{\mathrm{FLT}}_{\mathrm{CO}}$ stands for the CO mass fraction obtained from the

flamelet look-up table (FLT). Subsequently, the corrected reaction rate of CO is expressed as

$$\dot{\omega}_{\mathrm{CO}} = \dot{\omega}^{+}_{\mathrm{CO}} + \frac{Y^{\mathrm{tr}}_{\mathrm{CO}}}{Y^{\mathrm{FLT}}_{\mathrm{CO}}} \dot{\omega}^{-}_{\mathrm{CO}} \,, \tag{3.34}$$

which allows CO to evolve based on its own time scale [116]. In this case, the CO mass fraction, the production rate, and the consumption rate need to be looked up from the flamelet manifold.

3.5 CFD implementation

The one-dimensional flame calculations for the generation of REDIM are conducted with the one-dimensional reacting flow solver INSFLA [117]. In this program package, the partial differential equation systems are solved with the linear implicit extrapolation method LIMEX [118]. This part of work is conducted by Dr.-Ing. Christina Strassacker from KIT.

The one-dimensional flame calculations for the generation of FGM, QFM, and QFM-EGR are performed with the universal laminar flame (ULF) solver [119]. Equations such as Eqs. (3.3), (3.4) and (3.5) are discretized with finite difference methods. Transport properties and species reaction rates are obtained from the open-source chemical kinetics software Cantera [120]. For steady-state flame configurations, e.g., one-dimensional freely propagating flames, the partial differential equations (PDE) are solved with a hybrid damped Newton method. For transient flame configurations, e.g., one-dimensional HOQ flames, an implicit, variable-order, variable-step method based on the Gear multi-value method [121] which is suitable for stiff DAE systems is applied for the integration of the PDEs.

The two and three dimensional simulations are performed with in-house pressure-based solvers based on OpenFOAM [122], which uses the finite volume method (FVM). For detailed kinetics, transport equations of all species are solved. For reduced kinetics, only transport equations of the control variables are solved. To efficiently solve the system of equations, the PIMPLE algorithm is adopted, where a pressure equation is solved to enforce the mass conservation, with an explicit correction to the velocity to satisfy the momentum conservation [123]. For the discretization of spatial gradients, a fourth-order interpolation method is used. The implicit second-order backward method is adopted for temporal discretization. For all simulations, the Courant-Friedrich-Lewy number is limited to CFL ≈ 0.1.

4 Strained laminar premixed CH_4-air head-on quenching[1]

Laminar HOQ is a suitable configuration for FWI investigations, since it contains essential characteristics of FWI while presenting enough simplicity. It is a transient process where the premixed flame propagates through either initially stagnant mixtures or convective flows, namely unstrained HOQ or strained HOQ, respectively, as illustrated in Fig. 4.1. Here the term strain is solely used to characterize the underlying flow field, which then results in a stretched flame. Most existing experimental [16, 19, 124] and numerical [15, 23, 27–30, 35, 45, 125–127] studies related to laminar HOQ flame have mainly focused on stagnant and therefore unstrained conditions. Specifically, the configuration of a freely propagating flame impinging on the wall has been studied in numerical simulations [15, 23, 27–30, 35, 45, 125–127], for varying fuel types, wall temperatures and pressures. By contrast, only a very limited number of investigations take into account the laminar strained flow conditions [20, 37, 43]. Moreover, numerical studies with detailed chemistry and diffusive transport that conduct a systematic variation of strain rate can be rarely found. To fill the gap, the transient HOQ processes of laminar premixed flames in a counterflow configuration for varying strain rates are investigated in this chapter, as shown in Fig. 4.1(b).

Figure 4.1: Schematic of unstrained HOQ (a) and strained HOQ (b).

The major objective of the chapter is twofold. The first is to analyze the influences of the strain rate on: (1) the global quenching quantities, (2) the near-wall micro-structure of the flame, and (3) the near-wall differential diffusion. The second is to find a suitable parametrization for the strain rate for manifold-based tabulation approaches.

4.1 Numerical implementation

The configuration studied in this chapter is schematically shown in Fig. 4.2. A stoichiometric homogeneous CH_4-air mixture is injected from a nozzle. Consistently with the experimental setup [20], the fresh gas is ignited downstream by a spark, and the established strained premixed flame propagates towards the wall. The coordinate system is defined so that x is in the axial direction, being zero at the wall surface and positive in the upstream direction, while r is in the radial direction. The bulk flow velocity at the nozzle exit is denoted U_0.

[1]This chapter is partly taken from the publication by Luo et al. [1], which was created during the work on this thesis. In Ref. [1], I was the main author of this part.

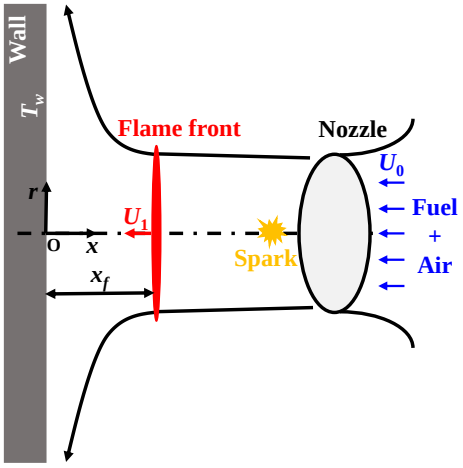

Figure 4.2: Schematic of the system configuration for the transient HOQ process [1].

4.1.1 Numerical description

The strained premixed HOQ configuration mentioned above is simulated using detailed kinetics with the one-dimensional unsteady opposed-flow equations. Beginning with the balance equations for mass, momentum, species, and energy described in Section 2.1.1, one assumption is made that all solutions are functions of time t and axial coordinate x only, which gives axial velocity $u = u(t, x)$, scaled radial velocity $v/r = V(t, x)$, temperature $T = T(t, x)$ and mass fraction $Y_k = Y_k(t, x)$. With some manipulations, the conservation equations for the system are given as

- Mass continuity:

$$\frac{\rho}{P}\frac{\partial p}{\partial t} - \frac{\rho}{T}\frac{\partial T}{\partial t} - \rho\overline{M}\sum_{k=1}^{n_s}\frac{1}{W_k}\frac{\partial Y_k}{\partial t} + \frac{\partial}{\partial x}(\rho u) + 2\rho V = 0\ , \tag{4.1}$$

  where p is the varying component of the total pressure P. It can be obtained via $p = P - p_{\text{ref}}$, where p_{ref} denotes a reference pressure.

- Axial momentum:

$$\rho\frac{\partial u}{\partial t} + \rho u\frac{\partial u}{\partial x} + \frac{\partial p}{\partial x} - 2\mu\frac{\partial V}{\partial x} - \frac{4}{3}\frac{\partial}{\partial x}\left(\mu\frac{\partial u}{\partial x}\right) + \frac{4}{3}\frac{\partial}{\partial x}(\mu V) = 0\ , \tag{4.2}$$

- Scaled radial momentum:

$$\rho\frac{\partial V}{\partial t} + \rho u\frac{\partial V}{\partial x} + \rho V^2 - \frac{\partial}{\partial x}\left(\mu\frac{\partial V}{\partial x}\right) + \Lambda = 0\ , \tag{4.3}$$

  where Λ is the eigenvalue of the system, which is a function of t alone, namely $\Lambda \equiv \frac{1}{r}\frac{\partial p}{\partial r} = \Lambda(t)$.

- Species:

$$\rho\frac{\partial Y_k}{\partial t} + \rho u\frac{\partial Y_k}{\partial x} + \frac{\partial}{\partial x}(\rho Y_k V_k) = \dot{\omega}_k\ , \tag{4.4}$$

where V_k is the diffusion velocity of species k. It is considered by a mixture-averaged diffusion model (Eq. (2.15)). Note that when evaluating the diffusion velocity, only species gradients in x direction are taken into account.

- Energy:

$$\rho c_p \frac{\partial T}{\partial t} + \rho c_p u \frac{\partial T}{\partial x} - \frac{\partial}{\partial x}\left(\lambda \frac{\partial T}{\partial x}\right) - \frac{\partial p}{\partial t} - u\frac{\partial p}{\partial x} + \rho\left(\sum_{k=1}^{n_s} c_p Y_k V_k\right)\frac{\partial T}{\partial x} + \sum_{k=1}^{n_s} \dot{\omega}_k h_k = 0\ . \tag{4.5}$$

GRI-Mech 3.0 [128] mechanism is used to describe the chemical reactions.

4.1.2 Computational domain and boundary conditions

The computational domain is one-dimensional and extends from the nozzle exit to the wall. The total length of the domain is 10 mm. Initially the domain is filled with fresh mixture at 1 atm. To avoid preheating, the unburned gas and the wall temperature are set to be equal. Stretched grid with local refinement near the wall is adopted, resulting in a mesh resolution of 5 μm in the near-wall region and 1200 total grid points.

At the inlet, a constant axial velocity u is applied, which equals to the value at the nozzle exit U_0. The scaled radial velocity V is set to zero. The temperature T and species mass fractions Y_k are set to be the same as the unburned gas.

At the wall, the axial velocity u is set to zero, while a zero-gradient boundary condition is applied for the scaled radial velocity V. The wall temperature T_w is considered constant. Consistently with a previous study [30], an inert and impermeable wall is assumed. Consequently, a zero-diffusion flux boundary condition $\rho V_k Y_k = 0$ is employed for all species.

Similarly to [129], the strain rate K_s is defined as the mean axial velocity gradient near the wall, which can be varied by adjusting the inlet velocity. Since the value of K_s changes during the transient flame propagation, it is calculated based on the initial state of the flow field prior to ignition. It is found that the wall temperature has only little impact on the exact value of the strain rate. In the present study, four different strain rates of 600 s^{-1}, 1200 s^{-1}, 1800 s^{-1}, and 2400 s^{-1} are investigated for two different wall temperatures (T_w = 300 K, 600 K) that are relevant for confined combustion [43], as summarized in Table 4.1. For reference, the wall distance where the magnitude of the axial flow velocity $|u|$ equals the unstretched adiabatic laminar burning velocity s_L^0 (T_w = 300 K) is also included.

Strain rate K_s **[s^{-1}]**	**Wall temperature** T_w **[K]**	**Wall distance [mm] where** $\lvert u\rvert = s_L^0$ **(T_w = 300 K)**
600	300, 600	0.662
1200	300, 600	0.325
1800	300, 600	0.212
2400	300, 600	0.161

Table 4.1: Summary of the investigated strained HOQ conditions.

4.1.3 Dimensionless parameters

To compare the current results with the literature and to quantify the effect of strain rate, dimensionless parameters previously used in near-wall combustion studies are employed.

The distance of any position to the wall x is normalized as

$$D_w = \frac{x}{\delta} \, . \tag{4.6}$$

Specifically, the distance between the flame front and the wall (x_f) is often expressed in its dimensionless form as a Peclet number [35]

$$Pe = \frac{x_f}{\delta} \, , \tag{4.7}$$

where the definition of the laminar flame thickness δ can be found in Eq.(2.32). The flame front position corresponds to the location of the maximum heat release rate, which is consistent with previous studies [27, 79].

The quenching instant (t_Q) is defined as the time instant when the wall heat flux achieves its maximum $q_{\mathrm{wall,max}} = (\lambda \partial T/\partial x|_{\mathrm{wall}})_{\mathrm{max}}$, which is consistent with other numerical studies [33]. Here, the subscript $_Q$ denotes the instant of quenching. The dimensionless form of the wall heat flux is $Q = q_{\mathrm{wall}}/[\rho s_L^0 c_p (T_{ad} - T_u)]$, where T_{ad} is the adiabatic flame temperature and T_u the temperature of the unburned gas. The distance between the flame front and the wall at the quenching instant is defined as quenching distance $x_{f,Q} = x_f(t = t_Q)$, with the corresponding Peclet number $Pe_Q = x_{f,Q}/\delta$. Based on the definitions above, a dimensionless time τ is expressed as

$$\tau = \frac{t - t_Q}{\delta / s_L^0} \, . \tag{4.8}$$

4.2 Results and discussion

In this section, firstly the numerical solver is validated with the available experimental data. Using the validated solver, the effects of strain rates and wall temperature are investigated in a systematic manner next.

4.2.1 Comparison between the simulation and the experiment

A simulation is performed based on the experimental setup in [20], and the results are compared to the experimental data, which includes the temperature and CO concentration measured through two-photon LIF and nanosecond CARS of nitrogen, respectively.

Figure 4.3 shows the variation of CO mole fraction X_{CO} for six different positions, i.e., x = 0.1 mm, x = 0.2 mm, x = 0.3 mm, x = 0.5 mm, x = 0.9 mm, x = 1.7 mm. Similar to [20], plots are presented in the phase space of CO-T, where T stands for the temperature. Also indicated are the two branches for CO formation and oxidation, which are characteristic of premixed flames, and more details can be found in [69]. Experimental results are shown as scatters and corresponding mean values, with the variances from the fluctuations shown as error bars. At different locations, the trends in the variation of CO against T are similar. In the beginning, the CO level increases along with the temperature (CO formation branch). After the peak value is reached, CO decreases due to oxidation. The CO level drops with initially increasing and later decreasing temperature depending on the wall distance. However, non-negligible differences between the simulations and experiments can be observed for positions near the wall, which is consistent with the findings in [37]. This can be seen mostly for the oxidation branch, e.g., Figs. 4.3(b) and 4.3(c), but also for the formation branch in the very near-wall position, as in Fig. 4.3(a). These differences can be partially attributed to experimental uncertainties in wall distance determination. The wall in the experiments is convex which is part of a sphere with a radius of R_{wall} = 300 mm. The maximum value of the uncertainty is estimated to be 100 μm [130]. Thus, simulation results shifted by 100 μm are additionally shown, as the black dashed lines in Fig. 4.3, which agree very well with the experiment for all wall distances. It is

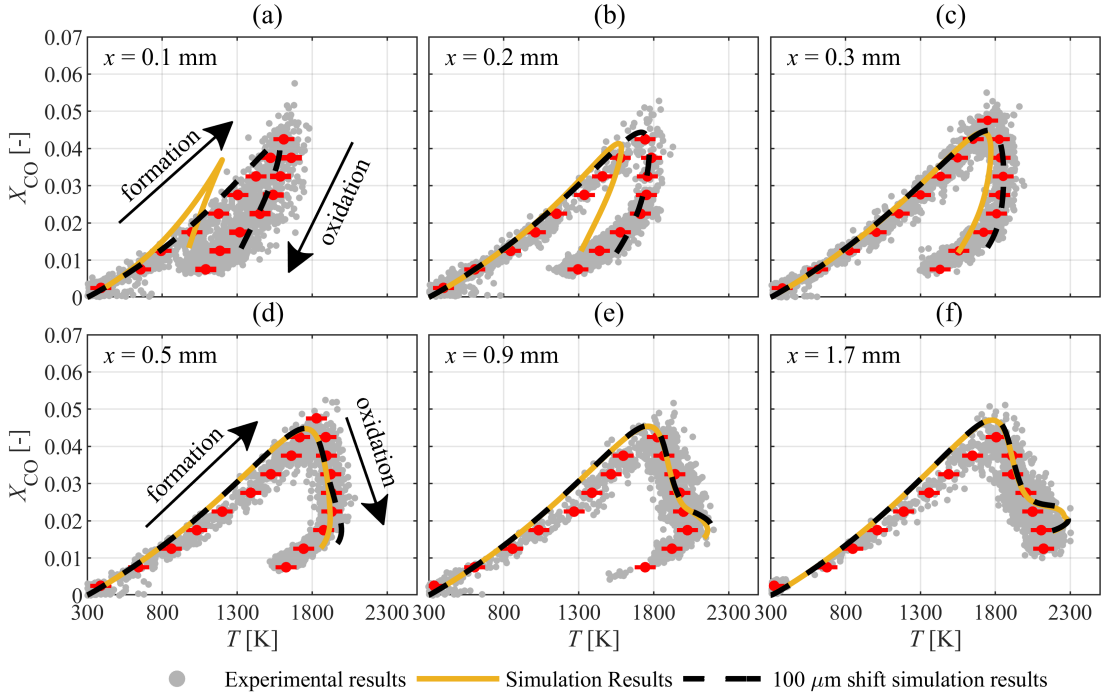

Figure 4.3: CO mole fraction over temperature for different positions until 0.5 ms after quenching. The error bars are obtained according to the experimental fluctuations [20].

evident that in the very near-wall region, the shift has a significant effect on the CO-T variation, see e.g., for $x = 0.1$ mm. However, such effects become almost negligible for locations far away from the wall, e.g., for $x = 1.7$ mm, because the wall influence on the flame structure decreases with increasing distance from the wall. Further away from the wall, the wall influence can be neglected and both CO formation and oxidation branches correspond to those of a freely propagating flame. For these regions, discrepancies between numerical results and the experimental data, especially in the formation branch, may be attributed to the chemical mechanism and the influence of initial ignition which is generated by placing an artificial time-decaying energy source near the inlet, with the latter effect becoming insignificant in the near-wall region.

Figure 4.4(a) shows the evolution of the temperature T as a function of the dimensionless time τ and the normalized wall distance D_w. It can be clearly seen that as the flame propagates towards the wall, the near-wall temperature increases. After quenching, the temperature first decreases in the near-wall region, and then spreads towards regions away from the wall. The corresponding evolution of X_{CO} is shown in Fig. 4.4(b). It can be seen that CO does not vanish during or even after quenching, and it remains high near the wall, which is consistent with the experimental data as reported above.

Overall, the comparison between the numerical and experimental results shows favorable agreement. Furthermore, the numerical results for this reference case are comparable to previously reported works, and the deviations from experimental results can be partially attributed to uncertainties in the determination of the wall position. In the following section, the influences of the strain on the quenching process both in terms of global quantities and local thermo-chemical structures are investigated.

4.2.2 Global quenching quantities

The quenching distance is a key parameter quantifying the thickness of the unburned layer. Dimensionless quenching distances (Pe_Q) for different strain rates and different wall temperatures, see Table 4.1, are

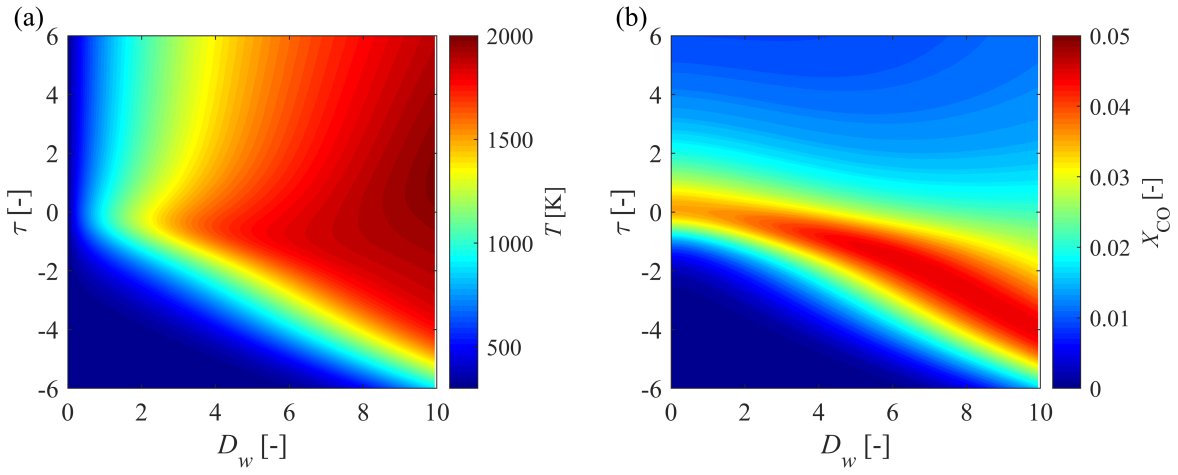

Figure 4.4: D_w-τ plots for the experimental setup [20]: (a) temperature, (b) CO mole fraction.

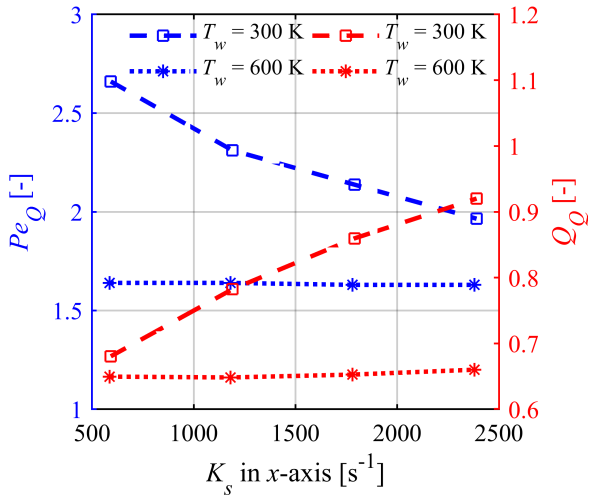

Figure 4.5: Normalized quenching distances and quenching wall heat fluxes.

plotted in Fig. 4.5. Overall, Pe_Q decreases with an increasing strain rate, which is a direct consequence of the underlying flow pushing the flame towards the wall. However, for a higher wall temperature, the strain rate effects on Pe_Q become less pronounced. For example, for T_w = 300 K, Pe_Q decreases from 2.66 to 1.96 for a strain variation of 600 s^{-1} to 2400 s^{-1}. By contrast, for T_w = 600 K, the maximum difference in Pe_Q is only 0.01. This can be explained by the increased laminar flame speed for higher temperature. As the flame itself propagates with a larger speed, the relative importance of the convective flow decreases. Comparing Pe_Q for different wall temperatures for the same strain rate, it can be seen that Pe_Q decreases as the wall temperature increases. This specific trend is consistent with previous findings in the literature for unstrained HOQ [131]. The gap becomes narrower as the strain rate increases.

The non-dimensional wall heat flux is another important quantity in FWI. Following the definition above and consistent with previous works, Q_Q denotes the normalized wall heat flux at the quenching instant. The red lines in Fig. 4.5 show Q_Q for different strain rates and different wall temperatures. Overall, a higher strain rate results in a larger wall heat flux. This is closely related to the variation in Pe_Q. It is interesting to note that the variation in Q_Q is more distinct for smaller strain rates. At higher wall temperatures, the

normalized wall heat flux almost stays constant at a value of 0.66 for varying strain rates, which is consistent with the unstrained value reported in [35].

4.2.3 Local thermo-chemical states

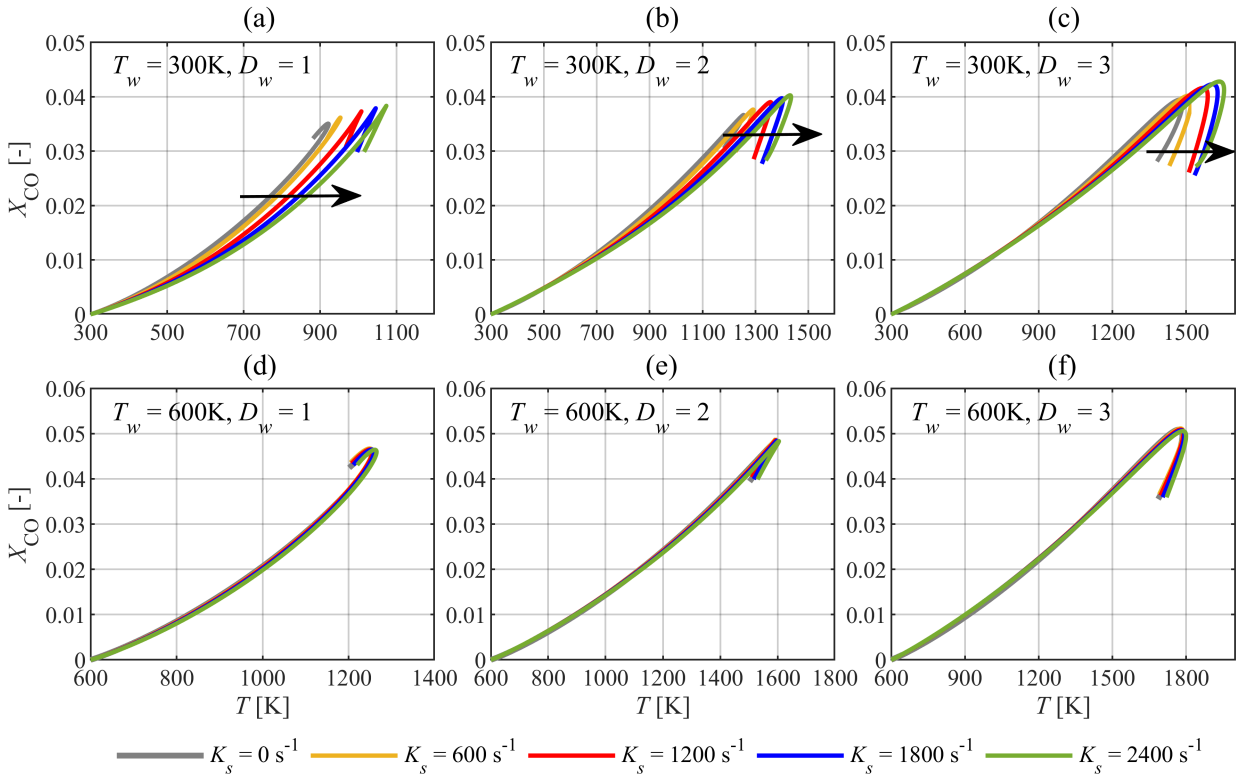

Figure 4.6: X_{CO}-T plots for different positions until 0.5 dimensionless time after quenching.

In this section, the local thermo-chemical states in the vicinity of the wall and how they are affected by the strain are discussed. Figures 4.6 and 4.7 present the variations of CO-T and CO_2-T, respectively, for different strain rates, wall distances, and wall temperatures. Position (a) is always within the quenching region, while other positions can be either in or outside the quenching layer, depending on the operating conditions, see the discussion on the Peclet number above. The results are recorded until $\tau = 0.5$. It is seen that all species profiles vary strongly at the different positions and for the two wall temperatures. Closer to the wall, the peak temperature decreases, which means that the chemical reactions happen under lower temperature conditions.

From the results, it is evident that the strain rate almost has no influence on the thermo-chemical states for $T_w = 600$ K. Non-negligible influences are observed for $T_w = 300$ K, which will be discussed in detail. At position (a), which is very close to the wall, the strain rate shows significant influences on the formation of both species, as well as the oxidation of CO. Moving further away from the wall to positions (b) and (c), different characteristics are observed. For CO, the strain rate effects on CO-T decrease with increasing wall distance and remain only important for the oxidation branch. This can be confirmed by looking specifically at $D_w = 3$, where the formation branches for different strain rates almost overlap. For CO_2, the impact of strain rate also decreases, especially for larger strain rates. As can be seen from Figs. 4.7(a)-(c), the difference between $K_s = 1800$ s^{-1} and $K_s = 2400$ s^{-1} shrinks significantly from $D_w = 1$ to $D_w = 3$.

Summarizing the analyses of quenching distances, wall heat fluxes, and CO-T and CO_2-T variation, the

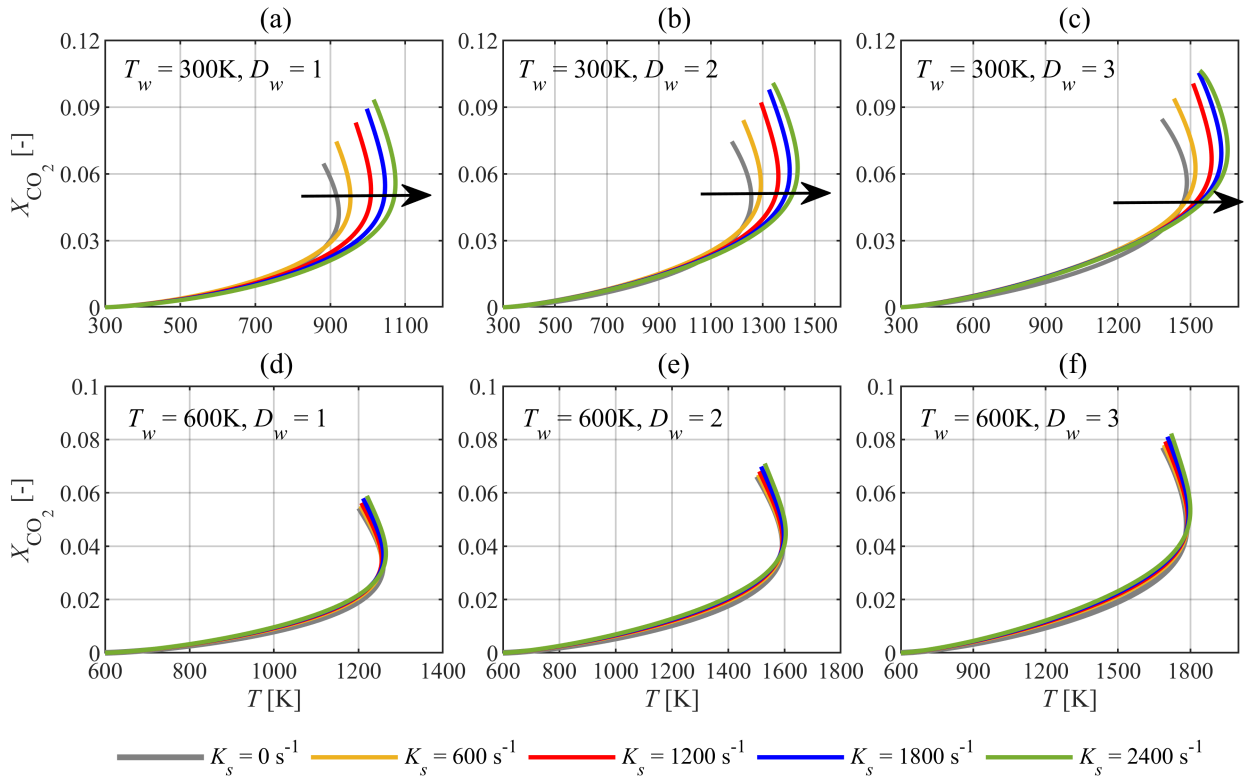

Figure 4.7: X_{CO_2}-T plots for different positions until 0.5 dimensionless time after quenching.

strain rate has a significant effect at lower wall temperatures. Contrarily, the effect almost diminishes at higher wall temperatures and this applies both for the global quantities and the local microstructure. Therefore, in the subsequent discussion, we focus on cases with $T_w = 300$ K to investigate the impact of the strain on differential diffusion.

4.2.4 Strain rate effects on differential diffusion

As a first step, the impact of differential diffusion on the quenching process for the case $T_w = 300$ K and $K_s = 600\ s^{-1}$ is quantified. Then, the influences of varying strain rates are analyzed.

Figure 4.8 shows profiles of the differential diffusion parameter Z_{HC} as functions of the normalized wall distance for different times. Symbols on the lower abscissa denote the flame front position at the respective time (indicated by the color). Note that the main focus of the present study is the variation of Z_{HC}, rather than the Z_{HC} value itself, which might strongly differ for other fuels. At different times, the minimum (largest absolute) value of Z_{HC} always occurs ahead of the position of maximum heat release towards the preheat zone, i.e., between the reaction zone and the wall. As the flame approaches the wall, the minimum of Z_{HC} moves towards the wall and the differential diffusion within the quenching distance becomes more pronounced. The smallest value of Z_{HC} is found just prior to quenching, and it exceeds the value of the propagating flame by a factor of up to 2 in terms of the absolute number. This is consistent with the findings above concerning the variation of the local thermo-chemical states during quenching.

For the subsequent analysis of differential diffusion during HOQ, the balance equation for Z_{HC} is considered.

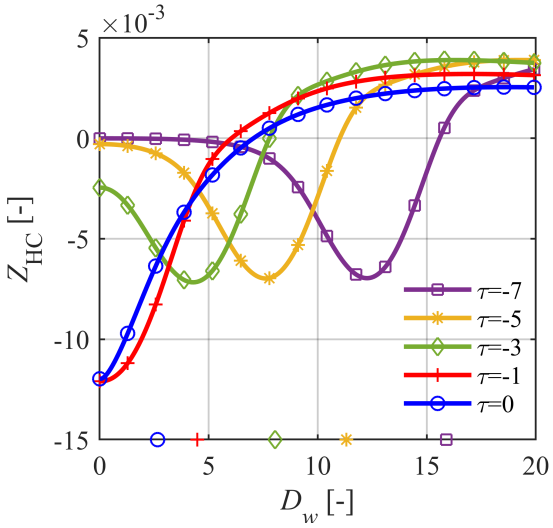

Figure 4.8: Differential diffusion parameter profiles at different times for T_w = 300 K, K_s = 600 s^{-1}.

Using Eq. (2.34), the total derivative can be expressed as

$$\rho\frac{DZ_{\mathrm{HC}}}{Dt} = \frac{1}{Y_{\mathrm{H},2}-Y_{\mathrm{H},1}}\rho\frac{DY_{\mathrm{H}}}{Dt} - \frac{1}{Y_{\mathrm{C},2}-Y_{\mathrm{C},1}}\rho\frac{DY_{\mathrm{C}}}{Dt}\ . \tag{4.9}$$

The balance equations for elemental mass fractions are

$$\begin{aligned}\rho\frac{DY_{\mathrm{H}}}{Dt} &= -\nabla\cdot\left(\sum_{k=1}^{n_s}\frac{a_{k\mathrm{H}}M_{\mathrm{H}}}{M_k}\rho Y_k V_k\right)\ ,\\ \rho\frac{DY_{\mathrm{C}}}{Dt} &= -\nabla\cdot\left(\sum_{k=1}^{n_s}\frac{a_{k\mathrm{C}}M_{\mathrm{C}}}{M_k}\rho Y_k V_k\right)\ ,\end{aligned} \tag{4.10}$$

where M stands for the molecular weight. $a_{k\mathrm{H}}$ is the number of atoms of element H in a molecule of species k, $a_{k\mathrm{C}}$ is the number of atoms of element C in a molecule of species k.

For a unity Lewis number assumption, the diffusion term for Z_{HC} can be expressed as $-\nabla\cdot(\rho D\nabla Z_{\mathrm{HC}})$, where D is the diffusion coefficient of Z_{HC} and all species. Combining Eqs. (4.9) and (4.10), the governing equation for Z_{HC} can be rearranged as

$$\begin{aligned}&\rho\frac{DZ_{\mathrm{HC}}}{Dt} - \nabla\cdot(\rho D\nabla Z_{\mathrm{HC}})\\ &= \frac{-\nabla\cdot\left(\sum_{k=1}^{n_s}\frac{a_{k\mathrm{H}}M_{\mathrm{H}}}{M_k}\rho V_k Y_k\right)}{Y_{\mathrm{H},2}-Y_{\mathrm{H},1}} - \frac{-\nabla\cdot\left(\sum_{k=1}^{n_s}\frac{a_{k\mathrm{C}}M_{\mathrm{C}}}{M_k}\rho V_k Y_k\right)}{Y_{\mathrm{C},2}-Y_{\mathrm{C},1}} - \nabla\cdot(\rho D\nabla Z_{\mathrm{HC}})\ .\end{aligned} \tag{4.11}$$

The right-hand side of Eq. (4.11) represents the deviation from a scalar with unity Lewis number and therefore it is a direct measure for the importance of differential diffusion.

Figure 4.9 presents the evolution of the source term at different times up to quenching for K_s = 600 s^{-1} (a) and K_s = 1800 s^{-1} (b), respectively. For reference, the Z_{HC} profiles are also plotted. Prior to quenching, the shape of the source term remains similar for all times with negative values just ahead of the flame front and positive values around the reaction zone, which is the expected profile for propagating flames without wall influence. When the flame is far away from the wall, the source term near the wall is zero, see e.g.,

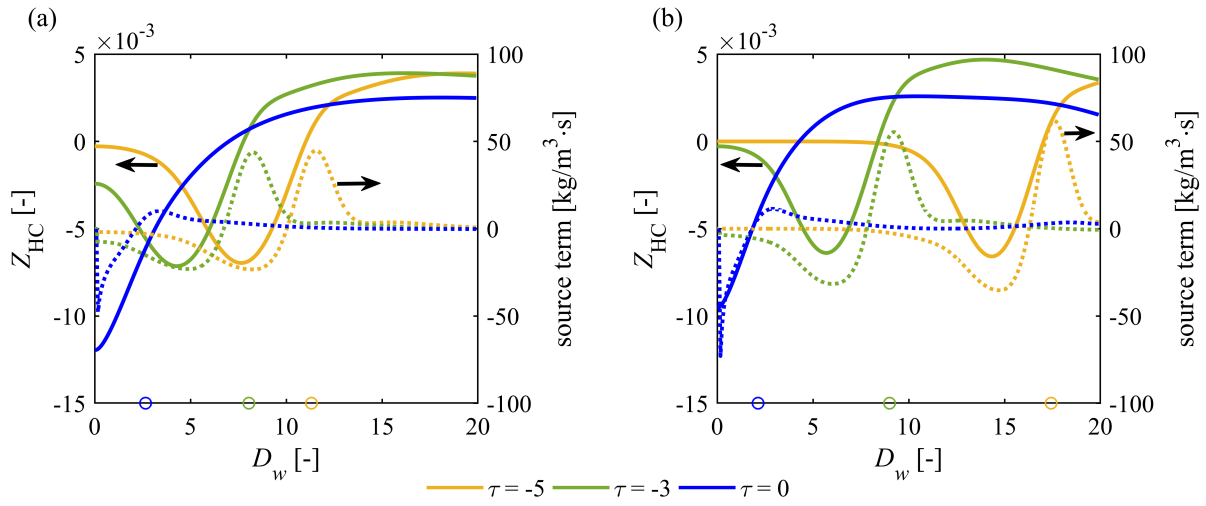

Figure 4.9: Profiles of source term (dotted lines) and Z_{HC} (solid lines) at different times for K_s = 600 s^{-1} (a) and K_s = 1800 s^{-1} (b).

τ = -5 for both strain rates. As the flame approaches the wall, the source term in the near wall region begins to decrease until the instant of quenching, when both positions of minimum source term and minimum Z_{HC} (see also Fig. 4.8) locate at the wall. Compared to the propagating flames, both Z_{HC} and its source term decrease to smaller values (larger absolute values).

Both maximum and minimum Z_{HC} source terms are amplified by higher strain rates for the propagating flames, resulting in a small difference in the minimum and maximum Z_{HC} values. However, when the flame interacts with the wall, the minimum Z_{HC} value for K_s = 600 s^{-1} at τ = 0 is significantly smaller compared to K_s = 1800 s^{-1}, meaning that the strain dampens differential diffusion near the wall during quenching. In contrast, the source term decreases with an increasing strain rate, which reflects the larger magnitude of species' gradients near the wall.

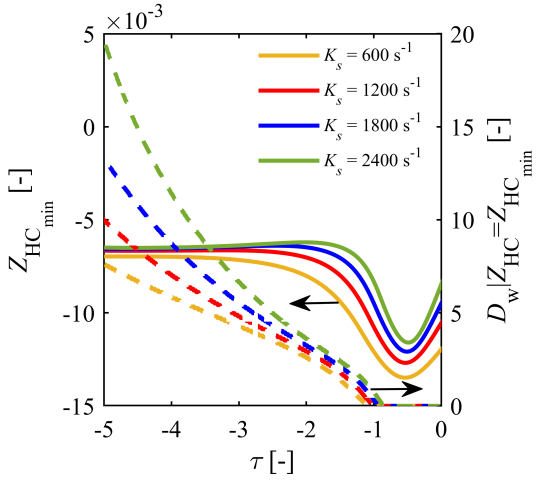

Figure 4.10: Minimum Z_{HC} values (solid lines) within D_w = 0–20 and their location $D_w|Z_{\mathrm{HC}}=Z_{\mathrm{HC_{min}}}$ (dashed lines) plotted over time.

This is further analyzed in Fig. 4.10, where minimum Z_{HC} values ($Z_{\mathrm{HC_{min}}}$) are plotted as a function of time, as is the location $D_w \,|\, Z_{\mathrm{HC}} = Z_{\mathrm{HC_{min}}}$. When the flame is far away from the wall, the minimum Z_{HC}

value is almost constant during propagation, confirming the rather small influence of strain as discussed above. However, when the flame enters the near-wall region (see discussion on Peclet number above), a minimum of $Z_{\mathrm{HC_{min}}}$ occurs right before the quenching with a slight delay (τ values closer to zero) for higher strain rates. Further, the higher the strain rate, the later starts the departure from the propagating flame and this is also reflected in the trajectory of $D_w \,|\, Z_{\mathrm{HC}} = Z_{\mathrm{HC_{min}}}$. The location of the minimum Z_{HC} value appears later in the quenching region for a higher strain rate. In fact, this explains why $Z_{\mathrm{HC_{min}}}$ does increase with strain. Although the source term is amplified by strain, the smaller residence time in the quenching layer leads to the dampening of differential diffusion.

4.2.5 Guidance to near-wall flamelet modeling

For the flamelet modeling of premixed unconfined combustion in strained conditions, an additional parameter has been introduced to characterize the strain rate effects [132–135]. The choice of the parameter should guarantee that it is sensitive to the strain rate and there is no overlap between different profiles, so that a unique value can be found during tabulation. This section mainly focuses on finding such a suitable strain parameter for near-wall flamelet modeling.

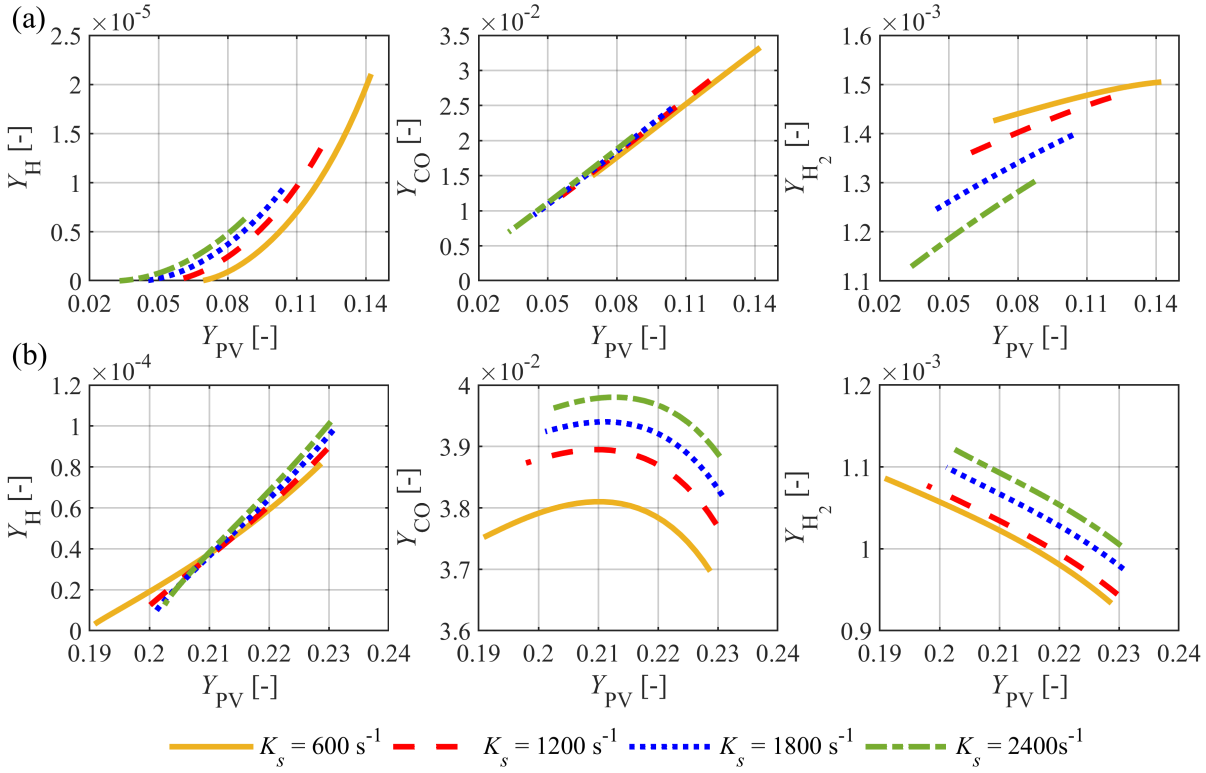

Figure 4.11: Different species plotted against progress variable for different strain rates at different time instants: (a) prior to quenching (τ = -1), (b) at quenching (τ = 0).

In Fig. 4.11, three different scalars previously used for strain parametrization, Y_{H}, Y_{CO} and $Y_{\mathrm{H_2}}$, are plotted against progress variable. Here, the progress variable (Y_{PV}) is defined as $Y_{\mathrm{PV}} = Y_{\mathrm{CO_2}} + Y_{\mathrm{H_2O}} + Y_{\mathrm{CO}} + Y_{\mathrm{H_2}}$ [132]. Two time instants are chosen: τ = -1 represents the time before quenching, while the other time τ = 0 corresponds to the quenching instant. As shown in Fig. 4.11(a), before quenching, both Y_{H} and $Y_{\mathrm{H_2}}$ show a strong sensitivity to the strain rate, while Y_{CO} varies only little. It is hard to distinguish Y_{CO} between different strain rates, so Y_{CO} is not a suitable choice for the time before quenching. At the instant of quenching, Y_{H} does not show a monotonic variation with the strain rate as before. Different

profiles overlap, so a lack of uniqueness will be encountered for tabulation. At the quenching instant, Y_{H_2} is a suitable strain rate parameter. Although the variation trend is opposite to the time before quenching, the monotonicity over the strain rate is retained. Based on the above analysis for the cases studied, H_2 shows to be promising to parameterize the strain rate for the near-wall flamelet modeling.

4.3 Summary

This chapter investigates the transient HOQ of stretched premixed laminar CH_4-air flames using detailed chemistry and transport. While previous studies in the literature focused on unstrained conditions, this work is the first study of laminar HOQ systematically varying the strain rate for different wall temperatures. After validating the numerical approach against experimental data, this work specifically focuses on the following four aspects:

1. The impact of the strain rate on the global quantities: The normalized quenching distance expressed as Peclet number Pe_Q decreases with an increasing strain rate, while the normalized wall heat flux increases. This can be directly attributed to the underlying flow field supporting flame propagation towards the wall. The impact of strain is generally higher for low wall temperatures while it is negligible at 600 K.

2. The impact of the strain on the near-wall thermo-chemical states: the local flame structure is analyzed with CO-T and CO_2-T profiles at various wall distances. In the region very close to the wall, strain influences the formation of both species, as well as the oxidation of CO. Away from the wall, the influences of the strain decrease. The impact of the strain is generally more pronounced for lower wall temperatures and it is negligible at 600 K, which is consistent with the findings for the global quantities above.

3. The impact of the strain on the near-wall differential diffusion: the effect of non-equal diffusivities is quantified by the parameter Z_{HC}. Differential diffusion is substantially enhanced in the quenching layer compared to propagating flames. While strain has little influence on the minimum/maximum Z_{HC} values in the propagating flame, higher strain rates do suppress the increase of differential diffusion in the near-wall quenching layer. This aspect is further quantified by studying the source term in the transport equation for Z_{HC}. While the source term is amplified by strain, the main effect is the reduction of residence time in the near-wall region for higher strain rates.

4. Parametrization of the strain rate for manifold-based tabulation approaches: It was shown in previous works that the strain effect on the structure of a stretched premixed flame can be parameterized by a reactive scalar. This finding is extended here for quenching flames. Results show that the H_2 is well-suited for parameterizing strain rate for both propagation and quenching, while other scalars previously used for propagating flames are not applicable during quenching. While the parametrization should only be used for the conditions tested, our findings can be considered a good starting point when looking at other conditions.

5 Laminar premixed CH_4-air side-wall quenching[2]

In this chapter, the FWI investigation is extended to a two-dimensional configuration. Specifically, the major focus is the development and application of manifold-based reduced kinetics for the laminar SWQ, considering a unity Lewis number assumption. In previous studies, manifold-based reduced kinetic models that have been successfully applied in the laminar SWQ configurations are all based on the parametrization in thermokinetic coordinates. Here the thermokinetic coordinates denote the coordinates in thermokinetic variable space, which are closely related to the values of the control variables. For example, Efimov et al. [78] proposed QFM to compute the two-dimensional laminar SWQ. Ganter et al. [77] and Steinhausen et al. [7] performed two-dimensional laminar SWQ simulations using REDIMs [34] generated based on the gradient estimation of one-dimensional HOQ flames, and the results are also in good agreement with the experimental data. In these studies, the reduced coordinates are chosen as CO_2 and enthalpy, where CO_2 acts as the reaction progress variable and enthalpy is used to account for the heat loss to the wall. In three-dimensional studies [75], an additional mixture fraction coordinate is used to account for the mixing between the main flow and coflow. Another way to parameterize the manifold is to use the generalized coordinates. Here, the generalized coordinates refer to the local coordinates on the manifold, which are independent of the specific values of the control variables. Although it is straightforward to use thermokinetic coordinates, this method also has shortcomings under some conditions. For manifolds that are not perfectly invariant, i.e., the vector fields including the reaction and diffusion terms are not exactly tangential to the manifolds, the results vary depending on the parametrization, as shown in Fig. 3.3(b). However, there are no such problems when using generalized coordinates, where all processes are first projected onto the tangential space of the manifold before being projected onto the reduced coordinates [32], as shown in Fig. 3.3(a). Therefore, for generalized coordinates, even for non-invariant manifolds, the results are independent of the choice of parametrization. This was proved in one-dimensional simulations of freely propagating flames and HOQ flames performed by Strassacker et al. [32]. However, reduced model equations in generalized coordinates have not yet been applied to FWI at higher dimensions, e.g., in two-dimensional/three-dimensional SWQ.

In this chapter, the reduced model equations in generalized coordinates are applied in two-dimensional simulations of SWQ of laminar CH_4-air premixed flames. The main objective of this chapter is twofold: (1) to illustrate the advantages of reduced model equations in generalized coordinates over thermokinetic coordinates. Here, REDIM reduced kinetics are used for the tabulation. Note that look-up tables generated based on other manifold-based reduced kinetic models also work, e.g., the QFM [78], and (2) to investigate possible simplifications of the gradient estimation, which is particularly relevant for the simulations using the REDIM for tabulation within the framework of reduced model equations in generalized coordinates.

5.1 Numerical implementation

The configuration investigated in this chapter is similar to the experimental setup [68], as shown in Fig. 5.1. A stream of stoichiometric CH_4-air mixture is issued from the nozzle, with a Reynolds number of 5000. A V-shaped flame is anchored by a rod downstream of the nozzle exit, with one branch interacting with the wall and the other developing freely. The wall is cooled by water, and its temperature T varies between 300

[2]This chapter is partly taken from the publication by Luo et al. [2], which was created during the work on this thesis. In Ref. [2], I was the main author of this part.

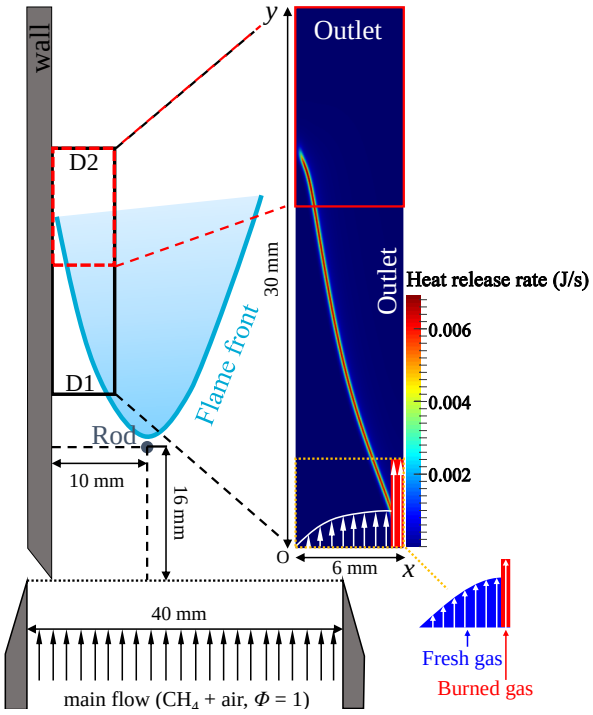

Figure 5.1: Illustration of the SWQ burner configuration and the computational domain. The area surrounded by a black solid box (D1) presents the computational domain for simulations with a coarser grid. The area highlighted with a red dashed frame (D2) denotes the computational domain for simulations with a finer grid.

and 350 K according to the thermocouple measurements. The coordinate system is defined so that y is in the streamwise direction and x is in the spanwise direction, with the origin being on the wall.

5.1.1 Numerical description

For the transport modeling, the unity Lewis number is assumed for simplicity, as usually used for CH_4-air SWQ flames [7, 75, 78]. The chemistry is described with a reduced chemical mechanism based on the CRECK model, which contains 26 species and 195 reactions and has already been successfully applied in SWQ simulations. More details can be found in [83].

Detailed kinetics

Under the unity Lewis number assumption, the diffusion flux can be expressed as Eq. (2.22). Therefore, the balance equation for species Eq. (2.4) can be simplified as

$$\frac{\partial(\rho Y_k)}{\partial t} + \nabla\cdot(\rho \boldsymbol{u} Y_k) = \nabla\cdot(\rho D \nabla Y_k) + \dot{\omega}_k \ , \tag{5.1}$$

and the transport equation of the total enthalpy h Eq. (2.6) can be written as

$$\frac{\partial(\rho h)}{\partial t} + \nabla\cdot(\rho \boldsymbol{u} h) = \nabla\cdot(\rho D \nabla h) \ . \tag{5.2}$$

Within the framework of detailed kinetics, Eqs. (2.1), (2.2), (5.1) and (5.2) are solved.

Reduced kinetics with REDIM

For a two-dimensional laminar FWI with $Le = 1$, the state vector ψ can be expressed as a function of a two-dimensional parametrization vector [32, 38]. One dimension relates to the progress variable to characterize the process from the unburned to the burned state where the specific mole number of CO_2 ($x_{CO_2} = \frac{Y_{CO_2}}{M_{CO_2}}$) is chosen in this chapter, and the other dimension relates to the total enthalpy which is used to consider the heat loss. Therefore, besides the governing equations for mass (Eq. (2.1)) and momentum (Eq. (2.2)), two more reduced model equations have to be solved in the CFD solver. Two different ways have been adopted to perform the computations, which can be either in thermokinetic coordinates or generalized coordinates.

REDIM

Within the context of thermokinetic coordinates, the system state vector ψ can be expressed as $\psi = \psi(\xi)$, where $\xi = (x_{CO_2}, h)^T$. When using generalized coordinates, the system state vector ψ can be expressed as $\psi = \psi(\theta)$, where $\theta = (\theta_1, \theta_2)^T$. Thus, θ_1 corresponds to the local coordinate in the direction of specific mole number of CO_2, and θ_2 corresponds to the local coordinate in the direction of enthalpy.

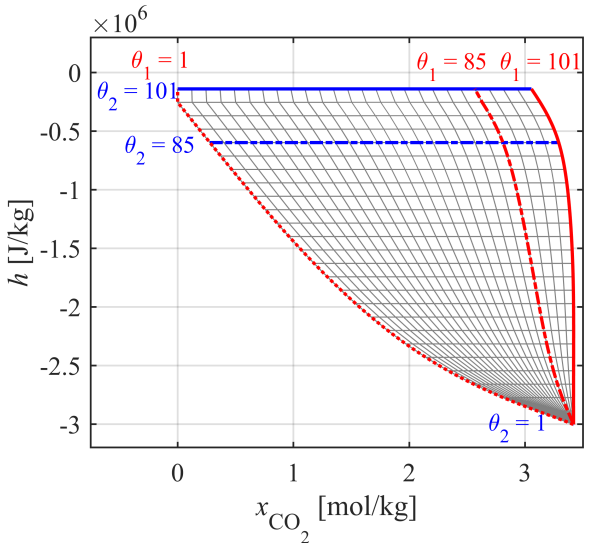

Figure 5.2: The coarsened 2D tabulation grid shown in the space of the control variables (the grid is coarsened by a factor of 4 based on the original grid for better presentation). The red lines are isolines for θ_1, and the blue lines are isolines for θ_2. The values correspond to the local coordinates in the original table for tabulation in the simulations.

In this chapter, several REDIMs are generated based on different gradient estimations, while the initial guesses are all based on the one-dimensional HOQ results from the detailed kinetic simulation. All REDIM tables used in this chapter are of the same size: 101×101 for $\theta_1 \times \theta_2$ (or for $x_{CO_2} \times h$). For a better understanding of the transformation between generalized and thermokinetic coordinates, the grid of the REDIM table generated based on the gradient estimation from the one-dimensional HOQ simulation using detailed kinetics is plotted in Fig. 5.2. Note that in order to show the grid clearly in Fig. 5.2, it has been coarsened by a factor of 4 based on the actual grid that is used for tabulation in the simulations. 6 lines are highlighted as examples: the red ones denote isolines for θ_1, and the blue ones are for θ_2. The specific values shown correspond to the localized coordinates in the actual table. Based on the above transformation, distributions of thermokinetic and transport properties can easily be projected from the thermokinetic coordinate space to the generalized coordinate space. Fig. 5.3 shows an example of the distribution of CO_2

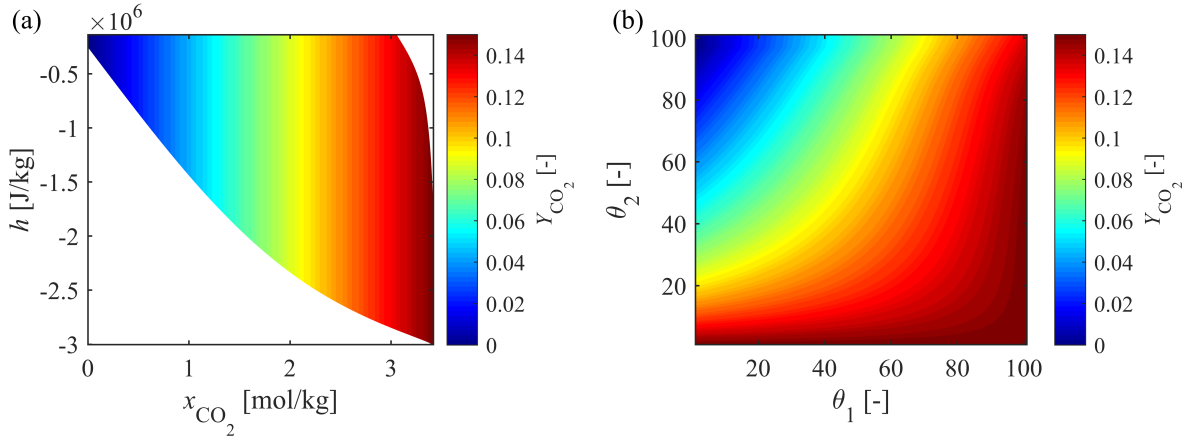

Figure 5.3: Distribution of the CO_2 mass fraction in the REDIM table generated based on the 1D HOQ simulation results with detailed kinetics: (a) in thermokinetic variable space, (b) in generalized coordinate space.

mass fraction in two different spaces, respectively.

Reduced model equations

When the governing equations are projected onto thermokinetic coordinates, Eq. (3.17) can be expressed in a more common way, which includes governing equations for enthalpy (Eq. (5.2)) and specific mole number of CO_2 (Eq. (5.3) below)

$$\frac{\partial(\rho x_{\mathrm{CO_2}})}{\partial t} + \nabla \cdot (\rho \boldsymbol{u} x_{\mathrm{CO_2}}) = \nabla \cdot (\rho D \nabla x_{\mathrm{CO_2}}) + \dot{\omega}_{x_{\mathrm{CO_2}}} \ , \tag{5.3}$$

where the diffusion coefficient D and the source term $\dot{\omega}_{x_{\mathrm{CO_2}}}$ can be obtained from the table directly.

When the governing equations are projected onto generalized coordinates, Eq. (3.15) is solved with $\boldsymbol{\theta} = (\theta_1, \theta_2)^T$.

5.1.2 Computational domain

The experimental configuration has already been simulated by Ganter et al. [76] using detailed kinetics. Similarly to their work, the simulations here are also conducted on a two-dimensional sub-domain of the experimental setup in order to save computational cost.

Two simulations are performed in the present study. One is on a larger domain with coarser grids, and the other is on a sub-domain of the larger domain with finer near-wall grid resolutions. Shown as the solid black box in Fig. 5.1, the larger computational domain (D1) is 6 mm $\times$ 30 mm in size, and covers almost 80% of the flame branch that interacts with the wall. A uniform Cartesian grid is used for the simulation, with a cell size of $\Delta x = \Delta y = 50$ μm, which results in 72000 cells in total. The simulation on the smaller domain (D2) is conducted to better resolve the near-wall processes. D2 is a sub-domain of D1, including the area where the flame tip interacts with the wall. As highlighted by the red dashed box in Fig. 5.1, the size of D2 is 6 mm $\times$ 12 mm. A non-uniform grid is used in this simulation. The grid is non-equidistant in x direction, where the finest grid resolution is $\Delta x = 10$ μm near the wall, and the coarsest grid resolution is $\Delta x = 50$ μm near the right outlet. In y direction, the cell size has a constant value of $\Delta y = 10$ μm. The total number of cells is 168000. The grid convergence study is illustrated in Appendix A.

5.1.3 Boundary conditions

For the detailed kinetic simulations conducted on D1, we follow the work of Ganter et al. [76]. The fresh CH_4-air mixture is injected from a 5.5 mm wide section at the inlet, and the hot burned exhaust gas under the equilibrium condition is injected from the remaining 0.5 mm wide section, which is shown in red in Fig. 5.1. The burned gas is used to stabilize the flame, since no rod is included in this sub-domain. The temperature and pressure of the fresh gas are set to 300 K and 1 atm, respectively. A parabolic velocity profile is applied to the fresh gas mixture with a maximum velocity of 1.7 m/s, while the velocity of the burned gas keeps a constant value of 3.81 m/s, so that the flame shape can be retained. The wall is assumed to have a constant temperature of 300 K based on the experimental estimation, while a no-slip boundary condition is set for the velocity. Zero-gradient boundary conditions are applied to the species mass fractions, since the wall is considered to be inert. The right and upper boundaries are treated as open outlets. Thus, zero-gradient boundary conditions are applied to the temperature, velocity, and species mass fractions. The simulations performed on D1 provide initial and boundary conditions for the corresponding simulations conducted on D2.

For simulations conducted on D2, the upper outlet, the right outlet, and the wall coincide with those of D1. The only difference is the location of the inlet. For these simulations, the inlet is 18 mm downstream of that in the first simulation. Thus, the boundary conditions for the upper outlet, the right outlet, and the wall remain unchanged. The inlet boundary conditions are extracted from simulations conducted on D1.

In order to solve reduced model equations, boundary conditions in reduced coordinates are required. Since it is not straightforward to directly define boundary conditions in generalized coordinates, they can be converted from those in thermokinetic coordinates. At the inlet, fixed value boundary conditions are assumed for x_{CO_2} and h in thermokinetic coordinates ($\boldsymbol{\xi}$ = constant). Correspondingly, it can be expressed as $\boldsymbol{\theta}$ = constant in generalized coordinates. For the right and upper outlets, zero-gradient boundary conditions are applied for both x_{CO_2} and h in thermokinetic coordinates ($\nabla\boldsymbol{\xi} = 0$, namely $\boldsymbol{C}\nabla\boldsymbol{\psi} = 0$), which corresponds to $\boldsymbol{C}\boldsymbol{\psi}_{\boldsymbol{\theta}}\nabla\boldsymbol{\theta} = 0$ in generalized coordinates. On the wall, the zero-gradient boundary condition is adopted for x_{CO_2} in the thermokinetic coordinates, while the enthalpy value can be obtained by looking up the table using values of fixed temperature T (300 K) and x_{CO_2} obtained from the zero-gradient boundary condition. Similarly, in generalized coordinates, the values of x_{CO_2} obtained from the zero-gradient boundary condition and T obtained from the fixed value boundary condition are utilized to access the table to obtain θ_1 and θ_2.

5.2 Validation

In this section, the implementation of the reduced model equations in generalized coordinates is validated through the two-dimensional SWQ configuration illustrated in Section 5.1, and the suitability is evaluated by comparing the results to those from the detailed kinetics. The REDIM table is generated based on an initial guess and a gradient estimation from the one-dimensional HOQ simulation results using detailed kinetics. The gradient estimations for the enthalpy as well as for CO_2 are illustrated in Fig. 5.10. Due to the two different governing processes of heat loss to the wall and chemical reaction, the two gradient estimations differ significantly qualitatively and quantitatively. Details about the validation of the reduced model equations in thermokinetic coordinates can be found in [7], which are not presented here.

In order to make a qualitative comparison, the distribution of the OH mass fraction is studied, since it is used to determine the flame front positions in the experiment. For a quantitative comparison, distributions of CO mass fraction and temperature (T) along several lines are studied. Similarly to previous studies [75, 76], a relative coordinate system based on the quenching point is introduced. It should be noted that the quenching point can be determined based on several criteria, such as the wall heat flux, OH gradient, or CO_2 mass fraction. In this section, to remain consistent with the experiment, the quenching point is defined at the location where the local OH gradient drops below half of its maximum value. For more details, see [68].

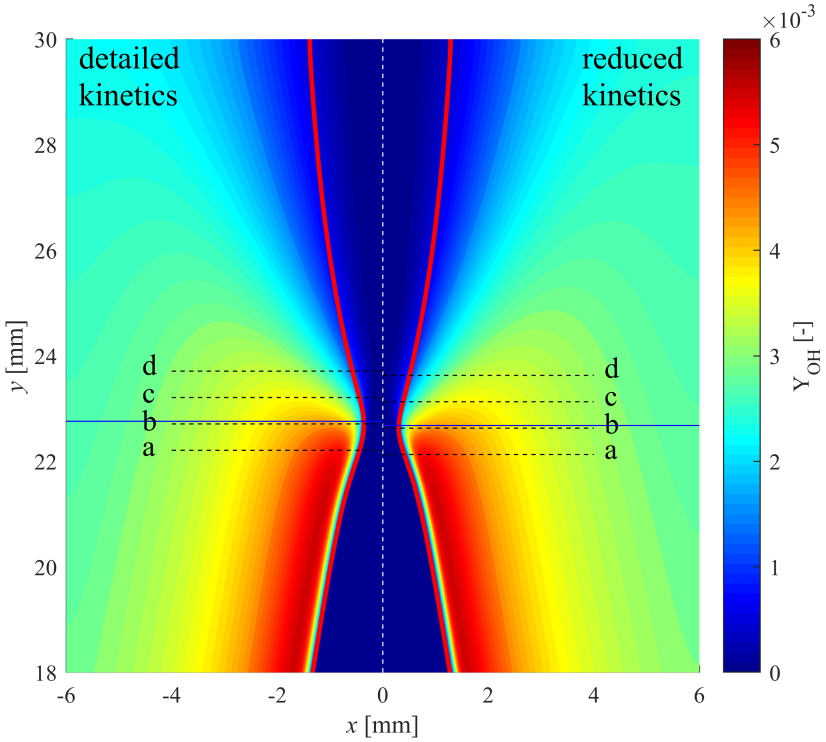

Figure 5.4: Distributions of the OH mass fraction. The flame shape is also shown by an isoline of the temperature T = 1500 K (red). The horizontal line at quenching height is shown in blue. The four black dashed horizontal lines near the flame tip depict the extraction lines for CO and temperature data. The positions (a), (b), (c), and (d) are defined by the vertical offsets to the quenching point of -0.55, -0.05, 0.45, and 0.95 mm, respectively.

Within the relative coordinate system, the quenching height is defined as $y_q = 0$, and negative for upstream, positive for downstream.

The distributions of the OH mass fractions are shown in Fig. 5.4. The overall flame shape can be reproduced by the reduced model equations in generalized coordinates. Additionally, the quenching heights predicted by the two simulations are very close to each other: 21.83 mm and 21.81 mm for the detailed kinetics and the reduced model equations in generalized coordinates, respectively. For reference, they are shown as blue solid lines in the figure.

In order to make quantitative comparisons, variations in the CO mass fraction and temperature (T) are investigated over four different lines vertical to the wall: y_q = -0.55 mm, y_q = -0.05 mm, y_q = 0.45 mm, y_q = 0.95 mm, with the former two lying upstream of the quenching point, while the latter two downstream of the quenching point, as denoted by (a), (b), (c), (d), respectively in Fig. 5.4. Figure 5.5 shows the results obtained from simulations using detailed kinetics and reduced model equations in generalized coordinates. The experimental mean values are also included for reference. To check whether the REDIM table that is used is suitable for the SWQ configuration, an *a-priori* analysis is also carried out based on results from the detailed kinetics. Specifically, values of $x_{\mathrm{CO_2}}$ and h from simulations using detailed kinetics are used to access the table to obtain the corresponding generalized coordinates (θ_1 and θ_2). With the localized coordinates, it is easy to determine the value of CO mass fraction and temperature based on the table, and the results are shown as the red solid lines in Fig. 5.5. It is found that the overall variations in both CO mass fraction and temperature can be well captured by both simulations using detailed kinetics and reduced model equations in generalized coordinates. The discrepancies between the simulations and the

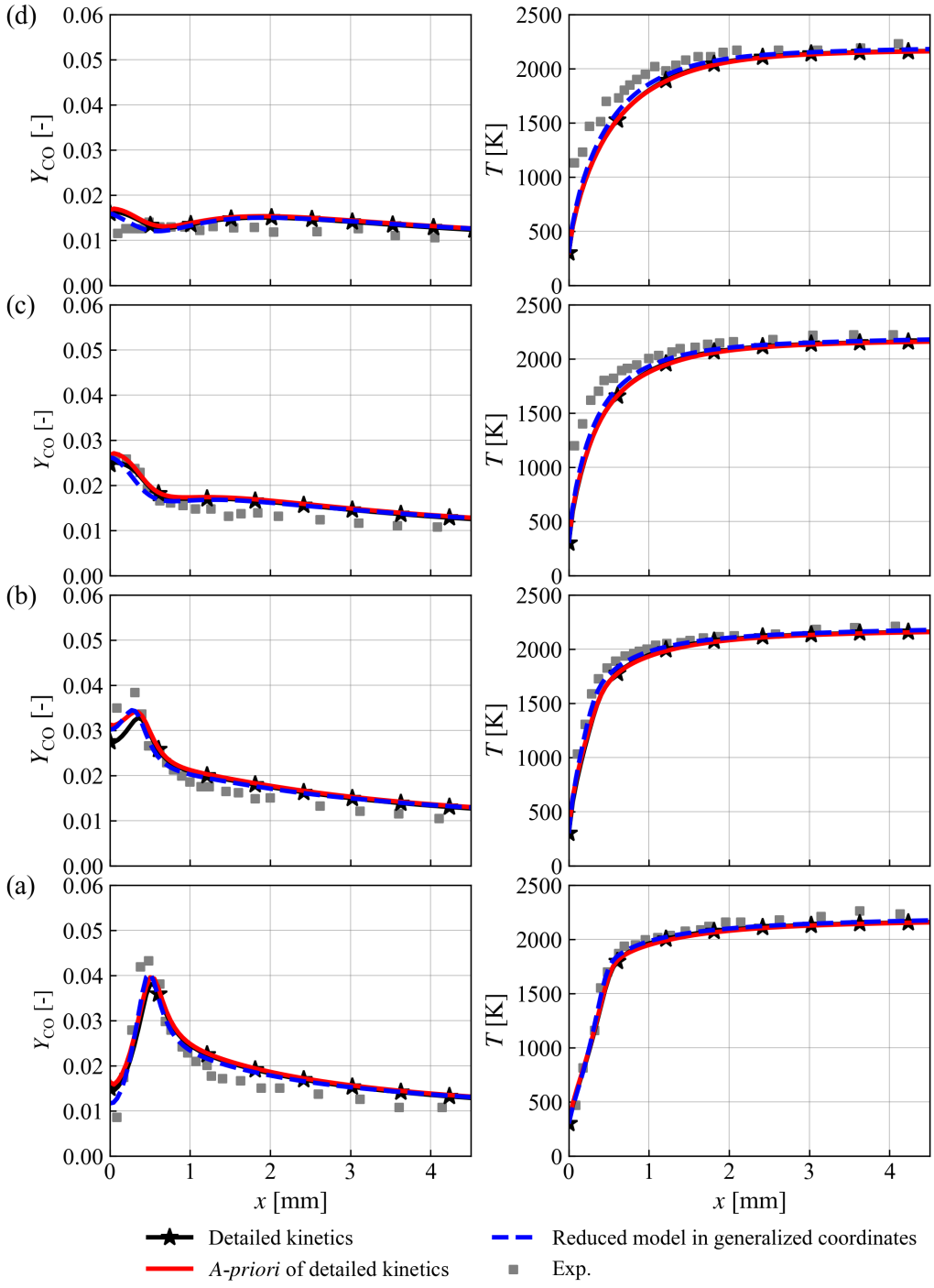

Figure 5.5: Comparison of CO mass fraction and temperature, contrasting the simulation results obtained with detailed kinetics, the a-priori predictions, and reduced model equations in generalized coordinates against the experimental data at different positions: (a) y_q = -0.55 mm, (b) y_q = -0.05 mm, (c) y_q = 0.45 mm, (d) y_q = 0.95 mm.

experiment are due to experimental uncertainties and the simple transport model used in the simulations [76]. Meanwhile, the simulation results using reduced model equations in generalized coordinates agree well with those using detailed kinetics. For regions far away from the wall, there is nearly no difference

between the two simulation results for both CO mass fraction and temperature. For positions very close to the wall, i.e., $x < 0.5$ mm, the temperature profile still shows small difference, while the discrepancies in CO mass fraction become more obvious. Closer to the quenching point, the CO mass fraction is slightly overpredicted by reduced model equations in generalized coordinates, e.g., y_q = -0.05 mm. However, it is a good match with the *a-priori* results. Therefore, it can be concluded that such a discrepancy is not caused by the reduced model equations, but by the table used, since HOQ and SWQ are similar but not exactly the same physical process. As stated in [78], the enthalpy gradient near the wall is relatively larger in HOQ than in SWQ, which raises the magnitude of the scalar diffusion rate. Thus, it is reasonable that the CO mass fraction predicted by reduced model equations using the REDIM table generated based on the HOQ is slightly higher than that computed by detailed kinetics near the quenching point.

As shown above, the reduced model equations in generalized coordinates perform well on the SWQ configuration.

5.3 Results and discussion

In Section 5.2, the implementation of reduced model equations in generalized coordinates and the application of the REDIM table generated based on the gradient estimation from the one-dimensional HOQ (see Fig. 5.10) in SWQ simulations are shown to be suitable. This section begins with comparing the reduced model equations in generalized and thermokinetic coordinates, and the advantages of the reduced model equations in generalized coordinates are demonstrated. Then, within the framework of generalized coordinates, together with the REDIM for tabulation, possible simplifications of the gradient estimations for REDIM generation are studied. To achieve this, REDIM tables generated from different simplified gradient estimations are applied to the SWQ simulation using reduced model equations in generalized coordinates, and the results are compared to those using the REDIM generated based on the gradient estimations from the one-dimensional HOQ.

In both subsections below, global quenching quantities such as the quenching height and wall heat flux are first analyzed. Then local thermo-chemical states are investigated in CO-T and OH-T spaces. CO-T and OH-T variations are sampled over three lines: y_q = -0.5 mm, y_q = 0 mm, and y_q = 0.5 mm. In contrast to Section 5.2, the quenching point is determined based on the maximum wall heat flux in this section, since it connects the local thermo-chemical states with the global quenching quantities. Such a definition is also a common choice in other works [75, 87].

5.3.1 Comparison of reduced model equations in different coordinates

In this section, the differences between the results of reduced model equations in generalized and thermokinetic coordinates are discussed. As already mentioned, the system dynamics is calculated in the tangential subspace of the manifold if the reduced model equations in generalized coordinates (Eq. (3.15)) are used. In contrast, if the reduced model equations in thermokinetic coordinates (Eq. (3.17)) are adopted, the processes are not projected onto the tangential space of the manifold. Therefore, in order to investigate this difference in more detail, different REDIMs are employed for computations with reduced kinetics. In order to generate several REDIMs, the gradient estimation based on the one-dimensional HOQ using detailed kinetics ($\boldsymbol{\chi}|_{\mathrm{HOQ,\ DK}}$) is varied by a factor α, namely $\boldsymbol{\chi} = \alpha \cdot \boldsymbol{\chi}|_{\mathrm{HOQ,\ DK}}$. For $\alpha = 1$, the gradient estimation refers to that of the detailed flame calculation of the HOQ system (see Fig. 5.10). For $\alpha \neq 1$, the diffusive process is overestimated ($\alpha > 1$) or underestimated ($\alpha < 1$) and the REDIM changes. This means that, e.g., for $\alpha = 1.1$ the local gradient estimations are increased by 10%. The introduction of this parameter allows the description of a perturbation of the gradient guess and possible uncertainties which differ from the burning behavior of a non-disturbed FWI. Afterwards, the results of the REDIMs with different gradient estimations can be systematically analyzed. For example, by increasing the gradient estimation ($\alpha > 1$),

larger gradients are used to create the reduced model. As a result, the system dynamics must also change. One example is the wall heat flux, which depends directly on the temperature gradient and must increase for a higher gradient estimation. Note, that only the results of $\alpha = 1$ are compared with the detailed solution in this work and the results of the cases where $\alpha \neq 1$ are not directly compared for reasons of clarity. The cases where $\alpha \neq 1$ are used to show the robustness of the method when the gradient estimations show considerable deviations from the actual gradients, and should not reproduce the results of the detailed kinetics well. The different REDIM tables with different α are applied to SWQ simulations using different reduced model equations. The performance of the reduced model equations is evaluated based on how they respond to the variation of the manifold (whether they can correctly capture the variation in the manifold). In the following discussion, the abbreviation GC is used for the generalized coordinates, and TC for the thermokinetic coordinates.

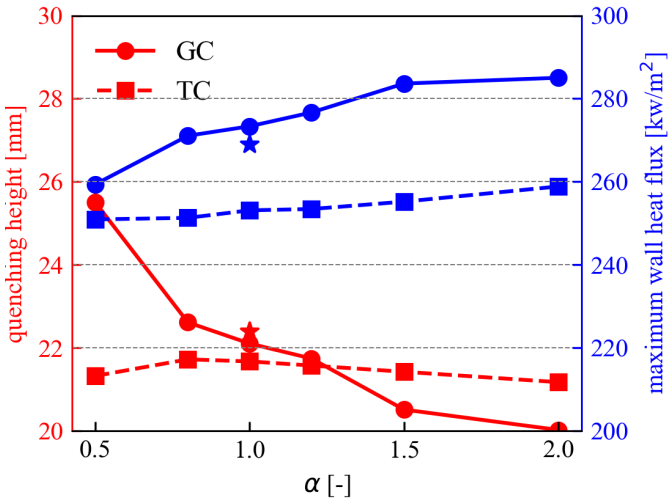

Figure 5.6: Variations in the quenching height and the maximum wall heat flux against the varying factor α in the gradient estimation for reduced model equations both in generalized coordinates (GC) and thermokinetic coordinates (TC). Results from the detailed kinetics are shown as the stars.

Variations in global quantities such as the quenching height and maximum wall heat flux are plotted in Fig. 5.6 for different α. The quenching height is an indicator of the laminar burning velocity which is a very important parameter in premixed combustion. It is found to decrease monotonically with increasing α when reduced model equations are solved in generalized coordinates. According to [32], this trend is physically correct overall since the laminar burning velocity should increase with the increasing gradient estimation. Moreover, when $\alpha = 1$, the quenching height obtained from reduced model equations in generalized coordinates is 22.11 mm, which is close to the 22.46 mm obtained from the detailed kinetics. In contrast, reduced model equations in thermokinetic coordinates fail to capture this variation. When $\alpha < 1$, the quenching height even increases slightly with increasing α, while it shows the opposite trend for $\alpha > 1$. Therefore, it can be concluded that only reduced model equations in generalized coordinates yield reliable results when the manifold is not perfectly invariant, which is consistent with the findings in [32]. In the following, the reasons are explained in detail. As already mentioned, the changing gradient estimation due to varying α leads to a greater ($\alpha > 1$) or smaller ($\alpha < 1$) influence of the diffusive process. In the REDIM generation process, states are found where the diffusive processes and the chemical reaction of the complete state vector are perfectly balanced normal to the manifold. This means that the source term differs for the REDIMs generated with different α. Using the reduced model equations in generalized coordinates (Eq. (3.15), the system evolves tangentially to the REDIM and the quenching height changes for different α

because the influence of the diffusive process varies. Using the reduced model equations in thermokinetic coordinates (Eqs. (5.2) and (5.3)), only the state variables adopted for the parametrization are used for the reduced computation, which leads to an oversimplification. In this case, the system dynamics is not part of the tangential subspace of the manifold because the influence of those state variables which are not part of the parametrization vector is neglected. This means that the changing influence of the diffusive process can not be reproduced with Eqs. (5.2) and (5.3). As for the wall heat flux, it increases slightly as α increases for reduced model equations in both generalized and thermokinetic coordinates, with the latter exhibiting less variation. The wall heat fluxes calculated using reduced model equations in generalized coordinates are generally larger than those obtained from thermokinetic coordinates.

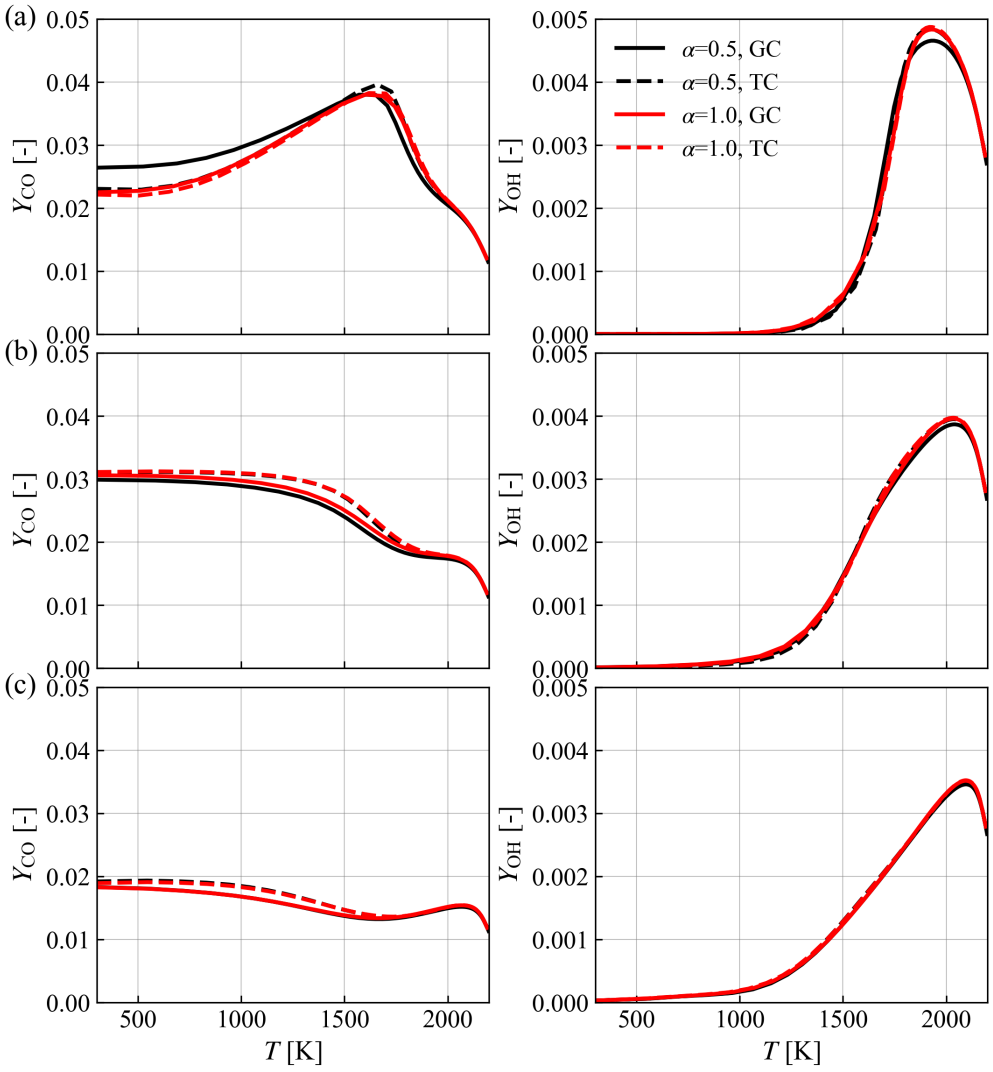

Figure 5.7: CO and OH mass fraction variations over temperature (T) for reduced model equations in generalized coordinates (GC) and thermokinetic coordinates (TC) with two REDIM tables generated based on the gradient estimations varied from the 1D HOQ by varying factors α = 0.5 and α = 1.0 for different positions: (a) y_q = -0.5 mm, (b) y_q = 0 mm, (c) y_q = 0.5 mm.

Shown in Fig. 5.7 are the CO-T and OH-T variations over three lines with y_q = -0.5 mm (a), y_q = 0 mm (b), and y_q = 0.5 mm (c), respectively. For better visualization, only results for α = 0.5 and α =

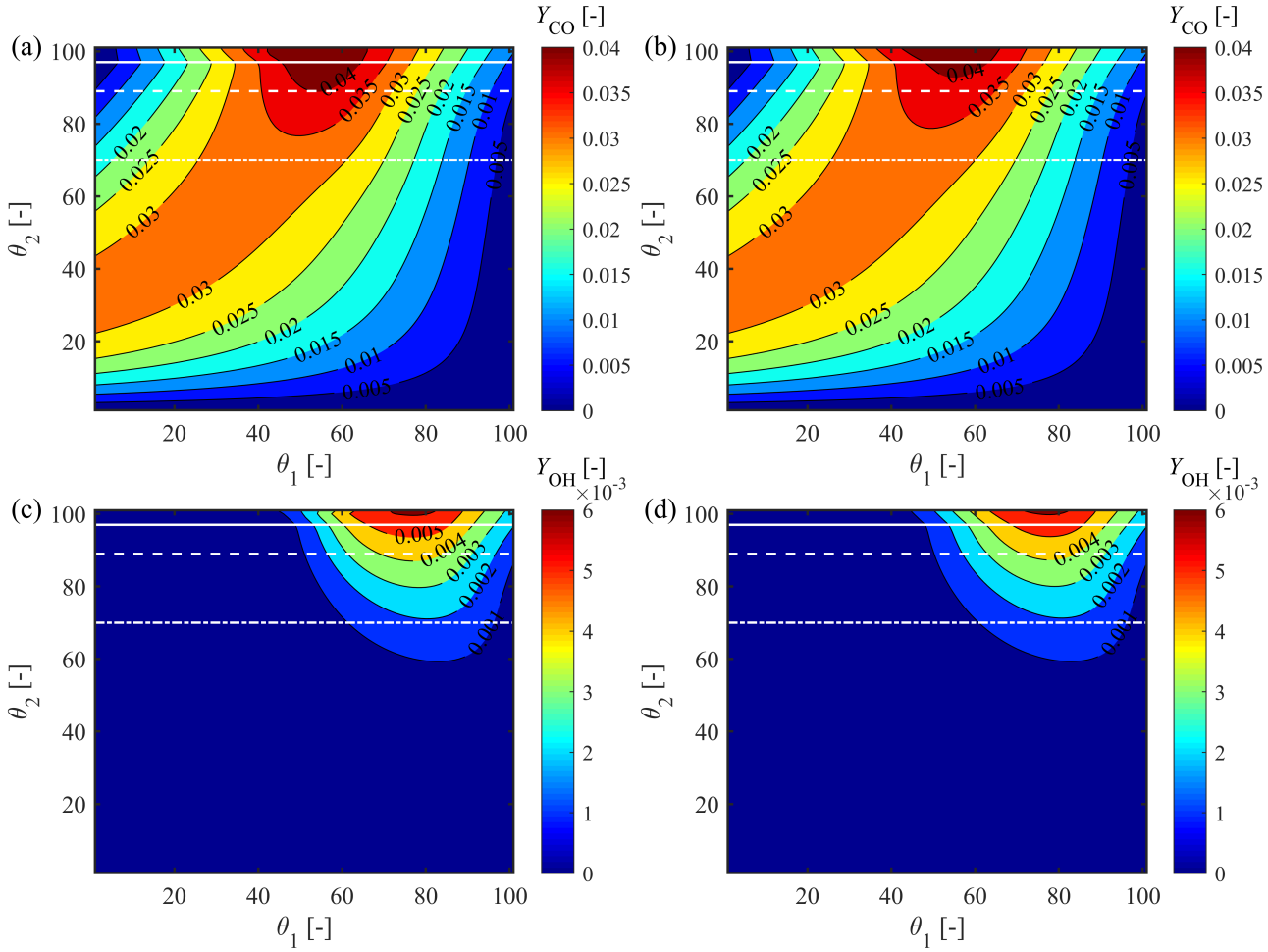

Figure 5.8: Species mass fraction distributions in REDIM tables generated based on the gradient estimations varied from the 1D HOQ by a varying factor α: (a) CO mass fraction for REDIM table with α = 0.5, (b) CO mass fraction for REDIM table with α = 1.0, (c) OH mass fraction for REDIM table with α = 0.5, (d) OH mass fraction for REDIM table with α = 1.0. The white solid lines correspond to θ_2 = 97, the white dashed lines correspond to θ_2 = 89, and the white dash-dot lines correspond to θ_2 = 70.

1.0 are shown. When $\alpha = 1.0$, results obtained by using reduced model equations in generalized and thermokinetic coordinates agree well. However, when the value of α changes to 0.5, larger discrepancies can be seen, especially for the near-wall region upstream of the quenching point, e.g., at y_q = -0.5 mm. In order to analyze these discrepancies in detail, distributions of the CO and OH mass fractions in generalized coordinate space for REDIM tables are plotted in Fig. 5.8. The white solid line $\theta_2 = 97$ corresponds to a one-dimensional freely propagating flame with unburned gas temperature 300 K. The thermo-chemical states above this line ($\theta_2 > 97$) are obtained from one-dimensional freely propagating flames with unburned gas temperature higher than 300K, while the thermo-chemical states below this line ($\theta_2 \leq 97$) are obtained from a one-dimensional HOQ. Differences in the CO mass fraction distribution are found to mainly exist in regions near the adiabatic freely propagating flame. When $\alpha = 0.5$, the high CO mass fraction covers a wider range than $\alpha = 1.0$. For reference, the white dashed line $\theta_2 = 89$ and the white dash-dot line $\theta_2 = 70$ are added in the plot. For better illustration, the variation of CO and OH mass fractions over these isolines of θ_2 are plotted in Fig. 5.9. It is shown that when the enthalpy (θ_2) decreases, the discrepancies

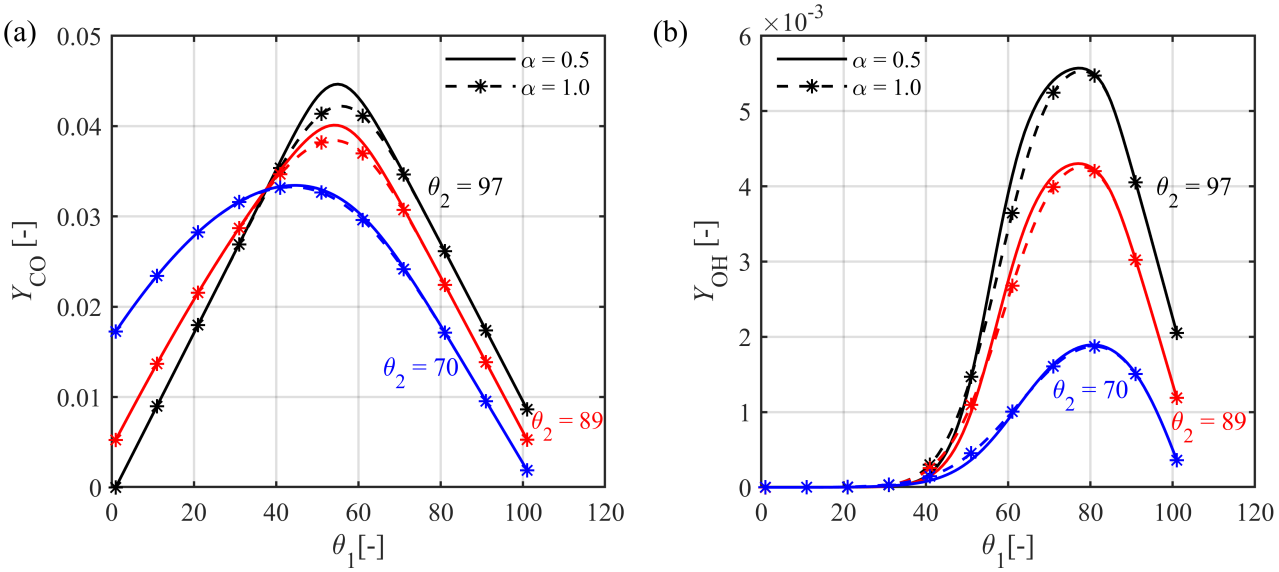

Figure 5.9: Species variations over several isolines of θ_2 (97, 89 and 70): (a) CO mass fraction, (b) OH mass fraction.

between the two tables decrease. Similar findings are observed for the OH mass concentration, although the differences between the two tables are smaller. This can explain why the influence of α is and should be larger in regions that are slightly upstream of the quenching point. However, the reduced model equations in thermokinetic coordinates fail to capture this phenomenon.

5.3.2 Simplification of gradient estimations

In Section 5.3.1, the advantages of reduced model equations in generalized coordinates over thermokinetic coordinates are demonstrated. Therefore, investigations in this section focus on the reduced model equations in generalized coordinates, together with the REDIM for tabulation. The major purpose is to find possible simplifications within this combined framework. As stated before, the REDIM is generated based on an initial guess and a gradient estimation. According to Strassacker et al. [136], there are only slight differences between REDIMs generated with gradient estimation from the one-dimensional HOQ flame using detailed kinetics and the two-dimensional SWQ flame using detailed kinetics. The use of the REDIM table based on the simplified gradient estimation from the one-dimensional HOQ flame is also justified in the previous sections of this chapter. In this section, the aim is to find out whether the gradient estimation can be further simplified for the SWQ application. To this end, three more REDIM tables are generated.

Figure 5.10 shows the gradient estimations obtained by a detailed solution of the HOQ system. The gradients differ a lot for the different states. The maximum gradient estimation of h is around 15×10^9 J/(kg·m), but only in a very small region directly in front of the wall. In regions far away from the wall (e.g., the region of the freely-propagating flame), the gradient estimation of h is 0. For the gradient estimation of x_{CO_2}, it is very high between the near-wall region and the reaction zone, while nearly 0 elsewhere. In order to simplify the gradient estimation to reduce the information that is needed before the REDIM is generated, both gradient estimations of h (χ_h) and x_{CO_2} (χ_{CO_2}) are assumed to be constant for the first REDIM. Therefore, 2.5×10^9 J/(kg·m) and 2000 mol/(kg·m) are chosen for χ_h and χ_{CO_2}, respectively for the first REDIM. Those values are both averaged between minimum and maximum gradients. For the second REDIM, χ_h has a constant value of 2.5×10^9 J/(kg·m), while χ_{CO_2} is interpolated from the values of a freely propagating flame to zero at the equilibrium point. The gradient estimations of the freely propagating

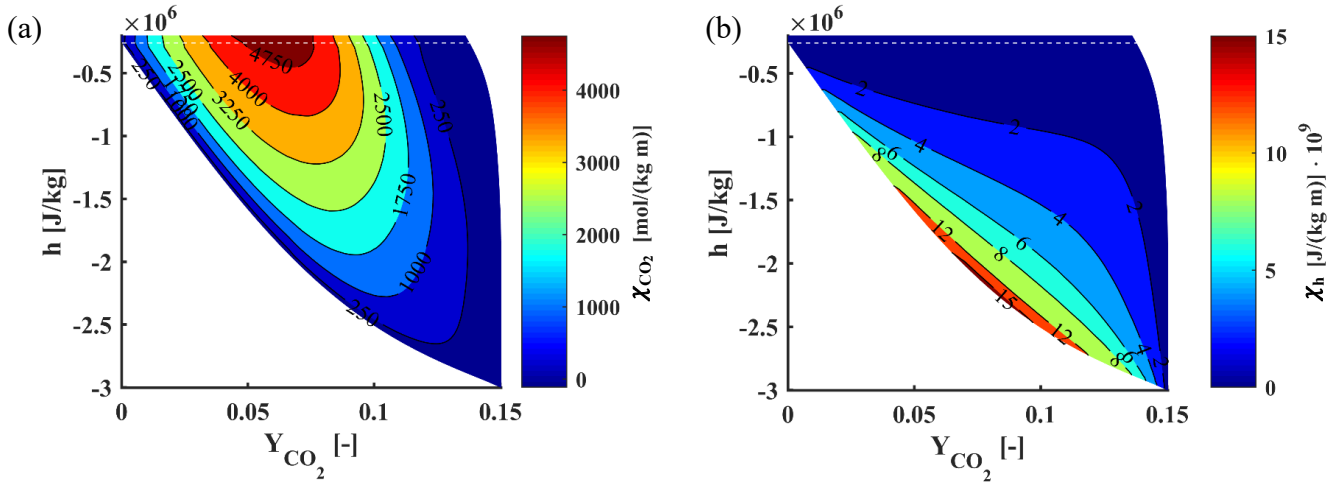

Figure 5.10: Gradient estimations obtained by the detailed solution of the HOQ simulation. Shown are the gradient estimations of the specific mole number of CO_2 (χ_{CO_2}) (a) and the enthalpy (χ_h) (b), as functions of the specific enthalpy and mass fraction of CO_2. The states of the freely-propagating flame are illustrated with the white dashed lines.

flame are illustrated in Fig. 5.10 with white dashed lines. The equilibrium point is given by the state with the smallest specific enthalpy and the largest value of CO_2. The interpolation of the χ_{CO_2} leads to values that are closer to the values of the gradients of the HOQ system than the constant values. For the third REDIM, χ_h increases to a constant value of 5×10^9 J/(kg·m), while χ_{CO_2} is still obtained from interpolation. These three REDIMs with a parametric variation of the gradient estimations are named REDIM-A, REDIM-B, and REDIM-C, respectively, as listed in Table 5.1. They are applied to the SWQ configuration. For comparisons, the results obtained from reduced model equations in generalized coordinates using the REDIM table generated based on the one-dimensional HOQ flame are used for reference.

Label	χ_{CO_2} from	χ_h from
REF	1D HOQ flame	1D HOQ flame
REDIM-A	Const. value 2000 mol/(kg·m)	Const. value 2.5×10^9 J/(kg·m)
REDIM-B	Freely propagating flame	Const. value 2.5×10^9 J/(kg·m)
REDIM-C	Freely propagating flame	Const. value 5.0×10^9 J/(kg·m)

Table 5.1: Identified manifolds for different gradient estimations.

The quenching heights calculated using the three different REDIMs are 22.14 mm, 19.73 mm, and 19.28 mm, respectively. The result predicted by REDIM-A agrees well with the reference value of 22.11 mm, while the other two exhibit underpredictions. As for the maximum wall heat flux, the calculated results are 266, 278, and 288 kW/m^2. Figure 5.11 shows thermo-chemical states in CO-T and OH-T spaces for three different positions. For the region where $T < 1800$ K, results from all REDIM tables are generally in good agreement with the reference results. Especially for REDIM-A, the CO-T and OH-T variations for all positions match the reference results very well. Meanwhile, for REDIM-B and REDIM-C, good agreement is achieved at the quenching height and downstream, while some discrepancies are observed in the CO variation in the near-wall low-temperature region upstream of the quenching point. These findings indicate that the results are not very sensitive to gradient estimation. Moreover, the weak dependence on gradient estimation can also be demonstrated by comparing REDIM-B and REDIM-C, where the scalar dissipation in enthalpy direction ($\lambda/\rho c_p|\chi_h|^2$) is varied by a factor of 4, while there are very small differences in the results

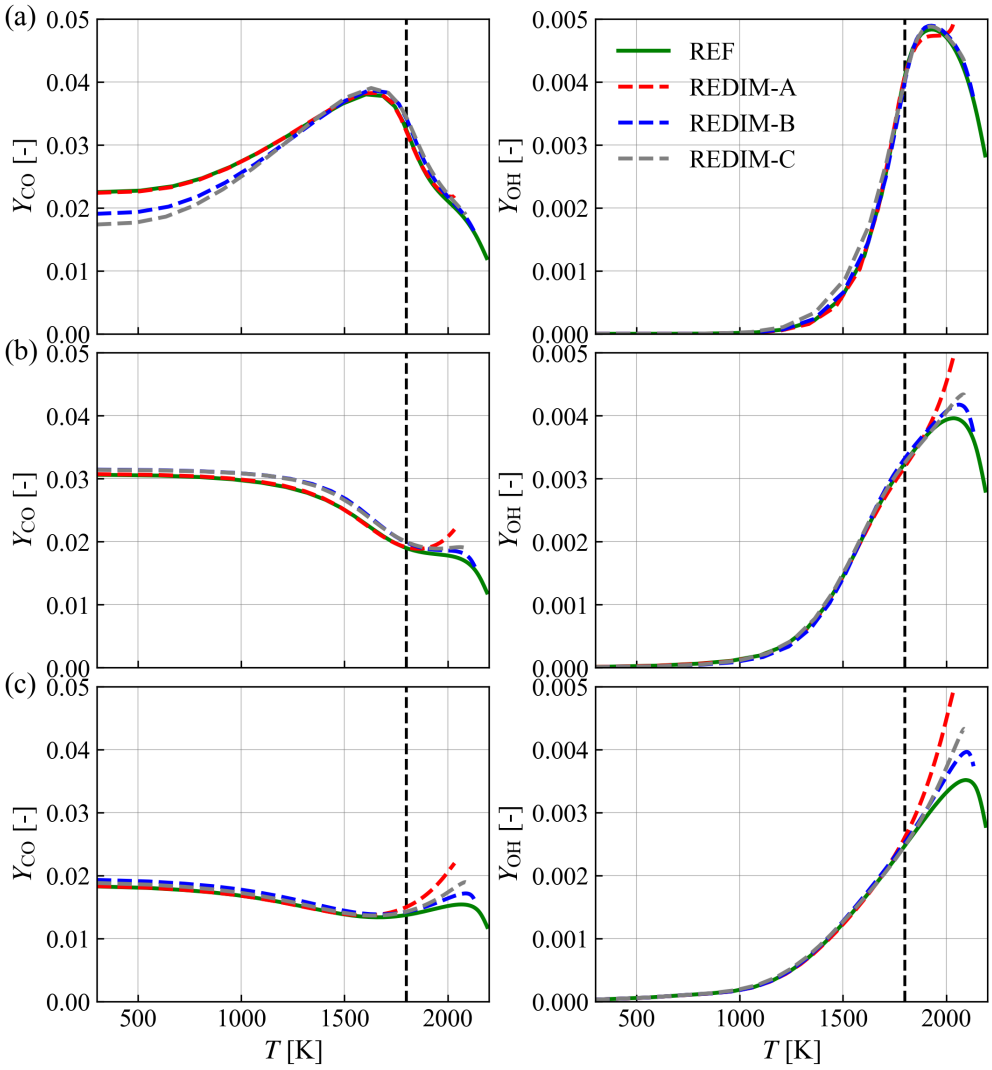

Figure 5.11: CO and OH mass fraction variations over temperature (T) obtained by solving reduced model equations in generalized coordinates with REDIMs generated based on different gradient estimations (REF: both χ_h and χ_{CO_2} are obtained from the 1D HOQ; REDIM-A: χ_h = 2.5 $\times$ 10^9 J/(kg·m) and χ_{CO_2} = 2000 mol/(kg·m); REDIM-B: χ_h = 2.5 $\times$ 10^9 J/(kg·m) and χ_{CO_2} is interpolated from the values of a freely propagating flame; REDIM-C: χ_h = 5.0 $\times$ 10^9 J/(kg·m) and χ_{CO_2} is interpolated from the values of a freely propagating flame) for different positions: (a) y_q = -0.5 mm, (b) y_q = 0 mm, (c) y_q = 0.5 mm. The vertical dashed line indicates the position of T = 1800 K.

for both global quenching quantities and local thermo-chemical states. However, the maximum temperature of the burned gas is underpredicted for all the REDIM tables considered for all positions. For REDIM-A, the maximum temperature is almost 150 K lower than that of the reference result. It is also found that all REDIM tables fail to predict the CO and OH variations in the high-temperature region where $T > 1800$ K. This is due to the significant overpredictions of gradients of x_{CO_2} and h. For a better understanding, the gradients of x_{CO_2} and h of the two-dimensional SWQ (REF case) for the region $T > 1800$ K over the three lines we investigate are plotted in Fig. 5.12. Over all the three lines, h shows very small gradient when $T > 1800$ K since it is approaching the post flame zone. At $y_q = 0$ and $y_q = 0.5$ mm, the gradients of x_{CO_2} are very

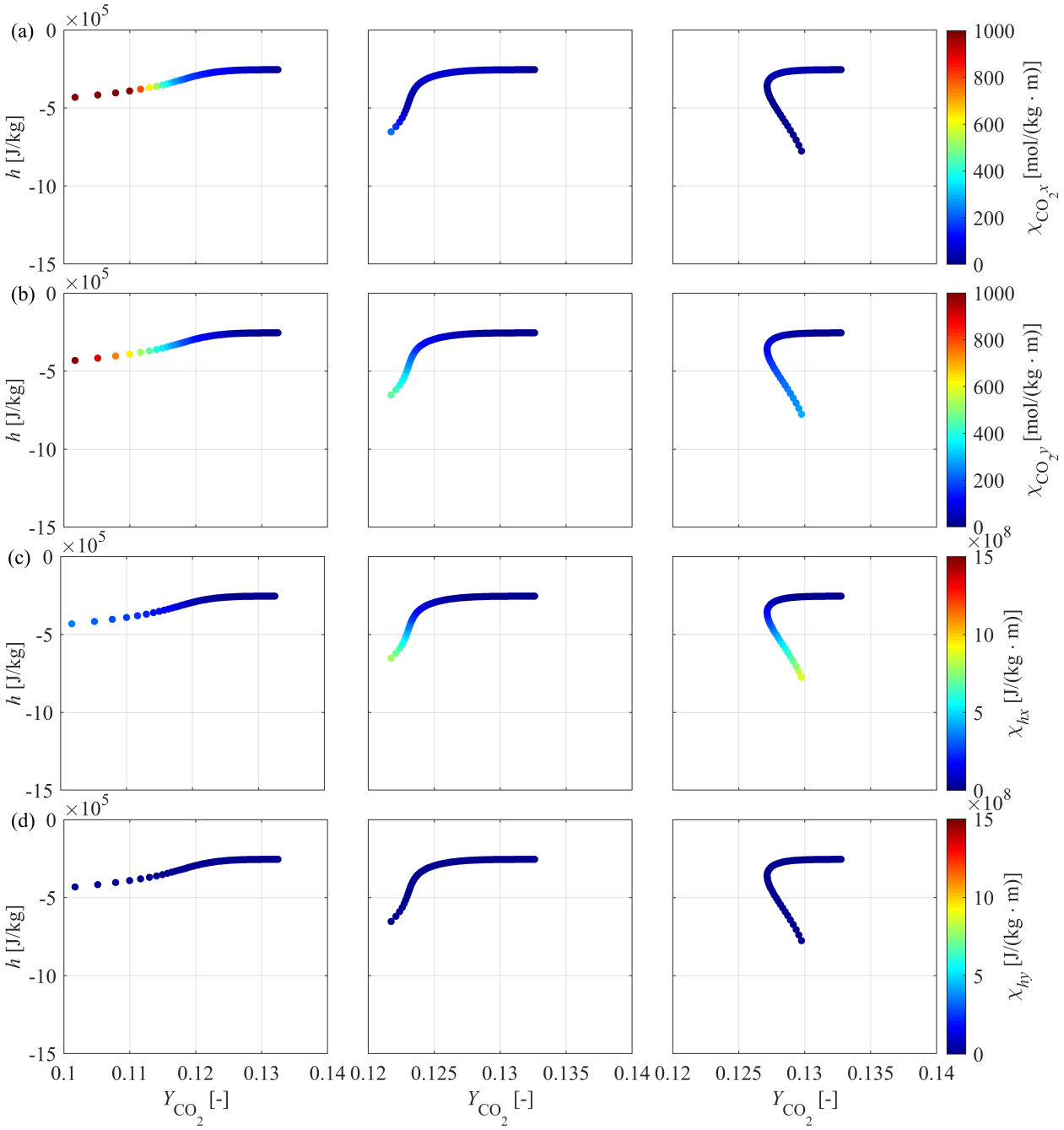

Figure 5.12: Gradients of the specific mole number of CO_2 and enthalpy as functions of CO_2 mass fraction and enthalpy for regions $T > 1800$ K from 2D SWQ results (REF case): (a) gradients of x_{CO_2} in x direction, (b) gradients of x_{CO_2} in y direction, (c) gradients of h in x direction, (d) gradients of h in y direction. The magnitude of the gradients are indicated by the colors. The left column corresponds to y_q = -0.5 mm, the middle column corresponds to y_q = 0 mm, and the right column corresponds to y_q = 0.5 mm.

small when $T > 1800$ K (maximum gradient less than 500 mol/(kg·m)). At $y_q = -0.5$ mm, the gradient of x_{CO_2} decreases to a similar small magnitude when $T > 1950$ K. However, the gradient estimation of x_{CO_2} (χ_{CO_2}) remains a very high level for REDIM-A, and the gradient estimation of h (χ_h) remains very high for

all the three REDIMs (REDIM-A, B, and C), which may lead to deviations. The influence of overprediction of χ_{CO_2} can be illustrated by comparing REDIM-A and REDIM-B which have a same χ_h. It is shown that REDIM-B performs better since χ_{CO_2} is less overpredicted than REDIM-A where χ_{CO_2} always keeps at a high level. Meanwhile, the influence of the overprediction of χ_h can be explained by comparing REDIM-B and REDIM-C which have a same χ_{CO_2}. Apparently, REDIM-B shows relatively better performance, which is due to the fact that χ_h of REDIM-B is only half of REDIM-C. The sensitivity in the high temperature region may be reduced by increasing the dimension of the REDIMs, since it was proved that the REDIMs with higher dimensions would be even less sensitive with respect to the gradient estimation [34]. Generally speaking, based on the above analysis, the near-wall characteristics can mostly be reproduced with the REDIM table even based on very simplified gradient estimations (constant gradient estimations), especially for regions very close to the wall.

5.4 Summary

In this chapter, a solver is developed for reduced model equations in generalized coordinates. It is applied to FWI simulations where the REDIM is used as an example of the reduced kinetic model. Specifically, the work focuses on the following three aspects:

1. The implemented reduced kinetic model equations in generalized coordinates are validated. The validity is confirmed by the good agreement with the results obtained with detailed kinetics for a two-dimensional SWQ. Based on this implementation, a model reduction *on the fly* can be implemented by coupling the simulation with REDIM reduced kinetics and the REDIM generation process itself. In this way, the reduced kinetic model can directly react to changes in the combustion system. The implementation of this model reduction technique will be described in the next chapter.

2. Reduced kinetic model equations in generalized and thermokinetic coordinates are compared based on an experimental laminar two-dimensional SWQ configuration, and the reduced model equations in generalized coordinates are found to perform better than thermokinetic coordinates when the manifold is not perfectly invariant. Analyzing both global quenching quantities and local thermo-chemical states in CO-T and OH-T spaces, it is found that the physically correct trend can only be captured using reduced model equations in generalized coordinates.

3. Within the combined framework of reduced model equations in generalized coordinates and the REDIM, reasonable simplifications for the application in two-dimensional SWQ are found, specifically regarding the simplification of the gradient estimation. By applying REDIM tables generated based on different simplified gradient estimations in an SWQ configuration, it is found that the gradient estimation has relatively little influence on the global quenching quantities and local thermo-chemical states, especially for the near-wall low-temperature region. Thus, if we are only interested in near-wall behavior, even REDIM tables generated with very simple gradient estimations, e.g., constant values, can produce promising predictions.

6 Model reduction *on the fly* for the example of laminar premixed CH_4-air side-wall quenching[3]

In manifold-based reduced models, a manifold is often generated based on an *a-priori* identification. Subsequently, a successful reduced kinetic computation is largely dependent on the proper choice of the model assumption. As an example in SWQ configurations, the major challenge is to find a generic configuration that can accurately describe the species and enthalpy gradients in the near-wall region [78]. This is reflected in the history of the application of different manifolds. At the beginning, the standard FGM [59] approach was adopted in the simulation of CH_4-air SWQ flames [7, 75, 76]. However, it fails to predict the near-wall accumulation of CO, due to that the heat loss is not included in the manifolds. To remedy this drawback, Efimov et al. [78] developed the QFM, where the manifolds were generated based on one-dimensional HOQ solutions. Similarly, REDIMs generated based on the initial guess and gradient estimation from one-dimensional HOQs were used in two-dimensional laminar SWQ simulations [7, 77]. With manifolds generated based on HOQ results, great improvements were achieved in the prediction of near-wall CO since gradients of enthalpy and species in the near-wall region were both accounted for. However, discrepancies between the reduced kinetics and the detailed kinetics still exist, which can also be observed from results in Chapter 4. This is due to the different magnitudes of the scalar dissipation rates between HOQ and SWQ. A varying rate of cooling was introduced in [78] to partially compensate for this difference. Nevertheless, it leads to an increase in the dimension of the manifold and complex definitions of the control variables.

To overcome the restrictions shown in the manifold-based reduced models mentioned above, model reduction *on the fly* can be a solution, which was applied to simplify the chemical kinetics in the past years. Li et al. [137] demonstrated the tabulated dynamic adaptive chemistry approach for MILD combustion. Chi et al. [138] presented an *on the fly* artificial neural network framework for the tabulation of chemical reaction terms for direct numerical simulations. He et al. [139] used the element flux analysis for the reduction of kinetic mechanisms. However, these methods only focus on the reduction of chemical kinetics.

In this chapter, a reduction technique for the *on the fly* generation of a manifold-based reduced kinetic model accounting for both chemical kinetics and molecular transport (REDIM) is proposed. It is realized based on the combined framework of REDIM and the reduced model equations in generalized coordinates developed in Chapter 5. The applicability of the method is validated on the two-dimensional laminar CH_4-air SWQ configuration investigated in Chapter 5.

6.1 Numerical implementation

The configuration adopted in this chapter is exactly the same as in Chapter 5, therefore the numerical description, the computational domain, the boundary and initial conditions, and the numerical scheme also keep unchanged, which are not illustrated again here. Only the coupling of the REDIM reduced kinetics with the generation of the REDIM will be introduced in detail, which is the core of the method.

[3]This chapter is partly taken from the publication by Luo et al. [3], which was created during the work on this thesis. In Ref. [3], I was the main author of this part.

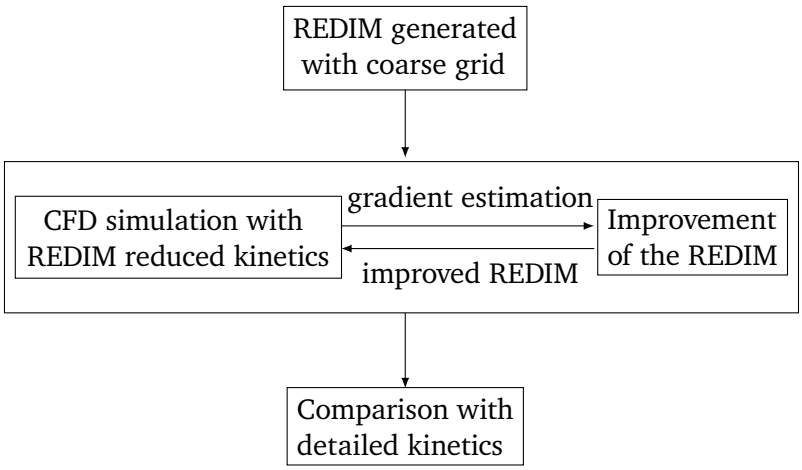

Figure 6.1: General workflow of the REDIM reduced kinetics on the fly.

In order to apply the model reduction *on the fly* for the REDIM method, the REDIM integration process of Eq. (3.1) and the reduced calculation described in Section 5.1.1 need to be coupled. This means that the REDIM is generated and improved during the reduced calculations of the SWQ case. Specifically, an *on the fly* REDIM is obtained based on the *on the fly* update of the gradient estimation, and the details will be discussed in the following.

Before the procedure for the model reduction *on the fly* can be started, an initial mesh serving as the starting solution, and an estimation of the gradients χ need to be provided for the REDIM generation. Afterwards, the REDIM can be calculated and the results of the REDIM are directly used in the CFD simulation, leading to certain states and spatial gradients in the computational domain. These updated gradient estimations are then used to improve the REDIM. Specifically, based on the updated spatial gradients in x and y directions, a new gradient estimation is obtained via a Singular Value Decomposition [136]. Then the REDIM equation is solved in two directions (e.g., see [136, 140] for more information) again, using this new two-dimensional gradient estimation. This means in Eq. (3.1), terms related to χ are updated due to the change of $\mathrm{grad}\psi$ and subsequently, all other quantities change in order to fulfill the balance of the equation, i.e., the evolution equation is solved for the changed gradient estimation. Note that if this procedure is applied to unsteady flames, then the manifold would change slowly, resulting in a very fast evolution of Eq. (3.1) with minimal effort for each time step. The resulting manifold is again applied in a new coupled reduced computation. Such an iterative procedure is performed until the reduced kinetic results do not show much variation anymore. Then the results of each reduced kinetic computation are compared with the detailed kinetics to evaluate the performance of the *on the fly* reduction technique. The principal workflow is also illustrated in Fig. 6.1. Note that the detailed kinetic results are used as a reference to validate the proposed approach in the current study due to its straightforwardness. However, model evaluation can also be performed without the detailed kinetics, i.e., through a simple analysis of the attractive properties of the manifold or by solving for an additional variable in parallel (linear extension in a coordinate perpendicular to the manifold). Furthermore, a mathematical identification of the model reduction error based on sensitivity analyses was reported recently [141].

6.2 Results and discussion

In this section, three reduced kinetic computations using evolving REDIMs are presented. Following the work in Chapter 5, the REDIM-A in Section 5.3.2 is used as the starting REDIM, where the initial mesh is

obtained based on a detailed sample solution of a one-dimensional HOQ configuration, and constant values are simply used for the gradient estimation. The evaluation of each gradient estimation is listed in Table 6.1.

REDIM for RK1	REDIM for RK2	REDIM for RK3
constant values	from RK1 results	from RK2 results

Table 6.1: Gradient estimations used to generate REDIMs for the first (RK1), the second (RK2), and the third (RK3) reduced kinetic simulations.

DK	RK1	RK2	RK3
22.46 mm	22.14 mm	22.37 mm	22.36 mm

Table 6.2: Quenching heights obtained from the detailed kinetics (DK) and the first (RK1), the second (RK2), and the third (RK3) reduced kinetic simulations.

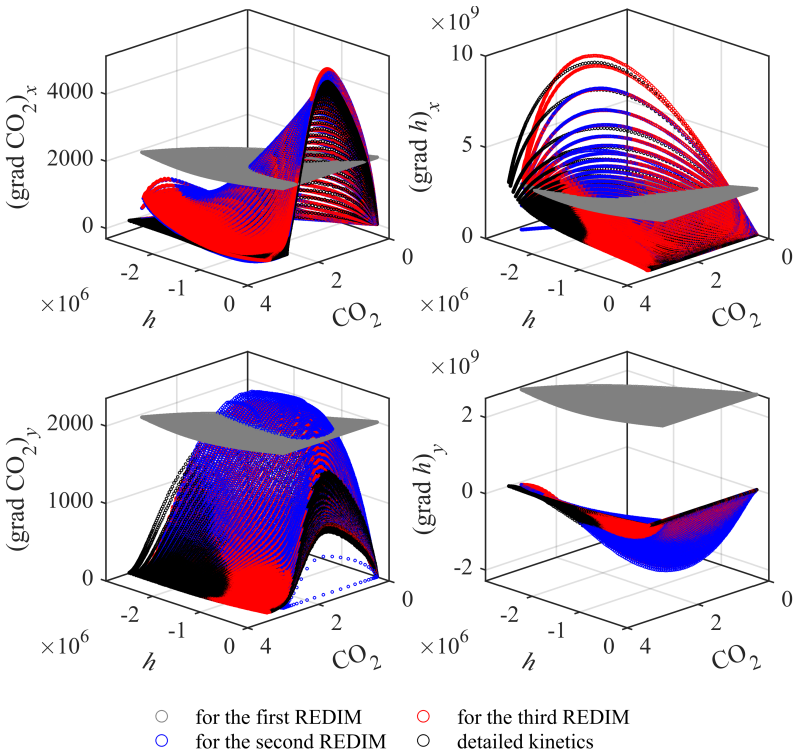

Figure 6.2: Spatial gradients (gradient estimation) in x and y directions used for the REDIMs for the first (gray), the second (blue), the third (red) reduced kinetic computations, and from the detailed kinetics (black): (left) gradients of the specific mole number of CO_2 (in mol/(kg · m)), (right) gradients of the specific enthalpy h (in J/(kg · m)).

Table 6.2 lists the quenching height obtained from both detailed and reduced kinetics. Here, the quenching point is determined by the position where the maximum wall heat flux occurs, similarly to Section 5.3. It is observed that the quenching height is initially slightly underpredicted by reduced kinetics, indicating an overpredicted laminar flame speed. This can be attributed to the rough estimation of gradients in some parts of the first REDIM. Shown in Fig. 6.2 are the spatial gradients of CO_2 and h in x and y directions,

which are used to evaluate the gradient estimations of the generalized coordinates for all the three REDIMs used in the reduced kinetic computations, together with the values obtained from the detailed kinetics for reference. It is clear that in the region close to the freely propagating flame, the enthalpy gradients in both x and y directions and the CO_2 gradient in y direction are significantly overestimated. The observed discrepancy here is consistent with [142], where an overestimation of the enthalpy gradient leads to an increased laminar flame speed in the HOQ. With evolving REDIMs, the results are getting closer to the result of the detailed kinetics. After only one iteration, the difference between the reduced and detailed kinetics reduces to 0.4%. Such a good agreement can be expected since the gradient estimation improves greatly when generating the second REDIM, as can be seen from Fig. 6.2.

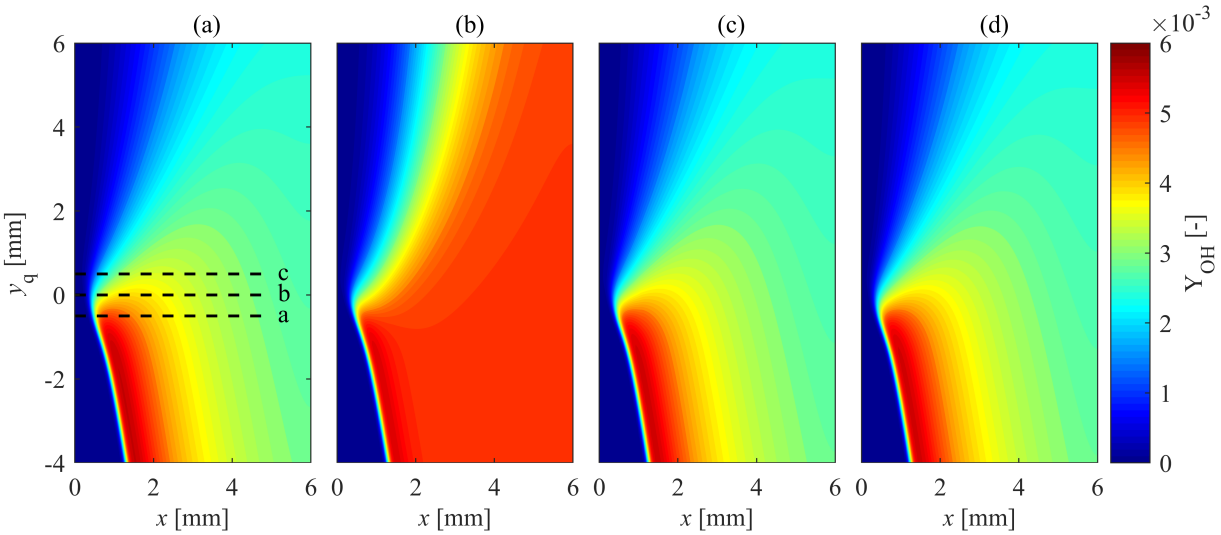

Figure 6.3: OH contours: (a) the detailed kinetic simulation (DK), (b) the first reduced kinetic simulation (RK1), (c) the second reduced kinetic simulation (RK2), (d) the third reduced kinetic simulation (RK3). The black dashed lines denote the positions where quantitative analysis are conducted for species. b corresponds to the quenching height determined by the maximum wall heat flux.

Next, more local details about the flame are investigated. To make a qualitative comparison, the OH distributions for the reduced kinetic simulations at different iterations are presented in Fig. 6.3, where Fig. 6.3(a) from the detailed kinetics serves as a reference. Here, a new streamwise coordinate based on the quenching point is introduced, where the quenching height is defined as $y_q = 0$, while being positive for the downstream and negative for the upstream. It is found that the overall flame shape can be well reproduced by all reduced kinetic calculations, even for the calculation with the initial gradient estimation. However, when inspecting the details of the flame structure, it is found that with the initial REDIM, the first reduced kinetic calculation shows significant deviations from the reference result. According to the first reduced kinetics, OH remains at a high level almost everywhere except in the fresh gas, which makes it fail to predict the transition from reaction zone to post-flame zone, as shown in Fig. 6.3(b). Nevertheless, using the REDIM generated based on the gradient estimation from the first reduced kinetic computation, the result improves significantly. As can be seen from Fig. 6.3(c), almost no differences can be observed for OH, meaning that good prediction can be obtained after only one iteration. Furthermore, the result of the third reduced kinetic simulation is shown in Fig. 6.3(d), which presents similar characteristics as those from the second reduced kinetic computation.

To allow a quantitative comparison, species profiles near the quenching point are analyzed over three

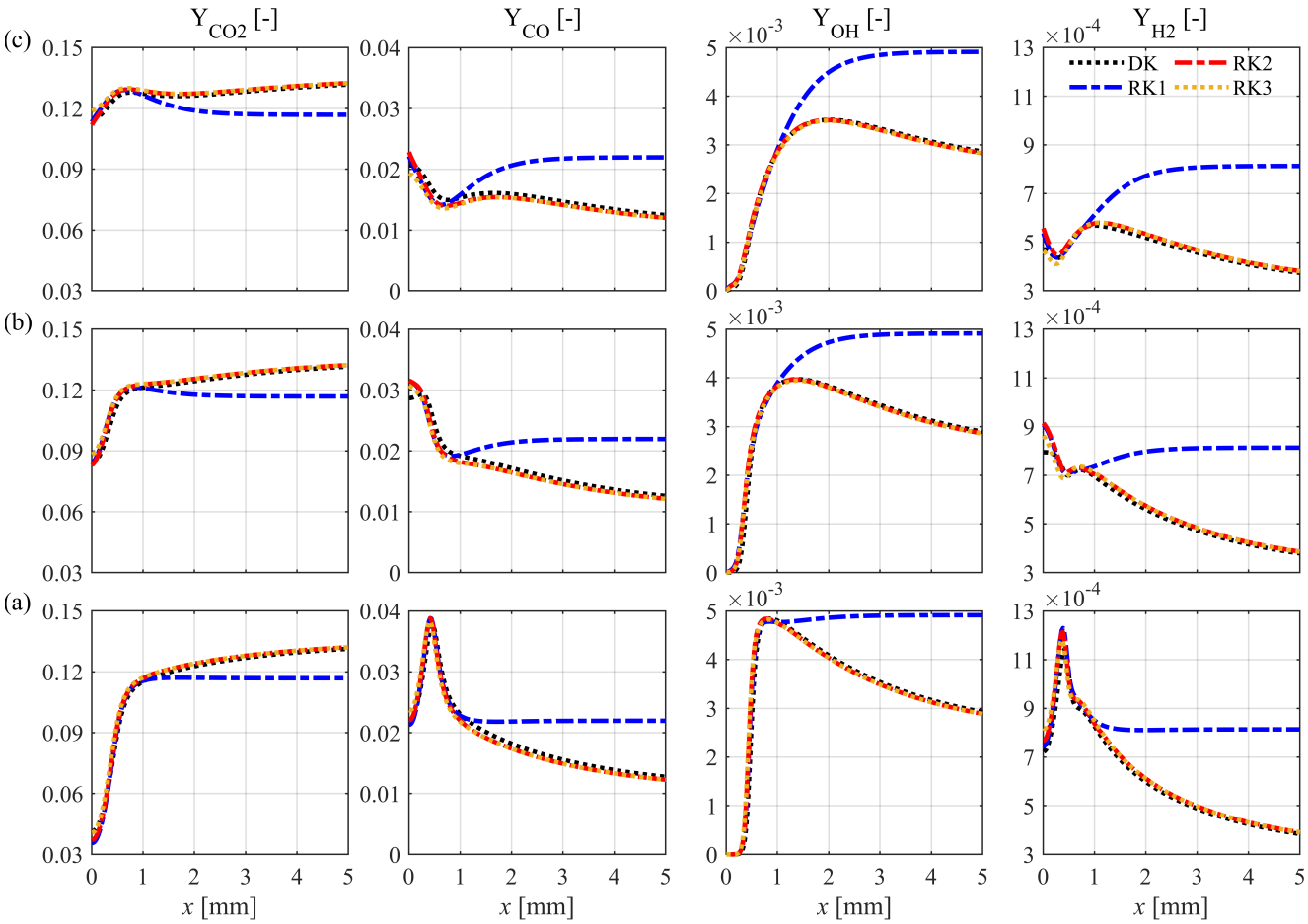

Figure 6.4: Profiles of CO_2, CO, OH, and H_2 mass fractions over three positions: (a) y_q = -0.5 mm, (b) y_q = 0 mm, (c) y_q = 0.5 mm. Black lines correspond to the detailed kinetics (DK). Red, green, and blue lines denote the first (RK1), the second (RK2), and the third (RK3) reduced kinetics, respectively.

horizontal lines vertical to the wall (black dashed lines in Fig. 6.3), i.e., y_q = -0.5 mm (a), y_q = 0 mm (b), and y_q = 0.5 mm (c). Figure 6.4 illustrates the distributions of CO_2, CO, OH, and H_2 mass fractions from both the detailed and reduced kinetic simulations. At all three positions, all species near the wall are well-predicted by all reduced kinetic computations. However, the first reduced kinetic results show considerable deviations from the detailed kinetics away from the wall, e.g., at $x > 1$ mm, for both major and small species. Table 6.3 lists the maximum deviations from the detailed kinetics for all species considered among positions (a), (b), and (c). Larger deviations can be found for small species, e.g., for H_2, the maximum discrepancy even reaches up to 127% in the first reduced kinetic computation. However, these deviations decrease substantially after only one iteration, with maximum values reducing to below 4%, as can be seen in Table 6.3. Observing from Fig. 6.4, the results from the second reduced kinetics almost overlap with those from the detailed kinetics, both for regions near and far from the wall. With further iterations, i.e., for the third reduced kinetic computation, the results show negligible changes. To explain the reasons for the evolution, gradients of specific mole number of CO_2 and enthalpy h at the quenching height (b) are plotted in Fig. 6.5. The good agreement between the first reduced kinetics and the detailed kinetics in the near-wall region is due to that the constant gradients used are comparable to the detailed kinetics to some extent. This demonstrates (1) that the relatively weak sensitivity of the REDIM to the gradient estimation, and (2)

that the constant gradient estimation used here is within the insensitivity range of the REDIM, similar to the findings in Chapter 5. However, in regions away from the wall, the gradients of CO_2 and h in both directions tend to zero in the detailed kinetic simulation, while the values remain at a high level for the gradients used to generate the first REDIM. Therefore, the significant overprediction in the gradient estimation for the first REDIM leads to a discrepancy in the first coupled reduced kinetic computation. Although species show deviations between the first reduced kinetics and the detailed kinetics in regions away from the wall, the gradients match quite well, as can be seen in Fig. 6.5. This is the reason for the good performance of the second reduced kinetics, since the generation of the REDIM depends on the gradient estimation instead of the thermo-chemical variables themselves. Besides, similar performance between the second and third reduced kinetics can also be explained by the similar gradients used for the generation of the second and third REDIMs.

	CO_2	CO	OH	H_2
RK1	11.8%	82.9%	77.8%	127%
RK2	0.5%	3.6%	1.2%	2.0%
RK3	0.5%	3.7%	1.4%	1.7%

Table 6.3: Maximum discrepancies in species mass fractions among positions (a), (b), and (c) at $x > 1$ mm, for the first (RK1), the second (RK2), and the third (RK3) reduced kinetic simulations (compared with the detailed kinetics).

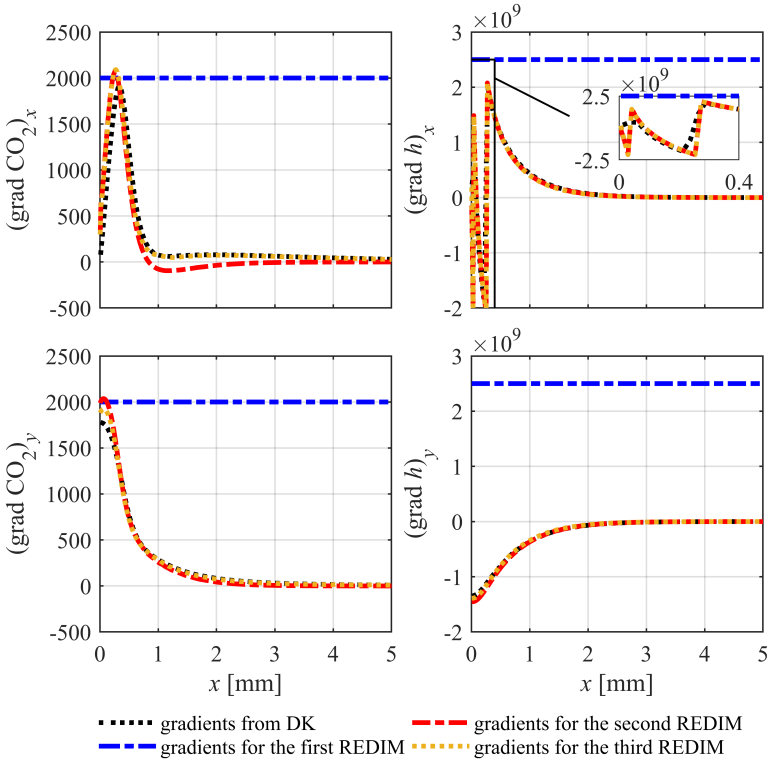

Figure 6.5: Spatial gradients of specific mole number of CO_2 (left) and enthalpy h (right) in x (top) and y (bottom) directions at y_q = 0.

Based on the above analysis in both global quantities and local thermo-chemical states, it can be concluded that for the configuration considered in the present study, the reduced kinetic results can match quite well with the detailed kinetics after only one iteration with the model reduction *on the fly* technique, both qualitatively and quantitatively.

Regarding the computational cost, the whole CPU time of the *on the fly* reduced model with two reduced calculations is only about 0.2 times that of the detailed kinetics for the present configuration. Note that a reduced mechanism for CH_4-air is used in the present study, therefore the advantage will be even more prominent for more complex fuels and mechanisms.

For unsteady calculations, such an iterative procedure can be performed for every single time step. As has been demonstrated, the reduced model reacts and adapts very fast to the gradient estimation. As a result, the suggested methodology looks promising to be implemented in unsteady or even turbulent combustion processes because the reduced model automatically reacts to the spatial gradients resulting from the reduced calculations. Since the manifold properties vary continuously for reasonably small time steps, the accumulation of the numerical error is assumed to be small.

6.3 Summary

In this chapter, a model reduction *on the fly* technique is developed by coupling the reduced kinetic simulation with REDIM and the REDIM generation process itself. With such a technique, the manifold automatically reacts to the given conditions due to the iterative procedure, therefore the generation of the manifold becomes less problem-dependent, meaning that it is unnecessary to find a proper generic configuration during the manifold generation for a specific problem. A straightforward coupling is realized by solving the reduced model equations in generalized coordinates in the CFD solver, consistent with the generation of the REDIM. In this way, the REDIM can be directly used in the coupled simulations without remapping.

The method is applied to a two-dimensional stoichiometric premixed CH_4-air SWQ configuration. Three reduced kinetic simulations are conducted, and the results of the detailed kinetics are used as a reference to evaluate the performance of each reduced kinetic simulation. The reduced kinetic computation starts with a REDIM based on a very rough gradient estimation (constant values for the gradients of CO_2 and enthalpy h). Afterwards, each reduced kinetic simulation uses the REDIM generated based on the gradient estimation from its previous reduced kinetics. Through investigations on thermo-chemical states, it is found that the first reduced kinetic results show significant deviations from the detailed kinetics, especially in the region away from the wall, where maximum discrepancies of 11.8%, 82.9%, 77.8%, and 127% are shown in CO_2, CO, OH and H_2, respectively. However, the first reduced kinetic results provide a more accurate gradient estimation for the next REDIM, resulting in substantially improved results in the second reduced kinetic computation, and the maximum differences in species reduce to below 4%. With a further iteration, i.e., for the third reduced kinetic computation, the results do not change much. A similar evolution is also observed in the quenching height. Therefore, within the configuration considered, only after one iteration, the reduced kinetics model is able to produce quite comparable results as the detailed kinetics, indicating a robust and efficient coupling strategy. With the satisfactory results obtained for the SWQ setup, the model reduction technique *on the fly* shows to be promising for other complex applications where good accuracy is hard to achieve with the traditional manifold-based methods or an increase in manifold dimension is required, e.g., partially premixed flame, as an outlook.

7 Laminar premixed DME-air side-wall quenching[4]

For previous chapters related to SWQ, the unit Lewis number assumption is adopted since the CH_4-air mixture is used as the fuel. However, such a simplification is unsuitable for some other fuels, e.g., DME. The importance of differential diffusion effects in near-wall DME flames was revealed by several laminar and turbulent experimental studies [70, 71], which is different from unconfined turbulent DME flames (not influenced by walls) where the unity Lewis number assumption can be used with good accuracy [143]. Kosaka et al. [70] performed experiments on turbulent premixed DME SWQ flames, and found a correlation between increased heat release rate and negative curvature, which can only be explained by differential diffusion effects. Substantial differential diffusion effects were also reported in a recent experimental study conducted by Zentgraf et al. [71], investigating a laminar lean DME-air SWQ flame. In this experiment, CO, CO_2 mole fractions and temperature were simultaneously measured, and the unity Lewis number assumption was found to be not suitable when predicting thermo-chemical states. These findings indicate that detailed diffusion models need to be considered for the numerical modeling of wall-bounded DME flames. Thus, it is necessary to extend the existing manifold-based reduction methods and their CFD coupling so that they can describe the differential diffusion effects in SWQ.

Although differential diffusion effects were incorporated in many manifold-based reduction techniques for different flame configurations without significant influences from the wall [144–147], they have not yet been taken into account in SWQ problems. To fill the gap, a reduced kinetic method considering both strong heat loss and differential diffusion effects is proposed in this chapter, and the approach is applied to a lean DME-air SWQ flame.

Compared to SWQ cases with $Le = 1$, further complexities due to differential diffusion effects and their interactions with the strong heat losses to the wall pose additional challenges to the manifold-based methods [96]. Specifically, for those manifolds parameterized with thermokinetic variables, the major difficulty lies in finding a unique parametrization, which is often realized by a particular choice of the so-called progress variable that is taken as a combination of several species. In this case, reduced kinetics formulated and solved in generalized coordinates shows superiority, since it depends very little on the monotonic parametrization in thermokinetic variable space, e.g., see REDIM-coupled simulations in generalized coordinates [32]. Besides, as stated before, within such a framework, the procedure for solving the reduced model equations in the CFD solver becomes consistent with the generation of the manifold. In Chapter 5, reduced kinetics in generalized coordinates has already been successfully applied to CH_4-air SWQ flames with the unity Lewis number assumption.

In this chapter, the research in Chapter 5 is extended to incorporate differential diffusion effects. For validation, the experimental configuration in [71] is chosen, where pronounced differential diffusion effects exist. Two different reduced kinetic models are analyzed, one based on a REDIM table generated from HOQ solutions and the other based on a REDIM table generated from the SWQ solution. Therefore, the objective of this chapter is twofold: Firstly, to assess the capability of the REDIM reduced kinetics to describe the FWI processes with strong differential diffusion effects through comparison with the reference data obtained from the detailed kinetic simulation and the experiment. Specifically, the following three aspects are analyzed: (1) global quenching characteristics, (2) local thermo-chemical states, and (3) variation of

[4]This chapter is partly taken from the publication by Luo et al. [4], which was created during the work on this thesis. In Ref. [4], I was the main author of this part.

stretch in the near-wall region. Secondly, to compare the performance of the two reduced kinetic models, identifying their advantages and disadvantages. This can be important for calculations employing reduced kinetics in larger-scale or more complex configurations.

7.1 Numerical implementation

The SWQ burner investigated in this study is similar to Chapter 5, as shown in Fig. 5.1. A lean homogeneous DME-air mixture at 300 K and ambient pressure is injected from the nozzle, with the Reynolds number of the main flow maintained at approximately 5900, evaluated based on the hydraulic diameter of the nozzle exit and the bulk flow velocity. The equivalence ratio ϕ of the fresh gas is 0.83. The flow passes a ceramic rod, where a V-shaped flame stabilizes. One branch of the flame interacts with a stainless steel wall at approximately 333 K, while the other branch of the flame develops freely.

7.1.1 Numerical description

Differential diffusion effects are considered via a mixture-averaged model [100]. All computations are performed with a mechanism created for atmospheric DME-air combustion, which includes 20 species and 93 reactions [8].

Detailed kinetics

When considering differential diffusion effects, the evolution of species Eq. (2.4) can be written as

$$\frac{\partial\left(\rho Y_k\right)}{\partial t}+\nabla\cdot\left(\rho\boldsymbol{u}Y_k\right)-\nabla\cdot\left(\rho D_k Y_k\right)-\nabla\cdot\left(\rho\frac{Y_k}{\overline{M}}D_k\nabla\overline{M}\right)=\dot{\omega}_k\ , \tag{7.1}$$

The transport equation of the total enthalpy h Eq. (2.6) can be rewritten as

$$\frac{\partial\left(\rho h\right)}{\partial t}+\nabla\cdot\left(\rho\boldsymbol{u}h\right)-\nabla\cdot\left(\frac{\lambda}{c_p}\nabla h\right)+\sum_{k=1}^{N}\left(h_k\frac{\lambda}{c_p}\nabla Y_k\right)+\sum_{k=1}^{N}\left(\rho h_k D_k\nabla Y_k\right)+\sum_{k=1}^{N}\left(\rho h_k\frac{Y_k}{\overline{M}}D_k\nabla\overline{M}\right)=0\ . \tag{7.2}$$

Within the framework of detailed kinetics, Eqs. (2.1), (2.2), (7.1) and (7.2) are solved.

Reduced kinetics with REDIM

The REDIM method is used to generate the manifolds that are parameterized in generalized coordinates. In line with the generation of the REDIM, reduced model equations are solved in generalized coordinates as well in the coupled simulations, i.e., Eq. (3.15), together with Eqs. (2.1) and (2.2) are solved.

To obtain a REDIM, a spatial gradient estimation $\nabla\psi$ and an initial guess have to be provided. In this chapter, two different approaches are applied, resulting in two different REDIMs. One REDIM is generated based on the one-dimensional DME-air HOQ results from the detailed kinetic simulation (REDIM-HOQ), while the other relies on the two-dimensional DME-air SWQ results from the detailed kinetic simulation (REDIM-SWQ). The adopted HOQ and SWQ configurations are illustrated in Fig. 7.1, where the SWQ configuration is the same as the one used for the coupled simulation. Note that, to provide the gradient estimation for the REDIM generation, the SWQ detailed kinetic simulation here is performed on a very coarse grid, not the one for analysis, since the REDIM shows relatively weak dependence on the applied gradient estimation [34, 142]. More details about the two REDIMs will be discussed in the following.

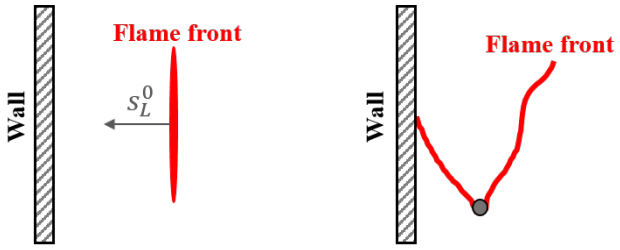

Figure 7.1: Schematic of HOQ (a) and SWQ (b) configurations adopted in the present study (s_L^0 denotes the laminar flame speed).

REDIM-HOQ

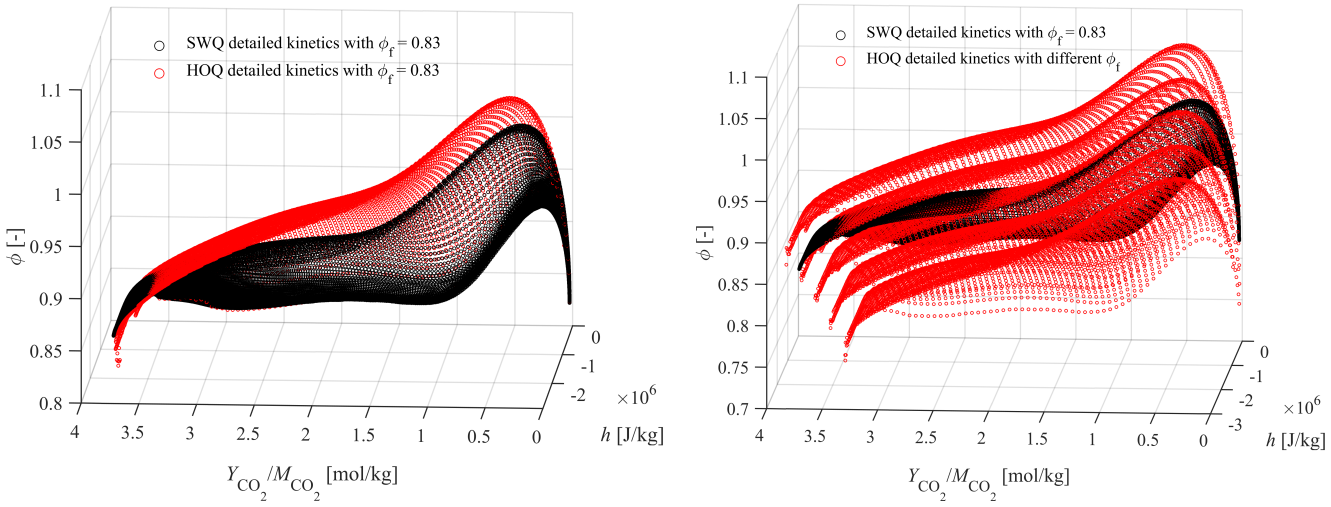

(a) (b)

Figure 7.2: Distributions of the local equivalence ratio ϕ over Y_{CO_2}/M_{CO_2} and h of the 2D SWQ and the 1D HOQ with the same fresh gas composition (ϕ_f = 0.83) (a), and the 2D SWQ with ϕ_f = 0.83 and a series of 1D HOQs with different ϕ_f (b).

In previous SWQ simulations with $Le = 1$ using manifold-based reduced methods, it is a common choice to generate manifolds based on the one-dimensional HOQ calculation with a same fresh gas composition and temperature [7, 77, 78]. For REDIM, the initial manifold for FWI is usually characterized with a two-dimensional parametrization vector, with one characterizing the progress of the chemical reaction and the other describing the heat loss to the wall [7, 77]. However, such a parametrization may lead to a wrong flame shape when differential diffusion effects are taken into account, since the local equivalence ratio distribution differs significantly between HOQ and SWQ for the same fresh mixture, as shown in Fig. 7.2(a). In order to consider differences in the local equivalence ratio ϕ, HOQ simulations are performed for five different equivalence ratios of fresh gas (0.77, 0.8, 0.84, 0.86, 0.9), so that the states in SWQ can be covered by this series of one-dimensional HOQ solutions, as shown in Fig. 7.2(b). In this case, a three-dimensional initial guess is built through the combination of the initial guesses of the two-dimensional REDIMs for HOQs of different mixtures. Therefore, the initial manifold is parameterized with (Y_{CO_2}/M_{CO_2}), h and ϕ. Note

that this parametrization is only important for the construction of the initial mesh, and has a negligible influence on the actual integration procedure and subsequently the final REDIM, which is scale-invariant [34]. Figure 7.3(a) shows the initial guess for the three-dimensional REDIM generation.

With the given gradient estimation and initial guess, Eq. (3.1) is integrated, and the stationary solution leads to a three-dimensional REDIM, which is parameterized by the generalized coordinates $\boldsymbol{\theta}$, where $\boldsymbol{\theta} = (\theta_1, \theta_2, \theta_3)^T$. Here θ_1 corresponds to the local coordinate in the direction of (Y_{CO_2}/M_{CO_2}), θ_2 the local coordinate in the direction of h and θ_3 the local coordinate in the direction of ϕ. The size of the REDIM is $60 \times 60 \times 5$ for $\theta_1 \times \theta_2 \times \theta_3$.

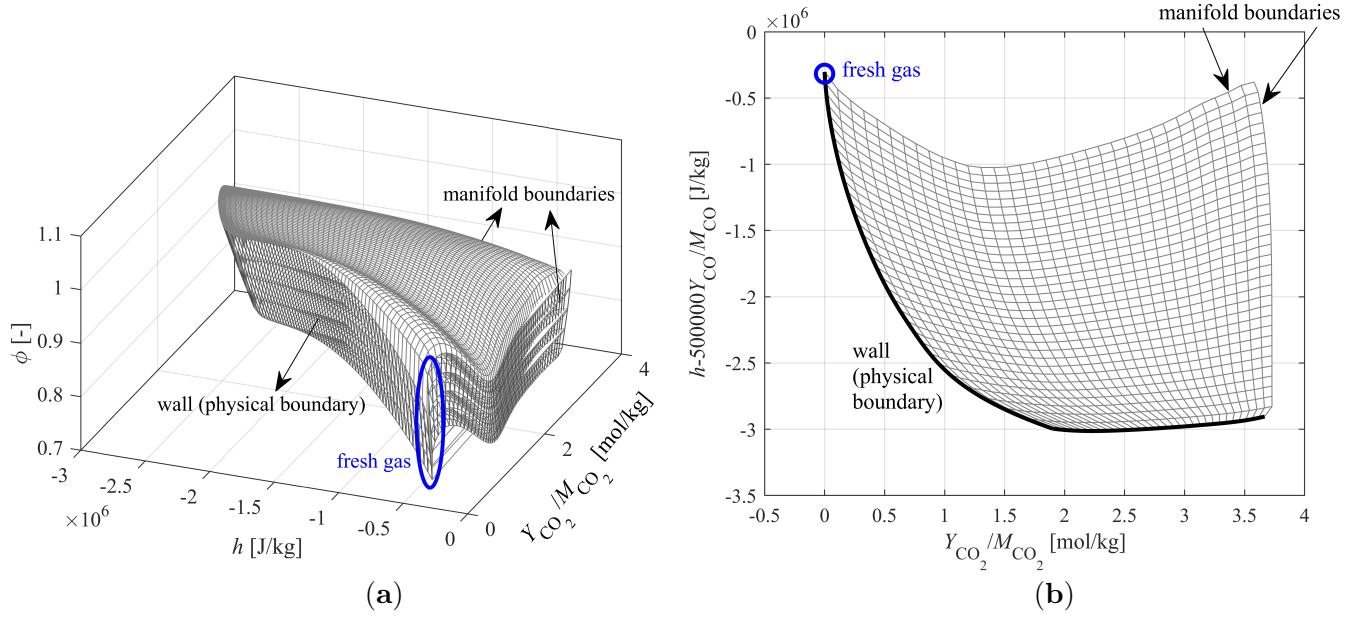

Figure 7.3: Initial guesses of the REDIM based on HOQs projected to (Y_{CO_2}/M_{CO_2}), h, and ϕ (a), and the REDIM based on a SWQ projected to (Y_{CO_2}/M_{CO_2}) and (h - 500000 Y_{CO}/M_{CO}) (500000 is a constant in J/mol) (b). For clear interpretation, the grid in (b) is twice coarser than the actual grid used in the computation.

REDIM-SWQ

Through analyzing the two-dimensional SWQ results from the detailed kinetics, it is found that although ϕ is not constant over the whole domain, its variation over (Y_{CO_2}/M_{CO_2}) and h is almost unique, especially in the near-wall region, as shown in Fig. 7.4(a). Therefore, when both the spatial gradient estimation $\nabla\psi$ and the initial guess are evaluated based on the two-dimensional DME-air SWQ results from the detailed kinetic simulation on a coarse grid, it is reasonable to assume that the manifold can be described with a two-dimensional parametrization vector. However, if (Y_{CO_2}/M_{CO_2}) and h are used for parametrization, foldings may be encountered in a small region away from the wall, as denoted by the red circle in Fig. 7.4(a). To guarantee a monotonic parametrization of the REDIM, the initial manifold is parameterized with (Y_{CO_2}/M_{CO_2}) and (h - 500000 Y_{CO}/M_{CO}). Here, 500000 is a constant with a unit of J/mol. The states of the SWQ using detailed kinetics projected onto (Y_{CO_2}/M_{CO_2}) and (h - 500000 Y_{CO}/M_{CO}) space has been plotted in Fig. 7.4(b). Again, it is noted that the REDIM is independent of the parametrization of the initial guess, since it is usually formulated and computed in generalized coordinates. Figure 7.3(b) shows the

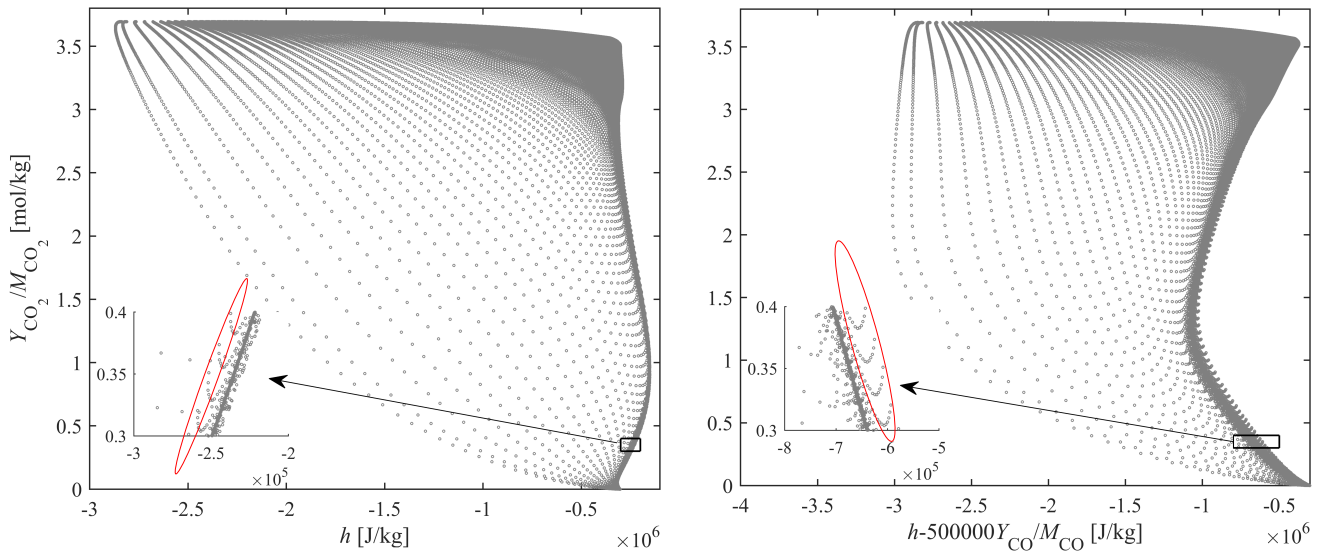

(a) (b)

Figure 7.4: States of SWQ using detailed kinetics over (Y_{CO_2}/M_{CO_2}) and h (a), and (Y_{CO_2}/M_{CO_2}) and (h - 500000 Y_{CO}/M_{CO}) (b).

initial guess for the REDIM generation.

The stationary solution of Eq. (3.1) gives the two-dimensional REDIM parameterized by $\boldsymbol{\theta} = (\theta_1, \theta_2)^T$. The size of the REDIM is 100 $\times$ 100 for $\theta_1 \times \theta_2$.

Reduced model equations

For reduced kinetics with REDIM-HOQ, governing equations Eq. (3.15) are solved for θ_1, θ_2 and θ_3. For reduced kinetics with REDIM-SWQ, governing equations Eq. (3.15) are solved for θ_1 and θ_2.

7.1.2 Computational domain and boundary conditions

The computational domain is the same as Chapter 5, with D1 being the large computational domain with coarse grids and D2 being the subdomain with finer grids. The boundary conditions for the detailed kinetic simulation on domain D1 are similar to [76], where the fresh gas issues from a 5.5 mm wide section at the inlet, and the hot burned exhaust gas is injected from the remaining 0.5 mm wide section to stabilize the flame. A parabolic profile is applied to the fresh gas velocity with a maximum value of 2.11 m/s, while a constant velocity of 4.32 m/s is assumed for the burned gas, partially compensating for the density difference between the fresh and burned gas. The impermeable wall is assumed to be inert due to the low temperature [35, 36]. Therefore, at the wall, a zero-gradient boundary condition is applied to all species, and a no-slip boundary condition is used for the velocity. The initial and inlet boundary conditions for simulations on domain D2 are obtained from the results from D1.

In reduced kinetic simulations, boundary conditions are specified for $\boldsymbol{\theta}$. At the inlet, fixed values are used, i.e., $\boldsymbol{\theta}$ = constant. At the right and upper boundaries, a zero-gradient boundary condition is applied, which corresponds to $\boldsymbol{C}\,\boldsymbol{\psi\theta}\,\nabla\boldsymbol{\theta} = 0$. Here, $\boldsymbol{C} = \left(\begin{smallmatrix} 0 & 0 & 1 & \cdots & 0 \\ 1 & 0 & 0 & \cdots & 0 \end{smallmatrix}\right)$. On the wall, a zero-gradient boundary condition is adopted for all species. For the three-dimensional REDIM (REDIM-HOQ), the value of ϕ, (Y_{CO_2}/M_{CO_2}) and the fixed wall temperature are then used to access the table to determine θ_1, θ_2 and θ_3 on the wall. For

the two-dimensional REDIM (REDIM-SWQ), the value of (Y_{CO_2}/M_{CO_2}) and the fixed wall temperature are utilized to access the table to determine θ_1 and θ_2 on the wall.

7.2 Results and discussion

In this section, the performance of the reduced kinetics (RK) with REDIMs in generalized coordinates including differential diffusion effects is assessed in an SWQ configuration by comparison with the detailed kinetics (DK) and experimental data from [71]. In the following, the reduced kinetic computation based on REDIM-HOQ is abbreviated as RK-HOQT, and the reduced kinetic computation based on REDIM-SWQ is denoted as RK-SWQT.

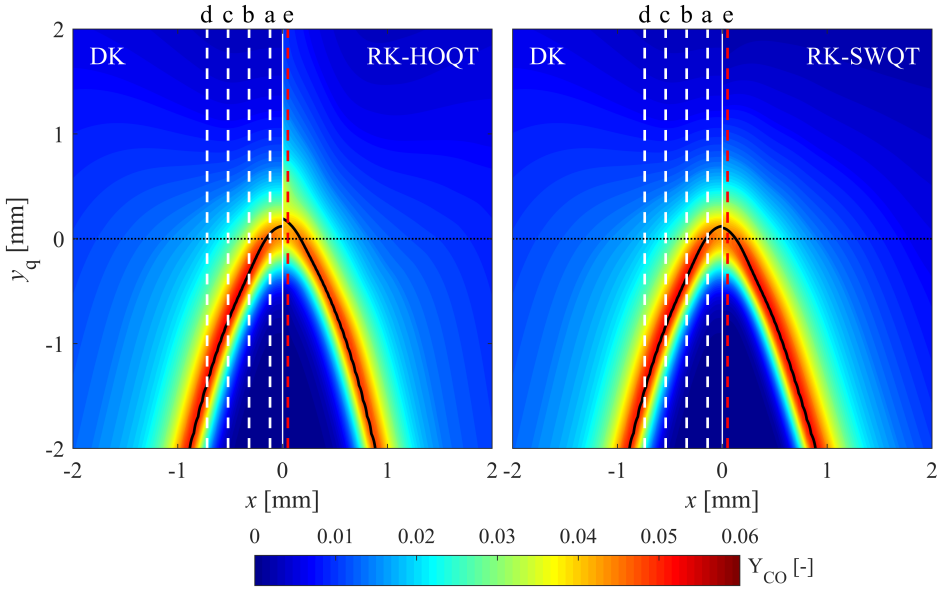

Figure 7.5: Comparison of CO distributions between detailed kinetics (DK) and reduced kinetics (RK): (left) DK and RK-HOQT, (right) DK and RK-SWQT. The black solid curve marks the flame location where the flame stretch is evaluated. The black dashed line corresponds to the quenching height. The white dashed lines are positions where the experimental data, detailed kinetic results, and reduced kinetic results are compared. The red dashed line denotes a further position very close to the wall where the detailed kinetics and the reduced kinetics are compared. $x = 0$ corresponds to the wall.

Figure 7.5 shows the CO contour, where the comparison between DK and RK-HOQT is shown on the left, and the comparison between DK and RK-SWQT on the right. A new streamwise coordinate y_q is defined based on the quenching point, determined by the OH gradient, similarly to [71] and Section 5.2. In this coordinate, $y_q = 0$ mm stands for the quenching height, while negative/positive values are set at upstream/downstream locations, respectively. The black solid curve in Fig. 7.5 marks the flame location defined by the fuel mass fraction $Y_f = Y_{f,\mathrm{iso}}$ [84]. Here, $Y_{f,\mathrm{iso}}$ corresponds to the fuel mass fraction at the maximum heat release rate in a one-dimensional unstretched freely propagating flame at the same equivalence ratio. Overall, both RK-HOQT and RK-SWQT reproduce a similar general flame shape as DK. Due to diffusion, near-wall CO does not vanish but remains at a high level near the quenching point, and this trend is well captured by both reduced kinetics. Slight differences can only be observed in the proximity very close to the wall for the two reduced kinetic models, where the CO distribution from RK-HOQT appears more diffusive than RK-SWQT.

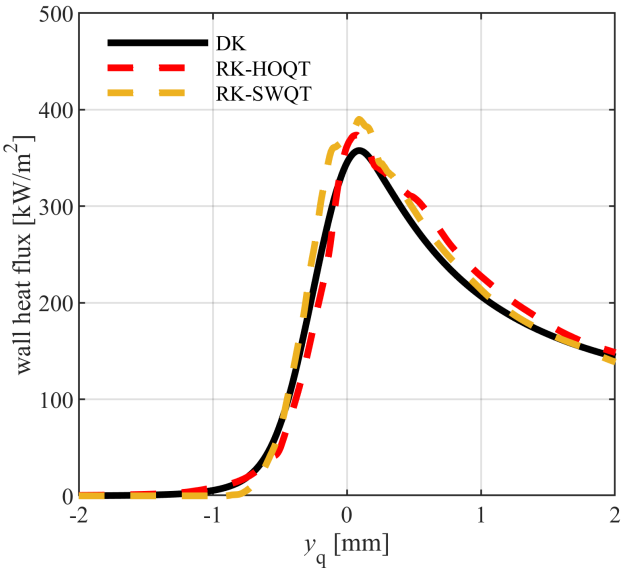

Figure 7.6: Variations in wall heat flux for both detailed kinetics (black solid line) and reduced kinetics (red dashed line for RK-HOQT and yellow dashed line for RK-SWQT).

The quenching distance and wall heat flux are two important global metrics to quantitatively describe the SWQ process. The quenching distance is defined as the wall-normal distance between the flame front (determined by the OH gradient) and the wall at the position of quenching [70]. In the SWQ flame configuration investigated here, the quenching distance is calculated to be about 0.254 mm for both DK and RK-SWQT, while the value is about 0.274 mm for RK-HOQT. Distribution of the wall heat flux, defined as $Q = -\lambda\,(\partial T/\partial x)_{\text{wall}}$, along y_q is shown in Fig. 7.6 for both detailed kinetics and reduced kinetics. Overall good agreement is observed, although the wall heat flux is overestimated in a small region near the quenching point for both RK-HOQT and RK-SWQT. The maximum value is about 358 kW/m^2 for DK, while 376 kW/m^2 for RK-HOQT and 396 kW/m^2 for RK-SWQT. For both reduced kinetics, the deviation in maximum wall heat flux is below 10%. Besides, it is consistent between the detailed kinetics and the reduced kinetics that the position where the maximum wall heat flux occurs is slightly downstream of the quenching point determined from the OH gradient.

To quantify differential diffusion effects, the differential diffusion parameter Z_{HC} is evaluated. Figure 7.7 shows the Z_{HC} contour, where negative values are observed in the region of interest, near the quenching point. The wall has a pronounced influence on its variation. Away from the wall and the reaction zone, i.e., at 1 mm $< x <$ 2 mm, Z_{HC} is almost constant with small absolute values close to 0. Moving towards the wall, strong variations near the flame can be found, and the absolute value tends to increase. The maximum absolute value is reached on the wall, slightly upstream of the quenching height, indicating that the strongest differential diffusion effects appear across the quenching zone. This is in agreement with the experimental findings in [71]. Therefore, for any manifold-based reduced method for such a flame, it is necessary to include differential diffusion effects. The main characteristics mentioned above are well reproduced by both RK-HOQT and RK-SWQT, except that the influence of differential diffusion extends to the further downstream region in the very near-wall layer for RK-HOQT.

To summarize, comparing the results obtained with detailed and reduced kinetics in Figs. 7.5, 7.6 and 7.7, it is observed that the global features of the SWQ are well reproduced by both reduced kinetics, extended to include differential diffusion effects in this study, with RK-SWQT performing slightly better than RK-HOQT in the region very close to the wall.

To analyze the local thermo-chemical states, CO, CO_2 mole fractions and gas temperature from simulations

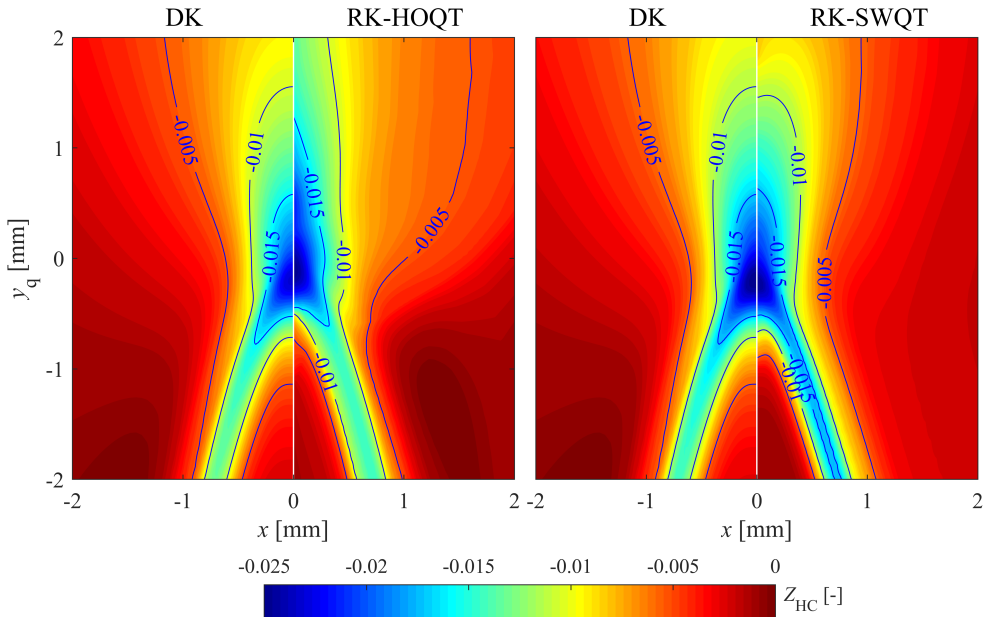

Figure 7.7: Distributions of the differential diffusion parameter Z_{HC}: (left) DK and RK-HOQT, (right) DK and RK-SWQT. x = 0 corresponds to the wall.

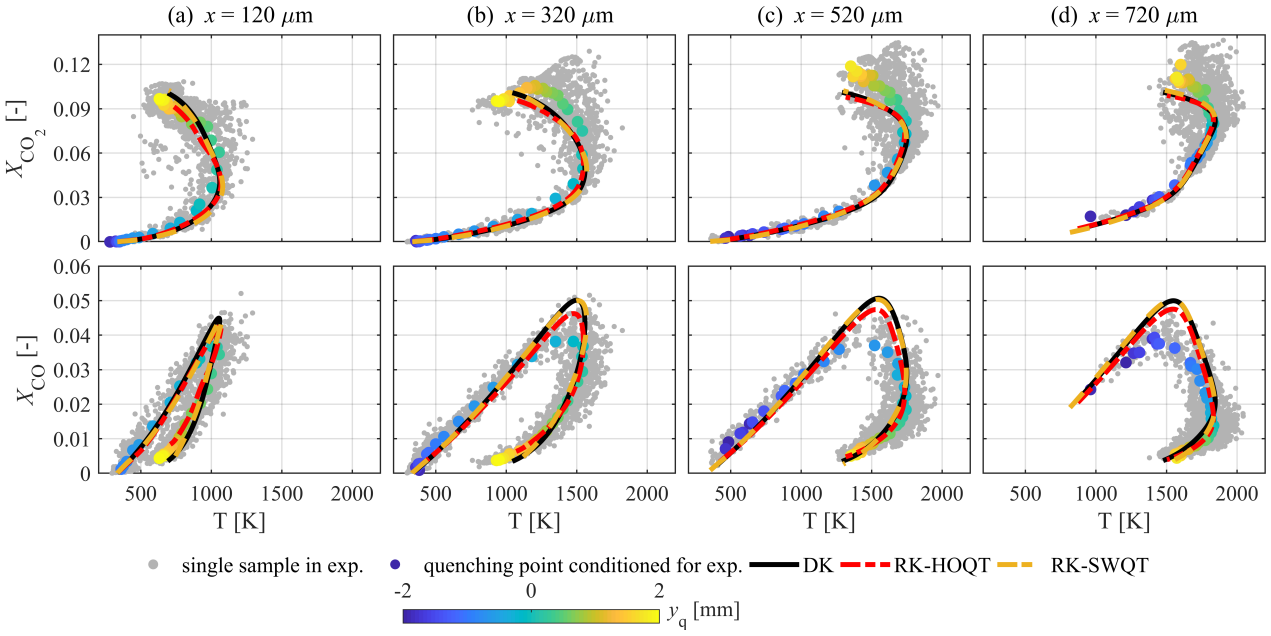

Figure 7.8: Mole fractions of CO_2 (X_{CO_2}) and CO (X_{CO}) over gas temperature T at wall distances of 120 μm, 320 μm, 520 μm, and 720 μm. Gray dots correspond to the instantaneous experimental data which is collected between y_q = -2 mm and y_q = 2 mm. Colored dots are experimental results averaged on the spatial bins with respect to the quenching height. Black solid lines denote results from DK, red dashed lines are results from RK-HOQT, and yellow dashed lines are results from RK-SWQT.

are compared with the experimental data (previously presented in [71]) at several positions, denoted by white dashed lines in Fig. 7.5. Figure 7.8 illustrates the species variations over temperature, where the

instantaneous experimental data are represented by gray scatters, together with the conditioned average binned with 100 μm increments based on the y_q coordinate, denoted by colored scatters, and the simulation results are presented as lines, in black for DK, in red for RK-HOQT and in yellow for RK-SWQT. The results of both experiments and simulations are sampled between y_q = -2 mm and y_q = 2 mm. At all positions, the experimental data and the simulation results are found to cover almost the same range in state space, indicating that there is a similar variation in the physical space relative to the quenching point. For the CO_2 mole fraction, all simulation results agree well with the averaged experimental data. Small discrepancies are mainly found in the region downstream of the quenching point. Regarding CO, numerical simulations are able to reproduce the variation in both the production and oxidation branches, except for a slight overprediction in the peak value. This is consistent with the findings in [71]. These deviations between the simulations and experiment may be due to (1) three-dimensional effects in the experiment, which are not included in the computation, (2) unsteadiness in the experiment, and (3) the assumed inlet boundary conditions in the simulation. Similar discrepancies were also observed in previous works investigating CH_4-air SWQ flames [7]. When comparing results from the detailed kinetics and the reduced kinetics, it can be observed that RK-SWQT yields almost the same variation as DK, while slightly larger discrepancies can be found in the prediction of RK-HOQT. This is consistent with the previous findings from contours of CO and Z_{HC}. The major reason for the deviation may be the different scalar dissipation rates in HOQ and SWQ. Nevertheless, the overall good agreement between the detailed kinetics and the reduced kinetics further verifies the validity of the reduced kinetic models used in the present study.

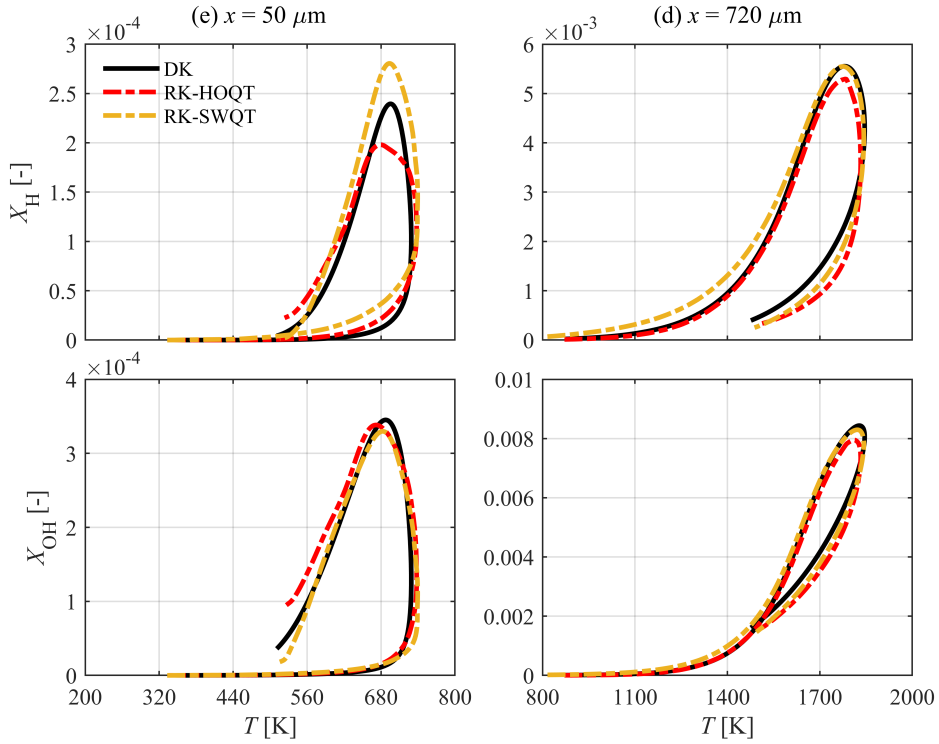

Figure 7.9: Mole fractions of H (X_H, top) and OH (X_{OH}, bottom) at wall distances of 50 μm (left) and 720 μm (right) between y_q = -2 mm and y_q = 2 mm.

Additionally, minor species that cannot be quantified in the experiment are compared between the detailed kinetics and the reduced kinetics in Fig. 7.9. H and OH radicals are sampled over two lines parallel to the wall, namely x = 50 μm (e) and x = 720 μm (d), representing positions very close to the wall and away from the wall, respectively. Overall, both reduced kinetic results match well with those based on detailed

kinetics, although the deviations are slightly larger than for major species such as CO_2 and CO. A relatively large deviation in the peak value of the H radical at $x = 50\,\mu m$ is mainly due to the strong differential diffusion effects in the region very close to the wall, and similar findings were reported in [148].

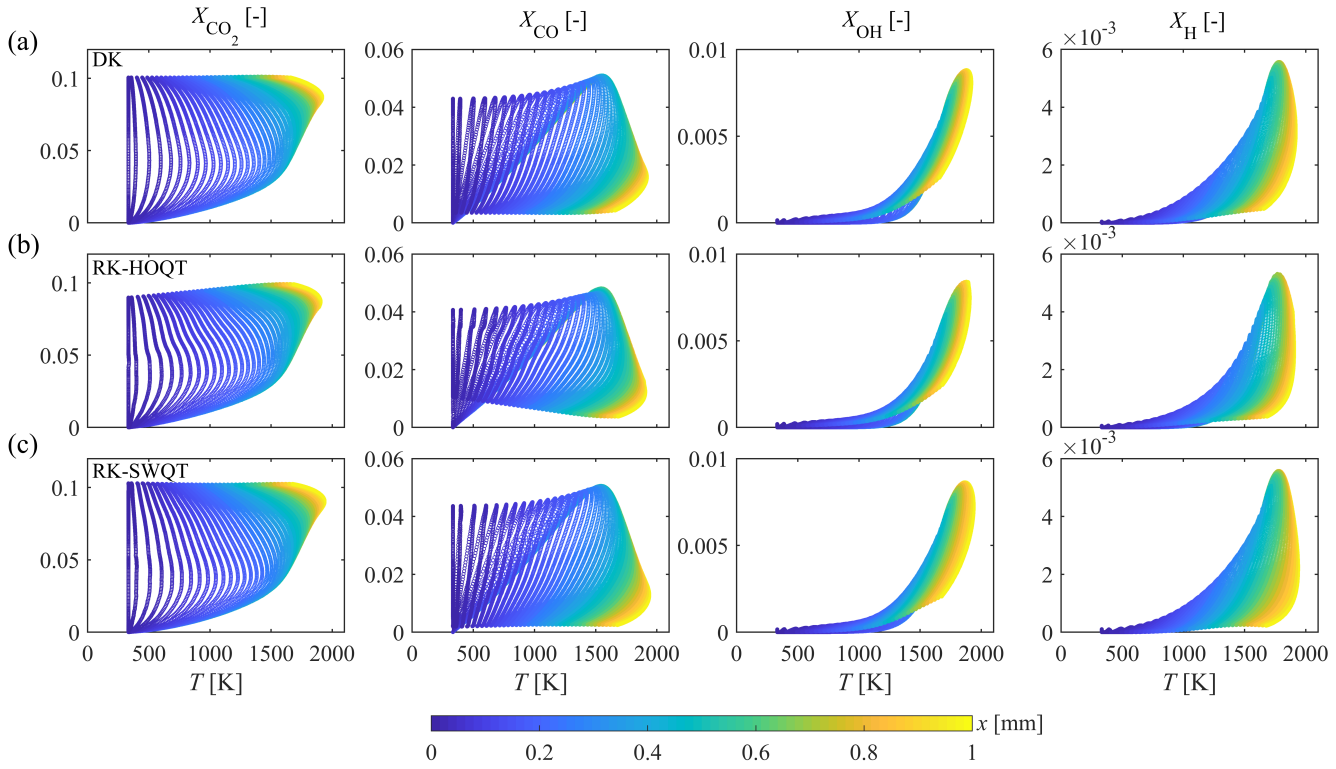

Figure 7.10: Variations of the mole fractions of CO_2, CO, OH, and H over temperature between y_q = -2 mm and y_q = 2 mm for $x < 1$ mm of DK (a), RK-HOQT (b), and RK-SWQT (c). The scatter is colored by the wall-normal coordinate x.

The continuous variations of thermo-chemical states in CO_2-T, CO-T, OH-T, H-T between y_q = -2 mm and y_q = 2 mm for $x < 1$ mm are illustrated in Fig. 7.10. It is observed that the overall spreading of the scatter data appears similar for DK, RK-HOQT, and RK-SWQT. Small differences mainly exist in the region very close to the wall for RK-HOQT, where CO_2 is slightly underpredicted and CO is slightly overpredicted.

Good agreement between the detailed and both reduced kinetics in Figs. 7.8, 7.9, and 7.10 indicates (1) that both manifolds are able to describe thermo-chemical states both near and away from the wall, and (2) that not only major species, but also small species can be predicted well by both manifolds.

Finally, the flame stretch K in the near-wall region is investigated. It is defined based on Eq. (2.28). Here the flame surface is identified by $Y_f = Y_{f,\mathrm{iso}}$ [84]. According to Zhang et al. [84], the sign of K_s is strongly correlated with FWI. Specifically, the existence of the cold wall leads to a negative K_s, while a freely propagating flame corresponds to a positive value. In the present study, the variation in K_s and K over the flame surface, represented by the black solid curve in Fig. 7.5, is plotted in Fig. 7.11 for both detailed and reduced kinetics. Here, the total stretch is normalized as $K^+ = K\,\delta/s_L^0$, where s_L^0 is the laminar flame speed of an unstretched freely propagating flame and δ is the thermal flame thickness based on Eq. (2.33) [84]. K_s is similarly normalized, resulting in the non-dimensional value K_s^+. Negative K_s^+ is observed in the region very close to the wall where $x/\delta < 1$, while the values remain at approximately zero in the region away from the wall, for both DK and RK-SWQT. It must be noted that not only the trend but also the position where the sign of K_s^+ turns negative are consistent with the finding from [84], where a different fuel mixture, CH_4-air, was investigated. For RK-HOQT, the variation trend appears similar, while

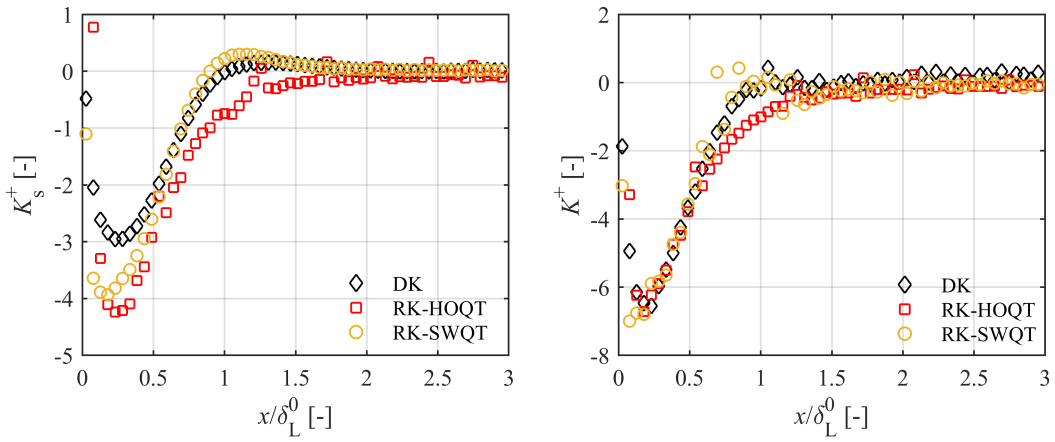

Figure 7.11: Comparison of the normalized strain K_s^+ (left) and total stretch K^+ (right) over the normalized wall distance x/δ between detailed and reduced kinetics.

the transition of K_s^+ and K^+ to negative values occurs slightly further from the wall. Despite the small difference presented in RK-HOQT, the general good agreement between the detailed kinetics and both reduced kinetics in strain and total stretch indicates that the coupled reduced kinetic computations are able to well reproduce the flame's response to the flow and the curvature, which are affected by the heat loss.

Regarding the computational cost, the total CPU time for both coarse and fine grids is compared between the detailed kinetics and the reduced kinetics. Note that the cost of REDIM generation is not included here, since it is almost negligible compared to the CFD simulation and the REDIM only needs to be generated once, not for every reduced calculation. For the detailed kinetic simulation, the CFD calculation costs about 3060 core-h, while the time is about 640 core-h for the reduced calculation of RK-SWQT and about 1210 core-h for RK-HOQT. The advantages of the reduced computational time of the reduced kinetics over the detailed kinetics are evident. Note that a small mechanism for DME-air mixture is used in the present study, with only 20 species and 93 reactions. Therefore, the speed up of the reduced kinetics would be even more significant for more complex fuels and larger chemical mechanisms.

Based on the above observations, it can be concluded that both reduced kinetic computations (RK-HOQT and RK-SWQT) show good prediction in the SWQ process considering differential diffusion effects, with RK-SWQT performing slightly better in the region very close to the wall. Comparing these two reduced kinetic methods, both have advantages and drawbacks. The major advantage of RK-HOQT is that only one-dimensional calculations are required before the REDIM is generated. However, although RK-SWQT requires a two-dimensional calculation in advance to generate the REDIM, the computational cost for the CFD simulation is only half of that of RK-HOQT since the manifold dimension is reduced. This indicates that for the investigation of near-wall physics in more complex scenarios, such as SWQ in real devices, it may be promising to use REDIMs based on generic SWQ simulation results, or to apply the *on the fly* technique proposed in Chapter 6.

7.3 Summary

In this chapter, reduced kinetics for SWQ, using the REDIM method constructed and applied in generalized coordinates, is extended to account for differential diffusion effects. Using the current approach, species diffusion is considered when solving the equation for the REDIM, while no additional terms are needed for the coupled simulation since the governing equations are solved in generalized coordinates. For the application in a two-dimensional laminar lean DME-air SWQ flame, two different reduced kinetic models are proposed,

i.e., RK-HOQT and RK-SWQT. RK-HOQT uses a three-dimensional REDIM based on the one-dimensional HOQ solutions and RK-SWQT uses a two-dimensional REDIM based on the two-dimensional SWQ results. The performance of the two reduced kinetic computations is assessed by a combined comparison with the detailed kinetic results and experimental data, and following conclusions can be drawn:

1. Both reduced kinetic models show good prediction in SWQ processes. It is found that both reduced kinetics are not only able to reproduce the global quenching quantities, but also have a good prediction in the local flame structure. Looking at the local thermo-chemical states, it is found that major and minor species in regions both near and far from the wall can be predicted well with the reduced kinetics. Furthermore, from the analysis of the flame dynamics, a negative stretch is observed in the near-wall region for the DME-air mixture, similar to previous findings in [84] for CH_4-air mixtures. The capability of the reduced kinetics to capture both strain and stretch effects on the flame quenching characteristics is demonstrated by its good agreement with the reference results.

2. When comparing the two reduced kinetic computations, it is shown that RK-SWQT performs slightly better than RK-HOQT in the region very close to the wall. The major advantage of RK-HOQT is the relative simplicity in REDIM generation. However, due to the increased dimension of the REDIM, RK-HOQT requires almost twice the computational cost as RK-SWQT for the CFD simulation.

In summary, the reduced kinetics with the REDIM method in generalized coordinates accounting for differential diffusion enables SWQ phenomena to be accurately modeled at a reduced computational cost. The straightforward construction of the manifold and its coupling with the CFD solver in generalized coordinates are of significant relevance for numerical investigations of multi-dimensional near-wall combustion processes with manifold-based reduction methods.

8 Turbulent premixed CH_4-air side-wall quenching[5]

Previous chapters focused on laminar FWI. In this chapter, a turbulent SWQ flame in a fully developed channel flow is simulated using LES with three different flamelet manifolds: FGM [59], QFM [78], and QFM-EGR [111]. The heat losses to the wall are considered via different approaches in FGM and QFM, with the former based on flamelets with exhaust gas recirculation and the latter based on HOQ flamelets. Compared to QFM, QFM-EGR additionally accounts for the flame dilution with cooled combustion products, which relates to the mixing process caused by the flame-vortex interaction observed in both experiments [72] and simulations [111] of turbulent FWI, through an increase in the dimensions. To the best of the author's knowledge, it is the first time that both, QFM and QFM-EGR, are applied in a coupled LES of turbulent FWI, and compare the performance of FGM, QFM, and QFM-EGR following an *a-posteriori* approach. Moreover, a comprehensive comparison and assessment is conducted among FGM, QFM, and QFM-EGR, which helps to provide guidance for the choice of chemistry manifolds for the simulation of practical turbulent FWI processes.

The performance of FGM, QFM, and QFM-EGR are evaluated using the flame resolved simulation (FRS) performed by Steinhausen et al. [88] as reference. The main objective of this chapter is twofold: (1) to assess the predictive capabilities of the existing flamelet manifolds for FWI in the context of LES; (2) to evaluate the relevance and statistical importance of the FVI mechanism in turbulent FWI, based on comparison between QFM and QFM-EGR, with the latter taking into account the effects of burned gas recirculation.

8.1 Numerical implementation

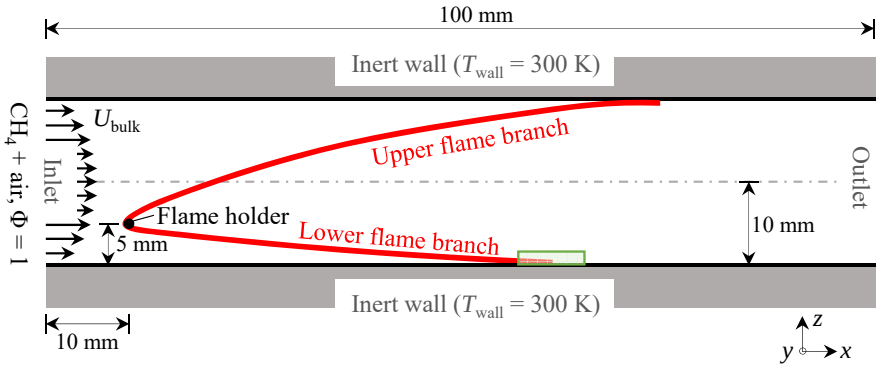

Figure 8.1: Schematic illustration of the configuration investigated. The x, y, and z coordinates are the streamwise, lateral, and wall-normal directions, respectively. The dimension in the lateral direction is 30 mm. The region of interest analyzed in Fig. 8.9 is denoted by the green rectangle.

The configuration has been studied by Steinhausen et al. [88, 111] with an FRS. A V-shaped premixed flame stabilized by a flame holder in a fully developed turbulent channel undergoes FWI at the channel

[5]This chapter is partly taken from the publication by Luo et al. [6], which was created during the work on this thesis. In Ref. [6], I was the main author of this part.

walls, as shown in Fig. 8.1. The coordinates are defined as follows: x, y, and z correspond to streamwise, lateral, and wall-normal directions, respectively.

8.1.1 Numerical description

All computations are performed with a reduced version of the CRECK mechanism [149], which was reduced ad hoc for FWI conditions using the approach described in [150] and consists of 24 species and 165 chemical reactions. The unity Lewis number assumption is adopted for the calculation of the molecular diffusion. The choice of the chemical mechanism and the transport model is consistent with the FRS studies [88, 111].

FGM and QFM tables are of the same size, which is 101 $\times$ 101 for $Y^*_{\mathrm{PV}} \times h^*$. The dimension of the QFM-EGR table is 150 $\times$ 201 $\times$ 101 for $Y^*_{\mathrm{PV}} \times Y^*_{\mathrm{PV2}} \times h^*$.

Within the framework of LES, the large scales of the turbulence are explicitly calculated, while the effects of the smaller ones are modeled through subgrid closure rules. To correctly capture the turbulence-chemistry interaction (TCI), the ATF approach mentioned in Section 3.3.1 is adopted. Therefore, Eqs. (2.52) and (2.53) are solved to obtain the flow field. In addition, governing equations for the progress variable (Eq. (3.30)) and enthalpy (Eq. (3.31)) are solved for FGM and QFM. For QFM-EGR, the second progress variable has to be transported as well, namely Eq. (3.32) is additionally solved.

8.1.2 Computational domain and boundary conditions

The inflow is a stoichiometric CH_4-air mixture at 300 K. The Reynolds number of the inert channel flow is $Re = (U_{\mathrm{bulk}} H)/\nu \approx 5540$, where U_{bulk} is the mean axial flow velocity (4.4 m/s), H the channel height (20 mm) and ν the kinematic viscosity of the inflow. Similarly to [87], the flame holder is modeled as a cylindrical region (r = 0.9 mm) filled with burned gas. It is placed at a distance of $H/4$ from the bottom wall. Both the upper and lower walls are assumed to be inert and have a fixed temperature that is equal to the inflow temperature, namely T_{wall} = 300 K.

An inert turbulent channel flow is simulated in a pre-processing step to provide proper inflow boundary conditions for the reactive case. For the inert case, the dimensions of the computational domain are $7H$, $1.5H$, and H in x, y, and z directions, respectively. A stretched structured grid is adopted, which is uniform in x and y directions and refined towards the wall in z direction. In the core flow, the non-dimensional grid resolution in x, y, and z directions is $\Delta x^+ = \Delta y^+ = \Delta z^+$ = 5.14, where the superscript $^+$ denotes non-dimensionalization with the viscous length scale. The finest grid spacing in the z direction is Δz^+ = 1. The total number of cells is 7.4 million. A no-slip boundary condition is applied to the channel walls, and a periodic boundary condition is used for lateral and streamwise boundaries. The inflow velocity field is used as the inflow boundary condition for the reactive case, and it is stored with a time interval of 17 μs.

Regarding the reactive case, the computational domain is similar to the inert case, except that the length is reduced from $7H$ to $5H$. With the same grid resolution as the inert case, the resulting total number of cells is 5.3 million. The boundary conditions employed are as follows: at the inlet, the inflow velocity field obtained from the inert case is spatially and temporally interpolated at every time step, which is about $\Delta t \approx$ 2.5 μs. At the outlet, a zero gradient boundary condition is applied for the velocity, progress variables, and enthalpy. At the channel walls, a no-slip boundary condition is employed for the velocity, a zero-gradient boundary condition for the progress variables, and a fixed value of 300 K for the temperature. In the lateral direction, periodic boundary conditions are adopted.

8.2 Results and discussion

In the following, the performances of FGM, QFM, and QFM-EGR are assessed by comparison with the FRS results from Steinhausen et al. [88, 111]. Firstly, profiles of mean flow field quantities are analyzed.

Secondly, probability density functions (PDFs) of CO are evaluated. Finally, the importance of FVI is studied based on cross-comparison of the simulation results.

The coordinates of the quenching point are defined as (x_Q, y_Q, z_Q). The axial position of the quenching point x_Q is determined by the maximum wall heat flux. For all simulations, the wall heat flux is evaluated over the horizontal plane $z = 50\ \mu m$. Therefore, the quenching point is defined as the position on the flame front ($T = 1500$ K) where $x = x_Q$. Based on the quenching point, a relative coordinate system is introduced. Within these coordinates, y and z remain unchanged and x_q denotes the coordinate parallel with the wall defined by $x_q = x - x_Q$.

8.2.1 Comparison of mean quantities

The major flame characteristics are assessed based on several mean flame quantities, which are obtained based on both time and space averaging of the instantaneous fields. Firstly, the instantaneous results are averaged over a sufficiently long time, i.e., more than 10 flow-through times, to ensure time independence. Afterwards, the time-averaged quantities are further averaged along the y direction. These are referred to as mean quantities in the following, as denoted by $< \cdot >$.

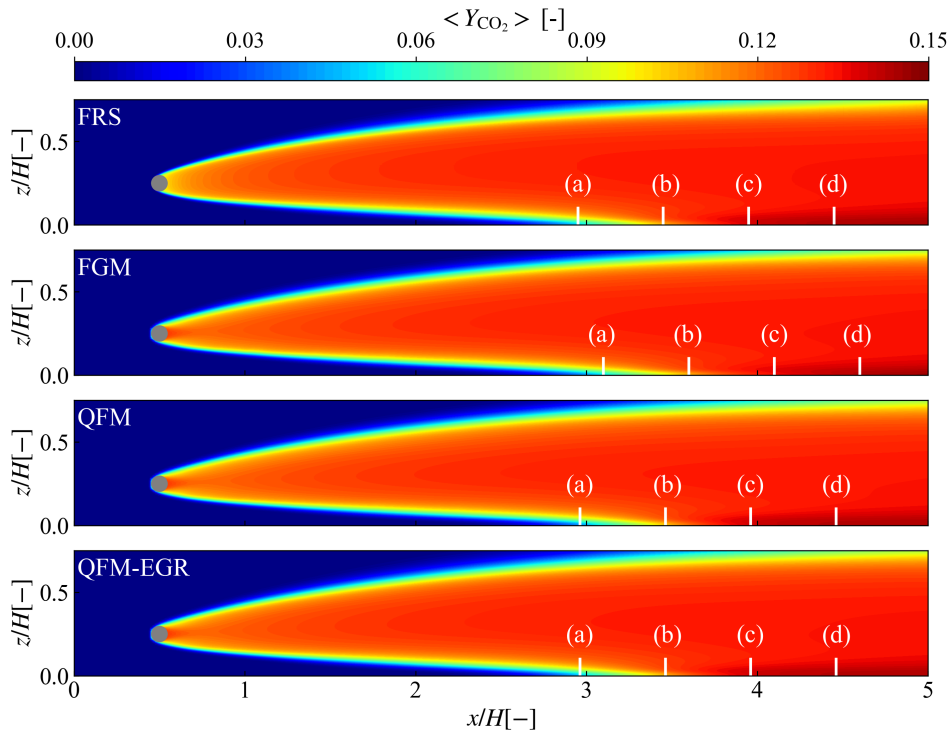

Figure 8.2: Contour of mean Y_{CO_2}, which is averaged both temporally and spatially in the lateral (y) direction. White lines denote positions where mean values of velocity and thermo-chemical quantities are extracted: (a) $x_q = -0.5H$, (b) $x_q = 0$, (c) $x_q = 0.5H$, (d) $x_q = H$. Here, (b) $x_q = 0$ corresponds to the axial position of the mean quenching point.

The mean CO_2 mass fraction is displayed in Fig. 8.2. It is observed that the overall flame appears similar comparing all the simulations. To enable a quantitative comparison between FRS, FGM, QFM, and QFM-EGR, the mean quenching points are first determined based on the profiles of the mean wall heat fluxes. As shown in Fig. 8.3, the general trend observed for all simulations is that there is no heat transfer to the wall from the inlet until $x/H = 2$, then the mean wall heat flux gradually rises to reach a peak where the

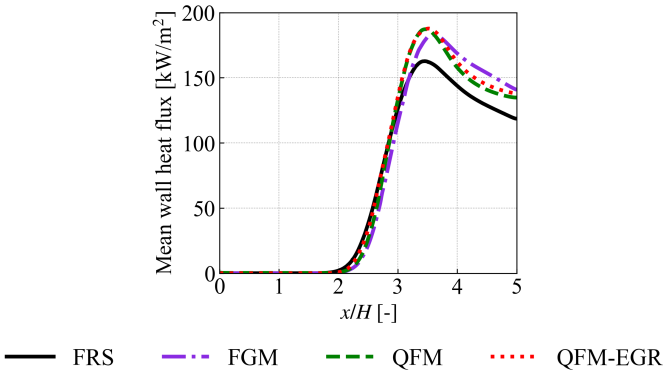

Figure 8.3: Distributions of the mean wall heat flux along the axial coordinate x. The reference FRS results are denoted by the black solid line. The violet, the green, and the red dashed lines correspond to FGM, QFM, and QFM-EGR results, respectively.

mean quenching point is defined, following which it decreases to a non-zero value until the outlet. Overall, FGM, QFM, and QFM-EGR show greater heat transfer to the wall than the FRS. FGM, QFM, and QFM-EGR give similar predictions of the peak value, at 183.0 kW/m^2, 187.2 kW/m^2, and 187.7 kW/m^2, respectively. However, they are all higher than the reference value 162.7 kW/m^2, and the overprediction remains in the downstream region. Regarding the position where the wall heat flux reaches a maximum, it is quite close when comparing different simulations, at x/H = 3.45, 3.6, 3.4625, 3.4625 for FRS, FGM, QFM, and QFM-EGR, respectively.

For a more detailed investigation, mean quantities of velocities, temperature, enthalpy, and progress variables are analyzed for four representative streamwise positions (white lines (a)-(d) in Fig. 8.2):

- (a) upstream of the quenching point ($x_q = -0.5H$)
- (b) at the quenching point ($x_q = 0$)
- (c) downstream of the quenching point ($x_q = 0.5H$)
- (d) close to the outlet ($x_q = H$).

Figure 8.4 shows the axial velocity u_x and the wall-normal velocity u_z plotted along the wall-normal lines. For each position, the axial velocity is zero at the wall, which fulfills the no-slip boundary condition, and increases monotonically with increasing wall distance. The gradient of the axial velocity reaches a maximum at the wall, and gradually decreases along the wall-normal direction. Different trends are observed for the gradient of the wall-normal velocity, which remains at a low level close to the wall. In addition, the variation in the wall-normal velocity is different for the four positions considered. For position (a), the wall-normal velocity is positive and increases with the wall distance. For position (b), the wall-normal velocity remains almost zero from the wall until z/H = 0.1. In contrast, a mainly negative wall-normal velocity is observed for positions (c) and (d), and the magnitude increases when moving away from the wall. These major characteristics are well captured by all manifolds. For both the axial and the wall-normal velocity, FGM, QFM, and QFM-EGR show good agreement with the reference data for all four axial positions considered.

Figure 8.5 presents the results for the first progress variable, Y_{CO_2}, enthalpy, and the temperature. All flamelet manifolds yield profiles for the progress variable and temperature that are comparable to the reference. Small discrepancies are found in enthalpy distributions. The results from QFM-EGR are closest to the FRS for all positions. Meanwhile, QFM shows a slight overprediction in the near-wall region at position (a), and FGM leads to overprediction for all positions considered. However, in summary, the results from the three flamelet manifolds do not show much difference.

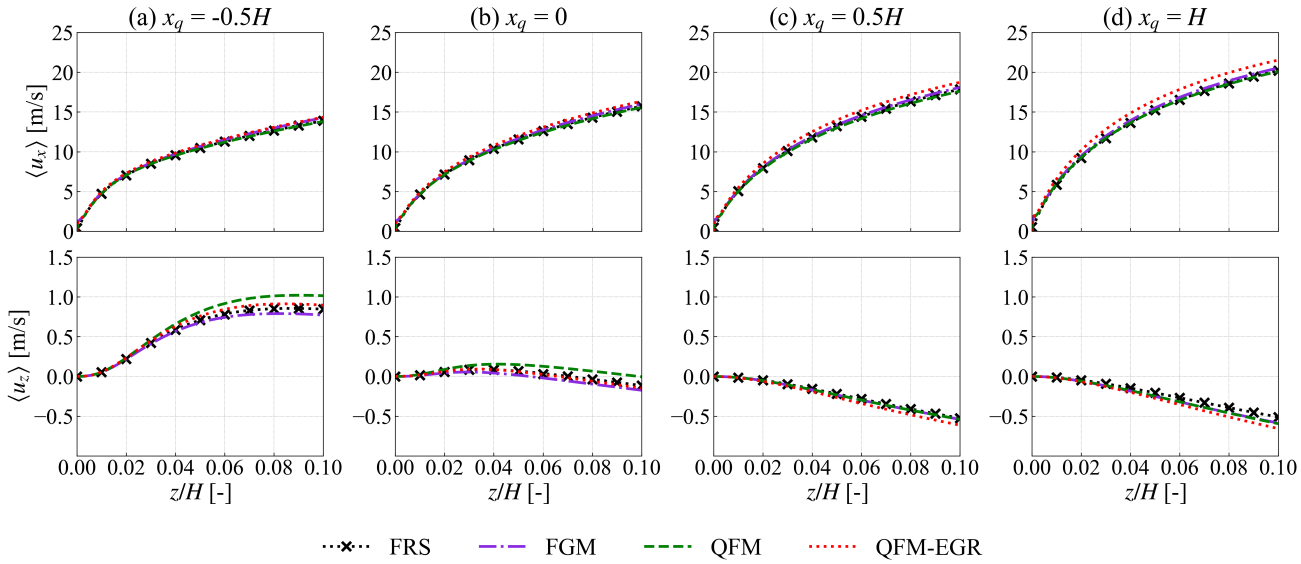

Figure 8.4: Distributions of the mean axial velocity (top) and wall-normal velocity (bottom) from the bottom wall to the height of 0.1H at different axial positions: (a) $x_q = -0.5H$, (b) $x_q = 0$, (c) $x_q = 0.5H$, (d) $x_q = H$. The reference FRS results are denoted by black dashed lines marked with cross symbols. The violet, the green, and the red dashed lines correspond to FGM, QFM, and QFM-EGR results, respectively.

To assess the capability of the flamelet manifolds to predict the pollutants and radicals, distributions of mean CO and OH for the same four positions shown in Fig. 8.2 are plotted in Fig. 8.6. Accurate predictions can still be observed for QFM and QFM-EGR, with QFM-EGR performing slightly better, which is similar to the findings for major species. In contrast, deviations from the reference results are shown for FGM, regarding both CO and OH. In the case of CO especially, even different variation trends are presented. For FRS, QFM, and QFM-EGR, the CO distribution does not change much near the wall, while FGM presents a notable decrease towards the wall. Consequently, the near-wall CO is significantly underpredicted by FGM, especially at positions (a) and (b), meaning that FGM is unable to reproduce the CO accumulation here. Even at position (d), which is close to the outlet, FGM still underestimates the CO at the wall.

Further, the CO mass fraction profiles in the streamwise direction for different wall distances are plotted in Fig. 8.7 to gain deeper insights into the CO prediction. The minimum wall distance considered in Fig. 8.7 corresponds to the unstretched laminar flame thickness δ calculated with Eq. (2.32). It is observed that CO is always underpredicted by FGM in the vicinity of the wall, e.g., position (a), which is consistent with previous studies [76]. With increasing wall distance, the deviations in CO prediction can still be found before the outlet, while the computed values at the outlet are close to reference results, such as positions (b), (c), and (d). Compared with FGM, results from QFM show evident improvement. This is similar to the findings in laminar SWQ cases [7, 78]. However, slight overprediction exists near the peak value. Compared to QFM, QFM-EGR provides an even better prediction, which shows excellent agreement with the FRS reference.

Based on the above discussions, it can be concluded that all three flamelet manifolds considered are capable of capturing the major global characteristics of the turbulent FWI. However, FGM shows significant deficiencies in the prediction of pollutants and radicals, similarly to the findings in laminar studies. Comparing QFM and QFM-EGR, the latter shows slight improvement in the prediction of the mean quantities. In the following chapter, results from these two approaches will be comprehensively compared.

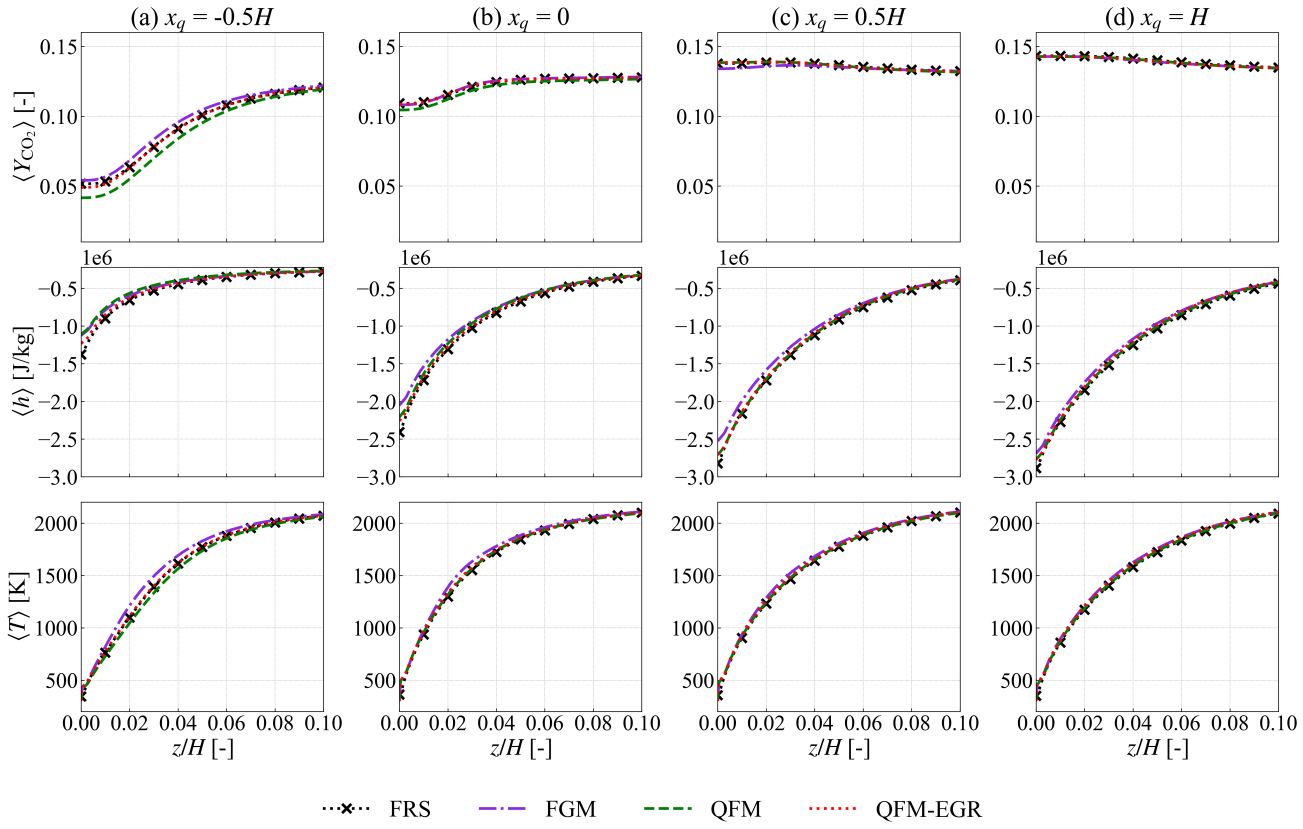

Figure 8.5: Distributions of mean progress variable (top), enthalpy h (middle) and temperature T (bottom) from the bottom wall to the height of 0.1H at different axial positions: (a) $x_q = -0.5H$, (b) $x_q = 0$, (c) $x_q = 0.5H$, (d) $x_q = H$. The FRS results are denoted by black dashed lines marked with cross symbols. The violet, the green, and the red dashed lines correspond to FGM, QFM, and QFM-EGR results, respectively.

8.2.2 Comparison of probability distribution functions

In addition to the mean quantities, the PDFs of the CO mass fraction are analyzed in this section, as shown in Fig. 8.8. The PDFs are extracted at different wall distances ($z = \delta,\ 2\delta,\ 3\delta$) for a given enthalpy interval ($h^* = 0.8 \pm 0.005,\ 0.6 \pm 0.005,\ 0.4 \pm 0.005$). Here, h^* denotes the normalized enthalpy $h^* = (h - h_{\min}) / (h_{\max} - h_{\min})$, with $h^* = 1$ corresponding to an undisturbed flame and $h^* = 0$ to a fully quenched state. The data are sampled from 10 time instants.

Unlike the observations regarding the mean quantities, which reveal only small differences between QFM and QFM-EGR, significant and non-negligible differences are found in the PDFs of CO, especially for positions very close to the wall. At the plane closest to the wall, i.e., $z = \delta$, the distribution of CO predicted by QFM-EGR agrees quite well with the FRS. The variation range of CO is almost the same when comparing QFM-EGR and FRS. However, the PDF of QFM is much narrower, and concentrates at higher CO values. This corresponds to the overprediction of the peak of the mean CO shown in Fig. 8.7. The deviation between QFM and QFM-EGR increases with increasing heat loss. For low enthalpy levels such as $h^* = 0.6$ and $h^* = 0.4$, a distinct peak can be observed in the PDF of QFM, while the PDF distribution is much wider in QFM-EGR and FRS. Moving further away from the wall to $z = 2\delta$, the discrepancies between QFM and QFM-EGR still exist, especially for $h^* = 0.6$. However, for high enthalpy losses, e.g., $h^* = 0.4$, the PDF of CO narrows, leading to a better agreement between QFM and QFM-EGR. This means that the enthalpy range

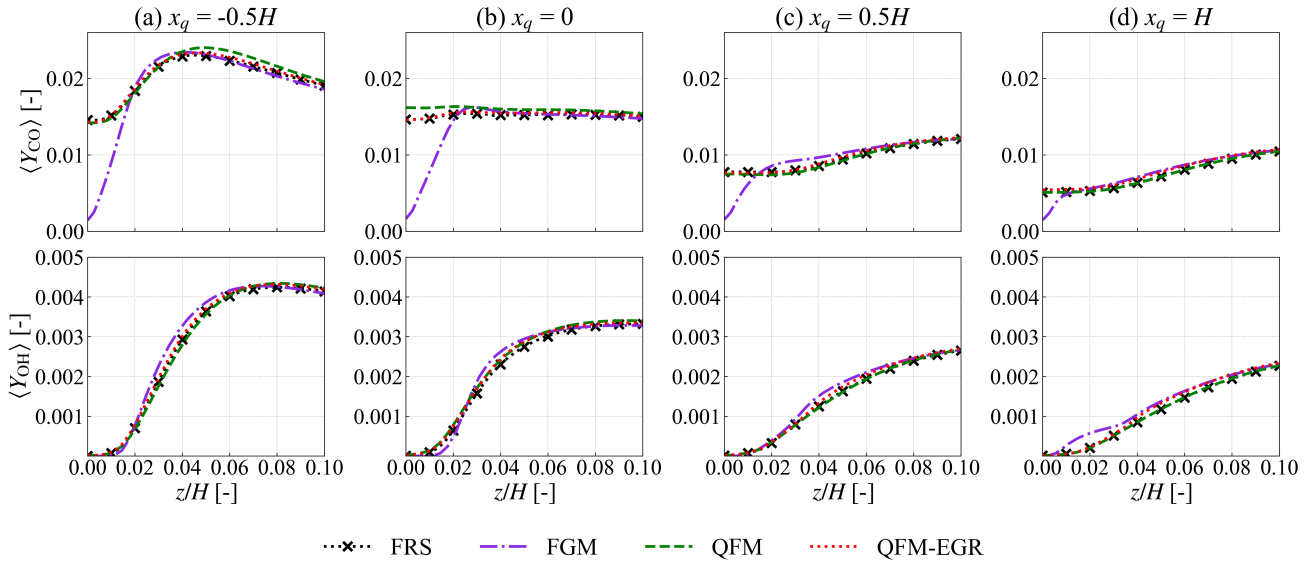

Figure 8.6: Distributions of mean mass fractions of CO (top) and OH (bottom) from the bottom wall to the height of $0.1H$ at different axial positions: (a) $x_q = -0.5H$, (b) $x_q = 0$, (c) $x_q = 0.5H$, (d) $x_q = H$. The reference FRS results are denoted by black dashed lines marked with cross symbols. The violet, the green, and the red dashed lines correspond to FGM, QFM, and QFM-EGR results, respectively.

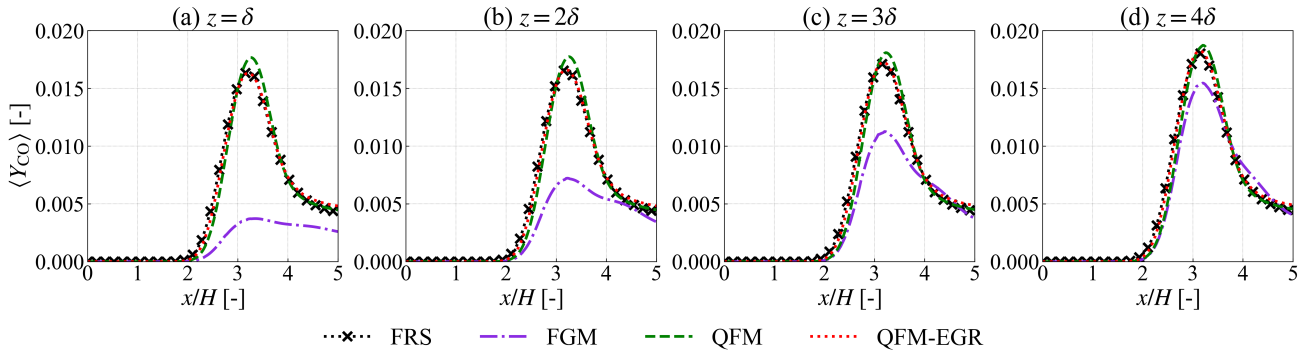

Figure 8.7: Distributions of mean CO mass fraction from the inlet to the outlet at different vertical positions: (a) $z = \delta$, (b) $z = 2\delta$, (c) $z = 3\delta$, (d) $z = 4\delta$. The reference FRS results are denoted by black dashed lines marked with cross symbols. The violet, the green, and the red dashed lines correspond to FGM, QFM, and QFM-EGR results, respectively.

where QFM and QFM-EGR differ significantly becomes smaller with increasing wall distance. At $z = 3\delta$, the PDFs from QFM and QFM-EGR are quite similar. Therefore, it is reasonable to deduce that there would be almost no differences between QFM and QFM-EGR in the case of positions far away from the wall. Based on the above findings, it can be concluded that the significant differences in the PDFs of CO between QFM and QFM-EGR mainly exist in the region near the flame tip, which is located close to the wall at an intermediate level of enthalpy loss. According to [72, 111], this is also the area where the FVI mechanism plays a role. Therefore, it is assumed that the characteristics of the PDFs shown above are related to this mechanism. To verify this, the FVI mechanism will be studied in the following sections.

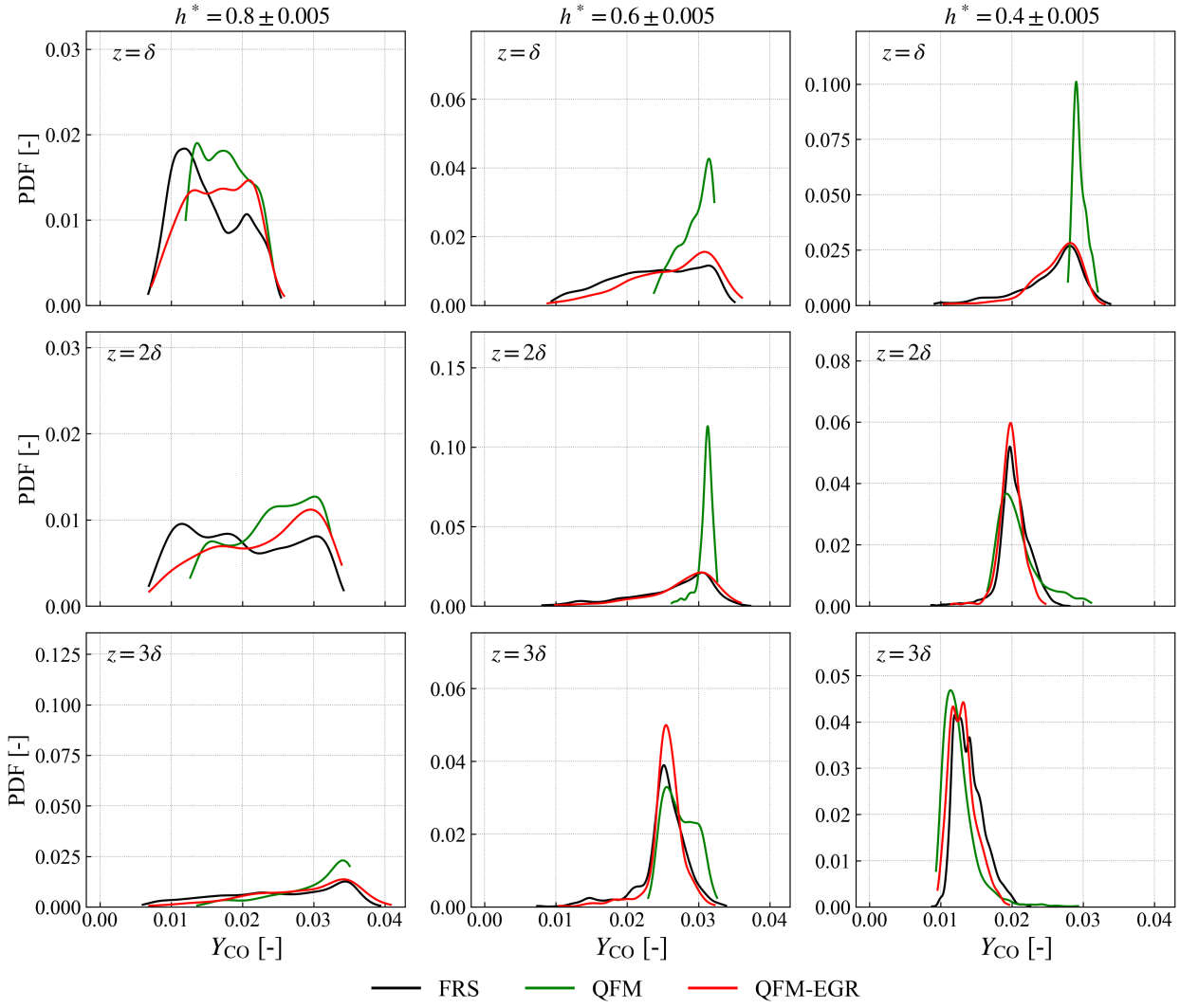

Figure 8.8: PDFs of CO conditioned on wall distance and enthalpy level.

8.2.3 Prediction of flame-vortex interaction

Firstly, the instantaneous thermo-chemical states that are directly influenced by the FVI mechanism are compared for FRS, QFM, and QFM-EGR, so that the importance of the mechanism can be illustrated. Afterwards, the flame dynamics of an FVI event using QFM-EGR is compared to the FRS based on a time-series analysis to further evaluate the performance of QFM-EGR in capturing the FVI mechanism.

Comparison of thermo-chemical states

To investigate the instantaneous local thermo-chemical states, quantities are evaluated over 10 time steps. For each time instant, data are collected from 31 independent slices parallel to the xz plane. For each slice, the region of interest covers a range of (x_Q - 50δ, x_Q + 50δ) in x direction and (0, z_Q + 10δ) in z direction, as denoted by the green rectangle in Fig. 8.1.

Figure 8.9 shows the thermo-chemical states in CO_2-CO space for the region of interest at different lateral positions and times instants, with results from FRS on the left, QFM in the middle, and QFM-EGR on the right. The data are colored by the normalized wall distance (z/δ). Additionally, the thermo-chemical

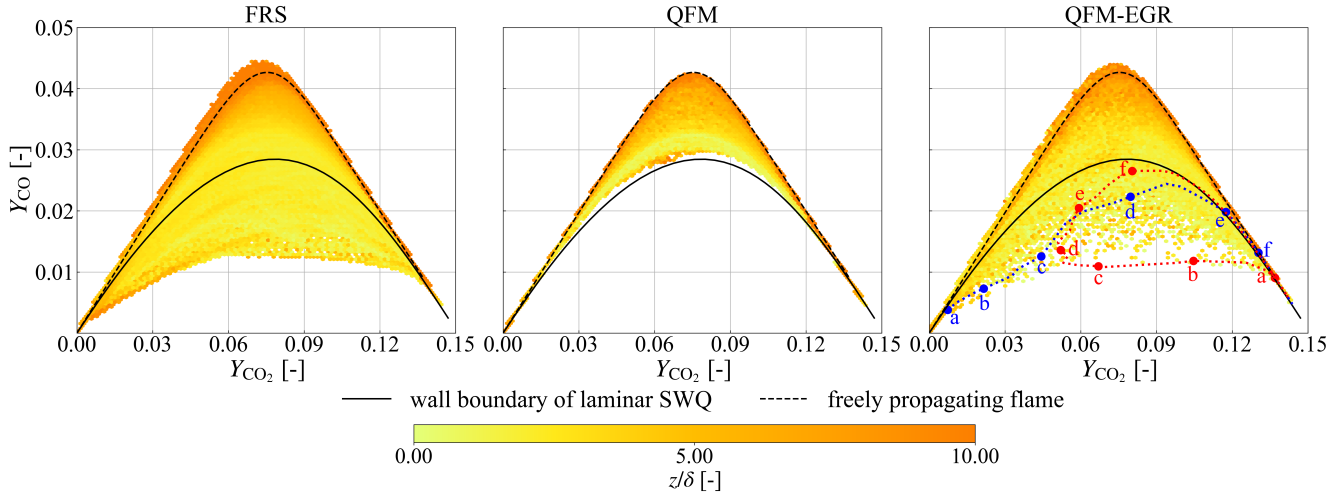

Figure 8.9: Thermo-chemical states near the quenching point for different lateral positions and time instants: (left) FRS, (middle) QFM, (right) QFM-EGR. The scatters are colored by the normalized wall distance z/δ. For reference, the states of a 1D freely propagating flame and on the wall boundary of a laminar SWQ are denoted by black dashed lines and black solid lines, respectively.

states on the wall boundary of a corresponding laminar SWQ are shown as black solid lines. Here, the laminar SWQ simulation is performed on a two-dimensional domain, similarly to [7]. The thermo-chemical states of a freely propagating flame are denoted by black dashed lines, where the composition and the temperature of the fresh gas remain the same as the current turbulent SWQ configuration. From the FRS results, it is observed that the state space spanned by the turbulent SWQ can not be fully covered by its laminar counterpart, as shown by the area surrounded by the black solid and dashed lines in Fig. 8.9. Especially for the region very close to the wall, i.e., the low-temperature region, the minimum value of the conditional CO mass fraction is significantly below the limit of the wall boundary of the laminar SWQ, namely $\min\left(Y_{\mathrm{CO}}|Y_{\mathrm{CO_2}}\right) < \left(Y_{\mathrm{CO}}|Y_{\mathrm{CO_2}}\right)_{\mathrm{laminar,z=0}}$. According to [72, 111], this is due to cooled burned products mixing with fresh gases in the vicinity of the quenching point. In the study by Steinhausen et al. [111], the QFM-EGR was introduced to incorporate the mixing effect in the thermo-chemical state and validated a priori. As a result, the LES with the QFM-EGR is able to correctly capture the local mixing processes caused by FVI in the turbulent flame, showing a large portion of the scatters below the limit of the wall boundary of the laminar SWQ. To further illustrate the mixing process, Lagrangian massless particles are placed in the flow field. Further, the trajectories of two Lagrangian particles in CO_2-CO space are additionally highlighted in the scatters of QFM-EGR in Fig. 8.9. The corresponding trajectories in the physical space projected onto a xz plane for 6 representative time instants are indicated in Fig. 8.10, where a slice of the flame in the lateral direction is shown for QFM-EGR. Note that the movement in the lateral direction is minor during these 1.375 ms in the case of both particles. A relative time t' is introduced and $t' = 0$ refers to the first time instant considered. Initially, the blue particle is located in the unburned part of the flame, while the red one is in the burned region. In the following, the particles move closer to each other until they almost collide at $t' = 0.55$ ms, consistent with the mixing process proposed in [72, 111]. Note that the movement of the red particle is against the mean flow direction due to the interaction with the turbulent vortices, which can be observed from its location relative to the flame tip. This is also reflected in the thermo-chemical states shown in Fig. 8.9, where both particles exhibit CO values far below the laminar limit that is also the lower bound of the QFM accessible range. After $t' = 0.825$ ms, the thermo-chemical states of both particles move in the direction of the burned gas. In contrast to the QFM-EGR, the QFM does

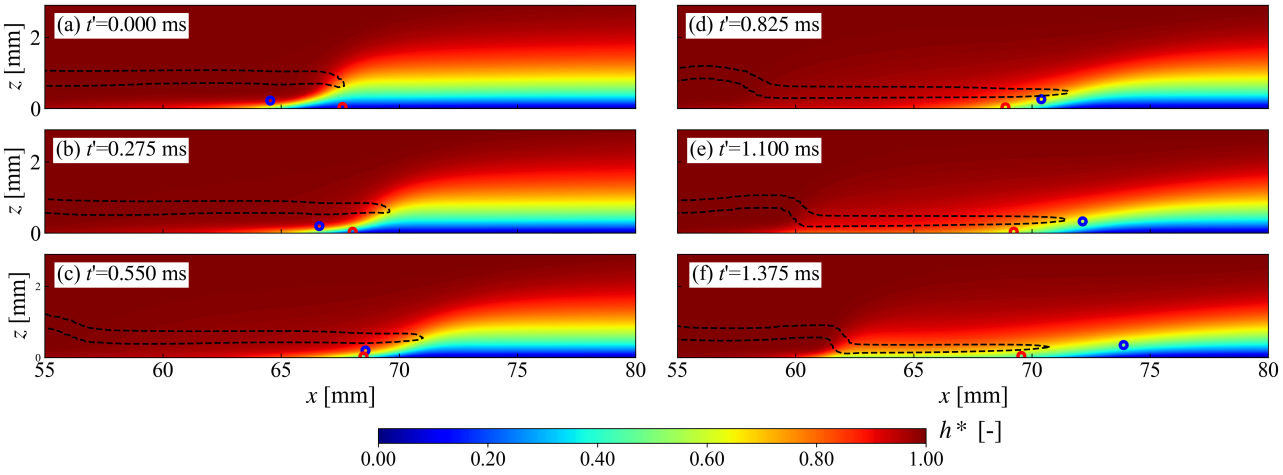

Figure 8.10: Time series of a slice in the lateral direction through the turbulent flame for QFM-EGR. Contours of the normalized enthalpy (h^*) are shown. Isocontours of heat release rate (0.1 $\times$ $\mathrm{HRR_{max}}$) are denoted by black dashed lines. The blue and red points correspond to the positions of the Lagrangian particles projected to a xz plane.

not incorporate the turbulent mixing process of burned and fresh gases in the manifold. As a result the state space spanned by the simulation is much narrower, restricted by the limit of CO for a given value of CO_2 from the laminar simulation. This limitation of the QFM also explains the narrow PDF distribution of QFM shown in Fig. 8.8, as well as the shift towards higher CO values. Considering the notable difference between QFM and QFM-EGR in Fig. 8.9, the importance of the FVI mechanism is verified. Therefore, in the prediction of transient thermo-chemical states in the near-wall region, the benefit of the QFM-EGR becomes evident.

Evolution of the FVI area

To further demonstrate the capability of QFM-EGR to correctly capture the FVI mechanism, the time evolution of the FVI area is investigated in this section. A time series for a slice of the flame in the lateral direction for both FRS and QFM-EGR is depicted in Fig. 8.11. Here, isolines of the heat release rate (0.1 $\times$ $\mathrm{HRR_{max}}$) are denoted by black dashed lines. The FVI region is surrounded by the white isocontour, which is identified based on $(Y_{\mathrm{CO}}|Y_{\mathrm{CO_2}}) < (Y_{\mathrm{CO}}|Y_{\mathrm{CO_2}})_{\mathrm{laminar,z=0}}$. The time series from the FRS is chosen to display the typical behavior found in the turbulent SWQ flame. For QFM-EGR, results from different time instants are used, so that they present similar flame movements to FRS. For each simulation, the time interval of the neighboring two slices stays at 0.55 ms. Similarly to the last section, the relative time t' is also introduced here; $t' = 0$ refers to the first time instant considered for each simulation in Fig. 8.11. Based on FRS results, it is observed that the flame is in an SWQ-like state at $t' = 0$, and FVI takes place in only a very small area. Afterwards, the angle between the flame and wall decreases and the FVI area begins to grow, e.g., at t' = 0.55 ms and 1.1 ms. As the flame-wall impact angle decreases further, the FVI region begins to shrink. Consequently, an HOQ-like event occurs at t' = 1.65 ms, with the FVI mechanism only playing a role in a very small region close to the wall. In the following, the quenching scenario transfers to SWQ-like again, as can be observed for t' = 2.2 ms. At this time instant, no FVI region is detected. For all time instants when FVI occurs, it is observed that the FVI area decreases with increasing wall distance, both in physical space and enthalpy space. This helps to explain the findings from Fig. 8.8 that significant differences between QFM and QFM-EGR are mainly seen in the vicinity of the wall, and the enthalpy range involved becomes smaller when moving further away from the wall. These major characteristics of the flame dynamics can also

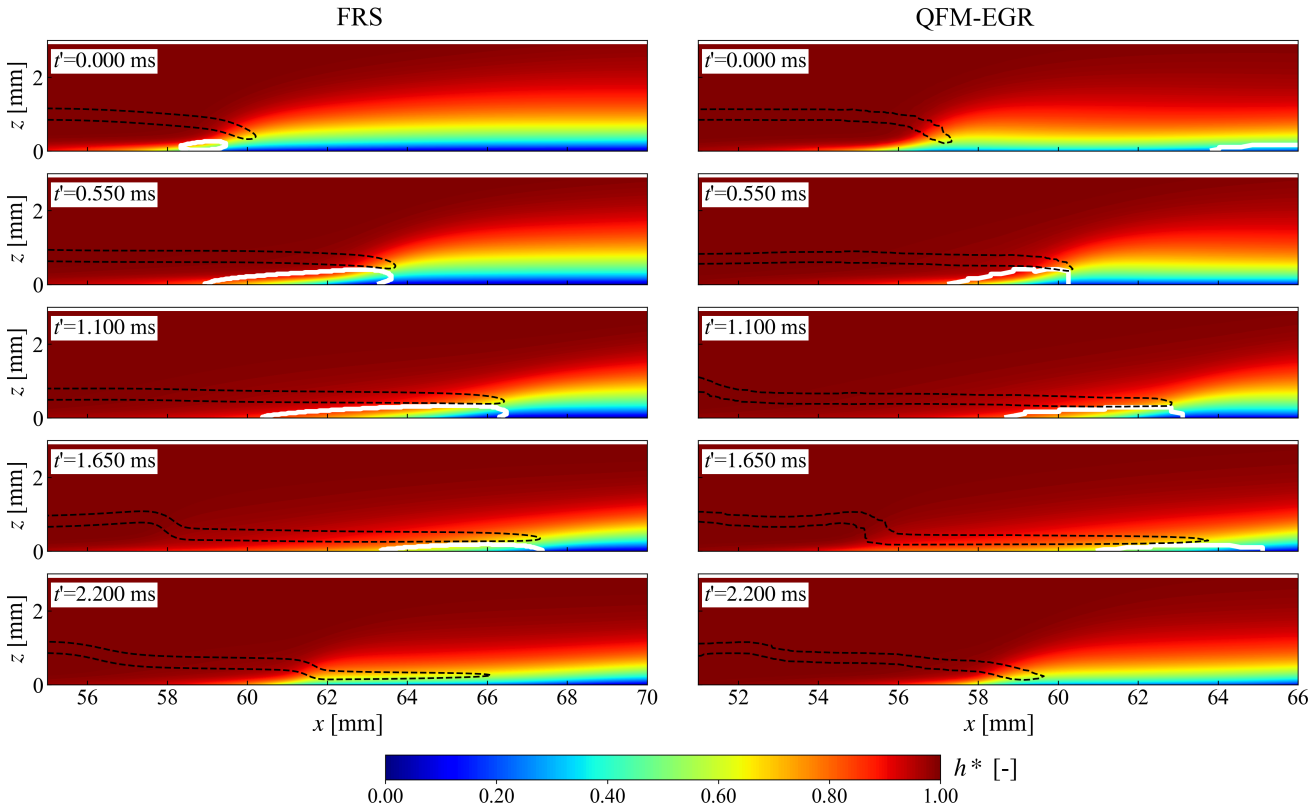

Figure 8.11: Time series of a slice in the lateral direction through the turbulent flame: (left) FRS, (right) QFM-EGR. Isocontours of heat release rate ($0.1 \times \mathrm{HRR}_{\mathrm{max}}$) are denoted by the black dashed lines. The white isocontour represents the area of FVI.

be found in QFM-EGR, as shown in the right-hand column of Fig. 8.11. According to [111], this repeated flame behavior is caused by the interaction between the flame and the vortex. Therefore, it indicates that QFM-EGR is able to correctly capture the dynamic evolution of the FVI mechanism.

8.3 Summary

In the current study, three flamelet manifolds with different levels of complexity are applied to the LES of a turbulent SWQ flame with the purpose of comprehensively evaluating their predictive capability in *a-posteriori* calculations. These help to provide guidance for practical applications. In FGM, heat losses are considered without the inclusion of species gradients in the enthalpy direction. This drawback is remedied by QFM, where heat losses to the wall are taken into account based on HOQ flamelets. QFM-EGR combines QFM with EGR to further consider the flame dilution, following our previous work [111]. Models are assessed with the results from an FRS as a reference, and the following conclusions can be drawn:

1. Regarding the mean quantities, all three flamelet manifolds are good at predicting general flame characteristics, such as the mean flow and temperature fields, as well as major species. However, the flamelet manifolds perform differently in the prediction of pollutants and radicals. FGM presents significant deviations from the reference results in the near-wall region. In contrast, results from QFM and QFM-EGR show great improvement, with QFM-EGR performing slightly better.

2. In the case of the PDFs of CO, significant differences are observed between QFM and QFM-EGR.

Compared to QFM, the distribution of CO covers a wider range in QFM-EGR, which shows better agreement with the reference.

3. Looking into the local thermo-chemical states, the scatter of QFM results is found to be restricted within the laminar counterpart, while QFM-EGR results span a much wider space, including a large portion of scatters below the limit of the wall boundary of the laminar SWQ. The results from QFM-EGR are more consistent with the FRS, indicating the importance of the FVI mechanism in the transient near-wall behavior. Moreover, the FVI mechanism is also illustrated in physical space with injected Lagrangian massless particles.

4. To further verify the capability of QFM-EGR to capture the FVI mechanism, the time evolution of the FVI is investigated. It is found that a flame dynamic similar to that shown in FRS also exists in QFM-EGR.

In conclusion, the FGM considering varying enthalpy levels, is the simplest manifold to build and accurately predicts general flame quantities, such as the flow field, temperature, and major species. However, it fails in the prediction of pollutants and radicals. For this purpose, the QFM shows an improved prediction accuracy at the cost of more complex manifold generation, while the manifold dimensions remain unchanged and the computational cost thus stays at a similar level. The QFM-EGR shows the overall best prediction accuracy by capturing the influence of FVI at the cost of an additional table dimension and thus increased computational cost and memory requirements. When these manifolds are applied in real combustors, the benefits and drawbacks of each model should be considered when choosing the manifold.

9 Laminar CH_4-H_2-air Bunsen flames[6]

Previous chapters focus on the studies of hydrocarbon fuels. As H_2 becomes a promising alternative fuel for decarbonization, investigation on the FWI of fuel blends with H_2 addition is also of great interest. As a starting point to develop flamelet models for H_2-enriched FWI, the FGM adopted in Chapter 8 is further developed in this chapter to consider special combustion characteristics of H_2, such as differential diffusion effects.

Accurately accounting for the differential diffusion effects is still challenging for models based on flamelet manifolds [96], mainly because the correct identification and accurate prediction of local mixing states are often non-trivial with only a few control variables. Nevertheless, previous studies by Vreman et al. [151] and de Swart et al. [144] show that at least two control variables are required for lean CH_4-H_2-air premixed flames to correctly predict how the mass burning rate will respond to stretch effects which are enhanced by differential diffusion. The approach proposed in [144] was later extended by Donini et al. [96], who applied a three-dimensional manifold parameterized with a progress variable, enthalpy and the Bilger mixture fraction to a non-adiabatic two-dimensional CH_4-air premixed slot flame. This work was developed further by Mukundakumar et al. [147] for a H_2-air premixed slot flame simulation. In their study, significant deviations still remained for important global flame characteristics such as the flame height and the heat release rate. The authors assumed non-unity, but constant Lewis numbers for all species and suggested an elaborate modeling approach to capture differential diffusion effects by transporting the control variables. In a slightly different approach, Schlup et al. [146] considered species diffusivities based on a mixture-averaged diffusion model in lean premixed H_2-air flames. Similarly to the work of Regele et al. [145], additional terms were included in the transport equation of the mixture fraction to describe differential diffusion effects. The closure was obtained by assuming a global one-step reaction which allowed the mixture fraction to be related to the progress variable transport. So far, this method has not been applied to hydrocarbon flames or hydrocarbon-H_2 fuel blends. Recently, a hybrid transported-tabulated chemistry method (HTTC) was proposed to reduce the size of the flamelet manifold [152–154], where major species instead of conventional control variables are transported. Using a mixture-averaged transport model, the tabulated chemistry method was validated against kerosene-air freely propagating flames [152] and a partially premixed methane-air flame [153, 154]. Adopting a similar approach, Böttler et al. [155] developed a method where major species and enthalpy are transported, and it has been successfully applied to predict the forced ignition and flame propagation in H_2-air mixtures. This method features a mixture-averaged diffusion model and employs the transported species to reconstruct the Bilger mixture fraction and the progress variable. Together with the enthalpy, these serve as control variables for the flamelet manifold.

In this chapter, extending from Chapter 8 and the work from Böttler et al. [155], a new flamelet modeling approach is proposed to cover multiple complex physics. Besides the differential diffusion effects considered in [155], other important factors related to a realistic flame configuration are additionally taken into account, specifically: heat loss, mixing-induced mixture fraction variation, and fuel blends instead of pure fuel. To the best of the authors' knowledge, the inclusion of all the aforementioned aspects within a flamelet model has not been reported in the literature. Besides, it is the first combined experimental-numerical study, including simulations with coupled flamelet modeling, to consider these physics simultaneously.

[6]This chapter is partly taken from the publication by Luo et al. [5], which was created during the work on this thesis. In Ref. [5], I was the main author of this part.

For validation, a Bunsen burner configuration is chosen, which offers sufficient complexity for model assessment. Furthermore, the combination of differential diffusion, heat losses, and mixing with an inert coflow poses additional challenges to the tabulation approach. The main objective of this chapter is threefold: Firstly, to accurately capture the differential diffusion effects in H_2-enriched flames using a flamelet-based reduced chemistry approach. Secondly, to account for the heat losses to the burner rim in the flamelet model, which are important for flame stabilization. Thirdly, to characterize the mixing between the main flow and an inert coflow.

9.1 Numerical implementation

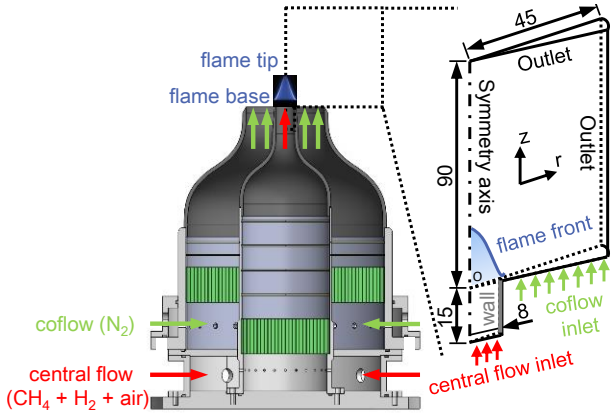

Figure 9.1: Experimental and numerical configuration of the Bunsen burner. Numbers indicate length in millimeters.

In the present study, the experiment has been carried out on a laminar jet burner which is formed by two concentric tubes, as shown on the left in Fig. 9.1. The central main flow is a lean fuel-air mixture with an equivalence ratio of 0.8, where the fuel consists of 60 vol.% CH_4 and 40 vol.% H_2. Such a fuel blend is of practical relevance for the current energy transition period [144]. The main flow tube is a contoured nozzle ending in a straight segment with an inner diameter of 16 mm and a wall thickness of 0.5 mm, which generates a velocity block profile at the exit. N_2 is chosen as the coflow, in order to prevent a secondary diffusion flame while stabilizing the premixed Bunsen flame. The inner diameter of the coflow tube is 67 mm. More details can be found in [156].

9.1.1 Numerical description

The species diffusion velocity is evaluated with a mixture-averaged model [100]. All calculations are conducted with a skeletal mechanism optimized for atmospheric CH_4-air combustion with 25 species and 176 reactions. The mechanism was obtained starting from the POLIMI kinetic mechanism using the reduction methodology described in [157] with the laminar burning velocity as the target property.

Detailed kinetics

To complement the experimental data for the burner configuration above, a detailed kinetic (DK) simulation is performed, solving the governing equations for the mass, momentum, species mass fractions, and enthalpy. Namely, Eqs. (2.1), (2.2), (7.1) and (7.2) are solved. The diffusion coefficients are calculated using Cantera [158].

Reduced kinetics

In this study, a flamelet-based approach is developed from the standard FGM to include differential diffusion effects, heat loss to the burner rim, and the mixing between the main flow and coflow.

To incorporate differential diffusion and non-adiabatic effects, a few major species and the enthalpy are transported instead of the control variables of the tabulated manifold. Then, the reaction progress variable and an approximate Bilger mixture fraction are evaluated from the transported species [155]. There are several merits adopting this approach: firstly, cross-diffusion can be treated quite straightforwardly; secondly, advanced transport models, e.g., the mixture-averaged model, can be directly applied. Furthermore, this approach allows capturing differential diffusion effects not only in the thin reaction zone, but also in regions distant from it, where species gradients are not necessarily aligned and the representation of mixing by one-dimensional flamelets could introduce modeling errors [159].

In order to describe the mixing between the main flow and the inert N_2 coflow in the Bunsen flame configuration, two different approaches are considered, with one relying on a 3D flamelet manifold and the other on a flamelet 4D manifold, which are abbreviated as FGM-3D and FGM-4D, respectively.

Generation of flamelet database

The flamelet manifolds are generated from a set of one-dimensional adiabatic, freely propagating premixed CH_4-H_2-air flamelets, which are stored in a look-up table parameterized by the control variables. The reaction progress variable (Y_{PV}) is chosen as $Y_{\mathrm{PV}} = Y_{\mathrm{CO_2}} + Y_{\mathrm{H_2O}}$. To account for the non-negligible differential diffusion and non-adiabatic effects, the enthalpy (h) and the Bilger mixture fraction (Z_{Bilger}) are also included as control variables. Here, $Z_{\mathrm{Bilger}} = (\beta - \beta_0)/(\beta_1 - \beta_0)$, where β is the sum of the weighted C, H, O elemental mass fraction, and β_1 and β_0 are constants for the fuel and oxidizer streams, respectively (details are given in [160]). In this work, Z_{Bilger} is approximated based on six species (CH_4, H_2, O_2, CO, H_2O and CO_2), which are the species to be transported in the CFD solver. To ensure the consistency between the pre-computed flamelets and the coupled simulation, the exact same definitions of the control variables are used. Thus, the flamelet manifolds are also parameterized with the progress variable, Bilger mixture fraction (both of which are based on the transported major species [155]) and enthalpy. Considering variations of h and Z_{Bilger}, laminar flamelets are solved for different unburned gas temperatures (varying from 300 K to 550 K) and equivalence ratios (ranging from 0.65 to 1). The states between pure air and the lean limit are obtained through interpolation, as well as the states between the rich limit and pure fuel. Since the temperature of the burner is lower than that of the flame, heat losses should be taken into consideration as well, which also requires the tabulation of multiple enthalpy levels. Flamelets with Exhaust Gas Recirculation (EGR) [59] are computed to expand the range of h to include heat losses, as described in Section 3.1.2. It was shown in [59] that the final results show little dependence on the choice of the enthalpy-reduction method for tabulation, indicating that other methods, such as one-dimensional burner stabilized flames [161], can also be used here. Furthermore, to account for the inert N_2 coflow, two different flamelet manifolds (a 3D flamelet manifold and a 4D flamelet manifold) are developed and utilized, which are presented next.

3D flamelet manifold

Due to the fact that the coflow is inert, and its mixing with the main flow mainly occurs outside the reaction zone, mixing is assumed to only result in a linear combination of species and enthalpy, while the chemical reactions remain unaffected. Therefore, the mixing between the main flow and the coflow can be incorporated in the CFD solver through algebraic operations only, without the cost of adding additional dimensions to the flamelet manifold. Consequently, in the FGM-3D approach, only thermo-chemical states

of the main flow are stored in the flamelet manifold, which can be parameterized by the reaction progress variable, enthalpy, and the Bilger mixture fraction, as mentioned before.

To access the 3D flamelet manifold, the coflow components have to be subtracted from the mixture first. In order to distinguish between variables related to the mixture directly obtained from the governing equations, on one hand, and variables related to the main flow, on the other hand, the latter are denoted by $\hat{\cdot}$ symbols. Thus, the “modified" set of control variables ($\hat{Y}_{\mathrm{PV}}$, $\hat{h}$ and $\hat{Z}_{\mathrm{Bilger}}$) can be calculated through

$$\hat{Y}_{\mathrm{PV}} = \frac{Y_{\mathrm{PV}}}{1 - Z_{\mathrm{mix}}} \,, \tag{9.1}$$

$$\hat{h} = \frac{h - Z_{\mathrm{mix}}\, h_{\mathrm{coflow}}}{1 - Z_{\mathrm{mix}}} \,, \tag{9.2}$$

$$\hat{Z}_{\mathrm{Bilger}} = \frac{\frac{\beta}{1-Z_{\mathrm{mix}}} - \beta_0}{\beta_1 - \beta_0} \,, \tag{9.3}$$

where Z_{mix} indicates the mass fraction of the coflow in the mixture, whose value varies from 0 to 1, representing the state from pure fresh gas to pure coflow, respectively. Here, it is evaluated through $Z_{\mathrm{mix}} = (Y_{\mathrm{N_2}} - \hat{Y}_{\mathrm{N_2}})/(1 - \hat{Y}_{\mathrm{N_2}})$, where $Y_{\mathrm{N_2}}$ denotes the mass fraction of N_2 obtained from its transport equation, $\hat{Y}_{\mathrm{N_2}}$ the N_2 mass fraction in the main flow (1 being the N_2 mass fraction in the coflow). As N_2 is the most abundant species with close to unity Lewis number diffusivity, the reference $\hat{Y}_{\mathrm{N_2}}$ is assumed to represent a lower bound that is readily determined from the fresh gas at the main flow inlet. The actual composition (Y_k) is obtained by a linear combination of species from the flamelet manifold ($Y_{k,\mathrm{FLT}}$) with the coflow ($Y_{k,\mathrm{coflow}}$), which can be expressed as

$$Y_k = Y_{k,\mathrm{FLT}}\,(1 - Z_{\mathrm{mix}}) + Y_{k,\mathrm{coflow}}\, Z_{\mathrm{mix}} \,. \tag{9.4}$$

Based on h and Y_k, the temperature, the density and all diffusion coefficients are obtained using Cantera. Specifically, h and Y_k of the mixture are used as inputs for Cantera to obtain all other thermo-chemical quantities.

For efficient access to the multi-dimensional flamelet manifold, some control variables are normalized. For the 3D manifold, values of $\hat{Y}_{\mathrm{PV}}$ and $\hat{h}$ are normalized, while $\hat{Z}_{\mathrm{Bilger}}$ keeps its original value since it already varies between 0 and 1. Therefore, the thermo-chemical states of the main flow stored in the manifolds can be expressed as: $\hat{\psi} = \hat{\psi}(\hat{Y}^*_{\mathrm{PV}}, \hat{h}^*, \hat{Z}_{\mathrm{Bilger}})$, where * denotes the corresponding non-dimensional form. The non-dimensional forms can be calculated as

$$\hat{Y}^*_{\mathrm{PV}} = \frac{\hat{Y}_{\mathrm{PV}} - \hat{Y}_{\mathrm{PV_{min}}}(\hat{h}^*, \hat{Z}_{\mathrm{Bilger}})}{\hat{Y}_{\mathrm{PV_{max}}}(\hat{h}^*, \hat{Z}_{\mathrm{Bilger}}) - \hat{Y}_{\mathrm{PV_{min}}}(\hat{h}^*, \hat{Z}_{\mathrm{Bilger}})} \,, \tag{9.5}$$

$$\hat{h}^* = \frac{\hat{h} - \hat{h}_{\mathrm{min}}(\hat{Y}^*_{\mathrm{PV}}, \hat{Z}_{\mathrm{Bilger}})}{\hat{h}_{\mathrm{max}}(\hat{Y}^*_{\mathrm{PV}}, \hat{Z}_{\mathrm{Bilger}}) - \hat{h}_{\mathrm{min}}(\hat{Y}^*_{\mathrm{PV}}, \hat{Z}_{\mathrm{Bilger}})} \,. \tag{9.6}$$

It should be noted that the maximum and minimum values used for normalization are not known in advance, therefore an iterative look-up approach is used to access the flamelet manifold. The dimensions of the 3D flamelet manifold are 101 × 20 × 22 for $\hat{Y}^*_{\mathrm{PV}} \times \hat{h}^* \times \hat{Z}_{\mathrm{Bilger}}$, respectively.

4D flamelet manifold

Contrary to the “linear mixing" assumption utilized for the FGM-3D method, the FGM-4D method is proposed, where an additional coflow stream is considered in the one-dimensional flamelet calculations. The blending of the coflow component is specified by the parameter Z_{mix}, which is directly calculated as

$Z_{\mathrm{mix}} = Y_{\mathrm{coflow}}/(Y_{\mathrm{coflow}} + Y_{\mathrm{main}})$. Here, Y_{coflow} is the mass fraction of the coflow and Y_{main} is the mass fraction of the original fresh fuel-air mixture. In this method, the 4D flamelet manifold can be parameterized by the reaction progress variable, enthalpy, the Bilger mixture fraction, and the parameter to characterize the mixing, which is chosen as the N_2 mass fraction here.

To access the 4D flamelet manifold, control variables (Y_{PV}, h, Z_{Bilger} and $Y_{\mathrm{N_2}}$) are directly constructed based on the variables from the transport equations, and the tabulated results directly correspond to the actual thermo-chemical variables.

Compared to the 3D flamelet manifold, one additional control variable $Y_{\mathrm{N_2}}$ is normalized. Its maximum/minimum values used for normalization are tabulated as $Y_{\mathrm{N_{2max/min}}} = Y_{\mathrm{N_{2max/min}}}(Y^*_{\mathrm{PV}}, h^*, Z_{\mathrm{Bilger}})$. By this means, the thermo-chemical states stored in the 4D flamelet manifold are expressed as $\psi = \psi(Y^*_{\mathrm{PV}}, h^*, Z_{\mathrm{Bilger}}, Y^*_{\mathrm{N_2}})$. The maximum and the minimum values used for normalization of each control variable are also stored in the manifold and depend on the other control variables, which entails an iterative look-up procedure. Hence, the 4D flamelet manifold is accessed in a similar manner as the 3D manifold. The dimensions of the 4D manifold are $101 \times 20 \times 22 \times 10$ for $Y^*_{\mathrm{PV}} \times h^* \times Z_{\mathrm{Bilger}} \times Y^*_{\mathrm{N_2}}$, respectively.

Governing equations for reduced kinetics

In the coupled simulations with the FGM approach, the mass and momentum transport equations are solved to obtain the flow field. Further, transport equations for major species and enthalpy are solved. Specifically, the species (CH_4, H_2, O_2, CO, H_2O, CO_2) are transported and used to determine the control variables Y_{PV} and Z_{Bilger}. N_2 is additionally transported to describe the mixing between the reacting main flow and the outer coflow. For FGM-4D, $Y_{\mathrm{N_2}}$ serves as a control variable. For FGM-3D, it is used to approximate the value of Z_{mix}, i.e., the mass fraction of the coflow.

For the transported species, the governing equation Eq. (7.1) is solved. During the runtime, coefficients such as the density ρ, the diffusion coefficient D_k, and the mean molecular weight $\overline{M}$ are directly retrieved from the flamelet manifold in FGM-4D, while they are obtained from Cantera in FGM-3D. This is additionally implemented because the linear assumption adopted for the enthalpy and species in FGM-3D is not applicable to these coefficients. Consequently, the "mixed" enthalpy and species are used in Cantera to obtain these quantities. In both FGM approaches, source terms are obtained from the flamelet manifold. For species such as CH_4, H_2, O_2, H_2O, CO_2, $\dot{\omega}_k$ is taken directly from the flamelet manifold, while the production rate $\dot{\omega}^+$ and consumption rate $\dot{\omega}^-$ taken from the flamelet manifold are used to calculate $\dot{\omega}$ for CO. Details can be found in Section 3.4.

For the total enthalpy, the transport equation Eq. (7.2) is solved, where the total enthalpy of the k-th species h_k is obtained from the flamelet manifold for FGM-4D and calculated using Cantera for FGM-3D.

9.1.2 Computational domain and boundary conditions

Due to the axial symmetry of the flame configuration, a two-dimensional, wedge-shaped computational domain is adopted in the numerical simulations, defined by an axial (z) and a radial (r) coordinate, as shown on the right in Fig. 9.1. In the simulations, a non-uniform grid is applied, where the finest grid resolution in the flame region is smaller than 40 μm, resulting in 0.45 million cells in total.

At the inlet of the main flow, a constant velocity of 1.4 m/s is used for the core of the flow, determined from the experimental PIV data, and a parabolic profile is applied for the region near the tube wall, which is evaluated based on the measured mass flow. The wall temperature is measured as 450 K and 310 K at the burner rim and 22 mm below it (not included in the computational domain), respectively. A linear temperature profile is prescribed along the wall, resulting in a 350 K wall temperature at the main flow inlet. The temperature of the injected fresh gas is set to be the same as the tube wall at the same height (350 K) to mimic the conditions in the experiment. On the tube wall, a no-slip boundary condition is applied for the

velocity and a zero-gradient boundary condition for the species. At the coflow inlet, a constant velocity of 0.5 m/s is applied, with a constant temperature of 300 K, in accordance with the experiment. The upper and right-hand boundaries are treated as open outlets.

9.2 Results and discussion

9.2.1 Comparison between detailed kinetics and experimental results

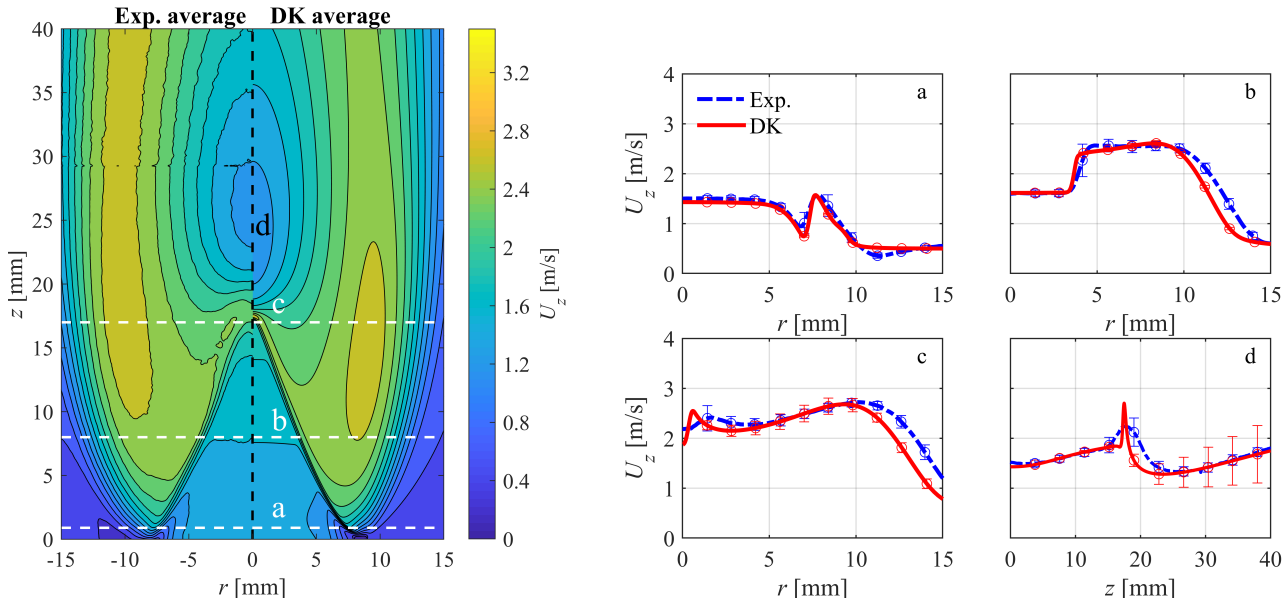

Figure 9.2: Comparison of the velocity between the experiment and the detailed kinetic (DK) simulation: (a) averaged axial velocity contour, (b) axial velocity profiles at three axial positions and along the centerline marked in (a).

In this section, the CFD solver for the simulation with detailed kinetics (DK) and the boundary conditions set in the simulation are first validated using the experimental data. Besides providing flow field information, the PIV data recorded in the experiments also allows comparing the overall flame shape. Note that fluctuations close to the flame tip exist in both the experiment and simulation, and the DK results are averaged over 11 flow-through times, based on the flame height. In Fig. 9.2a, contours of the averaged axial velocity are shown. It is observed that the overall flame shape and the flow field appear similar when comparing the experiment and DK results. For a quantitative comparison, averaged axial velocity profiles are sampled at three axial locations (white dashed lines in Fig. 9.2a) z = 1 mm (a), z = 8 mm (b) and z = 17 mm (c), and along the centerline (d, black dashed line in Fig. 9.2a). The three axial locations are chosen to represent regions near the flame base, flame flank and flame tip, respectively. The averaged axial velocity profiles are shown in Fig. 9.2b together with error bars, evaluated from the experiment (blue dashed lines) and the DK simulation (red solid lines). Upstream of the flame tip, the velocity fluctuations are small (small error bars) in both the experiment and the simulation, which corresponds to a relatively stable flame. Downstream of the flame tip, the DK simulation exhibits slightly larger fluctuation than the experiment. For the time-averaged velocity, variations in the experimental results are well captured by the DK simulation both in terms of the trend and the magnitude at all positions. Moreover, the good agreement

of the peak value position on the centerline between the experiment and the DK simulation indicates that the flame tip position is well reproduced by the simulation. Small discrepancies between the simulation and the experimental results can be attributed to the inlet velocity profile prescribed in the simulation, which is not known exactly inside the nozzle, and the linear temperature profile along the tube wall, which can exhibit moderate differences from the actual operating conditions in the experiment. The good agreement between the numerical and experimental results allows the DK results to be used as a reference for analyses of the thermo-chemical states in the following sections.

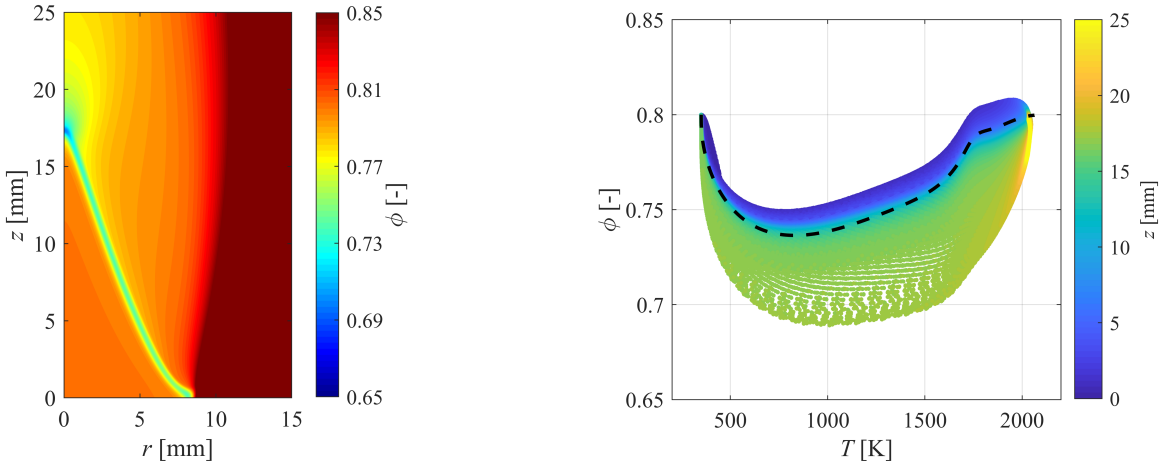

(a) (b)

Figure 9.3: Distribution of the local equivalence ratio: (a) in the physical space, (b) in the temperature space for the main flow region in (a). The black dashed line in (b) corresponds to the 1D freely propagating flame with the same fresh gas composition and temperature at the inlet of the Bunsen burner.

Moreover, analyses on DK results are performed to reveal the importance of differential diffusion effects for the fuel blends considered in the present study. Figure 9.3a shows the distribution of local equivalence ratio ϕ in the physical space. It is observed that ϕ is not constant, but varies in the flame zone, which is caused by the differential diffusion effects. The distribution of ϕ over temperature for the main flow region (filtered by $Y_{N_2} < 0.74$) is shown in Fig. 9.3b, and the wide spreading of the scatters further verify the prominent differential diffusion effects involved in the current configuration. The strong differential diffusion effects have also been reported for 60% vol. CH_4 + 40 %vol. H_2 flames with an equivalence ratio of 0.7 [144].

9.2.2 Comparison between detailed kinetics and FGM results

In this section, the performance of the two FGM approaches (FGM-4D and FGM-3D) is assessed by comparison to the DK results. All results from the DK and FGM simulations are averaged over the same time period, which is long enough to ensure time independence. Before the *a-posteriori* analysis performed in this section to validate the coupling between the manifolds and the CFD solver, an *a-priori* analysis has already been conducted to verify the applicability of the 3D and the 4D flamelet manifolds, as shown in Appendix E.

Figure 9.4 shows the temperature field for both the DK and FGM simulations. Overall, the flame shape is well reproduced by both fully coupled simulations. The flame tip position and the flame height are predicted well by the FGM simulations, showing discrepancies of less than 5% for the flame height. The FGM-4D simulation, in particular, yields only an approximately 1% difference, which is a smaller discrepancy

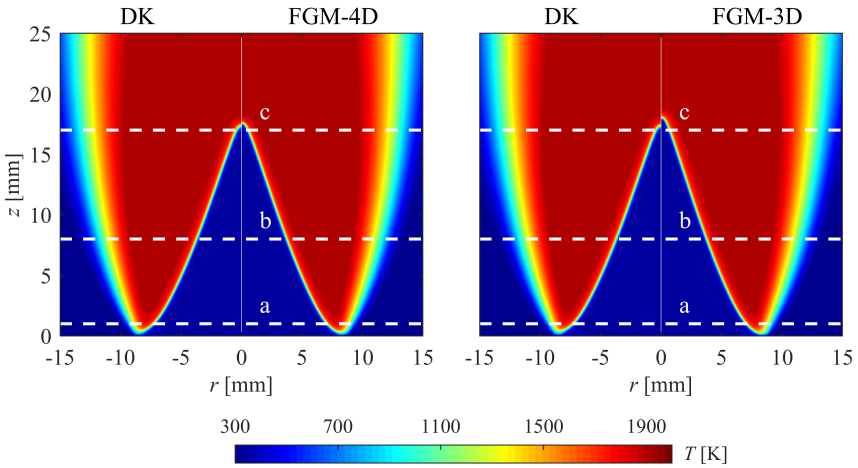

Figure 9.4: Comparison of the temperature field between the DK simulation and the FGM simulations: (left) DK and FGM-4D, (right) DK and FGM-3D.

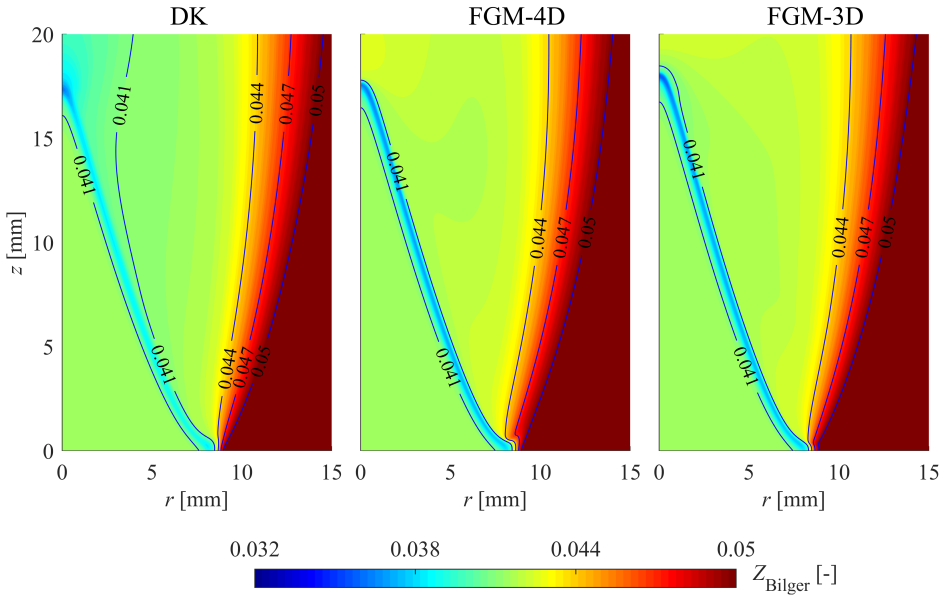

Figure 9.5: Bilger mixture fraction distribution from the DK simulation and the FGM simulations: (left) DK, (middle) FGM-4D, (right) FGM-3D.

compared to similar previous works using tabulated chemistry approaches [96]. It is worth mentioning that the flame tip poses a challenge for capturing differential diffusion effects in this flame configuration due to strong curvature effects and a variation in the local equivalence ratio (see Fig. 9.3a). The good agreement between the FGM solutions and DK reference results underlines that differential diffusion is well captured in both FGM approaches, although slightly better agreement is found for FGM-4D. The contour of Z_{Bilger} evaluated from all species is plotted in Fig. 9.5. Along the flame front, its value decreases monotonically downstream, with the minimum value appearing at the flame tip. This is caused by both the depletion and the diffusion of the fuel. The good prediction obtained by both FGM simulations along the flame front further verifies their capability to capture the differential diffusion effects. Figure 9.6 presents the distribution of HRR. The highest HRR appears at the flame base. Moving downstream along the flame front, less fuel is available, and the chemical reactions become weaker, until eventually only a small heat release is observed at the flame tip. This trend is well captured by both FGM approaches. However, it is observed that

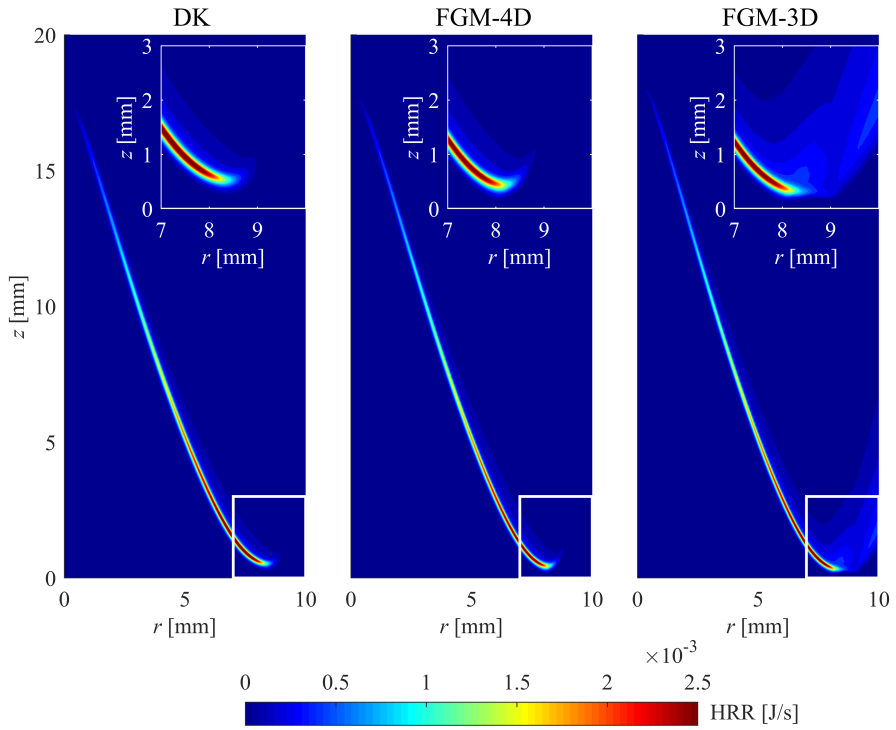

Figure 9.6: Heat release rate distribution from the DK simulation and the FGM simulations: (left) DK, (middle) FGM-4D, (right) FGM-3D. The insets show a zoom in the mixing layer region.

FGM-4D performs better than FGM-3D in the mixing layer region, highlighted by the zoomed region shown in the secondary plots of Fig. 9.6.

Next, quantitative comparisons between the DK simulation and the FGM simulations are conducted. Figure 9.7 shows the profiles of the CO_2, H_2, CO, OH mass fractions and HRR at three different axial locations $z = 1$ mm (a), $z = 8$ mm (b) and $z = 17$ mm (c), marked as white dashed lines in Fig. 9.4. Generally, good agreement is observed between the DK simulation and both FGM approaches, with FGM-4D being slightly more accurate than FGM-3D. At the flame base (a), FGM-4D is able to capture the profiles of all species and HRR accurately, indicating that the thermo-chemical state in the vicinity of the burner rim is well reproduced. At the flame flank (b), results from FGM-4D almost overlap with DK results, which entails good predictions for both flame position and the flame structure. Minor deviations are found at the flame tip (c), which is due to the small shift in the flame tip position mentioned above. When inspecting the results from FGM-3D, it is found that this method performs almost as well as FGM-4D in the inner part of the flame. However, examining the mixing layer between the main flow and the coflow, the results from FGM-3D show deviations from the DK simulation. The differences can be clearly observed in the profiles of OH and HRR at all three positions. In both results from DK and FGM-4D, the mass fraction of OH decreases more quickly in the mixing layer than in FGM-3D. Furthermore, the HRR is non-zero in the mixing layer for FGM-3D, which differs from DK and FGM-4D.

9.3 Summary

A Flamelet-Generated Manifold (FGM) approach considering differential diffusion, heat losses, and mixing between main flow and inert coflow is developed and applied to a non-adiabatic CH_4-H_2-air Bunsen flame. In contrast to most flamelet approaches, where transport equations are directly solved for the progress

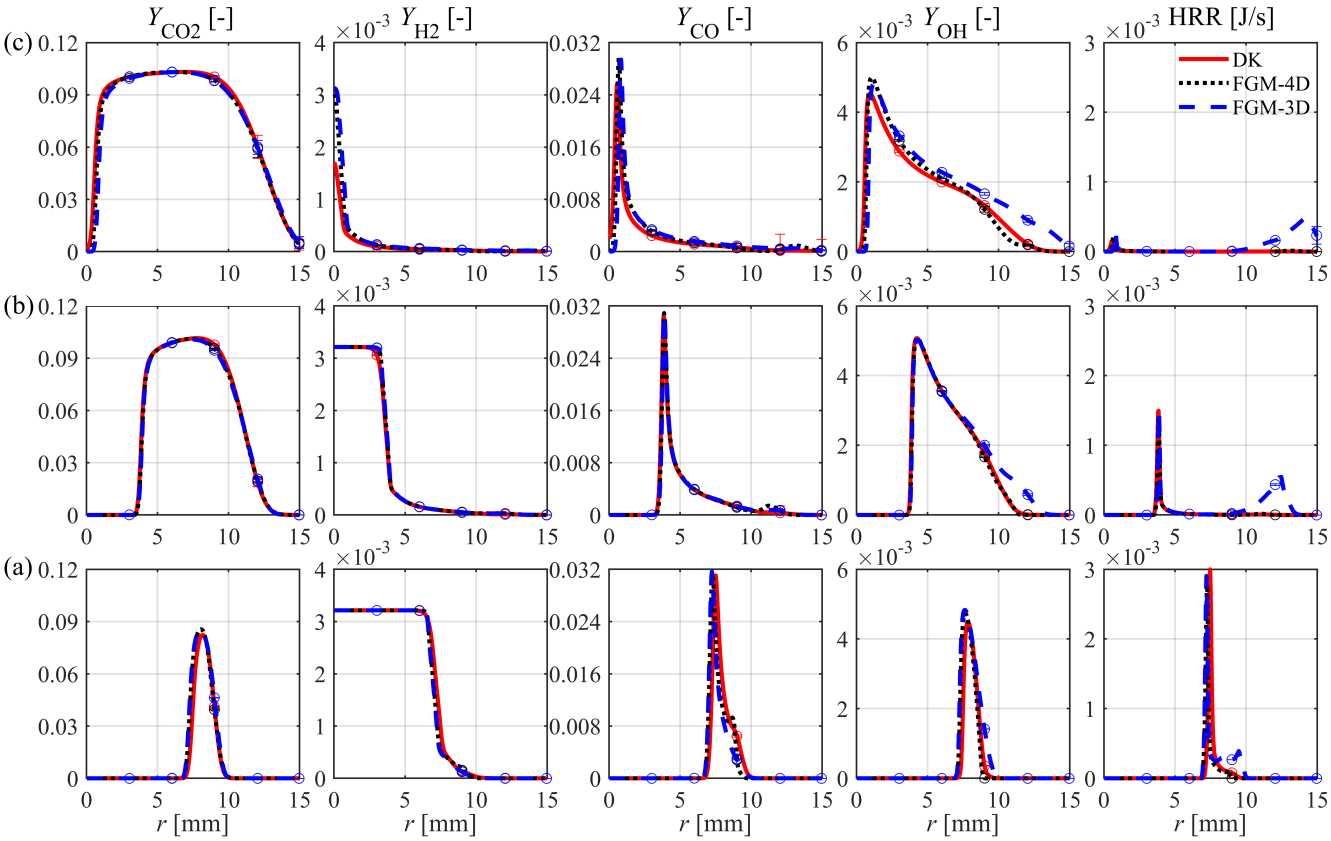

Figure 9.7: A-posteriori analysis: profiles of mass fractions of CO_2, H_2, CO, OH, and heat release rate (HRR) for several positions marked in Fig. 9.4 obtained from DK, FGM-4D, and FGM-3D simulations.

variable and mixture fraction, several major species are transported utilizing a mixture-averaged model and are then used to reconstruct a reaction progress variable and the Bilger mixture fraction. The latter quantities are used together with enthalpy, which is also transported, to access the tabulated manifold. Heat losses are taken into account by including lower enthalpy levels in the manifold through EGR. The mixing between the main flow and the N_2 coflow is considered using two different approaches: the FGM-3D model, which is based on a “linear mixing" assumption, and the FGM-4D model, which relaxes this assumption, but requires Y_{N_2} as an additional manifold dimension. Results from both FGM approaches show good qualitative and quantitative agreement with the detailed chemistry computation, which has been validated against experimental data. Comparing the two FGM approaches, it is found that both show accurate predictions in the flame zone, and only in the mixing layer, FGM-4D shows superior performance compared to FGM-3D. Both approaches recover local and global flame features, such as the flame shape, the flame tip position, and distributions of Z_{Bilger}, heat release rate, and species, underlining the fidelity of the overall modeling approach. It leverages accurate modeling of mixing processes by transporting additional scalars, i.e., a limited set of major species, while keeping the dimension of the manifold (thereby memory requirements) comparable to previous approaches.

10 Summary and outlook

This dissertation focuses on numerical analysis and model development for near-wall combustion. The main achievement of the work lies in the development of manifold-based reduced models, and the evaluation and application in various configurations (1D, 2D, and 3D) with different quenching scenarios (HOQ and SWQ). Complex physics involved in near-wall combustion, such as heat loss and differential diffusion, are accounted for in the newly developed models. The suitability of the models is validated by comparison with experimental data and the results from fully resolved simulations, for both laminar and turbulent flow conditions.

Firstly, the laminar HOQ process is simulated with detailed chemistry and transport to analyze the strain rate effects. It is revealed that the normalized quenching distance and the strain rate are negatively correlated, while the normalized wall heat flux is positively related to the strain rate. In addition, it is observed that not only the formation of major species such as CO_2, but also the formation and consumption of pollutants like CO in the near-wall region are influenced by the strain rate. For both global quenching quantities and the near-wall microstructure, the impact of the strain decreases with increasing wall temperature. Moreover, the strain rate prevents the enhancement of differential diffusion in the quenching layer by reducing the residence time of the reactive flow in the near-wall region. The mass fraction of H_2 is identified as a suitable parameter to characterize the strain rate effects within the flamelet tabulation.

Next, reduced model equations in generalized coordinates are implemented and applied in laminar SWQ processes. Specifically, in conjunction with the REDIM method, an *on the fly* technique is proposed to reduce the dependence on the accurate *a-priori* identification of the system, and two different models are introduced to take into account the differential diffusion effects. Applying the *on the fly* technique to the SWQ of a laminar premixed CH_4-air flame, convergent results can be obtained after only one iteration even if the initial REDIM is generated based on a very rough gradient estimation. For the prediction of species including OH radical, the maximum deviations from the detailed kinetics are below 4%, verifying the accuracy of the developed approach. For the SWQ of a laminar premixed lean DME-air flame, the pronounced differential diffusion is considered with both a 2D REDIM based on the gradient estimation from the SWQ solution and a 3D REDIM based on the solution from a HOQ process. Both manifolds show good prediction in not only the global quenching quantities, but also the local flame structure and the flame dynamics, with the 2D REDIM performing slightly better in the vicinity of the wall. This attributes to the more accurate gradient estimation used for the generation of the 2D REDIM.

Finally, reduced kinetic models based on the flamelet concept are extended to the framework of LES, where the ATF approach is adopted to describe the turbulence-chemistry interaction. The fully coupled model is applied to a turbulent SWQ process, and three flamelet manifolds with increasing complexity, namely FGM, QFM, and QFM-EGR, are evaluated by comparison with a flame-resolved simulation. In addition, the FGM model is further extended and applied to a laminar H_2-enriched Bunsen flame, focusing on the coupling effects of strong differential diffusion, heat losses, and mixing. For the turbulent SWQ, it is found that the mean profiles of the velocities, temperature, and major species can be accurately captured by all manifolds. However, FGM shows significant deficiencies in the prediction of pollutants and radicals. Although QFM gives improved prediction in mean CO profiles, large discrepancies from the reference exist in the transient statistics near the quenching point. This is due to the fact that the influence of the flame-vortex interaction is not included, and this drawback is remedied by QFM-EGR, which shows good agreement

with the flame-resolved simulation in both mean and instantaneous quantities. For the laminar Bunsen flame, two different approaches (FGM-3D, FGM-4D) are proposed, with the difference in the inclusion of the mixing process. Based on the comparison with the detailed kinetic results validated by experimental data, it is found that both approaches can accurately capture the major characteristics of the flame zone, while FGM-4D shows better performance in the prediction in the mixing layer. This is because the "linear mixing" assumption in FGM-3D is relaxed in FGM-4D.

Based on the outcome of this work, subsequent investigations might focus on the following points.

1. Investigate the Bunsen flame with increasing H_2 addition
   In order to obtain more comprehensive knowledge about the combustion characteristics of fuel blends with H_2. The investigation on CH_4-H_2-air Bunsen flame in Chapter 9 can be extended to fuel blends with higher H_2 percentages. With increasing H_2 addition, it is possible that flame instabilities occur, and polyhedral structures might be observed. In this case, three-dimensional simulations are required to correctly resolve the flame structure.

2. Investigate the FWI of different fuel types
   NH_3 is also a promising alternative fuel, however it is featured with low flammability, high NO_x emission, and low radiation intensity, which need to be further analyzed. Different from the hydrocarbon fuels already studied in this thesis, more attention should be put on the formation of NO_x instead of CO. Regarding the development of the manifold-based reduced models, accurate prediction of the pollutant NO_x should be an important aspect to be considered.

3. Investigate the FWI including surface chemistry effects
   For real conditions in engines, the wall temperature usually keeps at a high level. Therefore, surface chemistry needs to be taken into consideration. A reactive wall can be a catalyst that influences the adsorption and recombination of the radicals. As a result, the chemical kinetics of the gas phase may also be affected due to the change in the radical balance. For the development of the manifold-based reduced models, the mass conservation of the radicals should be considered in the manifold generation.

4. Investigate the turbulent FWI with increasing Reynolds number
   The study of the turbulent SWQ flame in a fully developed channel flow in Chapter 8 can be extended to higher Reynolds numbers that are relevant to the practical operating conditions for combustors. In this case, large variations of the velocity may happen within short distances near the wall, and the local flow velocity may exceed the laminar flame speed. Therefore, different flame dynamics and pollutant emission characteristics may be observed.

5. Investigate the FWI for more complex configurations
   The application of the manifolds adopted in this thesis can be extended to other configurations: (1) The experimental SWQ burners can be simulated with the flamelet manifolds. The turbulent lean DME-air SWQ flame investigated by Zentgraf et al. [72] can be an ideal case for atmospheric conditions. For this case, a key factor is to consider the interactions among the turbulence, differential diffusion, and strong heat losses in the flamelet manifolds. For high-pressure conditions that are closer to the real engines, the turbulent lean CH_4-air flames investigated by Johe et al. [73, 162] can be good choices. For this case, the major challenge is to take into account the pressure influences when generating the manifolds. (2) Other techniques used in the practical devices can be studied. For example, the effusion cooling [163] and permeable walls similar to [39–41, 164].

Bibliography

[1] Y. Luo, C. Strassacker, X. Wen, Z. Sun, U. Maas, and C. Hasse. Strain rate effects on head-on quenching of laminar premixed methane-air flames. *Flow, Turbulence and Combustion* 106 (2021), 631–647.

[2] Y. Luo, C. Strassacker, C. Hasse, and U. Maas. Simulation of side-wall quenching of laminar premixed flames with manifold-based reduced kinetic models implemented in generalised coordinates. *Combustion Theory and Modelling* 25 (2021), 669–694.

[3] Y. Luo, C. Strassacker, U. Maas, and C. Hasse. Model reduction on the fly: Simultaneous identification and application of reduced kinetics for the example of flame-wall interactions. *Proceedings of the Combustion Institute* (2022). DOI: https://doi.org/10.1016/j.proci.2022.07.227.

[4] Y. Luo, C. Strassacker, F. Ferraro, F. Zentgraf, A. Dreizler, U. Maas, and C. Hasse. A manifold-based reduction method for side-wall quenching considering differential diffusion effects and its application to a laminar lean dimethyl ether flame. *International Journal of Heat and Fluid Flow* 97 (2022), 109042.

[5] Y. Luo, F. Ferraro, A. Breicher, H. Böttler, A. Dreizler, D. Geyer, C. Hasse, and A. Scholtissek. A novel flamelet manifold parametrization approach for lean CH_4–H_2-air flames. *International Journal of Hydrogen Energy* 48 (2023), 407–421.

[6] Y. Luo, M. Steinhausen, D. Kaddar, C. Hasse, and F. Ferraro. Assessment of flamelet manifolds for turbulent flame-wall interactions in Large-Eddy Simulations. *submitted to Combustion and Flame* (2023).

[7] M. Steinhausen, Y. Luo, S. Popp, C. Strassacker, T. Zirwes, H. Kosaka, F. Zentgraf, U. Maas, A. Sadiki, A. Dreizler, et al. Numerical investigation of local heat-release rates and thermo-chemical states in side-wall quenching of laminar methane and dimethyl ether flames. *Flow, Turbulence and Combustion* 106 (2021), 681–700.

[8] A. Stagni, Y. Luo, M. Steinhausen, A. Dreizler, and C. Hasse. Chemistry effects in the wall quenching of laminar premixed DME flames. *Combustion and Flame* 232 (2021), 111529.

[9] J. Bissantz, J. Karpowski, M. Steinhausen, Y. Luo, F. Ferraro, A. Scholtissek, C. Hasse, and L. Vervisch. Application of dense neural networks for manifold-based modeling of flame-wall interactions. *Applications in Energy and Combustion Science* 13 (2023), 100113.

[10] BP. *Energy Outlook 2022*. 2022.

[11] A. Dreizler and B. Böhm. Advanced laser diagnostics for an improved understanding of premixed flame-wall interactions. *Proceedings of the Combustion Institute* 35 (2015), 37–64.

[12] I. Chterev and I. Boxx. Effect of hydrogen enrichment on the dynamics of a lean technically premixed elevated pressure flame. *Combustion and Flame* 225 (2021), 149–159.

[13] S. Vosen, R. Greif, and C. Westbrook. Unsteady heat transfer during laminar flame quenching. *Symposium (International) on Combustion* 20 (1985), 75–83.

[14] B. Saggau. Temperature profile measurements at head-on quenched flame fronts in confined CH_4/air and CH_3OH/air mixtures. *Symposium (International) on Combustion* 20 (1985), 1291–1297.

[15] O. Ezekoye, R. Greif, and R. Sawyer. Increased surface temperature effects on wall heat transfer during unsteady flame quenching. *Symposium (International) on Combustion* 24 (1992), 1465–1472.

[16] M. Bellenoue, T. Kageyama, S. Labuda, and J. Sotton. Direct measurement of laminar flame quenching distance in a closed vessel. *Experimental Thermal and Fluid Science* 27 (2003), 323–331.

[17] J. Sotton, B. Boust, S. Labuda, and M. Bellenoue. Head-on quenching of transient laminar flame: Heat flux and quenching distance measurements. *Combustion Science and Technology* 177 (2005), 1305–1322.

[18] B. Boust, J. Sotton, S. Labuda, and M. Bellenoue. A thermal formulation for single-wall quenching of transient laminar flames. *Combustion and Flame* 149 (2007), 286–294.

[19] F. Foucher, S. Burnel, C. Mounaım-Rousselle, M. Boukhalfa, B. Renou, and M. Trinite. Flame wall interaction: Effect of stretch. *Experimental Thermal and Fluid Science* 27 (2003), 431–437.

[20] M. Mann, C. Jainski, M. Euler, B. Böhm, and A. Dreizler. Transient flame–wall interactions: Experimental analysis using spectroscopic temperature and CO concentration measurements. *Combustion and Flame* 161 (2014), 2371–2386.

[21] A. Bohlin, M. Mann, B. D. Patterson, A. Dreizler, and C. J. Kliewer. Development of two-beam femtosecond/picosecond one-dimensional rotational coherent anti-Stokes Raman spectroscopy: Time-resolved probing of flame wall interactions. *Proceedings of the Combustion Institute* 35 (2015), 3723–3730.

[22] M. Rißmann, C. Jainski, M. Mann, and A. Dreizler. Flame-flow interaction in premixed turbulent flames during transient head-on quenching. *Flow, Turbulence and Combustion* 98 (2017), 1025–1038.

[23] W. Hocks, N. Peters, and G. Adomeit. Flame quenching in front of a cold wall under two-step kinetics. *Combustion and Flame* 41 (1981), 157–170.

[24] C. K. Westbrook, A. A. Adamczyk, and G. A. Lavoie. A numerical study of laminar flame wall quenching. *Combustion and Flame* 40 (1981), 81–99.

[25] I. S. Wichman and G. Bruneaux. Head-on quenching of a premixed flame by a cold wall. *Combustion and Flame* 103 (1995), 296–310.

[26] O. Ezekoye. Heat transfer consequences of condensation during premixed flame quenching. *Combustion and Flame* 112 (1998), 266–269.

[27] F. Dabireau, B. Cuenot, O. Vermorel, and T. Poinsot. Interaction of flames of H_2 + O_2 with inert walls. *Combustion and Flame* 135 (2003), 123–133.

[28] C. Hasse, M. Bollig, N. Peters, and H. Dwyer. Quenching of laminar iso-octane flames at cold walls. *Combustion and Flame* 122 (2000), 117–129.

[29] M. Chauvy, B. Delhom, J. Reveillon, and F.-X. Demoulin. Flame/wall interactions: Laminar study of unburnt HC formation. *Flow, Turbulence and Combustion* 84 (2010), 369–396.

[30] B. Jiang, R. L. Gordon, and M. Talei. Head-on quenching of laminar premixed methane flames diluted with hot combustion products. *Proceedings of the Combustion Institute* 37 (2019), 5095–5103.

[31] C. Straßacker, V. Bykov, and U. Maas. REDIM reduced modeling of quenching at a cold inert wall with detailed transport and different mechanisms. 26th International Colloquium on the Dynamics of Explosions and Reactive Systems. ICDERS 2017 (Boston, MA, USA, July 30–Aug. 16, 2017).

[32] C. Strassacker, V. Bykov, and U. Maas. Parametrization and projection strategies for manifold based reduced kinetic models. *Proceedings of the Combustion Institute* 37 (2019), 763–770.

[33] C. Strassacker, V. Bykov, and U. Maas. REDIM reduced modeling of flame quenching at a cold wall – The influence of detailed transport models and detailed mechanisms. *Combustion Science and Technology* 191 (2019), 208–222.

[34] V. Bykov and U. Maas. The extension of the ILDM concept to reaction–diffusion manifolds. *Combustion Theory and Modelling* 11 (2007), 839–862.

[35] P. Popp and M. Baum. Analysis of wall heat fluxes, reaction mechanisms, and unburnt hydrocarbons during the head-on quenching of a laminar methane flame. *Combustion and Flame* 108 (1997), 327–348.

[36] P. Popp, M. Smooke, and M. Baum. Heterogeneous/homogeneous reaction and transport coupling during flame-wall interaction. *Symposium (International) on Combustion* 26 (1996), 2693–2700.

[37] C. Strassacker, V. Bykov, and U. Maas. REDIM reduced modeling of quenching at a cold wall including heterogeneous wall reactions. *International Journal of Heat and Fluid Flow* 69 (2018), 185–193.

[38] C. Strassacker, V. Bykov, and U. Maas. Reduced modeling of flame-wall-interactions of premixed isooctane-air systems including detailed transport and surface reactions. *Proceedings of the Combustion Institute* 38 (2021), 1063–1070.

[39] P. S. Salimath, I. S. Ertesvåg, and A. Gruber. Premixed hydrogen-air flames interacting with a hydrogen porous wall. *International Journal of Hydrogen Energy* 43 (2018), 3822–3836.

[40] P. S. Salimath, I. S. Ertesvåg, and A. Gruber. Computational analysis of premixed methane-air flame interacting with a solid wall or a hydrogen porous wall. *Fuel* 272 (2020), 117658.

[41] P. S. Salimath and I. S. Ertesvåg. Local entropy generation and entropy fluxes of a transient flame during head-on quenching towards solid and hydrogen-permeable porous walls. *International Journal of Hydrogen Energy* 46 (2021), 26616–26630.

[42] T. Poinsot, D. C. Haworth, and G. Bruneaux. Direct simulation and modeling of flame-wall interaction for premixed turbulent combustion. *Combustion and Flame* 95 (1993), 118–132.

[43] G. Bruneaux, K. Akselvoll, T. Poinsot, and J. Ferziger. Flame-wall interaction simulation in a turbulent channel flow. *Combustion and Flame* 107 (1996), 27–44.

[44] G. Bruneaux, T. Poinsot, and J. Ferziger. Premixed flame–wall interaction in a turbulent channel flow: Budget for the flame surface density evolution equation and modelling. *Journal of Fluid Mechanics* 349 (1997), 191–219.

[45] J. Lai and N. Chakraborty. Effects of Lewis number on head on quenching of turbulent premixed flames: A direct numerical simulation analysis. *Flow, Turbulence and Combustion* 96 (2016), 279–308.

[46] J. Lai and N. Chakraborty. Statistical behavior of scalar dissipation rate in head-on quenching of turbulent premixed flames: A direct numerical simulation analysis. *Combustion Science and Technology* 188 (2016), 250–276.

[47] J. Lai, N. Chakraborty, and A. Lipatnikov. Statistical behaviour of vorticity and enstrophy transport in head-on quenching of turbulent premixed flames. *European Journal of Mechanics-B/Fluids* 65 (2017), 384–397.

[48] J. Sellmann, J. Lai, A. M. Kempf, and N. Chakraborty. Flame surface density based modelling of head-on quenching of turbulent premixed flames. *Proceedings of the Combustion Institute* 36 (2017), 1817–1825.

[49] J. Lai, D. H. Wacks, and N. Chakraborty. Flow topology distribution in head-on quenching of turbulent premixed flame: A direct numerical simulation analysis. *Fuel* 224 (2018), 186–209.

[50] J. Lai, N. Chakraborty, P. Zhao, and L. Wang. Heat flux and flow topology statistics in oblique and head-on quenching of turbulent premixed flames by isothermal inert walls. *Combustion Science and Technology* 191 (2019), 353–381.

[51] J. Lai and N. Chakraborty. Modeling of progress variable variance transport in head-on quenching of turbulent premixed flames: A direct numerical simulation analysis. *Combustion Science and Technology* 188 (2016), 1925–1950.

[52] J. Lai and N. Chakraborty. A priori direct numerical simulation modeling of scalar dissipation rate transport in head-on quenching of turbulent premixed flames. *Combustion Science and Technology* 188 (2016), 1440–1471.

[53] J. Lai, M. Klein, and N. Chakraborty. Assessment of algebraic flame surface density closures in the context of large eddy simulations of head-on quenching of turbulent premixed flames. *Combustion Science and Technology* 189 (2017), 1966–1991.

[54] J. Lai, A. Moody, and N. Chakraborty. Turbulent kinetic energy transport in head-on quenching of turbulent premixed flames in the context of Reynolds Averaged Navier Stokes simulations. *Fuel* 199 (2017), 456–477.

[55] J. Lai, D. Alwazzan, and N. Chakraborty. Turbulent scalar flux transport in head-on quenching of turbulent premixed flames: A direct numerical simulations approach to assess models for Reynolds Averaged Navier Stokes simulations. *Journal of Turbulence* 18 (2017), 1033–1066.

[56] U. Ahmed, N. A. K. Doan, J. Lai, M. Klein, N. Chakraborty, and N. Swaminathan. Multiscale analysis of head-on quenching premixed turbulent flames. *Physics of Fluids* 30 (2018), 105102.

[57] J. Lai, U. Ahmed, M. Klein, and N. Chakraborty. A comparison between head-on quenching of stoichiometric methane-air and hydrogen-air premixed flames using Direct Numerical Simulations. *International Journal of Heat and Fluid Flow* 93 (2022), 108896.

[58] P. Pantangi, A. Sadiki, J. Janicka, M. Mann, and A. Dreizler. LES of premixed methane flame impinging on the wall using non-adiabatic flamelet generated manifold (FGM) approach. *Flow, Turbulence and Combustion* 92 (2014), 805–836.

[59] J. Van Oijen and L. De Goey. Modelling of premixed laminar flames using flamelet-generated manifolds. *Combustion Science and Technology* 161 (2000), 113–137.

[60] R. Cheng, R. Bill, and F. Robben. Experimental study of combustion in a turbulent boundary layer. *Symposium (International) on Combustion* 18 (1981), 1021–1029.

[61] T. Ng, R. Cheng, F. Robben, and L. Talbot. Combustion-turbulence interaction in the turbulent boundary layer over a hot surface. *Symposium (International) on Combustion* 19 (1982), 359–366.

[62] M. Enomoto. Sidewall quenching of laminar premixed flames propagating along the single wall surface. *Proceedings of the Combustion Institute* 29 (2002), 781–787.

[63] J. Lu, O. Ezekoye, R. Greif, and R. Sawyer. Unsteady heat transfer during side wall quenching of a laminar flame. *Symposium (International) on Combustion* 23 (1991), 441–446.

[64] A. Bohlin, C. Jainski, B. D. Patterson, A. Dreizler, and C. J. Kliewer. Multiparameter spatio-thermochemical probing of flame–wall interactions advanced with coherent Raman imaging. *Proceedings of the Combustion Institute* 36 (2017), 4557–4564.

[65] T. Häber and R. Suntz. Effect of different wall materials and thermal-barrier coatings on the flame-wall interaction of laminar premixed methane and propane flames. *International Journal of Heat and Fluid Flow* 69 (2018), 95–105.

[66] C. Jainski, M. Rißmann, S. Jakirlic, B. Böhm, and A. Dreizler. Quenching of premixed flames at cold walls: effects on the local flow field. *Flow, Turbulence and Combustion* 100 (2018), 177–196.

[67] C. Jainski, M. Rißmann, B. Böhm, and A. Dreizler. Experimental investigation of flame surface density and mean reaction rate during flame–wall interaction. *Proceedings of the Combustion Institute* 36 (2017), 1827–1834.

[68] C. Jainski, M. Rißmann, B. Böhm, J. Janicka, and A. Dreizler. Sidewall quenching of atmospheric laminar premixed flames studied by laser-based diagnostics. *Combustion and Flame* 183 (2017), 271–282.

[69] H. Kosaka, F. Zentgraf, A. Scholtissek, L. Bischoff, T. Häber, R. Suntz, B. Albert, C. Hasse, and A. Dreizler. Wall heat fluxes and CO formation/oxidation during laminar and turbulent side-wall quenching of methane and DME flames. *International Journal of Heat and Fluid Flow* 70 (2018), 181–192.

[70] H. Kosaka, F. Zentgraf, A. Scholtissek, C. Hasse, and A. Dreizler. Effect of flame-wall interaction on local heat release of methane and DME combustion in a side-wall quenching geometry. *Flow, Turbulence and Combustion* 104 (2020), 1029–1046.

[71] F. Zentgraf, P. Johe, M. Steinhausen, C. Hasse, M. Greifenstein, A. D. Cutler, R. S. Barlow, and A. Dreizler. Detailed assessment of the thermochemistry in a side-wall quenching burner by simultaneous quantitative measurement of CO_2, CO and temperature using laser diagnostics. *Combustion and Flame* 235 (2022), 111707.

[72] F. Zentgraf, P. Johe, A. D. Cutler, R. S. Barlow, B. Böhm, and A. Dreizler. Classification of flame prehistory and quenching topology in a side-wall quenching burner at low-intensity turbulence by correlating transport effects with CO_2, CO and temperature. *Combustion and Flame* 239 (2022), 111681.

[73] P. Johe, F. Zentgraf, M. Greifenstein, M. Steinhausen, C. Hasse, and A. Dreizler. Characterization of flow field and combustion dynamics in a novel pressurized side-wall quenching burner using high-speed PIV/OH-PLIF measurements. *International Journal of Heat and Fluid Flow* 94 (2022), 108921.

[74] J. Andrae, P. Björnbom, L. Edsberg, and L.-E. Eriksson. A numerical study of side wall quenching with propane/air flames. *Proceedings of the Combustion Institute* 29 (2002), 789–795.

[75] A. Heinrich, S. Ganter, G. Kuenne, C. Jainski, A. Dreizler, and J. Janicka. 3D numerical simulation of a laminar experimental SWQ burner with tabulated chemistry. *Flow, Turbulence and Combustion* 100 (2018), 535–559.

[76] S. Ganter, A. Heinrich, T. Meier, G. Kuenne, C. Jainski, M. C. Rißmann, A. Dreizler, and J. Janicka. Numerical analysis of laminar methane–air side-wall-quenching. *Combustion and Flame* 186 (2017), 299–310.

[77] S. Ganter, C. Straßacker, G. Kuenne, T. Meier, A. Heinrich, U. Maas, and J. Janicka. Laminar near-wall combustion: Analysis of tabulated chemistry simulations by means of detailed kinetics. *International Journal of Heat and Fluid Flow* 70 (2018), 259–270.

[78] D. V. Efimov, P. de Goey, and J. A. van Oijen. QFM: Quenching flamelet-generated manifold for modelling of flame–wall interactions. *Combustion Theory and Modelling* 24 (2020), 72–104.

[79] R. Palulli, M. Talei, and R. L. Gordon. Unsteady flame–wall interaction: Impact on CO emission and wall heat flux. *Combustion and Flame* 207 (2019), 406–416.

[80] A. Heinrich, G. Kuenne, S. Ganter, C. Hasse, and J. Janicka. Investigation of the turbulent near wall flame behavior for a sidewall quenching burner by means of a Large Eddy Simulation and tabulated chemistry. *Fluids* 3 (2018), 65.

[81] R. Palulli, M. Talei, and R. L. Gordon. Analysis of near-wall CO due to unsteady flame-cooling air interaction. *Flow, Turbulence and Combustion* 107 (2021), 343–365.

[82] R. Palulli, D. Brouzet, M. Talei, and R. Gordon. A comparative study of flame-wall interaction and flame-cooling air interaction. *International Journal of Heat and Fluid Flow* 92 (2021), 108888.

[83] T. Zirwes, T. Häber, F. Zhang, H. Kosaka, A. Dreizler, M. Steinhausen, C. Hasse, A. Stagni, D. Trimis, R. Suntz, et al. Numerical study of quenching distances for side-wall quenching using detailed diffusion and chemistry. *Flow, Turbulence and Combustion* 106 (2021), 649–679.

[84] F. Zhang, T. Zirwes, T. Häber, H. Bockhorn, D. Trimis, and R. Suntz. Near wall dynamics of premixed flames. *Proceedings of the Combustion Institute* 38 (2021), 1955–1964.

[85] Z. Wei, H. Liu, Z. Chen, Z. Liu, and H. Zhen. Quenching distance, wall heat flux and CO/NO thermochemical states in the wall vicinity of laminar premixed biogas-hydrogen impinging flame. *Fuel* 307 (2022), 121849.

[86] T. M. Alshaalan and C. J. Rutland. Turbulence, scalar transport, and reaction rates in flame-wall interaction. *Symposium (International) on Combustion* 27 (1998), 793–799.

[87] A. Gruber, R. Sankaran, E. R. Hawkes, and J. H. Chen. Turbulent flame–wall interaction: A direct numerical simulation study. *Journal of Fluid Mechanics* 658 (2010), 5–32.

[88] M. Steinhausen, T. Zirwes, F. Ferraro, S. Popp, F. Zhang, H. Bockhorn, and C. Hasse. Turbulent flame-wall interaction of premixed flames using Quadrature-based Moment Methods (QbMM) and tabulated chemistry: An a priori analysis. *International Journal of Heat and Fluid Flow* 93 (2022), 108913.

[89] B. Jiang, D. Brouzet, M. Talei, R. L. Gordon, Q. Cazeres, and B. Cuenot. Turbulent flame-wall interactions for flames diluted by hot combustion products. *Combustion and Flame* 230 (2021), 111432.

[90] A. Heinrich, F. Ries, G. Kuenne, S. Ganter, C. Hasse, A. Sadiki, and J. Janicka. Large Eddy Simulation with tabulated chemistry of an experimental sidewall quenching burner. *International Journal of Heat and Fluid Flow* 71 (2018), 95–110.

[91] N. Peters. Laminar diffusion flamelet models in non-premixed turbulent combustion. *Progress in Energy and Combustion Science* 10 (1984), 319–339.

[92] C. D. Pierce and P. Moin. Progress-variable approach for Large-Eddy Simulation of non-premixed turbulent combustion. *Journal of Fluid Mechanics* 504 (2004), 73–97.

[93] O. Gicquel, N. Darabiha, and D. Thévenin. Laminar premixed hydrogen/air counterflow flame simulations using flame prolongation of ILDM with differential diffusion. *Proceedings of the Combustion Institute* 28 (2000), 1901–1908.

[94] U. Maas and V. Bykov. The extension of the reaction/diffusion manifold concept to systems with detailed transport models. *Proceedings of the Combustion Institute* 33 (2011), 1253–1259.

[95] Y. Xuan, G. Blanquart, and M. E. Mueller. Modeling curvature effects in diffusion flames using a laminar flamelet model. *Combustion and Flame* 161 (2014), 1294–1309.

[96] A. Donini, R. Bastiaans, J. Van Oijen, and L. De Goey. Differential diffusion effects inclusion with flamelet generated manifold for the modeling of stratified premixed cooled flames. *Proceedings of the Combustion Institute* 35 (2015), 831–837.

[97] A. Ketelheun, C. Olbricht, F. Hahn, and J. Janicka. Premixed generated manifolds for the computation of technical combustion systems. *Turbo Expo: Power for Land, Sea, and Air*. Vol. 48838. 2009, 695–705.

[98] A. Ketelheun, G. Kuenne, and J. Janicka. Heat transfer modeling in the context of Large Eddy Simulation of premixed combustion with tabulated chemistry. *Flow, Turbulence and Combustion* 91 (2013), 867–893.

[99] U. Maas and S. B. Pope. Simplifying chemical kinetics: Intrinsic low-dimensional manifolds in composition space. *Combustion and Flame* 88 (1992), 239–264.

[100] C. F. Curtiss and J. O. Hirschfelder. Transport properties of multicomponent gas mixtures. *The Journal of Chemical Physics* 17 (1949), 550–555.

[101] T. Poinsot and D. Veynante. *Theoretical and numerical combustion*. RT Edwards, Inc., 2005.

[102] R. Barlow, G. Fiechtner, C. Carter, and J.-Y. Chen. Experiments on the scalar structure of turbulent $CO/H_2/N_2$ jet flames. *Combustion and Flame* 120 (2000), 549–569.

[103] J. Smagorinsky. General circulation experiments with the primitive equations: I. The basic experiment. *Monthly Weather Review* 91 (1963), 99–164.

[104] E. R. Van Driest. On turbulent flow near a wall. *Journal of the Aeronautical Sciences* 23 (1956), 1007–1011.

[105] P. Moin and J. Kim. Numerical investigation of turbulent channel flow. *Journal of Fluid Mechanics* 118 (1982), 341–377.

[106] M. Germano, U. Piomelli, P. Moin, and W. H. Cabot. A dynamic subgrid-scale eddy viscosity model. *Physics of Fluids A: Fluid Dynamics* 3 (1991), 1760–1765.

[107] F. Nicoud and F. Ducros. Subgrid-scale stress modelling based on the square of the velocity gradient tensor. *Flow, Turbulence and Combustion* 62 (1999), 183–200.

[108] F. Nicoud, H. B. Toda, O. Cabrit, S. Bose, and J. Lee. Using singular values to build a subgrid-scale model for large eddy simulations. *Physics of Fluids* 23 (2011), 085106.

[109] H. Pitsch and H. Steiner. Large-Eddy Simulation of a turbulent piloted methane/air diffusion flame (Sandia flame D). *Physics of Fluids* 12 (2000), 2541–2554.

[110] G. H. Golub and C. F. Van Loan. *Matrix computations*. JHU press, 2013.

[111] M. Steinhausen, T. Zirwes, F. Ferraro, A. Scholtissek, H. Bockhorn, and C. Hasse. Flame-vortex interaction during turbulent side-wall quenching and its implications for flamelet manifolds. *Proceedings of the Combustion Institute* (2022). DOI: https://doi.org/10.1016/j.proci.2022.09.026.

[112] O. Colin, F. Ducros, D. Veynante, and T. Poinsot. A thickened flame model for Large Eddy Simulations of turbulent premixed combustion. *Physics of Fluids* 12 (2000), 1843–1863.

[113] F. Charlette, C. Meneveau, and D. Veynante. A power-law flame wrinkling model for LES of premixed turbulent combustion Part I: Non-dynamic formulation and initial tests. *Combustion and Flame* 131 (2002), 159–180.

[114] J.-P. Legier, T. Poinsot, and D. Veynante. Dynamically thickened flame LES model for premixed and non-premixed turbulent combustion. *Proceedings of the summer program*. Vol. 12. Citeseer. 2000, 157–168.

[115] G. Kuenne, A. Ketelheun, and J. Janicka. LES modeling of premixed combustion using a thickened flame approach coupled with FGM tabulated chemistry. *Combustion and Flame* 158 (2011), 1750–1767.

[116] M. Ihme and H. Pitsch. Modeling of radiation and nitric oxide formation in turbulent nonpremixed flames using a flamelet/progress variable formulation. *Physics of Fluids* 20 (2008), 055110.

[117] U. Maas and J. Warnatz. Ignition processes in hydrogen-oxygen mixtures. *Combustion and Flame* 74 (1988), 53–69.

[118] P. Deuflhard, E. Hairer, and J. Zugck. One-step and extrapolation methods for differential-algebraic systems. *Numerische Mathematik* 51 (1987), 501–516.

[119] A. Zschutschke, D. Messig, A. Scholtissek, and C. Hasse. *Universal Laminar Flame Solver (ULF)*. `https://figshare.com/articles/ULF_code_pdf/5119855`. Version 2. 2017.

[120] D. G. Goodwin, H. K. Moffat, and R. L. Speth. *Cantera: An Object-oriented Software Toolkit for Chemical Kinetics, Thermodynamics, and Transport Processes. Version 2.3.0*. `http://www.cantera.org`. Version 2.3.0. 2017.

[121] G. B. Ferraris and D. Manca. BzzOde: A new C++ class for the solution of stiff and non-stiff ordinary differential equation systems. *Computers & Chemical Engineering* 22 (1998), 1595–1621.

[122] H. G. Weller, G. Tabor, H. Jasak, and C. Fureby. A tensorial approach to computational continuum mechanics using object-oriented techniques. *Computers in Physics* 12 (1998), 620–631.

[123] J. Ferziger and M. Peric. *Computational Methods for Fluid Dynamics*. Springer Berlin Heidelberg, 2012.

[124] J. Sotton, B. Boust, S. A. Labuda, and M. Bellenoue. Head-on quenching of transient laminar flame: heat flux and quenching distance measurements. *Combustion Science and Technology* 177 (2005), 1305–1322.

[125] B. Boust, J. Sotton, S. Labuda, and M. Bellenoue. A thermal formulation for single-wall quenching of transient laminar flames. *Combustion and Flame* 149 (2007), 286–294.

[126] T. Poinsot, D. Haworth, and G. Bruneaux. Direct simulation and modeling of flame-wall interaction for premixed turbulent combustion. *Combustion and Flame* 95 (1993), 118–132.

[127] J. Lai, M. Klein, and N. Chakraborty. Direct numerical simulation of head-on quenching of statistically planar turbulent premixed methane-air flames using a detailed chemical mechanism. *Flow, Turbulence and Combustion* 101 (2018), 1073–1091.

[128] G. P. Smith. GRI-Mech 3.0. *http://www. me. berkley. edu/gri_mech/* (1999).

[129] D. Escudié*, E. Haddar, and M. Brun. Influence of strain rate on a premixed turbulent flame stabilized in a stagnating flow. *Experiments in Fluids* 27 (1999), 533–541.

[130] A. Dreizler. Personal communication. 2019.

[131] P. A. Norden. Determination of quenching distance for carbon monoxide-air flames. *Journal of Engineering Physics* 9 (1965), 77–78.

[132] E. Knudsen, H. Kolla, E. R. Hawkes, and H. Pitsch. LES of a premixed jet flame DNS using a strained flamelet model. *Combustion and Flame* 160 (2013), 2911–2927.

[133] J. A. van Oijen and L. P. H. de Goey. Modelling of premixed counterflow flames using the flamelet-generated manifold method. *Combustion Theory and Modelling* 6 (2002), 463–478.

[134] P. Trisjono, K. Kleinheinz, E. R. Hawkes, and H. Pitsch. Modeling turbulence–chemistry interaction in lean premixed hydrogen flames with a strained flamelet model. *Combustion and Flame* 174 (2016), 194–207.

[135] N. Peters. *Turbulent combustion*. 2001.

[136] C. Strassacker, V. Bykov, and U. Maas. Comparative analysis of reaction-diffusion manifold based reduced models for head-on-and side-wall-quenching flames. *Proceedings of the Combustion Institute* 38 (2021), 1025–1032.

[137] Z. Li, M. T. Lewandowski, F. Contino, and A. Parente. Assessment of on-the-fly chemistry reduction and tabulation approaches for the simulation of moderate or intense low-oxygen dilution combustion. *Energy fuels* 32 (2018), 10121–10131.

[138] C. Chi, G. Janiga, and D. Thévenin. On-the-fly artificial neural network for chemical kinetics in direct numerical simulations of premixed combustion. *Combustion and Flame* 226 (2021), 467–477.

[139] K. He, I. P. Androulakis, and M. G. Ierapetritou. On-the-fly reduction of kinetic mechanisms using element flux analysis. *Chemical Engineering Science* 65 (2010), 1173–1184.

[140] R. Schießl, V. Bykov, U. Maas, A. Abdelsamie, and D. Thévenin. Implementing multi-directional molecular diffusion terms into Reaction Diffusion Manifolds (REDIMs). *Proceedings of the Combustion Institute* 36 (2017), 673–679.

[141] C. Yu and U. Maas. Sensitivity of reaction–diffusion manifolds (REDIM) method with respect to the gradient estimate. *Combustion Theory and Modelling* 26 (2022), 482–512.

[142] G. Steinhilber, V. Bykov, and U. Maas. REDIM reduced modeling of flame-wall-interactions: Quenching of a premixed methane/air flame at a cold inert wall. *Proceedings of the Combustion Institute* 36 (2017), 655–661.

[143] S. Popp, F. Hunger, S. Hartl, D. Messig, B. Coriton, J. H. Frank, F. Fuest, and C. Hasse. LES flamelet-progress variable modeling and measurements of a turbulent partially-premixed dimethyl ether jet flame. *Combustion and Flame* 162 (2015), 3016–3029.

[144] J. A. de Swart, R. J. Bastiaans, J. A. van Oijen, L. P. H. de Goey, and R. S. Cant. Inclusion of preferential diffusion in simulations of premixed combustion of hydrogen/methane mixtures with flamelet generated manifolds. *Flow, Turbulence and Combustion* 85 (2010), 473–511.

[145] J. D. Regele, E. Knudsen, H. Pitsch, and G. Blanquart. A two-equation model for non-unity Lewis number differential diffusion in lean premixed laminar flames. *Combustion and Flame* 160 (2013), 240–250.

[146] J. Schlup and G. Blanquart. Reproducing curvature effects due to differential diffusion in tabulated chemistry for premixed flames. *Proceedings of the Combustion Institute* 37 (2019), 2511–2518.

[147] N. Mukundakumar, D. Efimov, N. Beishuizen, and J. van Oijen. A new preferential diffusion model applied to FGM simulations of hydrogen flames. *Combustion Theory and Modelling* 25 (2021), 1245–1267.

[148] X. Wen, T. Zirwes, A. Scholtissek, H. Böttler, F. Zhang, H. Bockhorn, and C. Hasse. Flame structure analysis and composition space modeling of thermodiffusively unstable premixed hydrogen flames-Part I: Atmospheric pressure. *Combustion and Flame* 238 (2022), 111815.

[149] E. Ranzi, A. Frassoldati, R. Grana, A. Cuoci, T. Faravelli, A. Kelley, and C. Law. Hierarchical and comparative kinetic modeling of laminar flame speeds of hydrocarbon and oxygenated fuels. *Progress in Energy and Combustion Science* 38 (2012), 468–501.

[150] A. Stagni, A. Frassoldati, A. Cuoci, T. Faravelli, and E. Ranzi. Skeletal mechanism reduction through species-targeted sensitivity analysis. *Combustion and Flame* 163 (2016), 382–393.

[151] A. Vreman, J. Van Oijen, L. De Goey, and R. Bastiaans. Direct numerical simulation of hydrogen addition in turbulent premixed Bunsen flames using flamelet-generated manifold reduction. *International Journal of Hydrogen Energy* 34 (2009), 2778–2788.

[152] B. Duboc, G. Ribert, and P. Domingo. Description of kerosene/air combustion with hybrid transported-tabulated chemistry. *Fuel* 233 (2018), 146–158.

[153] B. Duboc, G. Ribert, and P. Domingo. Evaluation of chemistry models on methane/air edge flame simulation. *Proceedings of the Combustion Institute* 37 (2019), 1691–1698.

[154] B. Duboc, G. Ribert, and P. Domingo. Hybrid transported-tabulated chemistry for partially premixed combustion. *Computers & Fluids* 179 (2019), 206–227.

[155] H. Böttler, X. Chen, S. Xie, A. Scholtissek, Z. Chen, and C. Hasse. Flamelet modeling of forced ignition and flame propagation in hydrogen-air mixtures. *Combustion and Flame* (2022), 112125.

[156] S. Schneider. Auswirkungen der Wasserstoff-Zumischung auf die Flammenstruktur turbulenter stratifizierter Methan-Luft-Flammen. PhD thesis. Technische Universität Darmstadt, 2017.

[157] A. Stagni, A. Frassoldati, A. Cuoci, T. Faravelli, and E. Ranzi. Skeletal mechanism reduction through species-targeted sensitivity analysis. *Combustion and Flame* 163 (2016), 382–393.

[158] D. G. Goodwin, H. K. Moffat, and R. L. Speth. *Cantera: An Object-oriented Software Toolkit for Chemical Kinetics, Thermodynamics, and Transport Processes. Version 2.3.0*. `http://www.cantera.org`. Version 2.3.0. 2017.

[159] W. Han, A. Scholtissek, F. Dietzsch, and C. Hasse. Thermal and chemical effects of differential diffusion in turbulent non-premixed H_2 flames. *Proceedings of the Combustion Institute* 38 (2021), 2627–2634.

[160] J. Sutherland, P. Smith, and J. Chen. Quantification of differential diffusion in nonpremixed systems. *Combustion Theory and Modelling* 9 (2005), 365–383.

[161] B. Fiorina, R. Baron, O. Gicquel, D. Thevenin, S. Carpentier, and N. Darabiha. Modelling non-adiabatic partially premixed flames using flame-prolongation of ILDM. *Combustion Theory and Modelling* 7 (2003), 449.

[162] P. Johe, F. Zentgraf, M. Greifenstein, R. S. Barlow, and A. Dreizler. Laser-based investigation of flame surface density and mean reaction rate during flame-wall interaction at elevated pressure. *Proceedings of the Combustion Institute* (2022). DOI: `https://doi.org/10.1016/j.proci.2022.09.016`.

[163] R. Palulli. Direct numerical simulation of flame-wall interaction and flame-cooling air interaction. PhD thesis. The University of Melbourne, 2020.

[164] A. Gruber, P. S. Salimath, and J. H. Chen. Direct numerical simulation of laminar flame–wall interaction for a novel H_2-selective membrane/injector configuration. *International Journal of Hydrogen Energy* 39 (2014), 5906–5918.

Nomenclature

Abbreviations

ATF	Artificial thickened flame
CFD	Computational fluid dynamics
CFL	Courant–Friedrichs–Lewy
DK	Detailed kinetics
DME	Dimethyl ether
DNS	Direct numerical simulation
EGR	Exhaust gas recirculation
FGM	Flamelet-generated manifold
FLT	Flamelet look-up table
FRS	Flame-resolved simulation
FVI	Flame-vortex interaction
FVM	Finite volume method
FWI	Flame-wall interaction
GC	Generalized coordinates
HOQ	Head-on quenching
HRR	Heat release rate
LES	Large-eddy simulation
OP	Operator
PDF	Probability density function
QFM	Quenching flamelet-generated manifold
QFM-EGR	Quenching flamelet-generated manifold with exhaust gas recirculation
RANS	Reynolds averaged Navier–Stokes
REDIM	Reaction-Diffusion Manifolds
RK	Reduced kinetics

SWQ Side-wall quenching

TC Thermokinetic coordinates

TCI Turbulence-chemistry interaction

tr Transported

Greek Symbols

β_j The temperature exponent for reaction j in empirical Arrhenius law

$\boldsymbol{\chi}$ Gradient estimation

$\boldsymbol{\psi}$ State vector

$\boldsymbol{\tau}$ Viscous stress tensor

$\boldsymbol{\theta}$ Parametrization vector in generalized coordinates

$\boldsymbol{\xi}$ Parametrization vector in thermokinetic coordinates

Δh_f^0 Formation enthalpy

Δ Filter width

δ Flame thickness

Δ_x Local cell size

δ_{ij} Kronecker symbol

$\dot{\omega}_F$ Chemical source term of the fuel

$\dot{\omega}_k$ Chemical source term of species k

$\dot{\omega}_k^+$ Production rate of species k

$\dot{\omega}_k^-$ Consumption rate of species k

$\dot{\omega}_T$ Heat release due to the combustion

λ Thermal conductivity

μ Dynamic viscosity

ν Kinematic viscosity

ν''_{kj} The molar stoichiometric coefficients of species k in the backward direction of reaction j

ν'_{kj} The molar stoichiometric coefficients of species k in the forward direction of reaction j

ν_t Eddy viscosity

Ω Flame sensor

ϕ Local equivalence ratio

ρ Density

τ	Dimensionless time
τ_c	Chemical time scales
τ_t	Turbulent time scales
φ	Arbitrary quantity
Ξ_Δ	Subgrid scale wrinkling factor

Latin Symbols

$\boldsymbol{C}$	Constant parametrization matrix
$\boldsymbol{D}$	Diffusion matrix
$\boldsymbol{d}_j$	Diffusion driving force
$\boldsymbol{F}$	Source term vector
$\boldsymbol{f}$	Force vector
$\boldsymbol{I}$	Unit tensor
$\boldsymbol{j}_k$	Diffusion flux of species k
$\boldsymbol{q}$	Heat fluxes due to heat conduction and species diffusion
$\boldsymbol{S}$	Rate of strain tensor
$\boldsymbol{T}$	Stress tensor
$\boldsymbol{u}$	Velocity vector
$\boldsymbol{V}_k$	Diffusion velocity of species k
$\dot{Q}$	Heat source term
$\mathcal{D}_{kj}$	Binary diffusion coefficient
$\overline{M}$	Mean molecular weight
C_k	Universal Kolmogorov constant
c_p	Heat capacity at constant pressure
D	Molecular diffusivity
D_k^T	Thermal diffusion coefficient of species k
D_{kj}	Ordinary multicomponent diffusion coefficients of species k in species j
E	Efficiency function
E_j	The activation energy
F	Flame thickening factor
h	Total enthalpy

h_s Sensible enthalpy

K Flame stretch

K_c Curvature related component of flame stretch

K_e The equilibrium constant

K_s Strain

K_{fj} The forward rate constant for reaction j

K_{rj} The backward rate constant for reaction j

l_k Kolmogorov length scale

l_t Integral length scale

P Total thermodynamic pressure

p Varying component of total thermodynamic pressure

R Universal gas constant

r_j Rate of progress of reaction j

s_a Absolute flame speed

s_c Consumption speed

s_d Displacement speed

s_L^0 Laminar burning velocity

T Temperature

X_k Mole fraction of species k

x_k Specific mole number of species k

Y_{PV} Mass fraction of progress variable

Y_k Mass fraction of species k

Z_{Bilger} Bilger mixture fraction

Z_{HC} Differential diffusion parameter

Other Symbols

Da Damköhler number

Le Lewis number

Pe Peclet number

Pr Prandtl number

Re Reynolds number

Sc Schmidt number

Superscripts and Subscripts

b Burned

F Fuel

sgs Subgrid scale

t Turbulent

u Unburned

List of Figures

1.1 Illustration of typical experimental configurations of HOQ (a) and SWQ (b). This figure is adapted from [11]. . . . 2
1.2 Schematic representation of the time scales in chemically reacting flows, adapted from [99]. 7
1.3 Four configurations, including the laminar HOQ, the laminar SWQ, the turbulent SWQ, and the Bunsen flame, investigated in the thesis, with the purpose to develop manifold-based reduced kinetic models. The fuels considered range from pure hydrocarbon to H_2-enriched. 7

2.1 Flame structure of a 1D freely propagating lean flame. . . . 15
2.2 Illustration of the laminar flame thickness by different definitions. The width of the colored rectangle denotes the thickness based on scaling laws (red), the scalar gradient (blue), and the species source term (yellow). . . . 17
2.3 Minimum required total grid number for a 3D DNS for different Reynolds numbers. . . . 20

3.1 Canonical 1D flame configurations for FGM (a), QFM (b), and QFM-EGR (c). . . . 26
3.2 Illustration of the invariant manifold. The purple line denotes the vector field, and the blue line the projection of the vector field to the parametrization vector. The thick gray dashed line indicates the tangential space of the manifold. . . . 28
3.3 Projection of the governing equations when the manifold is non-invariant: (a) in generalized coordinates, and (b) in thermokinetic coordinates. The purple line denotes the vector field, and the blue line the projection of the vector field to the parametrization vector. The thick gray dashed line indicates the tangential space of the manifold. . . . 29
3.4 Schematic of the ATF approach. . . . 31

4.1 Schematic of unstrained HOQ (a) and strained HOQ (b). . . . 35
4.2 Schematic of the system configuration for the transient HOQ process [1]. . . . 36
4.3 CO mole fraction over temperature for different positions until 0.5 ms after quenching. The error bars are obtained according to the experimental fluctuations [20]. . . . 39
4.4 D_w-τ plots for the experimental setup [20]: (a) temperature, (b) CO mole fraction. . . . 40
4.5 Normalized quenching distances and quenching wall heat fluxes. . . . 40
4.6 X_{CO}-T plots for different positions until 0.5 dimensionless time after quenching. . . . 41
4.7 $X_{\mathrm{CO_2}}$-T plots for different positions until 0.5 dimensionless time after quenching. . . . 42
4.8 Differential diffusion parameter profiles at different times for T_w = 300 K, K_s = 600 s^{-1}. . 43
4.9 Profiles of source term (dotted lines) and Z_{HC} (solid lines) at different times for K_s = 600 s^{-1} (a) and K_s = 1800 s^{-1} (b). . . . 44
4.10 Minimum Z_{HC} values (solid lines) within D_w = 0–20 and their location $D_w \,|\, Z_{\mathrm{HC}}{=}Z_{\mathrm{HC_{min}}}$ (dashed lines) plotted over time. . . . 44
4.11 Different species plotted against progress variable for different strain rates at different time instants: (a) prior to quenching (τ = -1), (b) at quenching (τ = 0). . . . 45

5.1 Illustration of the SWQ burner configuration and the computational domain. The area surrounded by a black solid box (D1) presents the computational domain for simulations with a coarser grid. The area highlighted with a red dashed frame (D2) denotes the computational domain for simulations with a finer grid. 48
5.2 The coarsened 2D tabulation grid shown in the space of the control variables (the grid is coarsened by a factor of 4 based on the original grid for better presentation). The red lines are isolines for θ_1, and the blue lines are isolines for θ_2. The values correspond to the local coordinates in the original table for tabulation in the simulations. 49
5.3 Distribution of the CO_2 mass fraction in the REDIM table generated based on the 1D HOQ simulation results with detailed kinetics: (a) in thermokinetic variable space, (b) in generalized coordinate space. 50
5.4 Distributions of the OH mass fraction. The flame shape is also shown by an isoline of the temperature T = 1500 K (red). The horizontal line at quenching height is shown in blue. The four black dashed horizontal lines near the flame tip depict the extraction lines for CO and temperature data. The positions (a), (b), (c), and (d) are defined by the vertical offsets to the quenching point of -0.55, -0.05, 0.45, and 0.95 mm, respectively. 52
5.5 Comparison of CO mass fraction and temperature, contrasting the simulation results obtained with detailed kinetics, the *a-priori* predictions, and reduced model equations in generalized coordinates against the experimental data at different positions: (a) y_q = -0.55 mm, (b) y_q = -0.05 mm, (c) y_q = 0.45 mm, (d) y_q = 0.95 mm. 53
5.6 Variations in the quenching height and the maximum wall heat flux against the varying factor α in the gradient estimation for reduced model equations both in generalized coordinates (GC) and thermokinetic coordinates (TC). Results from the detailed kinetics are shown as the stars. 55
5.7 CO and OH mass fraction variations over temperature (T) for reduced model equations in generalized coordinates (GC) and thermokinetic coordinates (TC) with two REDIM tables generated based on the gradient estimations varied from the 1D HOQ by varying factors α = 0.5 and α = 1.0 for different positions: (a) y_q = -0.5 mm, (b) y_q = 0 mm, (c) y_q = 0.5 mm. 56
5.8 Species mass fraction distributions in REDIM tables generated based on the gradient estimations varied from the 1D HOQ by a varying factor α: (a) CO mass fraction for REDIM table with α = 0.5, (b) CO mass fraction for REDIM table with α = 1.0, (c) OH mass fraction for REDIM table with α = 0.5, (d) OH mass fraction for REDIM table with α = 1.0. The white solid lines correspond to θ_2 = 97, the white dashed lines correspond to θ_2 = 89, and the white dash-dot lines correspond to θ_2 = 70. 57
5.9 Species variations over several isolines of θ_2 (97, 89 and 70): (a) CO mass fraction, (b) OH mass fraction. 58
5.10 Gradient estimations obtained by the detailed solution of the HOQ simulation. Shown are the gradient estimations of the specific mole number of CO_2 (χ_{CO_2}) (a) and the enthalpy (χ_h) (b), as functions of the specific enthalpy and mass fraction of CO_2. The states of the freely-propagating flame are illustrated with the white dashed lines. 59
5.11 CO and OH mass fraction variations over temperature (T) obtained by solving reduced model equations in generalized coordinates with REDIMs generated based on different gradient estimations (REF: both χ_h and χ_{CO_2} are obtained from the 1D HOQ; REDIM-A: χ_h = 2.5 $\times$ 10^9 J/(kg·m) and χ_{CO_2} = 2000 mol/(kg·m); REDIM-B: χ_h = 2.5 $\times$ 10^9 J/(kg·m) and χ_{CO_2} is interpolated from the values of a freely propagating flame; REDIM-C: χ_h = 5.0 $\times$ 10^9 J/(kg·m) and χ_{CO_2} is interpolated from the values of a freely propagating flame) for different positions: (a) y_q = -0.5 mm, (b) y_q = 0 mm, (c) y_q = 0.5 mm. The vertical dashed line indicates the position of T = 1800 K. 60

5.12 Gradients of the specific mole number of CO_2 and enthalpy as functions of CO_2 mass fraction and enthalpy for regions $T > 1800$ K from 2D SWQ results (REF case): (a) gradients of x_{CO_2} in x direction, (b) gradients of x_{CO_2} in y direction, (c) gradients of h in x direction, (d) gradients of h in y direction. The magnitude of the gradients are indicated by the colors. The left column corresponds to y_q = -0.5 mm, the middle column corresponds to y_q = 0 mm, and the right column corresponds to y_q = 0.5 mm. 61

6.1 General workflow of the REDIM reduced kinetics *on the fly*. 64

6.2 Spatial gradients (gradient estimation) in x and y directions used for the REDIMs for the first (gray), the second (blue), the third (red) reduced kinetic computations, and from the detailed kinetics (black): (left) gradients of the specific mole number of CO_2 (in mol/(kg · m)), (right) gradients of the specific enthalpy h (in J/(kg · m)). 65

6.3 OH contours: (a) the detailed kinetic simulation (DK), (b) the first reduced kinetic simulation (RK1), (c) the second reduced kinetic simulation (RK2), (d) the third reduced kinetic simulation (RK3). The black dashed lines denote the positions where quantitative analysis are conducted for species. b corresponds to the quenching height determined by the maximum wall heat flux. 66

6.4 Profiles of CO_2, CO, OH, and H_2 mass fractions over three positions: (a) y_q = -0.5 mm, (b) y_q = 0 mm, (c) y_q = 0.5 mm. Black lines correspond to the detailed kinetics (DK). Red, green, and blue lines denote the first (RK1), the second (RK2), and the third (RK3) reduced kinetics, respectively. 67

6.5 Spatial gradients of specific mole number of CO_2 (left) and enthalpy h (right) in x (top) and y (bottom) directions at y_q = 0. 68

7.1 Schematic of HOQ (a) and SWQ (b) configurations adopted in the present study (s_L^0 denotes the laminar flame speed). 73

7.2 Distributions of the local equivalence ratio ϕ over Y_{CO_2}/M_{CO_2} and h of the 2D SWQ and the 1D HOQ with the same fresh gas composition (ϕ_f = 0.83) (a), and the 2D SWQ with ϕ_f = 0.83 and a series of 1D HOQs with different ϕ_f (b). 73

7.3 Initial guesses of the REDIM based on HOQs projected to (Y_{CO_2}/M_{CO_2}), h, and ϕ (a), and the REDIM based on a SWQ projected to (Y_{CO_2}/M_{CO_2}) and (h - 500000 Y_{CO}/M_{CO}) (500000 is a constant in J/mol) (b). For clear interpretation, the grid in (b) is twice coarser than the actual grid used in the computation. 74

7.4 States of SWQ using detailed kinetics over (Y_{CO_2}/M_{CO_2}) and h (a), and (Y_{CO_2}/M_{CO_2}) and (h - 500000 Y_{CO}/M_{CO}) (b). 75

7.5 Comparison of CO distributions between detailed kinetics (DK) and reduced kinetics (RK): (left) DK and RK-HOQT, (right) DK and RK-SWQT. The black solid curve marks the flame location where the flame stretch is evaluated. The black dashed line corresponds to the quenching height. The white dashed lines are positions where the experimental data, detailed kinetic results, and reduced kinetic results are compared. The red dashed line denotes a further position very close to the wall where the detailed kinetics and the reduced kinetics are compared. $x = 0$ corresponds to the wall. 76

7.6 Variations in wall heat flux for both detailed kinetics (black solid line) and reduced kinetics (red dashed line for RK-HOQT and yellow dashed line for RK-SWQT). 77

7.7 Distributions of the differential diffusion parameter Z_{HC}: (left) DK and RK-HOQT, (right) DK and RK-SWQT. $x = 0$ corresponds to the wall. 78

7.8 Mole fractions of CO_2 (X_{CO_2}) and CO (X_{CO}) over gas temperature T at wall distances of 120 μm, 320 μm, 520 μm, and 720 μm. Gray dots correspond to the instantaneous experimental data which is collected between y_q = -2 mm and y_q = 2 mm. Colored dots are experimental results averaged on the spatial bins with respect to the quenching height. Black solid lines denote results from DK, red dashed lines are results from RK-HOQT, and yellow dashed lines are results from RK-SWQT. 78

7.9 Mole fractions of H (X_H, top) and OH (X_{OH}, bottom) at wall distances of 50 μm (left) and 720 μm (right) between y_q = -2 mm and y_q = 2 mm. 79

7.10 Variations of the mole fractions of CO_2, CO, OH, and H over temperature between y_q = -2 mm and y_q = 2 mm for $x < 1$ mm of DK (a), RK-HOQT (b), and RK-SWQT (c). The scatter is colored by the wall-normal coordinate x. 80

7.11 Comparison of the normalized strain K_s^+ (left) and total stretch K^+ (right) over the normalized wall distance x/δ between detailed and reduced kinetics. 81

8.1 Schematic illustration of the configuration investigated. The x, y, and z coordinates are the streamwise, lateral, and wall-normal directions, respectively. The dimension in the lateral direction is 30 mm. The region of interest analyzed in Fig. 8.9 is denoted by the green rectangle. 83

8.2 Contour of mean Y_{CO_2}, which is averaged both temporally and spatially in the lateral (y) direction. White lines denote positions where mean values of velocity and thermo-chemical quantities are extracted: (a) $x_q = -0.5H$, (b) $x_q = 0$, (c) $x_q = 0.5H$, (d) $x_q = H$. Here, (b) $x_q = 0$ corresponds to the axial position of the mean quenching point. 85

8.3 Distributions of the mean wall heat flux along the axial coordinate x. The reference FRS results are denoted by the black solid line. The violet, the green, and the red dashed lines correspond to FGM, QFM, and QFM-EGR results, respectively. 86

8.4 Distributions of the mean axial velocity (top) and wall-normal velocity (bottom) from the bottom wall to the height of $0.1H$ at different axial positions: (a) $x_q = -0.5H$, (b) $x_q = 0$, (c) $x_q = 0.5H$, (d) $x_q = H$. The reference FRS results are denoted by black dashed lines marked with cross symbols. The violet, the green, and the red dashed lines correspond to FGM, QFM, and QFM-EGR results, respectively. 87

8.5 Distributions of mean progress variable (top), enthalpy h (middle) and temperature T (bottom) from the bottom wall to the height of $0.1H$ at different axial positions: (a) $x_q = -0.5H$, (b) $x_q = 0$, (c) $x_q = 0.5H$, (d) $x_q = H$. The FRS results are denoted by black dashed lines marked with cross symbols. The violet, the green, and the red dashed lines correspond to FGM, QFM, and QFM-EGR results, respectively. 88

8.6 Distributions of mean mass fractions of CO (top) and OH (bottom) from the bottom wall to the height of $0.1H$ at different axial positions: (a) $x_q = -0.5H$, (b) $x_q = 0$, (c) $x_q = 0.5H$, (d) $x_q = H$. The reference FRS results are denoted by black dashed lines marked with cross symbols. The violet, the green, and the red dashed lines correspond to FGM, QFM, and QFM-EGR results, respectively. 89

8.7 Distributions of mean CO mass fraction from the inlet to the outlet at different vertical positions: (a) $z = \delta$, (b) $z = 2\delta$, (c) $z = 3\delta$, (d) $z = 4\delta$. The reference FRS results are denoted by black dashed lines marked with cross symbols. The violet, the green, and the red dashed lines correspond to FGM, QFM, and QFM-EGR results, respectively. 89

8.8 PDFs of CO conditioned on wall distance and enthalpy level. 90

8.9 Thermo-chemical states near the quenching point for different lateral positions and time instants: (left) FRS, (middle) QFM, (right) QFM-EGR. The scatters are colored by the normalized wall distance z/δ. For reference, the states of a 1D freely propagating flame and on the wall boundary of a laminar SWQ are denoted by black dashed lines and black solid lines, respectively. 91
8.10 Time series of a slice in the lateral direction through the turbulent flame for QFM-EGR. Contours of the normalized enthalpy (h^*) are shown. Isocontours of heat release rate (0.1 $\times$ $\mathrm{HRR}_{\max}$) are denoted by black dashed lines. The blue and red points correspond to the positions of the Lagrangian particles projected to a xz plane. 92
8.11 Time series of a slice in the lateral direction through the turbulent flame: (left) FRS, (right) QFM-EGR. Isocontours of heat release rate (0.1 $\times$ $\mathrm{HRR}_{\max}$) are denoted by the black dashed lines. The white isocontour represents the area of FVI. 93

9.1 Experimental and numerical configuration of the Bunsen burner. Numbers indicate length in millimeters. 96
9.2 Comparison of the velocity between the experiment and the detailed kinetic (DK) simulation: (a) averaged axial velocity contour, (b) axial velocity profiles at three axial positions and along the centerline marked in (a). 100
9.3 Distribution of the local equivalence ratio: (a) in the physical space, (b) in the temperature space for the main flow region in (a). The black dashed line in (b) corresponds to the 1D freely propagating flame with the same fresh gas composition and temperature at the inlet of the Bunsen burner. 101
9.4 Comparison of the temperature field between the DK simulation and the FGM simulations: (left) DK and FGM-4D, (right) DK and FGM-3D. 102
9.5 Bilger mixture fraction distribution from the DK simulation and the FGM simulations: (left) DK, (middle) FGM-4D, (right) FGM-3D. 102
9.6 Heat release rate distribution from the DK simulation and the FGM simulations: (left) DK, (middle) FGM-4D, (right) FGM-3D. The insets show a zoom in the mixing layer region. . . 103
9.7 *A-posteriori* analysis: profiles of mass fractions of CO_2, H_2, CO, OH, and heat release rate (HRR) for several positions marked in Fig. 9.4 obtained from DK, FGM-4D, and FGM-3D simulations. 104

A.1 Distributions of OH mass fraction for two grids. The flame shape is also shown by an isoline of the temperature T = 1500 K (red). The three black dashed horizontal lines near the flame tip depict the extraction lines for the CO and temperature data. The positions (a), (b), and (c) corresponds to y = 21.6 mm, y = 22.1 mm, and y = 22.6 mm, respectively. 131
A.2 Comparison of CO mass fraction and temperature of two different grids at different positions: (a) y = 21.6 mm, (b) y = 22.1 mm, (c) y = 22.6 mm. 132

B.1 CO-T plots from computations of detailed kinetics and reduced model equations in generalized coordinates for different near-wall positions: (a) wall distance = 0.1 mm, (b) wall distance = 0.2 mm, (c) wall distance = 0.3 mm, (d) wall distance = 0.5 mm. The experimental data are represented as scatters. 133

C.1 The *a-priori* results for CO for the slice y = 15 mm. Results of FRS reference, *a-priori* of FGM, *a-priori* of QFM and *a-priori* of QFM-EGR are presented from the top to the bottom. (a), (b), and (c) are positions where thermo-chemical quantities are sampled, which corresponds to x_q = -0.5H, 0, and 0.5H, respectively. Here, $x_q = 0$ corresponds to the axial position of the quenching point. 135

C.2 The *a-priori* results for the mass fractions of CO, OH, and temperature T for (a) $x_q = -0.5H$, (b) $x_q = 0$, and (c) $x_q = 0.5H$ at the slice y = 15 mm. Results of FRS reference (black dashed lines marked with cross symbols), *a-priori* of FGM (violet dash-dotted lines), *a-priori* of QFM (green dashed lines), and *a-priori* of QFM-EGR (red dashed lines) are compared for $z/H <= 0.1$. 136

D.1 Workflow of the FGM-3D approach (ϵ is the tolerance set in the CFD solver). 137
D.2 Workflow of the FGM-4D approach (ϵ is the tolerance set in the CFD solver). 138

E.1 Comparison of the temperature field between the DK simulation and tabulated manifolds: (left) DK and FGM-4D (*a-priori*), (right) DK and FGM-3D (*a-priori*). 139
E.2 The *a-priori* analysis: profiles of mass fractions of CO_2, H_2, CO, OH, and heat release rate (HRR) for several positions marked in Fig. E.1 obtained from the DK simulation and both tabulated manifolds. 140

List of Tables

4.1 Summary of the investigated strained HOQ conditions. 37

5.1 Identified manifolds for different gradient estimations. 59

6.1 Gradient estimations used to generate REDIMs for the first (RK1), the second (RK2), and the third (RK3) reduced kinetic simulations. 65
6.2 Quenching heights obtained from the detailed kinetics (DK) and the first (RK1), the second (RK2), and the third (RK3) reduced kinetic simulations. 65
6.3 Maximum discrepancies in species mass fractions among positions (a), (b), and (c) at $x > 1$ mm, for the first (RK1), the second (RK2), and the third (RK3) reduced kinetic simulations (compared with the detailed kinetics). 68

F.1 Equilibrium states for $\phi = 0.768$, $T_{\mathrm{fuel}} = 300$ K, $Z_{\mathrm{mix}} = 0.5$. 141
F.2 Equilibrium states for $\phi = 0.768$, $T_{\mathrm{fuel}} = 550$ K, $Z_{\mathrm{mix}} = 0.5$. 141
F.3 Equilibrium states for $\phi = 0.97$, $T_{\mathrm{fuel}} = 300$ K, $Z_{\mathrm{mix}} = 0.5$. 141
F.4 Equilibrium states for $\phi = 0.768$, $T_{\mathrm{fuel}} = 300$ K, $Z_{\mathrm{mix}} = 0.9$. 142

Appendix A: Grid dependency study for the laminar CH_4-air side-wall quenching simulations

Prior to the CFD simulations performed in Chapter 5, a grid convergence study was conducted over two grid resolutions: Grid A and Grid B. Grid A refers to the one that is adopted in Chapter 5, where the grid is non-equidistant in x direction, with the finest grid resolution being $\triangle x = 10$ μm near the wall, and the coarsest grid resolution is $\triangle x = 50$ μm near the right outlet, while the grid resolution in y direction keeps constant of $\triangle y = 10$ μm, resulting a total number of cells 168000. Grid B refers to the one where the near-wall grid resolution is further refined since this region is most prone to be affected by the inadequate grid resolution. Grid B is also stretched in x direction, and the finest grid resolution is $\triangle x = 5$ μm near the wall, while the coarsest grid resolution is $\triangle x = 50$ μm near the right outlet. The grid resolution in y direction keeps the same as that of Grid A. The total number of cells of Grid B is 204000.

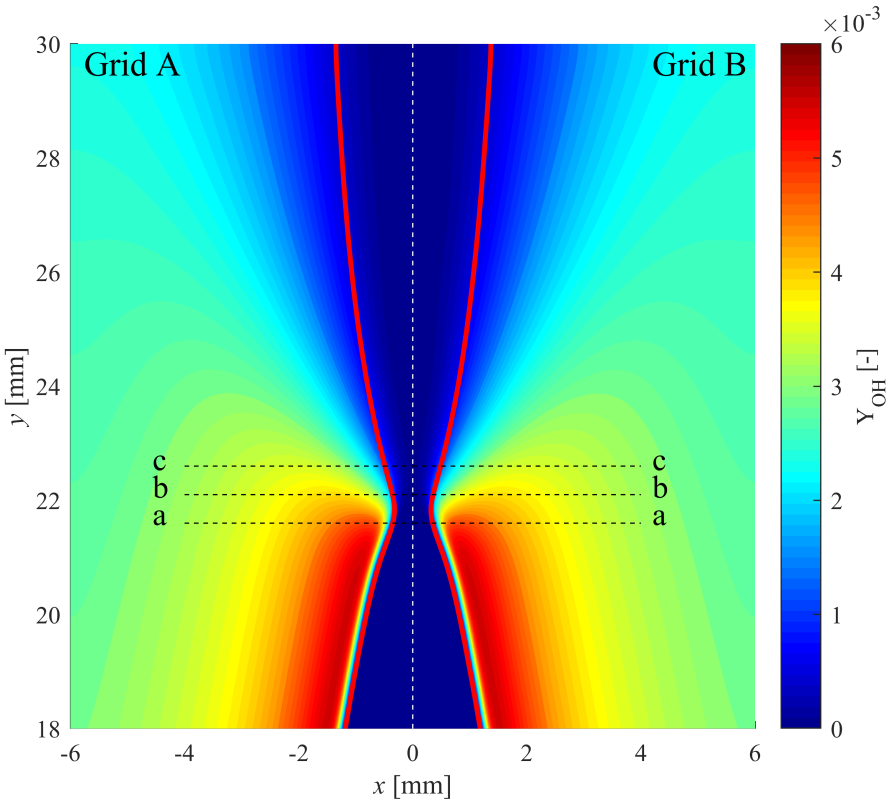

Figure A.1: Distributions of OH mass fraction for two grids. The flame shape is also shown by an isoline of the temperature T = 1500 K (red). The three black dashed horizontal lines near the flame tip depict the extraction lines for the CO and temperature data. The positions (a), (b), and (c) corresponds to y = 21.6 mm, y = 22.1 mm, and y = 22.6 mm, respectively.

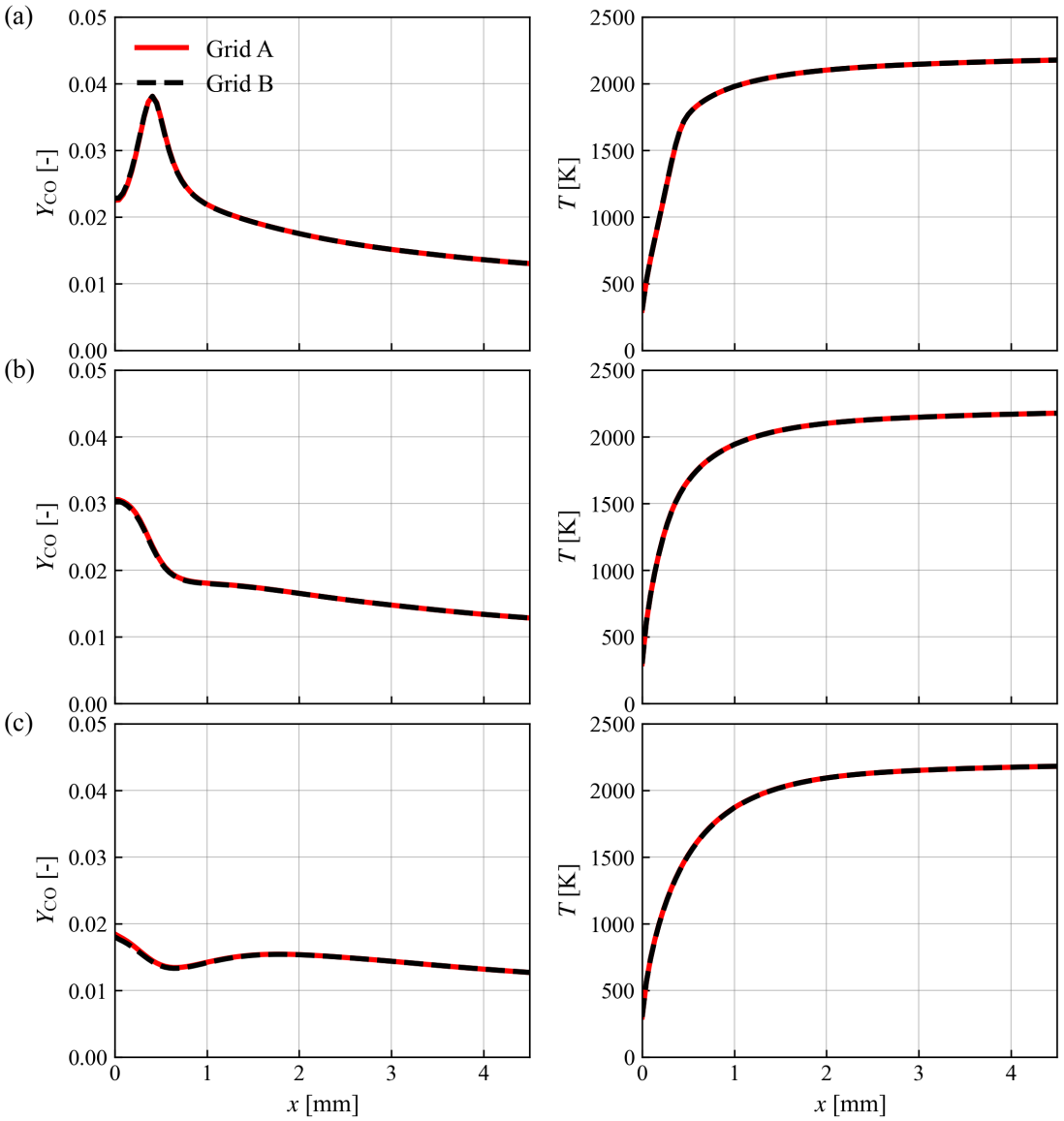

Figure A.2: Comparison of CO mass fraction and temperature of two different grids at different positions: (a) y = 21.6 mm, (b) y = 22.1 mm, (c) y = 22.6 mm.

Shown in Fig. A.1 is the comparison of the OH distribution of two grids. It is found that the flame shape from the coarse grid (Grid A) is similar to that from finer grid (Grid B). Also the quenching height determined by the maximum wall heat flux agrees quite well, which is 22.1 mm for both grids. For quantitative comparison, Fig. A.2 compares the CO mass fraction and temperature at different positions between Grid A and Grid B. It is shown that the resolution of Grid A is enough for the study in Chapter 5, since the results almost keep the same when further increasing the near-wall grid resolution.

Appendix B: Validation of the reduced model equations in generalized coordinates for head-on quenching

In the HOQ configuration, a planar flame propagates towards a wall with a constant temperature 300 K. The region between the flame and the wall is initially filled with a stoichiometric CH_4-air mixture at 300 K. The setup is similar to that in Chapter 4, except that the strain rate effects are not taken into account. The process is simulated using both detailed kinetics and reduced model equations in generalized coordinates.

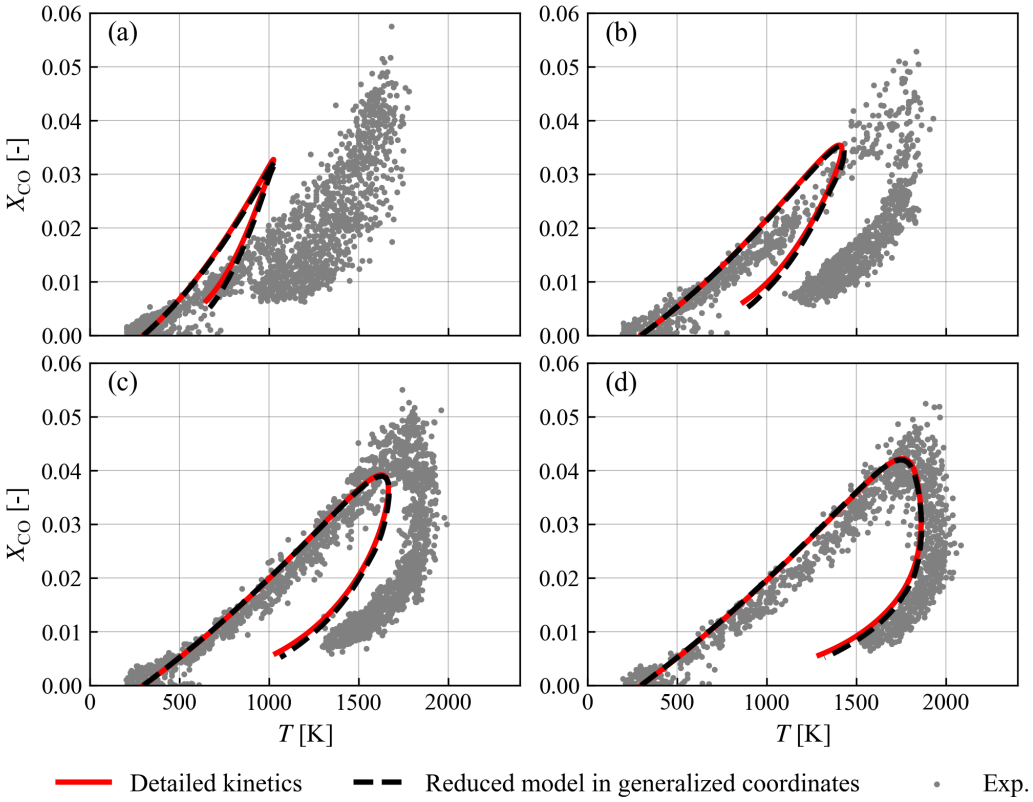

Figure B.1: CO-T plots from computations of detailed kinetics and reduced model equations in generalized coordinates for different near-wall positions: (a) wall distance = 0.1 mm, (b) wall distance = 0.2 mm, (c) wall distance = 0.3 mm, (d) wall distance = 0.5 mm. The experimental data are represented as scatters.

To validate the reduced model equations in generalized coordinates in Chapter 5, thermo-chemical states in the CO-T phase are investigated for the near-wall region at different distances from the wall. Four different positions are chosen, at distances to the wall of 0.1 mm, 0.2 mm, 0.3 mm, and 0.5 mm, respectively, as shown in Fig. B.1. Here, the experimental data obtained from a similar setup [20] is also included for reference.

The overall variation trend is well captured by the simulations. However, there are still discrepancies between the simulation results and experimental data, especially for positions close to the wall. Such differences may be attributed to both experimental uncertainties in the determination of the wall position [20] and the simple molecular transport model adopted in the simulation [33], with the former one being the dominant reason. As shown in Chapter 4, the uncertainty in wall position determination in the experiment has a significant influence on the overall trend. In contrast, the use of a simple molecular transport model only affects the value, but does not change the trend [33]. It is observed that good agreement is obtained between the simulation results using detailed kinetics and the reduced model equations in generalized coordinates, despite the differences between the simulations and the experiment. For all positions, the two results almost overlap, while the very small discrepancies may be attributed to numerical errors induced by table interpolations. Overall, the validity of the implemented reduced model equations in generalized coordinates is demonstrated.

Appendix C: An *a-priori* analysis for FGM, QFM, and QFM-EGR

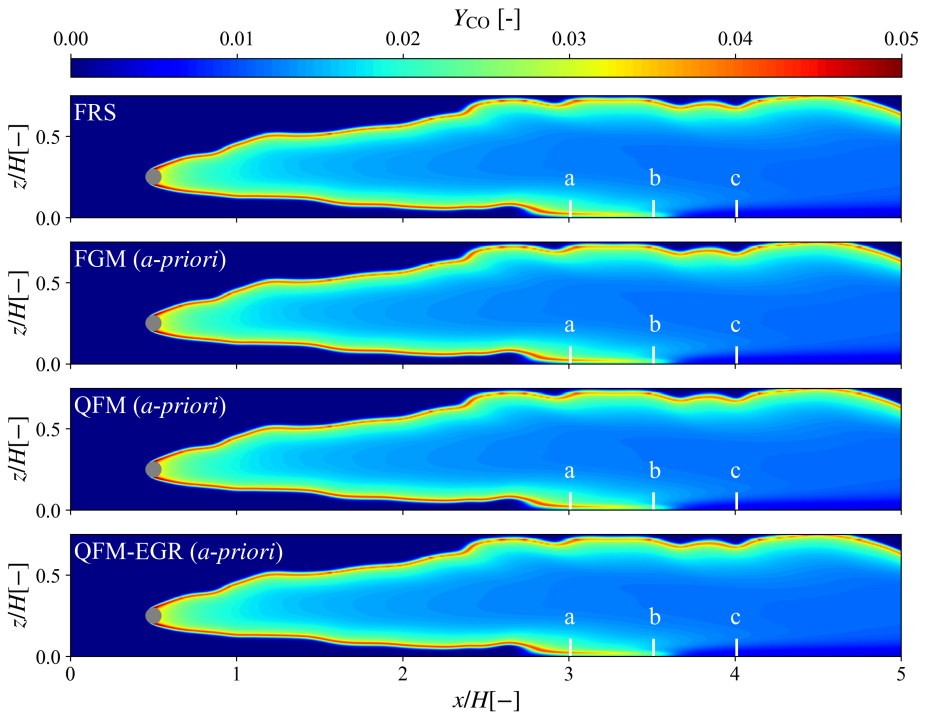

Figure C.1: The a-priori results for CO for the slice y = 15 mm. Results of FRS reference, a-priori of FGM, a-priori of QFM and a-priori of QFM-EGR are presented from the top to the bottom. (a), (b), and (c) are positions where thermo-chemical quantities are sampled, which corresponds to x_q = -0.5H, 0, and 0.5H, respectively. Here, $x_q = 0$ corresponds to the axial position of the quenching point.

To conduct an *a-priori* analysis for FGM, QFM, and QFM-EGR in Chapter 8, FRS results at a randomly chosen time instant are used. For better visualization, the *a-priori* results of a slice parallel to the xz plane with y = 15 mm are shown in Fig. C.1. From the CO contours, it is observed that *a-priori* results of FGM, QFM, and QFM-EGR all show similar characteristics as FRS. It is hard to distinguish the differences between FGM, QFM, and QFM-EGR. Therefore, for a more detailed investigation, quantitative comparison is made for several thermo-chemical quantities near the quenching zone. Specifically, three lines vertical to the wall are chosen, corresponding to x_q = -0.5H, 0, and 0.5H respectively, as denoted by the white lines (a), (b), and (c) in Fig. C.1. Note (b) corresponds to the axial quenching position of the FRS results, and (a) is $0.5x/H$ upstream, (c) $0.5x/H$ downstream. Figure C.2 shows the distribution of mass fractions of CO and OH, as well as the temperature T. At x_q = -0.5H, both *a-priori* results of QFM and QFM-EGR show good agreement with the reference data, while discrepancies exist in CO and T for FGM in the region very

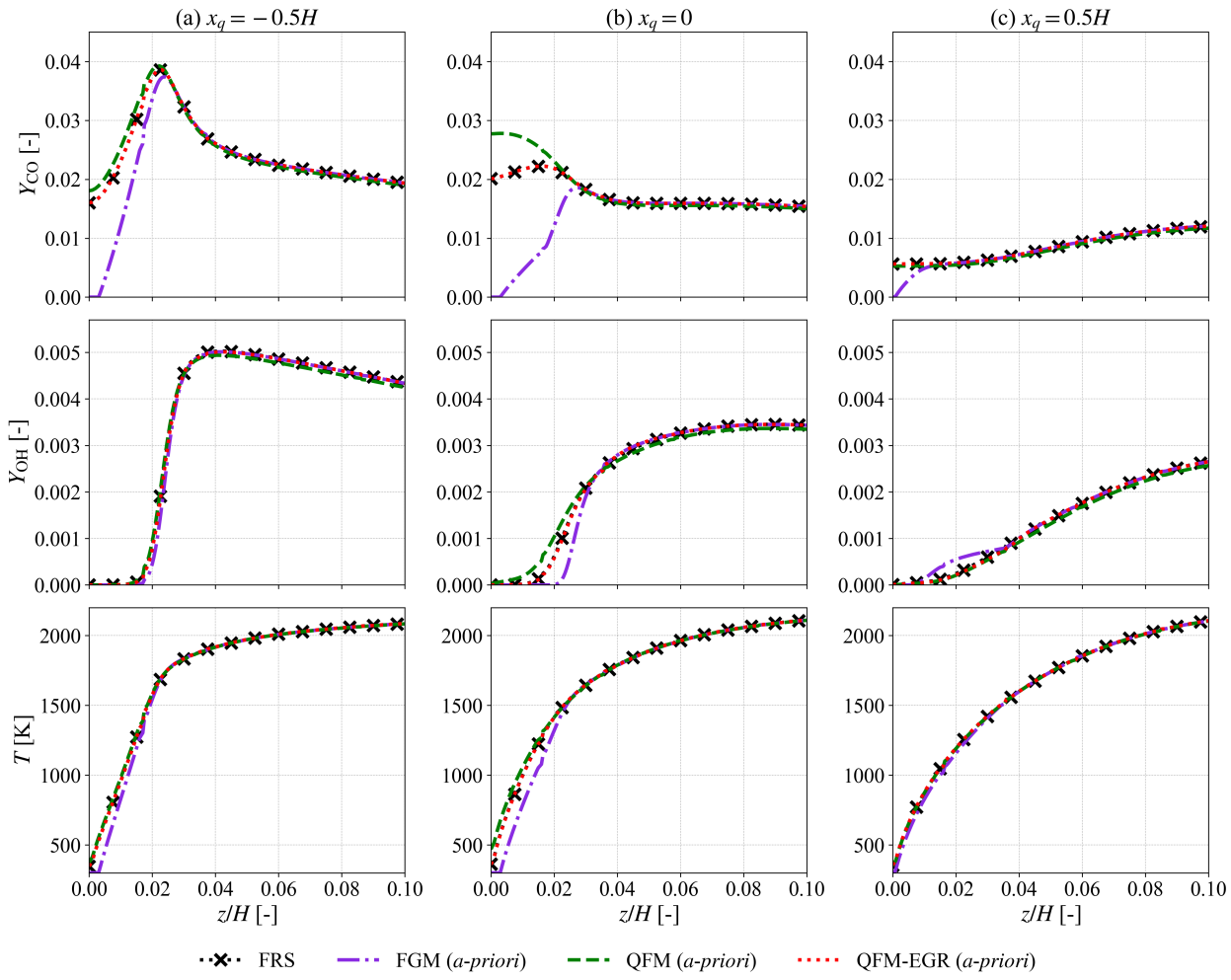

Figure C.2: The a-priori results for the mass fractions of CO, OH, and temperature T for (a) $x_q = -0.5H$, (b) $x_q = 0$, and (c) $x_q = 0.5H$ at the slice y = 15 mm. Results of FRS reference (black dashed lines marked with cross symbols), a-priori of FGM (violet dash-dotted lines), a-priori of QFM (green dashed lines), and a-priori of QFM-EGR (red dashed lines) are compared for $z/H <= 0.1$.

close to the wall. With FGM, At x_q = 0, the three manifolds show different performances. For QFM-EGR, all results almost overlap with those from FRS. For QFM, the temperature can be almost correctly predicted, while the species show deviations from FRS data. When using QFM, CO and OH are overpredicted in the vicinity close to the wall, especially for CO, with a maximum deviation up to 40%. In contrast, all near-wall quantities considered are underpredicted by FGM. The maximum deviation even reaches up to 100% for CO. This is consistent with the findings in laminar SWQ [76]. Moving downstream to x_q = 0.5H, both QFM and QFM-EGR show good prediction for the species and temperature, with QFM-EGR performing slightly better. For FGM, small deviations are observed in the near-wall region. Based on the above analysis, it can be concluded that QFM-EGR is able to reproduce comparable results as FRS, which presents the best performance among the three manifolds. Then the QFM shows comparatively worse agreement with FRS, and deviations mainly exist for regions near the quenching point, especially for CO. The prediction capability of FGM is the weakest among the three, with large discrepancies in the very near-wall region. This finding is consistent with the laminar SWQ studies [111].

Appendix D: Workflow of FGM-3D and FGM-4D

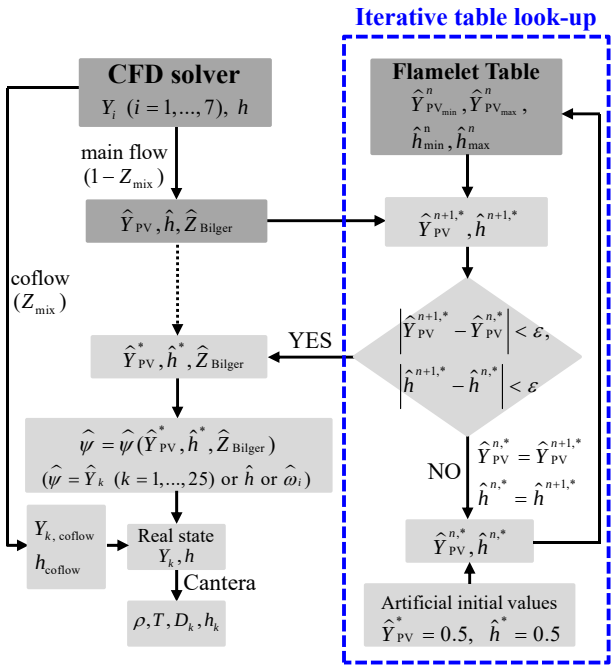

Figure D.1: Workflow of the FGM-3D approach (ϵ is the tolerance set in the CFD solver).

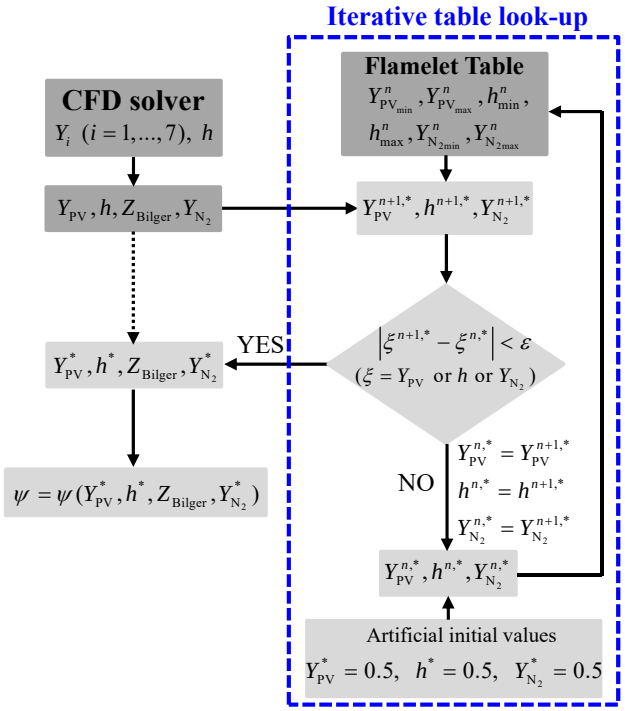

Figure D.2: Workflow of the FGM-4D approach (ϵ is the tolerance set in the CFD solver).

Appendix E: An *a-priori* analysis for FGM-3D and FGM-4D

To conduct an *a-priori* analysis for FGM-3D and FGM-4D in Chapter 9, the control variables are reconstructed based on DK results and used for accessing the tabulated manifolds. From the comparison of dependent quantities (e.g., temperature, species, and source terms, etc.) between DK and the tabulated manifold, the accuracy of the tabulation strategy can be assessed, provided that the control variables are accurately known.

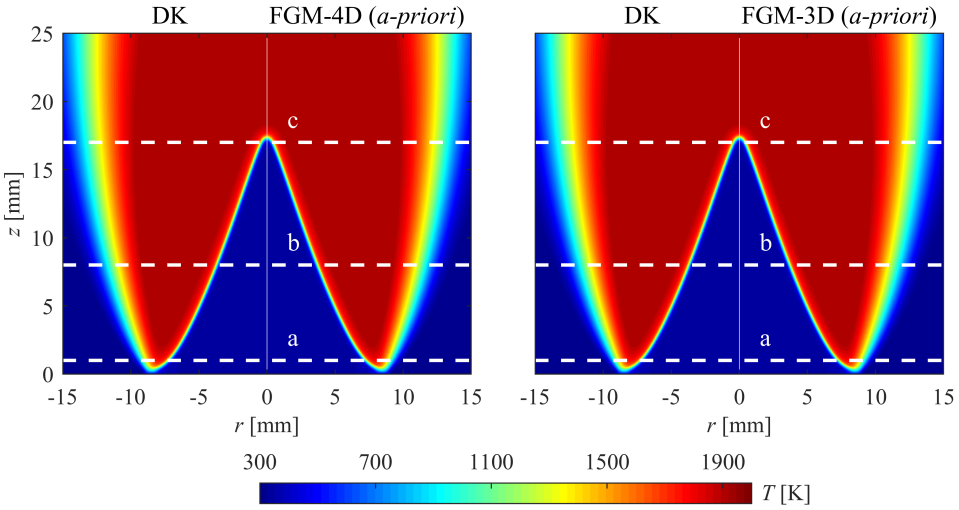

Figure E.1: Comparison of the temperature field between the DK simulation and tabulated manifolds: (left) DK and FGM-4D (a-priori), (right) DK and FGM-3D (a-priori).

Qualitative comparisons are first performed. To examine the general flame shape, the temperature field is shown in Fig. E.1. It can be found that both *a-priori* results agree very well with the DK.

Afterwards, the *a-priori* results of FGM approaches are quantitatively compared with DK results in Fig. E.2. Here, three axial positions are chosen, $z = 1$ mm (a), $z = 8$ mm (b), and $z = 17$ mm (c), as denoted by white dashed lines respectively in Fig. E.1. For CO_2, H_2, and CO mass fractions, the *a-priori* results of both FGM-3D and FGM-4D almost overlap with the DK results. For OH mass fraction and the heat release rate (HRR), the *a-priori* results of FGM-4D still show accurate agreement with the DK reference, while overpredictions are found in the mixing layer for FGM-3D. This is caused by the “linear mixing" assumption adopted in the FGM-3D approach. Specifically, the introduction of N_2 changes the local equilibrium of the burned products, therefore the mixing between coflow and the burned products is not simply a linear relation as assumed in FGM-3D. It is found that the difference is more pronounced on radicals such as OH where the deviation can be locally up to 2–3 orders of magnitude, while it is relatively small in the case of major species such as CO_2. A comparison of several equilibrium states corresponding to different fresh gas mixtures between FGM-3D and FGM-4D is provided in Appendix F.

Based on the above *a-priori* results, it is found that both FGM-4D and FGM-3D are capable of describing

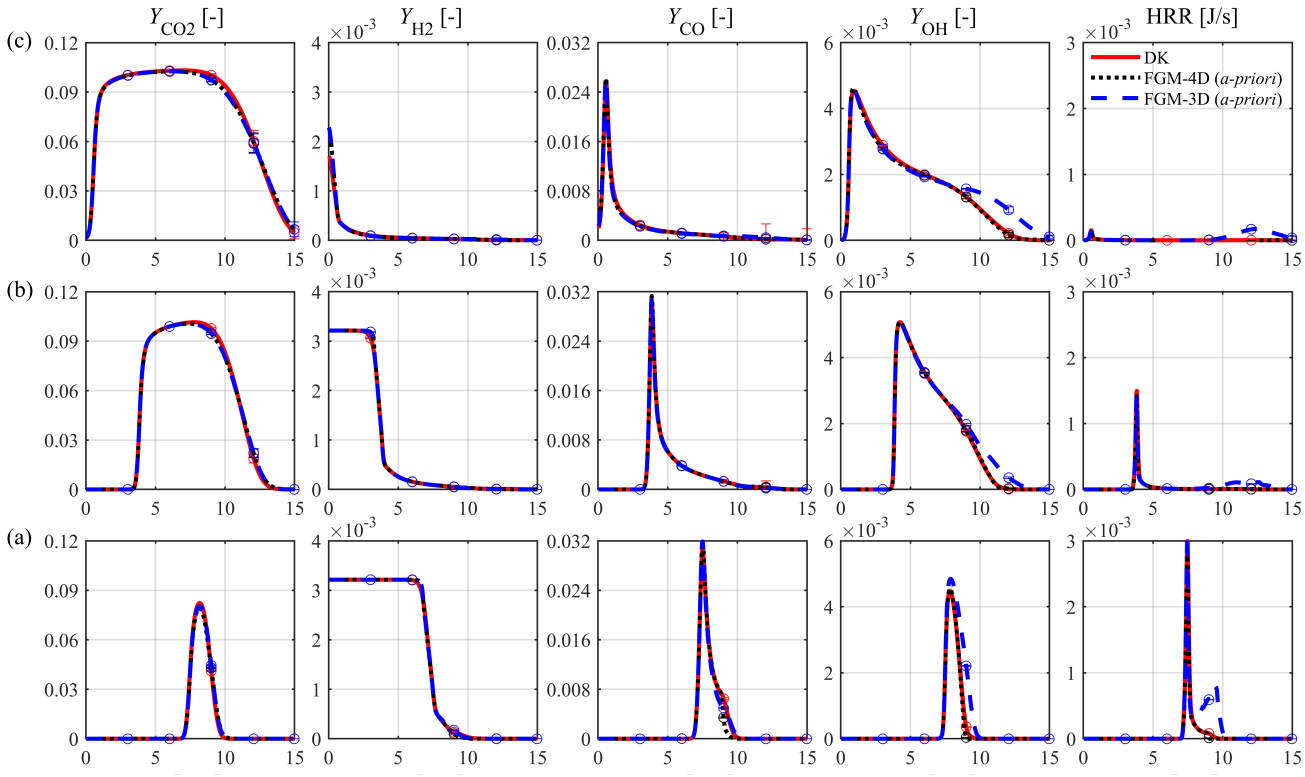

Figure E.2: The a-priori analysis: profiles of mass fractions of CO_2, H_2, CO, OH, and heat release rate (HRR) for several positions marked in Fig. E.1 obtained from the DK simulation and both tabulated manifolds.

the flame region accurately, while FGM-3D shows discrepancies for minor species and HRR in the mixing layer.

Appendix F: Comparison of equilibrium states from FGM-3D and FGM-4D approaches

To understand the deviations shown in the mixing layer for FGM-3D in Appendix E, several equilibrium states corresponds to different equivalence ratio (ϕ), temperature of the unburned gas (T_{fuel}), and mixture fraction of N_2 coflow mass (Z_{mix}) are compared between FGM-3D and FGM-4D, as listed in Tables F.1, F.2, F.3, and F.4. Here, the states for FGM-4D are directly obtained by calculating one-dimensional freely propagating flames with N_2 dilution in the fresh mixture. As for the FGM-3D, the equilibrium states corresponding to the one-dimensional freely propagating flames without N_2 addition are linearly combined with the states of pure N_2 based on Z_{mix} to obtain the final equilibrium states, similarly to Eq. (9.4). For better comparison, the relative difference is introduced, which is calculated as the division of the absolute differences between FGM-3D and FGM-4D by the results from FGM-4D.

Species	FGM-3D	FGM-4D	Relative difference
Y_{OH}	5.68e-4	4.50e-6	$> 100\%$
Y_{CO}	1.72e-4	8.36e-8	$> 100\%$
$Y_{\mathrm{CO_2}}$	5.03e-2	5.06e-2	$< 1\%$
$Y_{\mathrm{H_2O}}$	5.49e-2	5.53e-2	$< 1\%$

Table F.1: Equilibrium states for ϕ = 0.768, T_{fuel} = 300 K, Z_{mix} = 0.5.

Species	FGM-3D	FGM-4D	Relative difference
Y_{OH}	1.23e-3	2.59e-5	$> 100\%$
Y_{CO}	6.50e-4	9.93e-7	$> 100\%$
$Y_{\mathrm{CO_2}}$	4.96e-2	5.06e-2	$< 10\%$
$Y_{\mathrm{H_2O}}$	5.44e-2	5.52e-2	$< 10\%$

Table F.2: Equilibrium states for ϕ = 0.768, T_{fuel} = 550 K, Z_{mix} = 0.5.

Species	FGM-3D	FGM-4D	Relative difference
Y_{OH}	1.30e-3	3.04e-5	$> 100\%$
Y_{CO}	3.03e-3	1.11e-5	$> 100\%$
$Y_{\mathrm{CO_2}}$	5.84e-2	6.32e-2	$< 10\%$
$Y_{\mathrm{H_2O}}$	6.73e-2	6.90e-2	$< 10\%$

Table F.3: Equilibrium states for ϕ = 0.97, T_{fuel} = 300 K, Z_{mix} = 0.5.

Species	FGM-3D	FGM-4D	Relative difference
Y_{OH}	1.02e-3	5.26e-4	$< 100\%$
Y_{CO}	3.10e-4	9.88e-5	$> 100\%$
$Y_{\mathrm{CO_2}}$	9.06e-2	9.09e-2	$< 1\%$
$Y_{\mathrm{H_2O}}$	9.88e-2	9.91e-2	$< 1\%$

Table F.4: Equilibrium states for ϕ = 0.768, T_{fuel} = 300 K, Z_{mix} = 0.9.